University of Alberta

Synthesis and Microstructural Characterization of Manganese Oxide Electrodes for Application as Electrochemical Supercapacitors

by

Banafsheh Babakhani

A thesis submitted to the Faculty of Graduate Studies and Research
in partial fulfillment of the requirements for the degree of

Doctor of Philosophy

in Materials Engineering

Department of Chemical and Materials Engineering

Fall 2011

Edmonton, Alberta

To my parents for their endless love and support

Abstract

The aim of this thesis work was to synthesize Mn-based oxide electrodes with high surface area structures by anodic electrodeposition for application as electrochemical capacitors.

Rod-like structures provide large surface areas leading to high specific capacitances. Since templated electrosynthesis of rods is not easy to use in practical applications, it is more desirable to form rod-like structures without using any templates. In this work, Mn oxide electrodes with rod-like structures (~1.5 μm in diameter) were synthesized from a solution of 0.01 M Mn acetate under galvanostatic control without any templates, on Au coated Si substrates. The electrochemical properties of the synthesized nanocrystalline electrodes were investigated to determine the effect of morphology, chemistry and crystal structure on the corresponding electrochemical behavior of Mn oxide electrodes. Mn oxides prepared at different current densities showed a defective antifluorite-type crystal structure. The rod-like Mn oxide electrodes synthesized at low current densities (5 $mAcm^{-2}$) exhibited a high specific capacitance due to their large surface areas. Also, specific capacity retention after 250 cycles in an aqueous solution of 0.5 M Na_2SO_4 at 100 mVs^{-1} was about 78% of the initial capacity (203 Fg^{-1}).

To improve the electrochemical capacitive behavior of Mn oxide electrodes, a sequential approach and a one–step method were adopted to synthesize Mn

oxide/PEDOT electrodes through anodic deposition on Au coated Si substrates from aqueous solutions. In the former case, free standing Mn oxide rods (about 10 μm long and less than 1.5 μm in diameter) were first synthesized, then coated by electro–polymerization of a conducting polymer (PEDOT) giving coaxial rods. The one–step, co–electrodeposition method produced agglomerated Mn oxide/PEDOT particles. The electrochemical behavior of the deposits depended on the morphology and crystal structure of the fabricated electrodes, which were affected by the composition and pH of the electrolyte, temperature, current density and polymer deposition time. Mn oxide/PEDOT coaxial core/shell rods consisted of MnO_2 with an antifluorite–type structure coated with amorphous PEDOT. The Mn oxide/PEDOT coaxial core/shell electrodes prepared by the sequential method showed significantly better specific capacity and redox performance properties relative to both uncoated Mn oxide rods and co–electrodeposited Mn oxide/PEDOT electrodes. The best specific capacitance for Mn oxide/PEDOT rods produced sequentially was ~295 F g^{-1} with ~92% retention after 250 cycles in 0.5 M Na_2SO_4 at 100 mV s^{-1}.

To further improve the electrochemical capacitive behavior of Mn oxide electrodes, Co-doped and Fe-doped Mn oxide electrodes with a rod-like morphology and antifluorite-type crystal structure were synthesized by anodic electrodeposition, on Au coated Si substrates, from dilute solutions of Mn acetate and Co sulphate and Mn acetate and Fe chloride. Also, Mn-Co oxide/PEDOT coaxial core/shell rods were synthesized by applying a shell of PEDOT on Mn-Co

oxide electrodes. Mn-Co oxide/PEDOT electrodes consisted of MnO_2, with partial Co^{2+} and Co^{3+} ion substitution for Mn^{4+}, and amorphous PEDOT. Mn-Fe oxide electrodes consisted of MnO_2, with partial Fe^{2+} and Fe^{3+} ion substitution for Mn^{4+}. Electrochemical analysis showed that the capacitance values for all deposits increased with increasing scan rate to 100 mVs^{-1}, and then decreased after 100 mVs^{-1}. The Mn-Co oxide/PEDOT electrodes showed improved specific capacity and electrochemical cyclability relative to uncoated Mn-Co oxides and Mn-Fe oxides. Mn-Co oxide/PEDOT electrodes with rod-like structures had high capacitances (up to 310 Fg^{-1}) at a scan rate of 100 mVs^{-1} and maintained their capacitance after 500 cycles in 0.5 M Na_2SO_4 (91% retention). Capacitance reduction for the deposits was mainly due to the loss of Mn ions by dissolution in the electrolyte solution.

To better understand the nucleation and growth mechanisms of Mn oxide electrodes, the effects of supersaturation ratio on the morphology and crystal structure of electrodeposited Mn oxide were studied. By changing deposition parameters, including deposition current density, electrolyte composition, pH and temperature, a series of nanocrystalline Mn oxide electrodes with various morphologies (continuous coatings, rod–like structures, aggregated rods and thin sheets) and an antifluorite–type crystal structure was obtained. Mn oxide thin sheets showed instantaneous nucleation and single crystalline growth; rods had a mix of instantaneous/progressive nucleation and polycrystalline growth and continuous coatings formed by progressive nucleation and polycrystalline growth.

Electrochemical analysis revealed the best capacitance behaviour obtained for Mn oxide thin sheets followed by Mn oxide rods, with dimensions on the microscale, and then continuous coatings. The highest specific capacitance (~230 Fg^{-1}) and capacitance retention rates (~88%) were obtained for Mn oxide thin sheets after 250 cycles in 0.5 M Na_2SO_4 at 20 mVs^{-1}.

Acknowledgements

I would like to express my sincere gratitude to Prof. Douglas G. Ivey for his supervision, splendid guidance and encouragement during my PhD reasearch program. His support, encouragement and patience provided me with a great experience which is highly appreciated. I am also grateful to Dr. Liu and Dr. Choi from my supervisory committee for their wonderful advice.

The financial support from the Natural Sciences and Engineering Research Council (NSERC) of Canada is gratefully acknowledged. Also, I would like to acknowledge Micralyne Inc. for providing metalized wafers.

I also would like to thank Tina Barker (SEM/EDX), Dimitre Karpuzov (XPS), Shiraz Merali (XRD), Anqiang He (XPS) and all the technical support from the Alberta Centre for Surface Engineering and Science (ACSES). Roham Eslahpazir is acknowledged for assisting with SEM and TEM analysis.

I would like to thank Lily Laser for her kind support during my PhD program.

I also appreciate my family members including my mother Azam, my father Parviz, my sisters Bita and Mahshid and my brother Masoud who have invaluably supported me throughout my life. I am also thankful to our group members and all my friends especially Mohsen who made my life full of happiness.

Table of Contents

List of Tables

List of Figures

List of Symbols, Nomenclature, or Abbreviations

Abbreviations

AAO	Anodised aluminium oxide
AAS	Atomic absorption spectroscopy
AES	Auger electron spectroscopy
BF	Bright field
CV	Cyclic voltammetry
CPS	Counts per second
1D	One-dimentional
2D	Two-dimentional
3D	Three-dimentional
DF	Dark field
EDOT	Ethylenedioxythiophene
EDX	Energy-dispersive X-ray
EIS	Electrochemical impedance spectroscopy
FCC	Face centered cubic
FIB	Focused ion beam
PANI	Polyaniline
PEDOT	Polyethylenedioxythiophene
PPY	Polypyrrole
SAED	Selected area electron diffraction
SCE	Saturated calomel electrode
SDS	Sodium dodecyl sulfate
SEM	Scanning electron microscopy
TEM	Transmission electron microscopy
UPD	Underpotential deposition
XPS	X-ray photoelectron spectroscopy
XRD	X-ray diffraction

Symbols

A	Ampere
a	Activity
cm	Centimeter
C	Capacitance
ºC	Centigrade degrees
Co	Cobalt
ΔE	Splitting width
E	Energy
E	Operating potential
E_0	Standard potential
eV	Electron-volt
F	Faraday constant
μF	micro-Farad
Fe	Iron
g	Gram
h	Hour
ΔH	Change in Enthalpy
η	Overpotential
η_k	Current efficiency
Hz	Hertz
I	Current
i	Current density
k	Kinetic constant
M	Mole
m	Mass
mA	Milli-ampere
Mn	Manganese
mV	Milli-volt
N	Number of active sites
O	Oxygen

P	Power
ρ	Density
Q	Charge
R	Gas constant
Ru	Ruthenium
S	Supersaturation ratio
S	Siemens
s	Seconds
T	Temperature
t	Time
V	Vanadium
V	Voltage
W	Watt
W1	Warburg

Introduction

Research on electrochemical capacitors has generated growing interest from both academia and industry in recent years, with efforts focused on developing safe, stable, high energy/power density and low cost materials [1]. Electrochemical supercapacitors are charge storage devices that make use of electrochemical phenomena in order to store charge [1,2]. They are often used in conjunction with other energy storage devices, such as batteries, to improve the overall performance of the system by providing bursts of energy. Electrochemical supercapacitors are considered as promising power storage devices for back up power storage, peak power sources and hybrid electric and fuel cell vehicles, due to their high power density, short charge/discharge time, long cycle life and excellent reversibility [3-6].

Manganese (Mn) based oxides have been widely studied for electrochemical capacitors, because of their high energy density, low cost, natural abundance and the environmentally benign nature of Mn. As an active material for electrochemical capacitors, amorphous/crystalline Mn oxide shows high specific capacitance due to the utilization of both electric double layer and redox effects [7,8]. Mn oxide acts as a low cost replacement for noble metal oxides, such as ruthenium (Ru) oxide, providing high specific capacitance [9,10]. However, there is a drawback to the application of Mn oxides: the loss of Mn oxide through partial dissolution during cycling. The cause is generally considered to be the disproportionation of trivalent Mn during electrochemical cycling [11]. Generally, polymers are insoluble in water; therefore, the presence of a polymer coating may be able to suppress dissolution. Moreover, Mn oxide has poor electronic conductivity, which can be compensated through the addition of a conductive polymer [12]. To further improve electrochemical capacitors, much effort has focused on the development of bimetal composite materials. For example, the pseudocapacitive performance of Mn oxide electrodes has been improved by

addition of other transition metal oxides such as cobalt (Co) and vanadium (V) oxides [13,14].

Since both transition metal oxides and conductive polymers are important electroactive materials used in electrochemical energy storage, the combination of these two materials as rod-like structures can produce good electrical, electrochemical and mechanical properties for electrochemical energy storage [15,16]. Rod-like structures provide short transport/diffusion path lengths for both ions and electrons, leading to faster kinetics, and also large specific surface areas, resulting in high charge/discharge capacities [17,18]. Recently, coaxial core/shell metal oxide/conducting polymer electrodes with rod-like structures have attracted great attention in this field [17], although to date only a few reports have been published on the synthesis of these electrodes. It is more desirable to form rod-like structures without using any templates or catalysts to make the process simpler and cheaper.

Anodic electrodeposition is one of the most promising approaches among various techniques for fabrication of uniform thin films on various substrates of complex shape [19]. Surface morphology, uniformity and crystal structure of the oxide deposits that can affect the electrochemical behavior of deposits are easily controlled by adjusting the variables of electrochemical deposition and supersaturation ratio [20]. The aim of this research work is to study the anodic deposition process to synthesize Mn oxide electrodes with rod-like structures to improve the electrochemical behavior of Mn oxide electrodes. The morphology, chemistry and crystal structure of the Mn oxide coatings can be manipulated by adjusting deposition parameters such as deposition current density, electrolyte composition and pH, deposition time and temperature. The effects of applying a shell of a conducting polymer (polyethylenedioxythiophene or PEDOT) on Mn oxide rods and the addition of other transition metal oxides such as Co and Fe oxide on the morphology, chemistry and crystal structure of Mn oxide electrodes are investigated. The relationship between microstructural evolution of the

electrodes and the corresponding electrochemical behaviour of the electrodes is determined. Also, the nucleation and growth mechanisms of Mn oxide electrodes are investigated by considering the effects of supersaturation ratio on the morphology and crystal structure of electrodeposited Mn oxide electrodes.

Chapter 1 Literature survey

1.1 Capacitors

Capacitors are electrical circuit elements that store electrical energy on the order of microfarads. Capacitors are electrochemical devices where pseudo-reversible electrochemical charge–discharge processes occur. Capacitors have two main applications [21]:

(1) Charge or discharge electricity which is applied to smoothing circuits of power supplies, backup circuits of microcomputers and timer circuits that make use of the periods to charge or discharge electricity.

(2) Block the flow of direct current.

Capacitors are divided in three different groups [5]:

(1) Film (dielectric) capacitors

(2) Electrolytic capacitors

(3) Electrochemical supercapacitors

Table 1-1 shows the characteristics of different types of capacitors.

Table 1-1 Different types of electrochemical capacitors [5]

Type of capacitor	Advantages	Applications	Type of electrodes	Capacitance
Dielectric type	Prevents direct electrical contact of plates	High voltage and high temperature applications	Metallic electrode, e.g., Al	0.1-1μF
Electrolytic type	Higher capacitance compared to dielectric type	Power-supply conditioning	Al or Ta plate with an oxide dielectric layer and liquid electrolyte	1-10 μF
Electrochemical supercapacitors	Higher capacitance compared to others	Portable power sources; electronic vehicles	Carbon, transition metal oxides (Ru, Mn, Co, V, Mo); polymers; composites	Ru: 650-750 Fg^{-1} Mn: 150-250 Fg^{-1}

1.2 Electrochemical supercapacitors

Electrochemical supercapacitors are charge storage devices that make use of electrochemical phenomena in order to store charge. They consist of two electrodes, an electrolyte and a conducting path in order to operate [1,2].

Electrochemical supercapacitors are used in portable electronic devices, backup power storage, peak power sources and hybrid electric and fuel cell vehicles due to their high power density, short charge/discharge time, long cycle life and excellent reversibility. According to the intrinsic principles of charge storage and

discharge in electrochemical supercapacitors, there are two kinds of capacitance: double layer or electrostatic capacitance and pseudocapacitance. Double layer capacitance is a non-Faradaic process where charge is stored directly across the electrical double layer, while pseudocapacitance involves a Faradaic process which stores charge using a redox reaction [3-6,22].

The energy storage characteristics of electrochemical supercapacitors are dependent upon the physical characteristics of both the electrolyte and electrode materials such as concentration of redox active sites, surface area, pore volumes and pore size distributions, particle sizes and morphology [23,24].

Although recently developed batteries can provide high energy densities, they still suffer from low power densities. One solution to this problem is the use of nanostructured batteries, which can provide high power density by enhancing the charge/discharge rates [25,26]. Another approach is to use electrochemical supercapacitors, which produce necessarily high peak power in conjunction with a battery [27]. The energy (E) of any energy storage device under a constant current is given by [28]:

$$E = \int V \, \mathrm{d}q = \mathrm{I} \int V \, \mathrm{d}t \tag{1-1}$$

where V, q, I and t represent the voltage, charge, current and time, respectively.

Power is also defined as the energy generated or consumed in a time interval dt:

$$P = \mathrm{d}E/\mathrm{d}t = VI \tag{1-2}$$

Because the voltage changes linearly with time, the average power density becomes half of the maximum power density.

Batteries and low temperature fuel cells are typically low power devices, whereas conventional capacitors may have a specific power of $>10^6$ W/kg at very low specific energy (Figure 1-1). Electrochemical supercapacitors fill the gap between batteries and conventional capacitors in terms of both specific energy and power, i.e., they have a specific power as high as conventional capacitors and a specific energy close to that of batteries. Typically they exhibit 20-200 times more capacitance per unit volume or mass than conventional capacitors. Therefore, electrochemical supercapacitors can improve battery performance in terms of power density when combined with batteries [3,29,30].

Specific power refers to power per unit of mass. However, fuels and batteries are usually measured in terms of energy density which is the amount of energy stored in a system per unit mass.

$$\log(\text{energy}) = \log(\text{power}) + \log(\text{time}) \qquad (1\text{-}3)$$

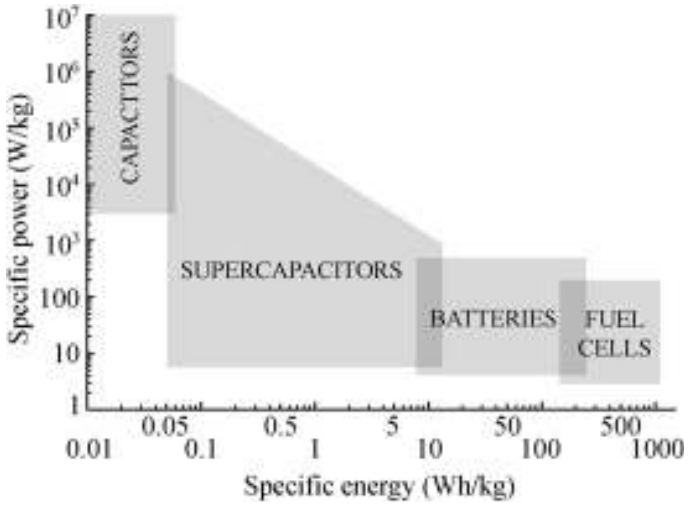

Figure 1-1 Ragone plot showing specific power versus specific energy for various energy storage devices [2].

1.2.1 Double layer capacitors

The first patent for double-layer capacitors was published in 1957, in which a capacitor based on high surface area carbon was described [3,5].

1.2.1.1 Double layer capacitance theory

Double layer capacitors store electric charge directly across the double layer of the electrode. This is a true capacitance effect as there is no charge transfer across the interface. Figure 1-2 shows an electrochemical double layer cell. Separation of ionic charges arises at the interface between the electrode and ionic solutions giving rise to the double layer. An accumulation of charge, Δq, of opposite sign takes place across the interface, which depends on the potential difference built up across the interface. This leads to double layer capacitance as described by

$$C = \Delta q/\Delta V \qquad (1\text{-}4)$$

The charge is stored electrostatically with no chemical reaction involved. Charging and discharging is reversible and so charge can be released by reversing the polarity of the system [3,5].

Since double layer capacitors make use of a double layer in order to store charge, more charge can be stored by increasing the double layer area, which creates a large current and large capacitance. So, electrodes with high surface area (>100 m^2g^{-1}) are used in this kind of capacitor.

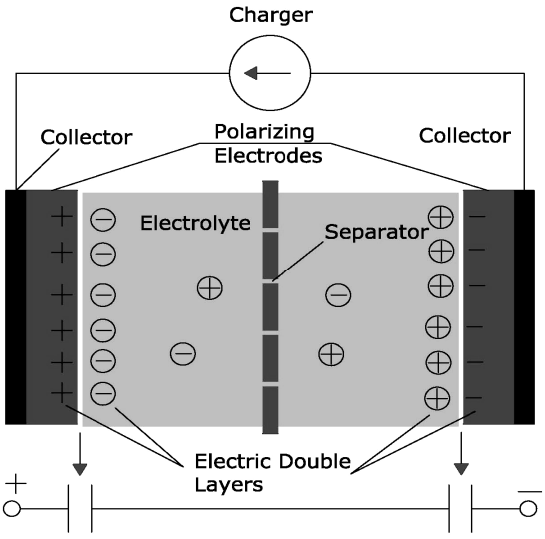

Figure 1-2 Typical configuration of an electrochemical double layer capacitor cell [21].

The cyclic voltammogram for a double layer capacitor exhibits a rectangular shape that is typical of an ideal capacitor with potential independent capacitance. For an ideal double layer capacitor, the current is constant and the applied scan rate (ν) is the inverse of the $\Delta t/\Delta V$ term so the capacitance is given by [1,31]:

$$C = i/\nu \qquad (1\text{-}5)$$

1.2.2 Faradaic capacitors

In addition to double-layer capacitance, there is also the possibility to utilize the large pseudocapacitance that is associated with electrosorption of ions or metal adatoms and especially some redox processes.

1.2.2.1 Faradaic capacitance theory

Pseudocapacitance involves a passage or exchange of charge across the double layer instead of the static separation of charge across the double layer [32]. Such pseudocapacitance occurs under certain thermodynamic conditions, such that

there is a relationship between the charge, q, required for progression of an electrode process (e.g., electrosorption or redox conversion of an oxidized species to a reduced species in liquid or solid solutions) and the potential, V. Then the derivative dq/dV corresponds to a Faradaic capacitance or pseudocapacitance [3].

During cyclic voltammetry, unlike double layer capacitors in which the current is constant, the current is not constant for pseudocapacitors. Pseudocapacitance can be produced with redox reactions, underpotential deposition and lattice intercalation [33]. The maximum capacitance in such systems, especially for the redox case, is larger than that for double layer systems [3].

1.2.3 Underpotential deposition

One of the processes giving rise to pseudocapacitance is underpotentioal deposition (UPD). In such systems, Faradaic desorption or adsorption of an electroactive species occurs onto the surface of the metal electrode [30] and it is common for deposition of hydrogen on catalytic metals such as Pt, Ru, and Ir. The area of the electrode surface that is covered depends on the amount of charge passing through the system and the potential of the system [34].

According to electrocrystallization theory, the most important parameters determining underpotential deposition of a deposit on a foreign substrate, in the initial stage, are the binding energy between deposit and substrate and crystallographic defects on the substrate [12].

1.2.4 Lattice intercalation pseudocapacitance

Lattice intercalation and underpotential deposition systems are quite similar in giving rise to pseudocapacitance behavior. Also, the shape of their cyclic voltammetry profiles is almost the same. However, for intercalation pseudocapacitance, the ions are inserted into the lattice structure, instead of surface adsorption which occurs in UPD systems. Li^+ intercalation into a layered

lattice host cathode material is a very common system for intercalation pseudocapacitance. Like the UPD systems, the amount of the charge passing through the system and the potential of the electrode are important factors, giving rise to pseudocapacitance [1,31].

1.2.5. Redox pseudocapacitance

This type of pseudocapacitance involves redox reactions to create the capacitance. Metal oxides or hydroxides of metals such as Ru [35,36], Mn [9,37,38], Co [39], V [40] and Fe [4] oxide and conducting polymers such as polyaniline (PANI) [3,41,42], polypyrrole (PPY) [3,43] and poly[3,4-ethylenedioxythiophene] (PEDOT) [3,28,44,45] are used in electrochemical supercapacitor applications. These materials show redox active behavior, giving rise to pseudocapacitance.

1.2.6 Materials for supercapacitors

For a material to be a potential candidate for supercapacitors, it should be able to oxidize and reduce reversibly between various oxidation states. Based on the type of supercapacitance to be utilized, supercapacitors can be made from various materials as shown in Figure 1-3 [3].

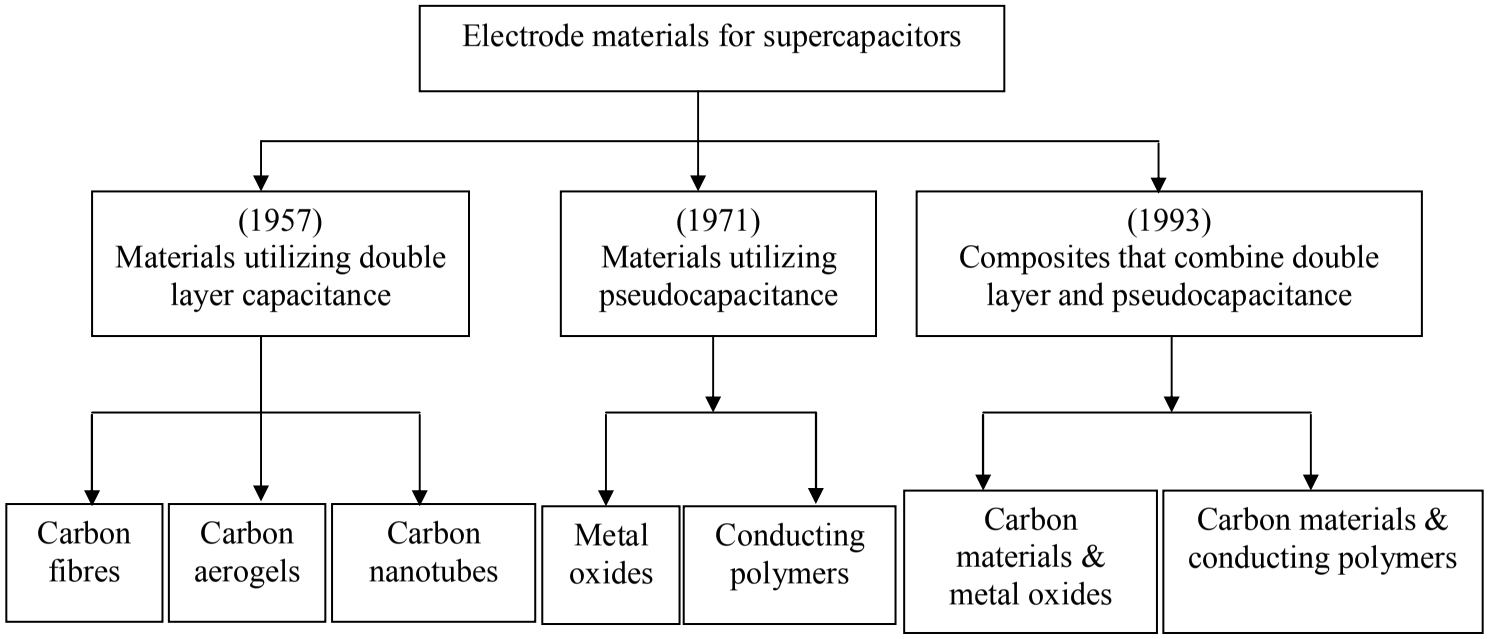

Figure 1-3 Taxonomy of supercapacitor materials [3].

Carbon-based materials are very popular for these applications because of their good conductivity, large specific area, cycle stability, low cost and availability. The double layer capacitance of carbon materials is proportional to their specific area and specific capacitance in terms of area. Carbon has a very wide potential range for application and is suitable to be a cathode in a supercapacitor [46]. Most carbon materials for capacitors have surface oxygen groups such as carboxyls, which enhance the carbon surface hydrophilicity in aqueous solutions and introduce processes that contribute pseudocapacitance to the overall capacitance. It has been found that both the stability and conductivity of the activated high surface area carbon decrease with increasing surface area, since the overall electrical conductivity decreases as the materials become more porous [47].

1.2.7 Transition metal oxides in redox pseudocapacitors

In general, charge storage properties of transition metal oxides are related to electrical conductivity in the solid phase and ionic transport within the pores. In this regard, a structure consisting of solids and pores on the nanometer scale could be a desirable candidate for application as active electrode materials [9,48].

1.2.7.1 Ru oxide

$RuO_2.xH_2O$ is a mixed electronic-protonic conductor, which has been reported to be the most promising material for supercapacitors. Ru oxide gives high and relatively constant capacitance ranging from 600 to 1000 Fg^{-1}, depending on the preparation procedure and measurement conditions. Another significant advantage is the ultra high stability and long cycle life. In addition, Ru oxide is stable in acidic solutions and shows metallic conductivity in the crystalline form. Hydrous RuO_2 is a mixed conductor that conducts protons and electrons in acidic solutions. This is a beneficial characteristic during the charging/discharging process in which electrons and protons are transferred between RuO_2 and the electrolyte solution. However, RuO_2 is very expensive, toxic in nature and requires the use of strong acidic electrolytes (5 M H_2SO_4), which have limited its

commercial applications as a supercapacitor material to aerospace and military applications [36,49,50,18,51].

A general redox process has been proposed for the electrochemical oxidation of Ru in a hydrated state.

$$RuO_x (H_2O)_\delta \longleftrightarrow RuO_{(x+\delta)} + 2\delta H^+ + 2\delta e^- \quad (1\text{-}6)$$

The total specific capacitance exhibited by the oxide film is due to both redox pseudocapacitance and double layer capacitance for the electrode [1].

Other metal oxides with lower cost have also been synthesized and tested for supercapacitor applications, including Mn oxide [9,37,38] and Co oxide [47]. Although these metal oxides are much more cost effective, their specific capacitance is much lower relative to RuO_2, normally less than 200 Fg^{-1}. Moreover, other properties such as the potential window and conductivity are also not comparable with Ru oxide. A potential window of ~1.5 V is available for RuO_2, while the potential window for MnO_2 is ~1 V. The conductivity of RuO_2 is ~0.17 Scm^{-1}, while for MnO_2 the conductivity is ~10^{-4} Scm^{-1} [9,50].

1.2.7.2 Mn oxide

Mn based oxides have been the subject of widespread investigation for electrochemical capacitors and batteries, because of their high energy density, low cost, natural abundance and the environmentally benign nature of Mn [9,52]. Mn oxide (typically MnO_2) stores electrochemical energy by simultaneous electron injection and charge compensating cations, like other electroactive transition metal oxides. Therefore, Mn oxide is potentially useful for charge storage applications such as electrochemical supercapacitors [9].

Since MnO_2 has a low electronic conductivity, the addition of other materials such as carbon improves the electrical conductivity as well as the porosity of the electrode. In this regard, Jiang *et al.* [29] reported a direct electrochemical method to prepare carbon-containing Mn oxide with good kinetic reversibility from an acetonitrile solution containing a Mn halide complex to improve the electrical conductivity [29].

The electrochemical properties of the electrode materials are affected by their microstructure and morphology [8]. One-dimensional (1D) nanostructured materials such as nanotubes, nanowires and nanorods have been demonstrated to have more favorable morphologies for electrode materials as they provide short diffusion path-lengths to ions, leading to high charge/discharge rates [53]. Furthermore, 1D nanostructures can reduce the diffusion resistance of electrolytes in rapid charge/discharge processes. Conventionally, MnO_2 nanowires have been prepared by hydrothermal treatment of MnO_2 nanoparticles in water or ammonia solution at high temperature (120–160°C) [54,55]. Recently, some researchers have used Pluronic P123, which is a copolymer, as a structure directing agent to synthesize MnO_2 nanowires at room temperature [56]. Dissolved Pluronic forms micelles, which are used as the backbone to make porous structures. However, this copolymer is very expensive.

1.2.7.3 Charge storage properties of Mn oxide

Until now, two mechanisms have been proposed to explain the charge storage behavior of MnO_2 as an active electrode material in aqueous electrochemical supercapacitors. The first mechanism is based on the surface adsorption of electrolyte cations (C^+) on MnO_2 through double layer capacitance, as given by [10]:

$$(MnO_2)_{surface} + C^+ + e^- \longleftrightarrow (MnOOC)_{surface} \qquad (1\text{-}7)$$

where $C^+ = H^+$, Na^+, K^+ or Li^+. The second mechanism involves the intercalation of protons (H^+) or alkali metal cations (C^+), such as Na^+, in the bulk of the material upon reduction followed by deintercalation upon oxidation through redox Faradaic processes given by:

$$MnO_2 + H^+ + e^- \longleftrightarrow MnOOH \qquad (E_0 = 0.81 \text{ V vs SHE}) \qquad (1\text{-}8)$$

$$MnO_2 + C^+ + e^- \longleftrightarrow MnOOC \qquad (1\text{-}9)$$

Although there has been general consensus that charge storage involves electron transfer at Mn sites, the interfacial reaction mechanism that balances the charge transfer remains unclear. Lee *et al.* [7] proposed that for both $MnO_2 \cdot nH_2O$ and $K_xMnO_{2+\delta} \cdot nH_2O$ (hydrated potassium Mn dioxide with a layered structure) supercapacitors with an aqueous KCl electrolyte solution, charge transfer at Mn sites is balanced by the chemisorption/desorption of K^+ [7].

Pang *et al.* [8] suggested that pseudocapacitance involves intercalation or insertion of protons within the near-surface region, which generally can be expressed as:

$$MnOOH_\delta + \lambda H^+ + \lambda e^- \longleftrightarrow MnO_{2-\lambda}(OH)_{\delta+\lambda} \qquad (1\text{-}10)$$

Kuo *et al.* [57] demonstrated that the charge transfer at Mn sites upon reduction and oxidation is balanced by bulk insertion/extraction of the solution cations into/from the hexagonal ε-MnO_2 structure within the poorly crystallized microstructure, which causes reversible expansion and shrinkage in the lattice spacing of the dioxide during charge/discharge cycles [57].

1.2.7.4 Co oxide

Co oxide is another candidate for supercapacitor applications [58-60]. Lin *et al.* [58] were the first group to synthesize Co oxide using a sol–gel technique. They found that the calcined oxide at 150ºC provides a high specific capacitance of approximately 290 Fg^{-1} and excellent cyclic stability [58]. Srinivasan *et al.* [59] have reported that electrodeposited Co oxide has a capacitance of only 164 Fg^{-1}, but exhibits better pseudocapacitive performance compared to the electrodes prepared by sol–gel processing [59]. In addition, Liu *et al.* [60] have indicated that a pseudocapacitive Co oxide film can be grown on Co metal by cyclic voltammetry in an aqueous solution of NaOH [60].

In general, it is noted that the major drawbacks of Co oxide compared to the Mn-based oxide are the narrow operation potential window of approximately 0.5V and the requirement of a basic working electrolyte such as NaOH for supercapacitor applications. Chang *et al.* [13] have shown that Co addition to Mn oxide may suppress the anodic dissolution of Mn during charge-discharge cycling and, therefore, improve the electrochemical stability of the oxide electrode [13].

1.2.8 Conducting polymers in redox pseudocapacitors

Conducting polymers are another group of materials used in high power energy storage devices, such as supercapacitors, because of their good electrical conductivity, fast charge/discharge rates, large pseudocapacitance and relatively low cost [3,28].

Conductive polymers can store energy by accumulating and releasing counter charges under an electric field due to their redox reactions [43,27]. Although redox supercapacitors made of conductive polymers can provide high specific capacitances, the interchange rate is usually slow because of the rate-determining process of counterion transport into the polymer layer for creating charge balance. This usually takes a few hundred milliseconds or more. This slow conversion rate

is the main obstacle for applications of these polymer films to devices requiring high charge/discharge rates, such as supercapacitors [61]. A solution to the slow interchange rate is to reduce the ion-transport resistance in the polymer by producing nanoscale porosity, which is embodied in the form of nanotubes, nanorods or random nanoporous structures. Nanostructured materials provide high surface areas leading to high charge/discharge capacities and short diffusion distances for ion transport causing fast charge/discharge rates [28,62]. Conducting polymers have low mechanical stability due to repeated intercalation and depletion of ions during charging and discharging [3].

Figure 1-4 illustrates the creation of pseudocapacitance behavior in conducting polymers. When the conducting polymer is being charged, it loses electrons producing polycations which cause the anions in the solution (Cl^- in this case) to intercalate into the conducting polymer in order to maintain electro-neutrality [3].

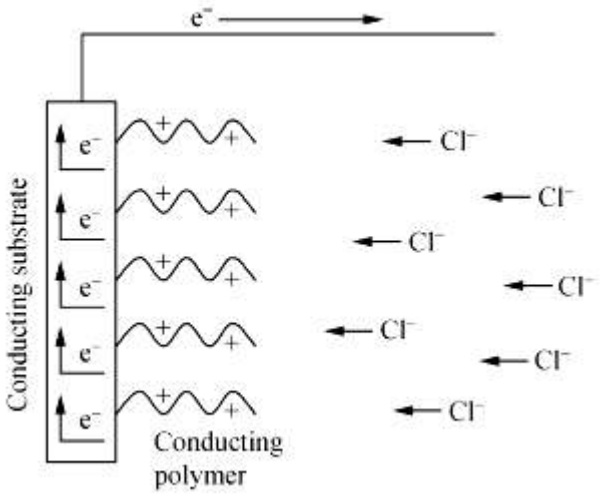

Figure 1-4 Illustration of pseudocapacitance in a conducting polymer [3].

The most commonly used conducting polymers include PANI [41,42], PPY [43] and PEDOT [44,45]. The electrochemical capacitance and charge storage

properties of conducting polymers can be studied by cyclic voltammetry [63], electrochemical impedance spectroscopy [64] and chronopotentiometry [65].

Although PPY and PANI have higher specific capacitance, PEDOT is widely used in supercapacitors as it has been reported that 66-86% of the electrochemical activity of PEDOT is maintained after 1200 cycles in acetonitrile and aqueous solutions, respectively. This is related to the good stability of the thin PEDOT film on the electrode surface [12].

The oxidation state or doping level of the polymer is the key factor in determining the mechanism of charge transfer to and from the conducting polymer [66]. At low doping levels or less positive potentials, the polymer chains are less conjugated and charge transfer occurs in a localized manner, so the polymer does not contribute to the capacitance. Increasing the doping level (potential becomes more positive) causes electron conjugation or delocalization along the polymer chain into the conduction band. Therefore, band theory governs the charge transfer, resulting in pseudo-capacitive behavior. Although the charge transfer processes at both low and high doping levels are Faradaic in nature, only at high doping levels can they contribute to the capacitance. Naturally, there should be a potential range where the polymer is partially doped and both charge transfer processes can co-exist [67].

1.2.9 Composite materials in redox pseudocapacitors

Recently, there has been a tendency to synthesize composite materials combining two or more pure materials for application in supercapacitors. Composites show improved thermal stability [68] and enhanced charge transport properties [69] compared with pure conducting polymers. They can then be used in biosensors with high sensitivity and fast response. It has been found that almost all types of materials can be coated with conducting polymers and the new composite materials produced can be used in various fields.

There are two main kinds of nanocomposites of conducting polymers and metals [70]:

1) Metal core nanoparticles covered with a conducting polymer shell. This type of composite is usually prepared by the chemical or electrochemical polymerization of a thin layer of a conducting polymer onto metal particles.
2) Metal nanoparticles embedded into a conducting polymer matrix. These composites can be obtained by the chemical reduction of metal ions from their salt solution at the interface of a conducting polymer and the solution.

Many conducting polymers in their reduced form have a high reducing power for some metal ions. Therefore, metal ions with a relatively high positive redox potential, like gold and platinum, can be reduced at a layer of conducting polymer to form clusters or small particles within a porous conducting polymer layer [71].

It has been shown that composites of carbon nanotubes (CNT) combined with RuO_2, MnO_2 and NiO are good for supercapacitor applications [3,72]. PEDOT/CNT films show much larger CV currents than pure conducting polymers, especially at potentials close to the negative limit, since composites have a significantly more porous structure for ion transport. The higher capacitance of the composite films results from the contribution of the embedded CNTs which is related to the following [3,72]:

1) The provision of interconnected pathways for electrons through the CNTs and ions through the pore network, regardless of the conductivity of the polymer.

2) The lower thickness of the polymer layer on each CNT minimizes the barriers both to ion transfer across the polymer/electrolyte interface and ion transport within the polymer phase.
3) The role of smaller cations in charge balancing due to the presence of the immobilized negatively charged CNTs.

1.2.9.1 Conducting polymer/metal oxide composite core/shell rods in redox pseudocapacitors

One-dimensional nanostructured materials are of interest in electrochemical energy storage devices as they provide short diffusion path lengths to ions, leading to high charge/discharge rates. Recently, coaxial nanorods have attracted more attention because of their particular properties such as high conductivity [17].

There are several physical, chemical and electrochemical routes for nanorod fabrication of metals and semiconductors. In electrodeposition, nanorods of large aspect ratio are commonly grown within pores of a membrane [73].

There have only been a few studies on coaxial nanorods with transition metal oxides and conductive polymers, although both are important electroactive materials in electrochemical energy storage applications. The main drawback of transition metal oxides such as Mn oxide is their poor electronic conductivity, which can be compensated for with a conductive polymer. The combination of these two materials may exhibit attractive electrical, electrochemical and mechanical properties for electrochemical energy storage [15,16].

In order to prepare metal oxide/conducting polymer coaxial nanorods, Liu *et al.* [17] have deposited coaxial MnO_2/PEDOT nanowires using an anodised aluminium oxide (AAO) membrane under potentiostatic control. The growth mechanism for coaxial nanorods within the pores of AAO is not yet sufficiently

understood. It has been suggested by Liu *et al.* [17] that sputtering Au at the bottom of the pores can direct the growth of PEDOT nanotubes leading to the preferential formation of a PEDOT shell. Furthermore, metal oxide and conductive polymers tend to exhibit phase segregation when coelectrodeposited at bulk electrode surfaces. The phase segregation of these two materials may force the metal oxide to grow in the spaces left by the conductive polymer shells as the cores [17].

1.3 Electrochemical synthesis

Oxide films are generally fabricated by techniques such as metal-organic chemical vapor deposition, pulsed laser deposition, sputtering and electrochemical deposition. Electrodeposition is the process of depositing a coating onto a substrate from an aqueous solution of a metal salt, while there are sufficient electrons supplied from an externally applied voltage. In electrochemical synthesis, an electric current is delivered between working and counter electrodes, which are separated by a conductive electrolyte. The working electrode is usually an electrically conducting plate [74].

Electrochemical deposition is the most simple approach for fabrication of thin films especially for obtaining thin and uniform films on conductive substrate [9,17,75,76]. The material properties depend on a number of parameters such as ion concentration, pH, stirring rate, temperature, current and deposition voltage. The optimization of these parameters allows fabricators to produce conducting layers with the desired structural, electronic and optical properties. The materials grown by electrodeposition are usually amorphous, nanocrystalline or microcrystalline and, therefore, this method is a convenient technique for growth of materials for nanotechnology research and applications [35].

In an electrochemical system, transfer of charge across the interface causes oxidation or reduction, which are called Faradaic processes. These processes are

governed by Faraday's law. Under some conditions, where charge transfer reactions are not kinetically or thermodynamically favorable, adsorption or desorption occurs through non-Faradaic processes [77].

There are several advantages for electrochemical synthesis compared with other synthetic methods [35,9,75,76]:

(1) The most attractive feature of electrochemical deposition is the low cost when compared with other growth techniques.
(2) Electrochemical deposition can be used for fabrication of uniform thin films on conductive substrates of complex shape with high reproducibility. It can be also used to synthesize nanostructured materials.
(3) Conducting films adhering well to a substrate need no binders or conductive additives to be deposited.
(4) The texture, surface morphology and uniformity of the oxide deposits can be easily controlled by adjusting the variables of electrochemical deposition such as the plating mode, deposition potentials, applied current densities, bath temperatures, precursor concentrations and the addition of complex or additive agents. The film thickness can be controlled by changing the electrical charge delivered during electrolysis.
(5) Electrochemical deposition is a low temperature process and is usually carried out in normal laboratory conditions without requiring a vacuum system.
(6) For microelectronic devices, such as solar panels and large area display devices, scalability is an important issue. Large area thin films can be produced by electrochemical deposition.

Therese *et al.* [76] have indicated that there are various techniques for electrochemical synthesis including anodic deposition, cathodic deposition, electromigration of reactant species, electrolysis of fused salts and alternate current synthesis [76].

Cathodic deposition involves a number of intermediate stages. The most important of these stages are [74]:

(1) Transport of the hydrated metal ion or complex from the bulk solution to the cathode.
(2) Charge transfer with the formation of adsorbed atoms on the surface of the cathode.
(3) Formation of crystal nuclei by diffusion of adsorbed atoms along the surface of the cathode.
(4) Joining of thermodynamically stable crystal nuclei to form a metallic layer on the cathode.

Transport of the metal ions from the bulk solution to the surface of the working electrode is due to convection and diffusion. The discharge of adsorbed ions to form adsorbed atoms takes place within the electrolyte double layer, which forms spontaneously at the metal-solution interface. In this state, and after passing through the electrolytic double layer, the ions are adsorbed on the working electrode surface where they form adsorbed atoms. For a coherent metal film to form, two further stages must happen: nucleation and crystal growth. Nucleation results from diffusion controlled migration of the adsorbed atoms on the surface and the growth process begins once the nuclei have reached a critical size [74].

Anodic deposition, which is used in this work, involves oxidation of metal cations with low oxidation states to a higher oxidation state on the anode surface. Anodic deposition can be used in both potentiostatic and galvanostatic mode. The electrochemical reactions for anodic oxidation are as follows [78]:

$$M^{n+} \longrightarrow M^{(n+\Delta)+} + \Delta e^{-} \qquad (1\text{-}11)$$

$$M^{(n+\Delta)+} + (n+\Delta)\ OH^{-} \longrightarrow M(OH)_{n+\Delta} \longrightarrow MO_{(n+\Delta)/2} + (n+\Delta)/2\ H_2O \quad (1\text{-}12)$$

Because of important applications such as batteries and capacitors, the anodic deposition of metal oxide films has become an interesting and important research topic. This technique has been widely used to fabricate RuO_2, MnO_2, Co_2O_3, V_2O_5, PbO_2, FeO and NiO. In addition to the good capacitive performance of oxide films prepared by anodic deposition, there are some other advantages including process simplicity, reliability, low cost and versatility for electrode preparation.

1.3.1 Transition metal oxides

Transition metal oxides such as Ru, Mn, V, Co and Fe oxide are widely used in various technological applications including intercalation electrodes with high surface area for lithium batteries, active materials in electrochromic devices and supercapacitors.

1.3.1.1 Mn oxide

For many years, Mn oxides and derivative compounds have attracted special attention, because of their outstanding structural flexibility combined with novel chemical and physical properties [1].

Mn has many stable valences (+2, +3, +4, +7) and so a variety of different oxides such as MnO, MnO_2, Mn_2O_3, and Mn_3O_4 can form. Also, there are several other oxides that can be formed synthetically such as Mn_4O_2, Mn_3O_8 and Mn_5O_8 [79]. MnO_2 stores more electrochemical energy relative to the other Mn based oxides. Also, according to XPS analysis presented in Chapters 2 and 3, the major part of the Mn oxide deposits obtained in this work is MnO_2. Therefore, MnO_2 is the focus of this section.

1.3.1.2 MnO_2 phases

MnO_2 is found to be both amorphous [80] and crystalline. When MnO_2 is crystalline, its most common polymorphs are α, β, γ, δ, ε and η. The basis of all MnO_2 compounds is a hexagonal close packing of the O^{2-} onions with half of the octahedral interstices occupied by Mn^{4+} cations. This leads to an octahedral form in which a Mn^{4+} cation is surrounded by six O^{2-} ligands. It is the arrangement of the MnO_6^{8-} octahedra that leads to the different MnO_2 polymorphs.

α-MnO_2 has two different forms, such as cryptomelane which has a tetrahedral unit cell created by cross linking of the MnO_6^{8-} octahedra, and psilomelane with a monoclinic unit cell, created by cross linking the double or triple chains of the MnO_6^{8-} octahedra [81,82].

Pyrolusite and ramsdellite are two different forms for β-MnO_2. Most of the various forms of Mn dioxide tend to transform into pyrolusite, which has a rutile-type structure with tetragonal symmetry in which MnO_6^{8-} octahedra share edges to form single chains along the c-axis. For ramsdellite, single chains of octahedra are replaced by double chains. β-MnO_2 is the most thermodynamically stable form of the MnO_2 phases [83].

γ-MnO_2 is a well-known structure for application in batteries. It has an intergrowth structure, which contains pyrolusite and ramsdellite [84]. These phases tend to have some defects and vacancies in their structure.

δ-MnO_2, or the phyllomanganate group, has a layered structure containing infinite 2D sheets of edge-shared MnO_6^{8-} octahedra [85].

η-MnO_2 has the same lattice structure as γ-MnO_2 with the only differences being the lattice parameters and the concentration of microdomains of pyrulosite within the ramsdellite matrix.

ε-MnO_2 has a defective NiAs hexagonal close packing of anions, with Mn^{4+} occupying half the available octahedral interstices. ε-MnO_2 is similar to γ-MnO_2 with both having a large number of defects and vacancies within the lattice leading to high specific surface area [86]. Therefore, ε-MnO_2 and η-MnO_2 are considered as a part of the γ-MnO_2 family.

Table 1-2 presents a list of common Mn oxide polymorphs along with their lattice parameters, diffracting lines and space groups [87].

Table 1-2 Structures of Mn dioxides [87]

Compound	Crystal system	Lattice parameters (nm)				Strongest diffracting lines (nm)			Space group
		a	b	c	d_1	d_2	d_3	d_4	
Psilomelane (α-MnO_2)	monoclinic	0.956	1.38	0.288	0.219	0.346	0.288	0.242	B21/d
Cryptomelane (α-MnO_2)	tetragonal	0.984	0.98	0.286	0.311	0.240	0.154	0.69	I4/m
Pyrulosite (β-MnO_2)	tetragonal	0.44	0.44	0.287	0.314	0.241	0.163	0.213	p42/mnm
Ramsdellite (β-MnO_2)	orthorhombic	0.927	0.43	0.287	0.407	0.161	0.136	0.254	Pnnm
γ-MnO_2	orthorhombic	0.935	0.44	0.285	0.24	0.14	0.21	0.16	P63/mmc

The crystallographic forms are generally believed to be responsible for the properties of the various Mn dioxides [84]. Perner *et al.* [88] showed that a two-phase product containing α-MnO_2 and β-MnO_2 (β-MnO_2 phase stabilized with α-MnO_2) components delivers better electrochemical results than single phase α-MnO_2 or β-MnO_2. It was shown that the β-MnO_2 phase is responsible for the high discharge capacities and the α-MnO_2 is responsible for a stable structure during lithium intercalation and extraction [88].

Although a cubic structure is not among the most common polymorphs of MnO_2, it is shown in Chapters 2 through 5 that a metastable face centered cubic (FCC)

structure, specifically an antifluorite-type structure [89,90], is obtained for MnO_2 deposits in this work.

Controlled synthesis of MnO_2 has been the focus of material scientists. With the development of 1D nanostructured materials, dimensionality and the size of the materials are also considered as critical factors that may bring some special properties such as isotropic or anisotropic behavior and region-dependent surface reactivity. So the synthesis of Mn dioxides with well-controlled dimensionality, size and crystal structure would be of great significance [91].

1.3.1.3 Mn-Co oxide

Mn-Co oxides exhibit a variety of interesting physicochemical properties including catalytic, electronic, magnetic and electrochemical properties which make them promising materials for electrochemical supercapacitors. Since Co and Mn oxides have different valences, a variety of stable oxides such as CoO, Co_3O_4 and $Mn_xCo_{3-x}O_4$ with ($0 < x < 3$) can exist. The most common crystal structure for divalent CoO is the rock salt-type structure ($Fm\bar{3}m$) [92].

Another metastable crystal structure for CoO is wurtzite, which can transform to the stable rock salt structure at 200ºC [93,94]. Three structure types at different compositional ranges are possible for $Mn_xCo_{3-x}O_4$. In the compositional range of $x < 1.4$ a cubic *Fd*3*m* spinel-type solid solution is formed, while for the $2 < x < 3$ range a tetragonal phase with the space group of *I*41/*amd* is formed for $Mn_xCo_{3-x}O_4$. For $1.4 < x < 2$, structures are a mixture of cubic and tetragonal spinel-type phases [95,96].

1.3.1.4 Mn-V and Mn-Fe oxides

Incorporation of other transition metal oxides into Mn oxide is a common approach for improving electrochemical performance. Nakayama *et al.* [14] have reported an electrochemical process to prepare amorphous films of mixed Mn and

V oxides, which is achieved by electrolysing Mn^{2+} precursors in aqueous solution with vanadate (VO_3). XRD analysis confirmed that the presence of vanadate ions inhibits the formation of crystalline Mn oxide lattice, leading to an amorphous-like phase in the as-deposited Mn–V oxide. A mechanism has been proposed in which protons generated during the electrolysis of Mn^{2+} with H_2O cause the protonation and dehydration of the VO^{3-} ions to form V (5+) oxide. The resultant porous structure allow easier ion transport to the Mn oxide surface [14]. Xie *et al.* [97] have used a precipitation method to synthesize Mn-V oxide. The specific capacitance of Mn-V oxide was increased from 166 Fg^{-1} for MnO_2 to 251 Fg^{-1} for Mn–V oxide [97].

Fe oxide is another cost-effective alternative which can exhibit good pseudo-capacitive performance. Wang *et al.* [98] reported that Fe_3O_4 electrodes demonstrate ideal capacitive behavior and possess a specific capacitance of 170 Fg^{-1} in Na_2SO_4 electrolytes [98]. It is desirable to fabricate Mn-Fe oxide electrodes which present unique pseudo-capacitive performance, combining the advantages from both single component oxides, since both Mn and Fe oxides can provide high specific capacitances. Lee et al. [99] have investigated the effect of Fe additions on the electrochemical capacitance behavior of Mn oxide electrodes prepared by electrodeposition [99]. A specific capacitance of 212 Fg^{-1} was obtained for Mn-Fe oxide deposits, which was 21% higher than that for Mn oxide.

1.3.1.5 Electrodeposition of Mn oxides

The electrochemical preparation of Mn oxide from an aqueous solution of Mn^{2+} salt has been extensively studied in previous research work. The following electrochemical reaction for the formation of Mn oxide takes place [100]:

$$Mn^{2+} + 2H_2O \rightarrow MnO_2 + 4H^+ + 2e^- \quad (1\text{-}13)$$

In neutral water chemistry, the oxidation states of Mn receiving the greatest attention are Mn(II) and Mn(IV). Solid phases with the composition MnO_2 have often been assumed to be common oxidation products of Mn^{2+}. However, it is now recognized that phases such as MnOOH(s), which has the Mn(III) state, are often initial products upon oxidation of Mn^{2+}. Mn(III) aqueous species have been recognized for some time in biochemistry, electrochemistry and analytical chemistry [101].

1.3.2 Conducting polymers

Conducting polymers can be prepared either by chemical or electrochemical polymerization. This type of material exhibits high conductivity (~25 Scm^{-1}), good stability and negligible solubility in aqueous solution [2,12]. At a sufficiently high positive (i.e., anodic) electrode potential, some monomers like PANI or PPY undergo electrochemical oxidation yielding cation radicals or other reactive species causing the polymerization process [70].

Chemical synthesis of conducting polymers can be achieved by oxidation of the monomers while using an oxidizing agent. It has been shown that chemical polymerization is a function of a wide variety of synthesis parameters such as pH, concentration of reactants, polymerization temperature and time [102]. The drawback of chemical polymerization is lower homogeneity and integrity of the polymerized product compared with the product produced by electrochemical polymerization. Chemically prepared conducting polymers are agglomerates or pressed pellets of small particles [3]. Adding an oxidant is not required in electrochemical polymerization and electrodeposited conducting polymers are naturally integrated as a continuous uniform film on the electrode, which saves the use of a binder. Consequently, both the contact resistance within the polymer and between the polymer and the current collector are smaller than that of chemically prepared ones. Therefore, electrodeposited films are ideal for the study of the electrochemical properties of composites and for practical applications such as supercapacitors [67]. Electrochemical polymerization is of interest in this work.

1.3.2.1 PEDOT properties

Polyethylenedioxythiophene (PEDOT) is an important π-conjugated conducting polymer, which is useful in the areas of batteries, sensors, electrochromic devices, supercapacitors, etc. PEDOT is generally prepared by electro-oxidation of its monomer, namely ethylenedioxythiophene (EDOT) and PEDOT forms as a coating on the anode surface [50,103]. PEDOT and its derivatives are polymers with low energy bandgaps and very high electrochemical stability, which can be doped either n-type or p-type [12,104]. Previous studies have shown that PEDOT is electroactive in aqueous solutions exhibiting a stability superior to that of other conducting polymers [105,106]. Furthermore, ion diffusion in PEDOT contacted by a polymer electrolyte is about three orders of magnitude faster than that for other conjugated polymers [107].

The electrochemical and optical properties of PEDOT can be changed by controlling synthetic processing, changing the components of the electrolytes and the counterions incorporated as the dopant during electropolymerization and introducing various functional groups into PEDOT's main chain [108,109,110].

PEDOT in its doped state is transparent, with high conductivities of up to 25 Scm^{-1}. Moreover, PEDOT has high stability in this state, which makes it suitable for application as an electrode for capacitors. Its crystal structure is pseudo-orthorhombic with lattice parameters of a= 1.40 nm, b= 0.68 nm and c= 0.78 nm. Previous research work by Aasmundtveit *et al.* [111] on PEDOT shows that during doping and undoping, the XRD peak positions and integrated intensities do not change, while the peak widths increase upon undoping and decrease upon doping. This indicates that the lattice parameters and the relative positions of the polymer do not change and the movement of the smaller ions between the polymer and electrolyte causes redox processes to occur. Furthermore, structural order increases upon doping and decreases upon undoping in a reversible manner.

These structural changes depend on the type of electrolyte as the doped material has better structural order than the undoped material [111]. Lai *et al.* [112] have reported an amorphous structure for PEDOT. In this case the effective conjugated length has been considered as an important parameter with regard to the conductivity properties of the polymer [112].

The doped and undoped (or redox) states have very different properties in terms of electronic, chemical and electro-chemical aspects. Thus, the reversible interchange between the redox states in the conductive polymer changes its properties, such as polymer conformation which refers to the geometric structure of the polymer. These changes include doping level, conductivity and color, which make the conductive polymer suitable for application in energy storage devices [43,113]. As mentioned previously, the slow interchange rate for conducting polymers is the main obstacle for applications of these polymer films to supercapacitors [61].

Among chemical oxidative polymerization processes, emulsion polymerization of PEDOT is the most promising process. However, the EDOT monomer is relatively insoluble in water, so its polymerization results in low yields and poor conductivity. Adding surfactants, such as sodium dodecyl sulfate (SDS) to an aqueous solution of EDOT significantly improves polymerization yield and solubility of the monomer and decreases its oxidation potential [109]. A surfactant containing sulfonate functional groups stabilizes the synthesized colloids and permits doping in one step, which yields PEDOT with high electrical conductivity. In general, the conductivity increases with increasing doping level of PEDOT from the surfactant. However, with an excess amount of the non-conductive surfactants on the outer surface of conductive particles, the conductivity of the film reaches a maximum and decreases with increasing surfactant amount [108]. Generally, surfactants can form micelles as the polymerization loci for the nucleation of particles, as well as stabilize the particles [114]. Increasing the concentration of surfactant decreases the average size of the

particles and they become more spherical in shape, since the hydrophilicity inside the growing particles increases. Moreover, thermal stability and the crystallinity of PEDOT increase with higher surfactant concentration [108].

1.3.2.2 Electropolymerization of conducting polymers

Electropolymerization or electrodeposition of conducting polymers occurs by the initial oxidation of the monomer being adsorbed on the electrode surface or coming from the solution. The reaction occurs through the formation of cation free-radicals of the monomer; their combination results in the formation of dimers, oxidation of the dimer and eventually the formation of the PEDOT polymer [115,116,117,118]. The electrochemical preparation of PEDOT involves oxidation of EDOT molecules at the electrode surface.

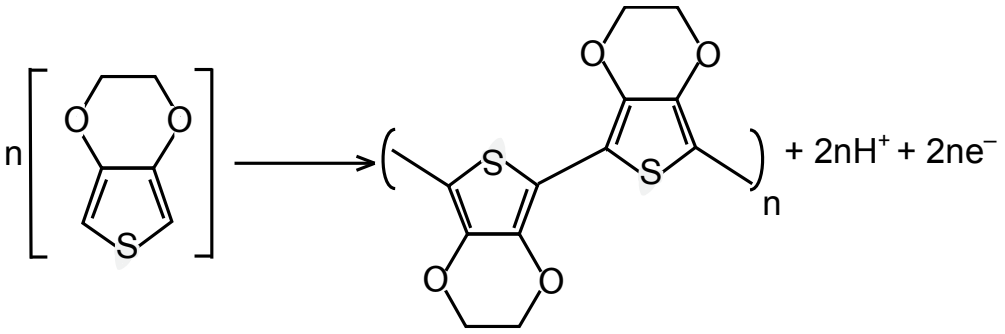

(1-14)

1.3.3 Nucleation and growth mechanisms

In preparation of electrode films, the relative rates of nucleation and growth of the film largely influence the morphology of the surface.

The initial stage of electrodeposition is considered as a suitable model system for the fundamental studies of nucleation mechanisms. The advantage of using electrodeposition over other methods to study the nucleation mechanism is that

the driving force for nucleation can be varied simply by varying the applied potential [119]. The electrodeposition process involves either instantaneous or progressive nucleation, depending on the rate of nucleation. Figure 1-5 shows schematic diagrams for instantaneous and progressive nucleation. These are modified from those provided by Booth *et al.* [120]. Majidi *et al.* [121] have reported that for instantaneous nucleation, the nucleation rate is high and all active sites available on the electrode surface are occupied in a short time period after applying an overpotential and then the nuclei grow [121]. However, Gomez *et al.* [122] have indicated that for instantaneous nucleation, the number of nuclei is constant and a limited number of nuclei grow, which is determined by the number of active sites on the substrate [122]. This seems to be in contradiction to Majidi's definition, which claims that a large number of nuclei are formed for instantaneous nucleation, due to a high deposition rate. Torabi *et al.* [123] have indicated that the number of nucleation sites is increased with an increase in the overpotential and solution concentration [123]. Milchev [124] has reported that instantaneous nucleation occurs when the nucleation stage is short compared with the growth stage. Therefore, the necessary conditions for instantaneous nucleation include a high nucleation rate or a relatively low number of active sites [124].

Since instantaneous nucleation favours the growth of existing nuclei instead of the formation of new ones, the crystalline quality is higher than that for progressive nucleation [122]. Therefore, instantaneous nucleation may lead to the preferential growth of single crystals.

Majidi *et al.* [121] have reported that when the nucleation rate is low, the nucleation mechanism is progressive. Thus, nuclei are continuously formed during the entire period during which the overpotential is applied [121]. However, Hwang *et al.* [125] have shown that progressive nucleation occurs on a larger number of active sites relative to instantaneous nucleation, resulting in the growth of compact grains. The nuclei not only form on substrate surface positions, but also on previously formed nuclei and gradually grow and overlap [125]. The

formation of a large number of nuclei is attributed to a high nucleation rate. This is in contradiction to Majidi's work, which reports a low nucleation rate for progressive nucleation.

Bennett et al. [126] have observed an instantaneous nucleation mechanism at low overpotentials ($\eta < 0.7$ V) for electrodeposition of Pt on diamond. There was a transition to a progressive mechanism at higher overpotentials ($\eta > 0.903$ V). They proposed that there were a relatively constant number of nucleation sites on the substrate at low overpotentials, with new nucleation sites developing over time at higher overpotentials [126]. Bennett's work indicates a higher formation rate for progressive nucleation relative to instantaneous nucleation.

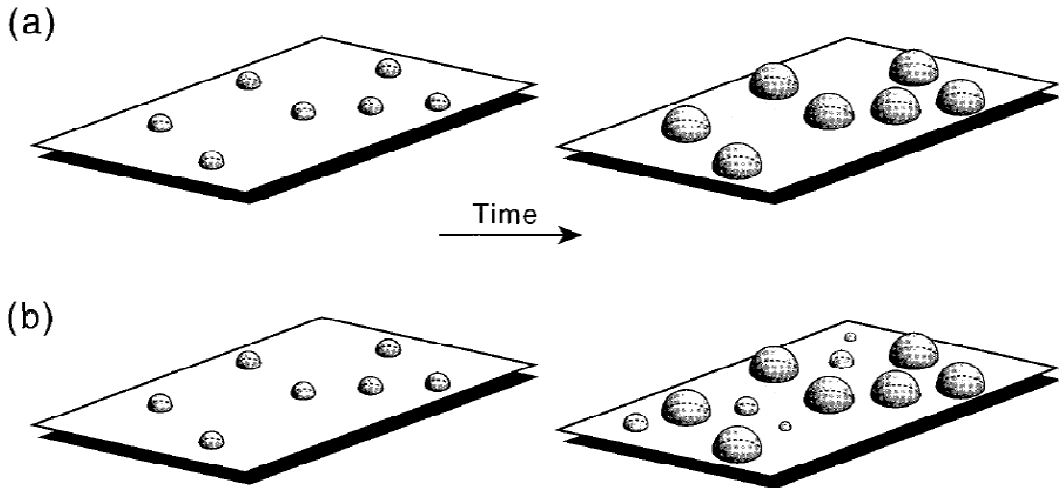

Figure 1-5 Schematic representation of (a) instantaneous nucleation; (b) progressive nucleation [modified from ref. 120].

Electrodeposition is normally associated with a 2D or 3D formation process. The growth process in electrodeposition can be classified into two categories: charge controlled and diffusion controlled. For charge controlled growth, the growth rate is limited by the speed at which ions are incorporated into the new phase. Diffusion controlled growth is limited by the rate of material transport through the solution to the electrode surface [127].

The possible growth modes for electrodeposition of a metal oxide on a metallic substrate, when the deposit is not epitaxial, are 1D [128,129,130], 2D [131,132] and 3D [129] growth and these growth modes may lead to single crystalline or polycrystalline structures. The deposition rate is the most important parameter which influences the diffusion of adatoms and deposit morphology [133]. 1D growth occurs at relatively low deposition rates [128,129]. During electrodeposition, the working electrode is normally parallel to the counter electrode and, thus, the electric field is perpendicular to the substrate. Preferential growth of rods perpendicular to the substrate at relatively low deposition rates is due to the higher atomic arrangement rate along the electric field direction relative to a high deposition rate, resulting in the formation of a rod–like structure since the growth rate of one direction (vertical direction) is faster than that of the others [129]. Most 1D nanowires made by electrodeposition are polycrystalline in nature [134-137]. However, Tian *et al.* [138] have reported the single-crystalline growth of Au, Ag and Cu wires by electrodeposition [138]. Ghahremaninezhad *et al.* [128] have shown that when the solution concentration is relatively low, the electrodeposition process exhausts all the ions near the surface of the electrode and for further electrodeposition ions must be supplied by transport. In this case, ions diffuse from the bulk of the solution toward the tips of the rods and deposit there because of the larger electric field gradients near the tip relative to the smooth substrate surface [128].

2D growth occurs at very low deposition rates where the reactions proceed slowly [131]. Therefore, the initial nuclei have sufficient time to grow in the lateral direction, leading to the formation of thin sheets [131]. Huang et al. [132] have studied 2D growth for electrodeposition of Co on Au substrates leading to single crystalline structures. They have reported that the active sites for the initial nucleation of metal are randomly distributed due to the polycrystalline nature and surface roughness of the Au substrate, which further facilitates random orientation of the initially formed nanocrystals [132].

For 3D growth, lateral growth and coalescence of nuclei and vertical growth of the deposit by continuous nucleation is expected. 3D growth of continuous coatings, which occurs at high deposition rates [129], is due to the fact that atoms do not have enough time to arrange on the lowest energy sites. As a result, the growth rate in all directions is almost the same, leading to a continuous coating [129]. Lee *et al.* [139] have reported that 2D growth occurs at low solution concentrations, while 3D growth occurs at high solution concentrations [139].

Epitaxial growth can also be obtained through electrodeposition. Three methods for epitaxial growth of thin films are distinguished [74,140]:

(1) 2D layer-by-layer growth (Frank-van der Merwe);
(2) 3D island growth (Volmer-Weber);
(3) A combination of 2D and 3D growth (Stranski-Krastanov).

Layer by layer growth occurs when the cohesive energy between the film and surface atoms is greater than the cohesive energy of the film atoms. Island growth occurs when the cohesive energy of the atoms within the film is greater than the cohesive energy between the film and atoms on the surface. Figure 1-6 shows the 2D layer growth and 3D island growth mechanisms. The third method involves growth of islands after the first monolayer has formed successfully. For the Stranski–Krastanov model to operate the bond strengths between the metal atoms being deposited and the substrate atoms must be stronger than those between the deposited atoms themselves and the lattice mismatch between substrate and deposited film must be substantial [74,141]. For 3D island growth, the growth rates are comparable in the directions parallel and perpendicular to the electrode surface. For 2D growth, the nuclei which are assumed to be circular discs, grow more quickly in the parallel direction within a monolayer than in the perpendicular direction until they meet and overlap [12,142].

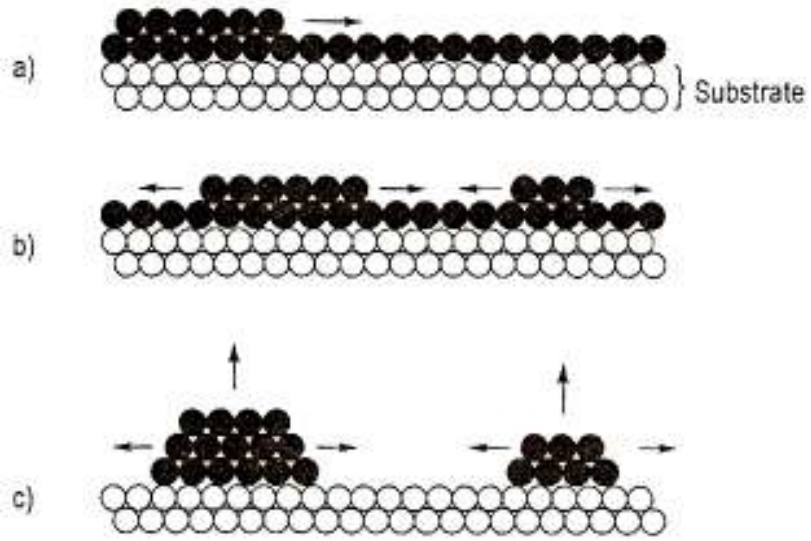

Figure 1-6 Schematic representation of (a) and (b) Frank-van der Merwe growth; (c) Volmer-Weber growth [142].

1.3.4 Electrochemical behavior of nanocomposites

Various organic polymers and inorganic solids have been combined to form nanocomposite structures. Nanocomposites have mechanical, catalytic, electronic and optical properties that are different from those of the pure component phases. Layered nanocomposites are usually a combination of an organic polymer between layers of an inorganic material, produced by either in-situ polymerization of intercalated monomers [143] or templated synthesis of inorganic material structures in a polymer-containing solution [144].

The crystallinity of an electrodeposited film strongly depends on the polymer concentration. For high polymer concentrations, the amorphous nature of the deposited film increases because of the increasing hydrophobic interaction of polycations, which decreases the electrostatic attractive force between the cations and negative charges on the metal oxide during electrodeposition [75].

In general, there are two electrochemical approaches used for making composites of metal oxides and conducting polymers. One is to make an electrode substrate with a metal oxide coating on which the conducting polymer is then electrodeposited [112]. Another is to dissolve the monomer in a suspension of metal oxide, and then co-deposit the polymer with the metal oxide into a composite coating on an electrode [17].

1.3.5 Coelectrodeposition of composite materials

Electrochemically co-deposited composites have a homogeneous network structure facilitating both electron and ion movement. Therefore, they exhibit greatly improved thermal stability and enhanced charge transfer properties leading to excellent electrochemical capacitance behavior [3].

Peng *et al.* [3] showed that the composites prepared by co-electrodeposition have uniform microstructures, which are different from conducting polymers deposited on pre-made carbon nanotube substrates [3]. Liu *et al.* [17] provided a one-step method to synthesize MnO_2/PEDOT coaxial nanorods by co-electrodeposition in a porous alumina template. The resulting coaxial nanorods, as shown in Figure 1-7, have high specific capacitances of up to 210 Fg^{-1} at high current densities [17].

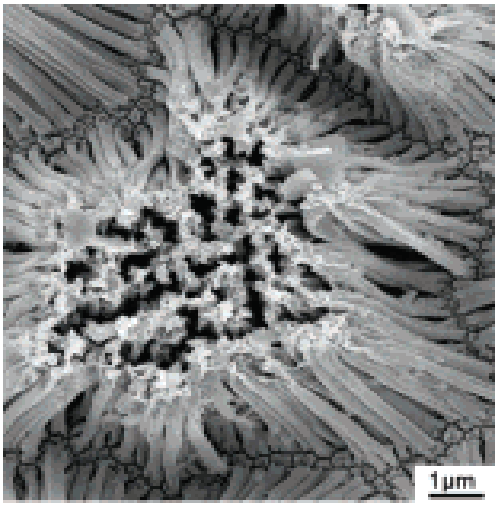

Figure 1-7 SEM image of MnO_2/PEDOT coaxial nanorods [17].

1.3.6 Electrochemical synthesis of composite nanorods

A porous structure can improve the charge and mass transfer through ion diffusion at the electrode/electrolyte interface, which is crucial for improving capacitance performance since the capacitive behavior of the composite electrode is mainly determined by surface area and surface reactivity of the electroactive materials.

Templated electrosynthesis is widely used to form nanoparticles and porous structures. A typical template electrosynthesis process is illustrated in Figure 1-8, showing ordered channels through the membrane. Electrochemical deposition of a material within the pores is obtained by coating one face of the template with a conductive film, by either ion sputtering or thermal evaporation of a metal, and using the conductive film as a working electrode for electroplating [112]. The conductive film may block all the holes or partially cover them [145]. The hard template method, in which materials are deposited in the cylindrical pores to form nanotubes or nanorods, has been performed using pressure injection, vapor deposition, chemical deposition or electrodeposition. The last two methods are the most popular in recent research work [146].

The deposited materials can be released after removing the template and conductive layer. The template can be removed using a NaOH solution. The target materials (nanowires), shown in Figure 1-8, can be metals, conducting polymers and semiconductors [112]. Template electrosynthesis has some advantages over other methods of synthesis of 1D nanomaterials. This process does not need high temperatures and high vacuum. It has a relatively high growth rate and the morphology of the deposited materials depends on the shape of template pores. Tuning of the template pore size and effective integrated charge passed in electrodeposition are used to tune the 1D materials obtained. Two or more components can be easily deposited into the membrane to form multisegmented materials. Some material parameters, such as crystallinity, can also be tuned [17,112]. However, it has been shown that the conditions employed promote surface diffusion of atoms and favor the growth of crystal nuclei. Most metal nanostructures obtained by templated electrodeposition are polycrystalline, however, pulsed electrodeposition has been used to fabricate Cu [138] and Pb [147] single crystal nanowires. Tian *et al.* [138] employed a low overpotential and a gelatine additive to assist the growth of single crystal Cu nanowires using templates [138]. As shown later in Chapter 5, single crystalline growth can be obtained by applying certain deposition conditions without using any template.

Templates employed in the electrosynthesis of nanorods are mostly of two kinds, anodised aluminium oxide (AAO) and track etched polycarbonate membranes [112]. To form track etched polycarbonate membranes a non-porous polycarbonate is bombarded with fission fragments of heavy nuclei or an accelerating ion beam, producing defect tracks in random space through the membrane. The tracks are then chemically etched to form uniform channels within the membranes [148].

AAO membranes are electrochemically prepared from aluminum metal in H_2SO_4. Membranes of this type possess highly anisotropic porous structures with pore

diameters ranging from 10–200 nm, pore lengths from 1–50 μm and pore areal densities in the 109–1011 cm^{-2} range. The pore diameters and densities of porous aluminium oxide films can be easily varied by changing the anodisation parameters, such as the electrolyte, its concentration and the anodising voltage [149].

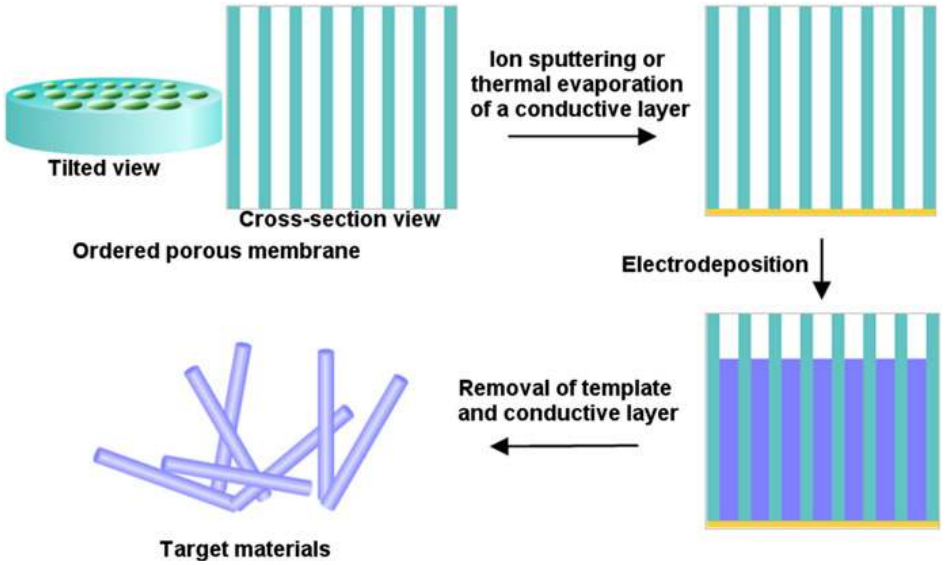

Figure 1-8 Schematic of electrosynthesis of nanomaterials within a template containing cylindrical pores [112].

Using the templated synthesis technique, several properties and potential applications of materials can be developed. It is predicted that this technique will be applied more intensively to form complex and functional materials and play an important role in nanoelectronics, optics, magnetics, bioanalytical chemistry and energy conversion [112].

Figure 1-9a and b show MnO_2 nanorods produced by templated synthesis after removal of the template and drying [17].

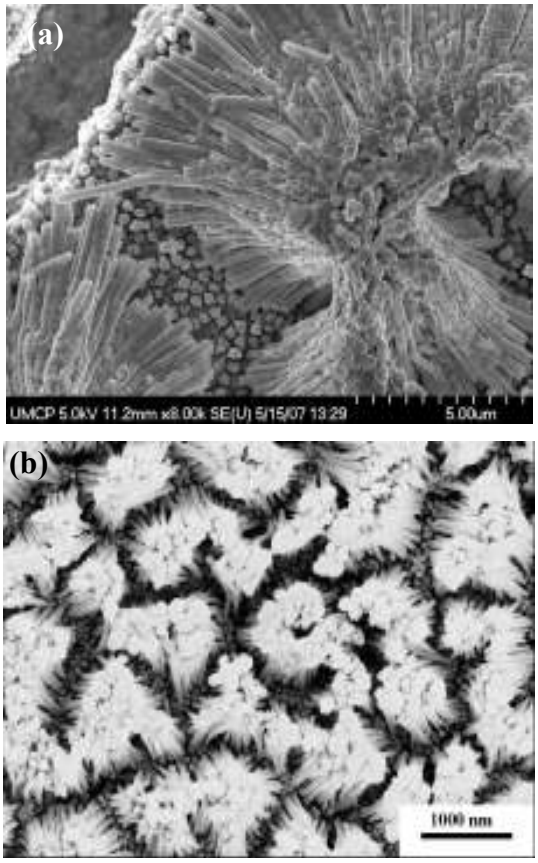

Figure 1-9 SEM images of MnO_2 nanorods grown on a) AAO [17]; b) AAO/Ti/Si [150] substrates, after removal of template and drying.

Template synthesis is not, however, easy to use in practical applications due to the fragility of the AAO template. Moreover, dissolution of the template is complicated and the morphology of the materials is often poor, because the AAO membrane pores can become impregnated with the reagents producing smooth-faced materials [151].

Liang *et al.* [152] designed a three step electrodeposition procedure to synthesize PANI nanorods without using a template. In the first step, a large current density was used to create nucleation sites on the substrate. The initial stage was followed by continued polymerization with reduced current density. A typical procedure involved electrochemical deposition in an aniline-containing electrolyte solution

using the substrate as the working electrode. The stepwise growth produced uniform, oriented nanorods on a variety of flat and rough surfaces [152].

1.4 Objectives and motivation

Electrodes with rod-like structures exhibit large specific surface areas, which promote efficient contact between the active material and the electrolyte, providing many active sites for electrochemical reactions. Structures with porosity and interconnectivity provide additional accessible space for ions, while maintaining sufficient conductivity for solid-state electronic transfer to improve the electrochemical capacity. This type of structure provides short diffusion path lengths to both ions and electrons and also sufficient porosity for electrolyte penetration to increase charge/discharge rates. This improves the electrochemical properties of synthesized electrodes. Therefore, electrodes with rod-like structures are promising candidate for applications to electrochemical capacitors.

An in-depth study of the electrochemical synthesis process is required to develop both scientific knowledge and technical applications for Mn oxide coatings. In this work, electrodeposition has been used because it offers high flexibility in controlling the morphology, chemistry and crystal structure, as well as being cost-effective. Detailed information regarding the anodic deposition process for nanocrystalline Mn oxide coatings is also part of this work.

The main objective of this research is to develop novel Mn oxide coatings with rod-like morphologies by anodic electrodeposition without using a template or surfactant, and to investigate the relationship between electrochemical synthesis parameters (deposition current density, electrolyte composition and pH, deposition time and temperature) and the morphology, chemistry and crystal structure of synthesized Mn oxide coatings. These coatings are anticipated to have major applications in charge storage devices such as electrochemical supercapacitors. The second objective of this work is to evaluate capacitance

behaviour and electrochemical cyclability of Mn oxide electrodes to determine the relationship between physicochemical feature evolution and the corresponding electrochemical behaviour of the electrodes. The third objective is to electrochemically synthesize Mn oxide/PEDOT coaxial core/shell rods by anodic deposition to investigate the influence of the presence of a PEDOT shell on the capacitance behavior and electrochemical cyclability of Mn oxide electrodes. Finally, the effect of Co, V and Fe additions on morphology, chemistry and crystal structure of Mn oxide electrodes and on the corresponding electrochemical behaviour of electrodes is studied.

1.5 Overview of thesis

The aim of this thesis work is to synthesize Mn oxide coatings with desirable morphologies, chemistries and crystal structures, by anodic electrodeposition without using a template or surfactant, for applications to electrochemical capacitors. In this section, the research subjects presented in each chapter are summarized briefly and the corresponding journal papers are also listed.

Chapter 2 deals with the anodic electrodeposition of Mn oxide nanocrystalline electrodes with rod-like structures, from a Mn acetate containing solution, on Au coated Si substrates. This chapter describes the electrodeposition of Mn oxide rods without using a template. The effects of deposition current density on morphology, chemistry, crystal structure and electrochemical behavior of Mn oxide coatings are investigated. Structural characterization is conducted using scanning electron microscopy (SEM), X-ray photoelectron spectroscopy (XPS) and transmission electron microscopy (TEM).

- Banafsheh Babakhani, Douglas G. Ivey, Anodic deposition of Mn oxide electrodes with rod-like structures for application as electrochemical capacitors, *Journal of Power Sources*, **195** (2010) 2110–2117.

Chapter 3 presents results of studies on Mn oxide/PEDOT coaxial core/shell rods. This chapter describes both a sequential synthetic approach and a one-step method to synthesize Mn oxide/PEDOT electrodes with rod-like structures. Detailed morphological and structural characterization of Mn oxide/PEDOT deposits are conducted using SEM, TEM, XPS and Auger electron spectroscopy (AES). In addition, this chapter demonstrates the distinct electrochemical properties for Mn oxide/PEDOT coaxial core/shell rods. Electrochemical properties, including specific capacitance and electrochemical cyclability of MnO_2 electrodes, are investigated to determine the relationship between physicochemical feature evolution and the corresponding electrochemical behaviour of synthesized electrodes.

- Banafsheh Babakhani, Douglas G. Ivey, Improved capacitive behavior of electrochemically synthesized Mn oxide/PEDOT electrodes utilized as electrochemical capacitors, *Electrochimica Acta*, **55** (2010) 4014–4024.

- Banafsheh Babakhani, Douglas G. Ivey, Microstructural characterization of Mn oxide/PEDOT electrodes with rod-like structures as electrochemical capacitors, *ECS Transaction*, **25 (35)** (2010) 173–182.

Chapter 4 discusses results obtained for Mn-Co doped oxide and Mn-Co oxide/PEDOT electrodes with rod-like structures for application as electrochemical capacitors. This chapter investigates the effect of Co additions on morphology, chemistry and crystal structure of Mn oxide electrodes. In addition, the capacitance and resistance properties of Mn-Co oxide and Mn-Co oxide/PEDOT electrodes at different scan rates are evaluated.

- Banafsheh Babakhani, Douglas G. Ivey, Investigation of electrochemical behavior of Mn-Co doped oxide electrodes for electrochemical capacitors, *Electrochimica Acta*, **56** (2011) 4753–4762.

- Banafsheh Babakhani, Douglas G. Ivey, Enhancement of electrochemical capacitance by doping rod-like Mn oxide electrodes with Co, *ECS Transactions*, **28 (30)** (2011) 21–31.

Chapter 5 deals with morphology-controlled growth of Mn oxide electrodes from acetate containing aqueous solutions. This chapter suggests that the morphology of Mn oxide is primarily determined by the influence of supersaturation ratio (deposition current density, electrolyte composition and pH, deposition time and temperature) on reaction kinetics in the aqueous solutions. Nucleation and growth mechanisms are proposed to account for the electrochemical response of the synthesized MnO_2 electrodes with different morphologies and crystal structures.

- Banafsheh Babakhani, Douglas G. Ivey, Effect of electrodeposition conditions on the electrochemical capacitive behavior of synthesized Mn oxide electrodes, *Accepted for Journal of Power Sources*, (2011).
- Banafsheh Babakhani, Douglas G. Ivey, Morphology-controlled growth of Mn oxide electrodes, *Accepted for MRS proceedings online library*, (2011).

In Chapter 6 Mn-Fe and Mn-V doped oxides are discussed. The effects of Fe additions on morphology, chemistry, crystal structure and electrochemical behaviour, as well as the effects of V additions on morphology, of Mn oxide electrodes are described.

Chapter 7 presents general conclusions and recommendations for future research.

References

[1] B.E. Conway, Kluwer Academic/Plenum Press, New York (1999).

[2] R. Kortz, M. Carlen. *Electrochim. Acta*, **45**, 2483 (2000).

[3] C. Peng, S. Zhang, D. Jewell and G.Z. Chen, *Prog. Nat. Sci*., **18**, 777 (2008).

[4] N. Nagarajan and I. Zhitomirsky, *J. App. Electrochem*., **36**, 1399 (2006).

[5] Y.M. Volfkovich and T.M. Serdyuk, *Russ. J. Electrochem*., **38(9)**, 1043 (2002).

[6] S.R.S. Prabaharan, R. Vimala and Z. Zainal , *J. Power Sources*, **161**, 730 (2006).

[7] H.Y. Lee, J.B. Goodenough, *J. Solid State Chem.*, **144(1)**, 220 (1999).

[8] S.C. Pang, M.A. Anderson and T.W. Chapman, *J. Electrochem. Soc*., **174(2)**, 444 (2000).

[9] M. Nakayama, T. Kanaya and R. Inoue , *Electrochem. Commun*., **9**, 1154 (2007).

[10] M. Toupin, T. Brousse and D. Belanger, *Chem. Mater.*, **16**, 3184 (2004).

[11] K. Naoi and P. Simon, *Electrochem. Soc. Interf.*, **17 (1)**, 34 (2008).

[12] H. Randriamahazaka, V. Noel and C. Chevrot, *J. Electroanal. Chem.*, **472**, 103 (1999).

[13] J. K. Chang, M.T. Lee, C.H. Huang and W.T. Tsai, *Mater. Chem. Phys.*, **108**, 124 (2008).

[14] M. Nakayama, M. Nishio and K. Ogura, *J. Mater. Res*., **18**, 2364 (2003).

[15] L.J. Pan, L. Pu, Y. Shi, S.Y. Song and Y.D. Zheng, *Adv. Mater.*, **19**, 461 (2007).

[16] M. Lahav, E.A. Weiss, Q.B. Xu and G.M. Whitesides, *Nano Lett.*, **6**, 2166 (2006).

[17] R. Liu and S.B. Lee, *J. Am. Chem. Soc*., **130**, 2942 (2008).

[18] C.C. Hu, K.H. Chang, M.C. Lin and Y.T. Wu, *Nano Lett.*, **6**, 2690 (2006).

[19] R.M. Rojas, E. Vila, O. G. Martinez, J.L. Vidales, *J. Mater. Chem.*, **4**, 1635 (1994).

[20] W. Wei, X.W. Cui, W.X. Chen and D.G. Ivey, *Electrochim. Acta*, **56**, 1619 (2011).

[21] M. Jayalakshmi and K. Balasubramanian, *Int. J. Electrochem. Sci.*, **3**, 1196 (2008).

[22] B. Djurfors, J.N. Broughton, M.J. brett, *J. Mat. Sci.*, **38** 4817 (2003).

[23] A.J. Roberts, A. Chandra and R.C. Slade, *ECS Transactions*, **16(1)**, 207 (2008).

[24] J. Zhang, W. Chu, J. Jiang and X.S. Zhao, *Nanotechnology*, **22** 125703 (2011).

[25] C.J. Patrissi and C.R. Martin, *J. Electrochem. Soc.*, **146**, 3176 (1999).

[26] N. Li, C.R. Martin and B. Scrosati, *Electrochem. Solid State Lett.*, **3**, 316 (2000).

[27] V.L. Pushparaj, M.M. Shaijumon, A. Kumar, S. Murugesan and P.M. Ajayan, *Proc. Natl. Acad. Sci. U.S.A.*, **104**, 13574 (2007).

[28] Cho and S.B. Lee, *Acc. Chem. Res.*, **41**, 699 (2008).

[29] J. Jiang and A. Kucernak, *Electrochim. Acta*, **47**, 2381 (2002).

[30] B.E. Conway and W.G. Pell, *J. Solid State Electrochem.*, **7**, 637 (2003).

[31] K. Brezesinski, J. Wang, J. Haetge, C. Reitz and T. Brezesinski, *J. Am. Chem. Soc.*, **132,** 6982 (2010).

[32] S. Trasatti, P. Kurzweil, *Platinum Metals Rev.*, **38 (2)**, 46 (1994).

[33] B.E. *Conway*, V. Birss and J. Wojtowicz, *J. Power Sources*, **66**, 1 (1997).

[34] B.E. Conway, *Electrochim. Acta*, **38**, 1249 (1993).

[35] I.M. Dharmadasa and J. Haigh, *J. Electrochem. Soc*., **153**, G47 (2006).

[36] K. Yokoshima*, W. Sugimoto,* Y. Murakami *and Y*. Takasu, *Electrochim. Acta*, **52(4)**, 1742 (2006).

[37] G.Y. Zhao, C.L. Xu and H.L. Li, *J. Power Sources*, **163**, 1132 (2007).

[38] M.S. Wu and P.J. Chiang, *Electrochem. Commun.*, **8** (2006) 383.

[39] S.G. Kandalkar, J.L. Gunjakar and C.D. Lokhande, *Appl. Surf. Sci.*, **254**, 5540 (2008).

[40] D.L. Silva, R.G. Delattore and G. Pattanaik, *J. Electrochem. Soc.*, **155**, 14 (2008).

[41] K. Naoi, K.I. Kawase, M. Mori and M. Komiyama, *J. Electrochem. Soc.*, **144**, L173 (1997).

[42] S.M. Yang, K.H. Chen and Y.F. Yang, *Synth. Met.*, **152**, 65 (2005).

[43] C. Arbizzani, M. Mastragostino and L. Meneghello, *Electrochim. Acta*, **41**, 21 (1996).

[44] J.L. Duvail, P. Retho, S. Garreau and S.D. Champagne, *Synth. Met.*, **131**, 123 (2002).

[45] S.I. Cho, D.H. Choi, S.H. Kim and S.B. Lee, Chem. Mater., **17**, 4564 (2005).

[46] E. Frackowiak, K. Metenier, V. Bertagna and F. Beguin, *Appl. Phys. Lett.*, **77(15)**, 2421 (2000).

[47] H.A. Andereas and B.E. Conway, *Electrochim. Acta*, **51(28)**, 6510 (2006).

[48] B.B. Owens, S. Passerini and W.H. Smyrl, *Electrochim. Acta*, **45**, 215 (1999).

[49] V.D. Patake, C.D. Lokhande and O.S. Joo, *Appl. Surf. Sci*., **255**, 4192 (2009).

[50] Y.R. Ahn, M.Y. Song and S.M. Jo, *Nanotechnology*, **17**, 2865 (2006).

[51] K.H. Chang, C.C. Hu and C.Y. Chou, *Chem. Mater.*, **19**, 2112 (2007).

[52] S. Jana, S. Praharaj, S. Panigrahi and T. Pal, *Org. Lett*., **9**, 2191 (2007).

[53] F. Tao, M. Guan, Y. Zhou, L. Zhang and J. Chen, *J. Cryst. Growth Des.*, **8**, 2157 (2008).

[54] Z. Yuan, Z. Zhang, G. Du and B.L. Su, *Chem. Phys. Lett.*, **378**, 349 (2003).

[55] X. Zhang, W. Yang, J. Yang and D.G. Evans, *J. Cryst. Growth*, **310**, 716 (2008).

[56] R. Jiang, T. Huang, J. Liu, J. Zhuang and A. Yu, *Electrochim. Acta*, **54**, 3047 (2009).

[57] S.L. Kuo and N.L. Wu. *J. Electrochem. Soc*., **153**, A1317 (2006).

[58] C. Lin, J.A. Ritter and B.N. Popov, *J. Electrochem. Soc.*, **145**, 4097 (1998).

[59] V. Srinivasan and J.W. Weidner, *J. Power Sources*, **108**, 15 (2002).

[60] T.C. Liu, W.G. Pell and B.E. Conway, *Electrochim. Acta*, **44**, 2829 (1999).

[61] P.J.S. Foot, F. Mohammed, *P.D. Calvert* and N.C. Billingham, *J. Phys. D: Appl. Phys.*, **20**, 1354 (1987).

[62] A.S. Arico, P. Bruce and B. Scrosati, *Nat. Mater.*, **4**, 366 (2005).

[63] J. Yang and D.C. Martin, *Sens. Actuat. A*, **113**, 204 (2004).

[64] K. Rouberg and L. Dunsch, *Electrochim. Acta*, **44**, 2061 (1999).

[65] M. Kalaji, L. Nyholm, L.M. Peter, *J. Electroanal. Chem.*, **325**, 269 (1992).

[66] J.C. Vidal, E.G. Ruiz, and J.R. Castillo, *Microchim. Acta*, **143**, 93 (2003).

[67] C. Peng, J. Jin and G.Z. Chen, *Electrochim. Acta*, **53**, 525 (2007).

[68] G. Han, J. Yuan and G. Shi, *Thin Solid Films*, **474(1)**, 64 (2005).

[69] E. Tamburri, S. Orlanducci and M.L. Terranova, *Carbon*, **43(6)**, 1213 (2005).

[70] A. Malinauskas, J. Malinauskiene and A. Ramanavicius., *Nanotechnology*, **16**, R51 (2005).

[71] A. Malinauskas, *Synth. Met.*, **107**, 75 (1999).

[72] M. Wu, G.A. Snook, V. Gupta, M. Shaffer and G.Z. Chen, *J. Mater. Chem.*, **15**, 2297 (2005).

[73] S. Banerjee, A. Dan and D. Chakravorty, *J. Mater. Sci.*, **37**, 4261 (2002).

[74] N. Kanani, Elsevier's Science and Technology, UK (2004).

[75] M. Nakayama, H. Tagashira, S. Konishi and K. Ogura, *Inorg. Chem.*, **43**, 8215 (2004).

[76] G.H.A. Therese and P.V. Kamath, *Chem. Mater*., **12**, 1195 (2000).

[77] A.J. Bard and L.R. Faulkner, 2nd ed., John Wiley & Sons, New York (2001).

[78] E. Preisler, *J. Appl. Electrochem*., **19**, 559 (1989).

[79] S. Fritsch and A. Navrotsky, *J. Am. Ceram. Soc*.**, 79**, 1761 (1996).

[80] K.W. Nam and K.B. Kim, *J. Electrochem. Soc.*, **153 (1)**, A81 (2006).

[81] J.B. Fernandes, B.D. Desai and V.N.K. Dalal, *J. Power Sources*, **15** 209 (1985).

[82] J.V. Smith, Natural Academy of Sciences, USA (1999).

[83] W. H. Baur, *Acta Cryst. B*, **2**, 2200 (1976).

[84] M.M. Thackeray, *Prog. Solid State Chem*., **25**, 1 (1997).

[85] Y. Chabre, J. *Prog. Solid State Chem.*, **23**, l (1995).

[86] P.M. De Wolff, J.W. Visser and R. Briltsch, *Chimia*, **32**, 257 (1978).

[87] M.A. Malati, *J. Chem. Ind*. 446 (1971).

[88] A. Perner, K. Holl, D. Ilic and M.W. Mehrens, *Eur. J. Inorg. Chem.*, 1108 (2002).

[89] W. Wei, X.W. Cui, W.X. Chen and D.G. Ivey, *Electrochim. Acta*, **54**, 2271 (2009).

[90] W. Wei, X.W. Cui, W.X. Chen and D.G. Ivey, *J. Phys. Chem. C*, **112***,* 15075 (2008).

[91] X. Wang and Y. Li, *Chem. Eur.*, **9(1)**, 300 (2003).

[92] C.N.R. Rao and B. Raveau, 2nd ed., Wiley-Vch, New York (1998).

[93] A.S. Risbud, L.P. Snedeker, M.M. Elcombe and R. Seshadri, *Chem. Mater.*, **17**, 834 (2005).

[94] J.F. Liu, S. Yin, H.P. Wu, Zeng, J.Z. Jiang, *J. Phys. Chem. B*, **110**, 21588 (2006).

[95] S. Naka, M. Inagaki and T. Tanaka, *J. Mater. Sci.*, **7**, 441 (1972).

[96] J.L.M. Vidales, O.G. Martinez, E. Vila and M.J. Torralvo, *MRS Bull.*, **28**, 1135 (1993).

[97] X. Xie, W. Liu, L. Zhao and C. Huang, *J. Solid State Electrochem.*, **14**, 1585 (2010).

[98] S.Y. Wang, K.C. Ho, S.L. Kuo and N.L. Wu, *J. Electrochem. Soc.*, **153**, A75 (2006).

[99] M.T. Lee, J.K. Chang and W.T. Tsai, *J. Electrochem. Soc.*, **154(9)**, A875 (2007).

[100] M.S. Wu, *Appl. phys. Lett.*, **87**, 153102 (2005).

[101] J. K. Klewicki and J.J. Morgan , *Environ. Sci. Technol*., **32**, 2916 (1998).

[102] Y. Cao, A. Andreatta, A.J. Heeger and P.Smith, *Polymer*, **30**, 2305 (1989).

[103] S. Patra, K. Barai and N. Munichandraiah, *Synth. Met.*, **158(10)**, 430 (2008).

[104] H. Gustafsson**,** C. Kvarnstrom **and** A. Ivaska**,** *Thin Solid Films*, 517(2**)**, 474 (2008).

[105] N. Sakmeche, J.J. Aaron, M. Fall and S. Aeiyach, *Chem. Commun.*, **24**, 2723 (1996).

[106] N. Sakmeche, J.J. Aaron, M. Fall and S. Aeiyach, *Langmuir*, **15**, 2566 (1999).

[107] J.C. Gustafsson, B. Liedberg and O. Inganas , *Solid State Ionics*, **69**, 145 (1994).

[108] C.A. Dai, C.J. Chang, H.Y. Chi and W.Y. Chiu, *J. Polymer Sci. A*, **46**, 5236 (2008).

[109] C. Li and T. Imae, *Macromolecules*, **37(7)**, 2411 (2004).

[110] R.D. McCullough, *Ad. Mat*., **10**, 93 (1998).

[111] K.E. Aasmundtveit, E.J. Samuelsen and O. Inganas, *Synth. Met*., **113**, 93 (2000).

[112] M. Lai and D.J. Riley, *J. Coll. Inter. Sci.*, **323**, 203 (2008).

[113] A. Kros, R.J.M. Nolte and N. Sommerdjik , *Ad. Mater*., **14**, 1779 (2002).

[114] F.T. Van, M. Carrier and C. Chevrot, *Synth. Met*., **142**, 251 (2004).

[115] M.C. Morvant and J. R. Reynolds, *Synth. Met.*, **92**, 57 (1998).

[116] M.A. Valle, P. Cury and R. Schrebler, *Electrochim. Acta*, **48**, 397 (2002).

[117] L. Pigani, A. Heras and A. Colina, *J. Electrochem. Commun.*, **6**, 1192 (2004).

[118] S. Patra and N. Munichandraiah, *J. Appl. Poly. Sci.*, **106 (2)**, 1160 (2007).

[119] A. Milchev and L. Heerman, *Electrochim. Acta*, **48**, 2903 (2003).

[120] J. Booth and R.G. Compton, *J. Phys. Chem. B*, **102**, 3980 (1998).

[121] M.R. Majidi, A.A. Zeynali and B. Hafezi, *Electrochimica Acta*, **54**, 1119 (2009).

[122] H. Gomez, G. Riveros and D. Ramirez, *J. Solid State Electrochem.*, (2011).

[123] M. Torabi and A. Dolati, *J. Appl. Electrochem.*, **40**, 1941 (2010).

[124] A. Milchev, *Electrochim. Acta*, **42(10)**, 1533 (1997).

[125] B.J. Hwang, R. Santhanam and Y.L. Lin, *J. Electrochem. Soc.*, **147**, 2252 (2000).

[126] J.A. Bennett and G.M. Swain, *J. Electrochem. Soc.*, **157(8)**, F89 (2010).

[127] M.E. Hyde and R.G. Compton, *J. Electroanal. Chem.*, **549**, 1 (2003).

[128] A. Ghahremaninezhad, E. Asselin, and D. G. Dixo, *J. Phys. Chem. C*, **115**, 9320 (2011).

[129] D. Chu, Y. Masuda and T. Ohji, *Langmuir*, **26(18)**, 14814 (2010).

[130] G. She, L. Mu and W. Shi, *Rec. Patents Nanotech.*, **3**, 182 (2009).

[131] S. Yue, J. Lu and J. Zhang, *Mater. Lett.*, **63**, 2149 (2009).

[132] X.H. Huang, G.H. Li and L.X. Zheng, *Nanoscale Res. Lett.*, **5**, 1057 (2010).

[133] Y.Y. Huang, Y.C. Zhou and Y. Pan, *Physica E*, **41**, 1673 (2009).

[134] O. Rabin, G. Chen and M.S. Dresselhaus, *Mat. Res. Soc.*, **793**, S541 (2004).

[135] L. Ion, I. Enculescu and S. Antohe, *J. Optoeceletron. Adv. Mater.*, **10 (11)**, 3241 (2008).

[136] S. Aravamudhan, K. Luongo, P. Poddar and S. Bhansali, *Appl. Phys. A*, **87**, 773 (2007).

[137] Q. Wang, G. Wang, B. Xu and J.G. Hou, *Mater. Lett.*, **59**, 1378 (2005).

[138] M. Tian, J. Wang, J. Kurtz and M.H.W. Chang, *Nano Lett.*, **3(7)**, 919 (2003).

[139] I. Lee, K.Y. Chan, D.L. Phillips, *Japanese J. Appl. Phys.*, **43(2)**, 767 (2004).

[140] M. Heuberger, G. Dietler and L. Schlapbach, *Surf. Sci.*, **314**, 13 (1994).

[141] N.V. Krainyukovaa and V.G. Belan, *Eur. Phys. J. D*, **43**, 169 (2007).

[142] M. Schlesinger and M. Paunovic, 4th ed, John Wiley Sons Inc, USA (2000).

[143] A. Oral, M.A. Tasdelen, A.L. Demirel and Y. Yagci, *Polymer*, **50**, 3905 (2009).

[144] P.H.C. Camargo, K.G. Satyanarayana and F. Wypych, *Mater. Res.*, **12(1)**, 1 (2009).

[145] J. Fu, S. Cherevko and C.H. Chung, *Electrochem. Commun.*, **10**, 514 (2008).

[146] C.R. Martin, *Science*, **266(5193)**, 1961 (1994).

[147] G. Yi and W. Schwarzacher, *Appl. Phys. Lett.*, **74**, 1746 (1999).

[148] B.E. Fischer and R. Spohr, *Rev. Mod. Phys.*, **55**, 907 (1983).

[149] F. Keller, M.S. Hunter and D.L. Robinson, *J. Electrochem. Soc.*, **100**, 411 (1953).

[150] C.L. Xu, S.J. Bao, L.B. Kong and H.L. Li, *J. Solid State Chem*., **179(5)**, 1351 (2006).

[151] F. Cheng, Z. Thao, J. Liang and J. Chen, *Chem. Mater.*, **2**, 667 (2008).

[152] L. Liang, J. Liu, C.F. Windisch, *Ang. Chem. Int. Ed*. (2002).

Chapter 2 Anodic deposition of Mn oxide electrodes with rod-like structures for application as electrochemical capacitors[1]

2.1 Introduction

Research on electrochemical capacitors has generated growing interest from both academia and industry in recent years, with efforts focused on developing safe, stable, high energy/power density and low cost materials. Electrochemical capacitors are considered as a promising power storage device for backup power storage, peak power sources and hybrid electric and fuel cell vehicles, due to their high specific capacitance, high charge/discharge rate, long cycle life and excellent reversibility [1-4].

Based on the intrinsic principles of charge storage and discharge in electrochemical capacitors, the energy stored is either capacitive (non-Faradaic) or pseudocapacitive (Faradaic) in nature. The non-Faradaic process relies on charge separation at the interface between the electrode and the ionic solution giving rise to an electrical double layer, whereas the Faradaic process consists of redox reactions occurring within the active electrode materials [2]. Based on the type of supercapacitance to be utilized, electrochemical capacitors can be made from various materials including carbon [5], conducting polymers [6-10], noble metal oxides such as RuO_2 [11-13] and IrO_2 [14] and transition metal oxides such as MnO_2 [15], NiO [16], Co_2O_3 [17], FeO [18], TiO_2 [19], SnO_2 [20], V_2O_5 [21-23] and MoO [24]. Among the transition metal oxides, Mn-based oxides have been widely studied for electrochemical capacitors and batteries, because of their high energy density, low cost, natural abundance and environmentally friendly nature. A Mn^{4+}/Mn^{3+} redox system involving single-electron transfer is responsible for MnO_2 pseudocapacitive behavior. Mn oxide stores electrochemical energy by simultaneous injection of electrons and charge-compensating cations, as with other electroactive transition metal oxides, which makes it potentially useful for

[1] *A version of this chapter has been published. Banafsheh Babakhani, Douglas G. Ivey. Journal of Power Sources, 195 (2010) 2110–2117.*

charge storage applications. Amorphous/crystalline Mn oxide shows high specific capacitance due to the utilization of both electric double layer and redox effects. Hydrated Mn oxides may exhibit specific capacitances within the 100–200 Fg^{-1} range in alkali salt solutions depending on the processing conditions. Although these values are much lower than those for RuO_2 (600-1000 Fg^{-1}), Mn oxide is still considered as an appropriate replacement for noble metal oxides in electrochemical capacitors [25-30]. In order to synthesize Mn oxide electrodes, several chemical techniques such as sol-gel [31] deposition from colloidal suspensions [32] and electrochemical deposition [25-30] have been adopted. Electrochemical deposition has some advantages over other techniques, e.g., the mass and thickness of the metal oxide film is easily controllable simply by adjusting the current, temperature and electrolyte chemical composition [33].

Past research has indicated that the electrochemical characteristics of electrode materials, such as specific capacitance and voltammetric capacitance reduction with cycling, are greatly dependent on the grain size, surface area, morphology, chemistry and crystal structure [34,35]. It has been noted that partial dissolution of MnO_2 films into the electrolyte during cycling, leading to gradual loss of active electrode materials, is a major reason for capacitance reduction with an increasing number of charge/discharge cycles, and is attributed to the disproportionation of trivalent Mn [35,36]. Gradual mechanical failure of the electrode materials can also lead to capacitance fading [37]. In addition, oxygen evolution strongly influences the cycle life of Mn oxide by affecting the electrode/current collector interface and increasing the equivalent series resistance of the cell [10].

It has been shown that a combination of Mn oxide with other materials, such as conducting polymers, may reduce both MnO_2 dissolution and mechanical failure and provide excellent electrochemical and mechanical properties for electrochemical energy storage [38,39]. In addition, electrode materials with ordered, high surface area structures can enhance the electrochemical characteristics and maintain them after repeated cycling [10,35]. One-dimensional

(1D) nanostructured materials provide short transport/diffusion path lengths for both ions and electrons, leading to faster kinetics and also large specific surface areas, resulting in high charge/discharge capacities [38,40]. Templates or catalysts have been widely used to grow 1D nanostructured materials. Templates are used to confine the growth of wires, while catalysts may act as the energetically favorable sites for the adsorption of reactant molecules. An anodic aluminum oxide (AAO) template offers a promising route to synthesize high surface area, ordered Mn oxide nanowire array electrodes. This method is not, however, easy to use in practical applications due to the fragility of the AAO template. Moreover, dissolution of the template is complicated and the morphology of the materials is often poor, because the AAO membrane pores can become impregnated with the reagents producing smooth-faced materials [41-43].

It is possible to prepare 1D nanostructured Mn oxides with desirable morphologies (e.g., rod-like structures) under controlled conditions without the presence of catalysts or templates. The formation of 1D Mn oxide structures may be kinetically preferable for many substances under certain conditions. In this chapter, 1D Mn oxide electrodes are synthesized through the oxidation of Mn^{2+} without catalysts or templates in order to determine the relationship between the physicochemical features of Mn oxide electrodes and corresponding electrochemical behavior. It is expected that this chapter may provide new technical insights to improve the electrochemical properties and cyclability of Mn oxide electrodes for applications to electrochemical capacitors.

2.2 Experimental procedure

Mn oxide coatings were anodically electrodeposited from two different types of dilute solutions (0.01 M $MnSO_4$ and 0.01 M $Mn(CH_3COO)_2$) onto Au coated Si substrates with dimensions of 15 mm × 8 mm × 1 mm using a hot water bath under galvanostatic control, i.e., 5 $mAcm^{-2}$ to 30 $mAcm^{-2}$. The working electrode consists of a Si wafer, an Au seed layer (500 nm thick) and a TiW adhesion layer

between the Si and Au (200 nm thick). The TiW adhesion layer and Au seed layer were deposited using sputtering. A platinum counter electrode, with the same dimensions as working electrode, was placed vertically 20 mm away from a vertical Au coated Si working electrode. The electrolyte pH value and electrolyte temperature were 7.5 and 60°C, respectively. Deposition times were 10 minutes for both solutions and all current densities. The operating potential changed form 0.27 V to 1.1 V for different deposition current densities from 5 to 30 $mAcm^{-2}$. Before anodic electrodeposition, the Au coated Si substrates were cleaned with acetone and then ethanol. During electrodeposition, agitation was applied with a magnetically driven Teflon® coated stirring bar at a speed of 300 rpm. After electrodeposition the working electrodes were rinsed with deionized water, dried at 100°C for 60 min in air to remove any residual water and then stored in a vacuum desiccator before further analysis. The mass of the Mn oxide deposits on the Au coated Si electrodes was determined from the weight difference between the Au coated Si electrode before and after anodic deposition, as measured using a microbalance (Sartorius BP211D) with an accuracy of 10 µg. The specific deposit mass was controlled to be 0.20-0.25 mg cm^{-2}.

The morphology and chemistry of the Mn oxide deposits, in as-deposited and cycled electrodes, were investigated using a Hitachi S-2700 scanning electron microscope (SEM) operated at 20 kV and equipped with an ultra-thin window (UTW) X-ray detector. Chemical state analysis was carried out by X-ray photoelectron spectroscopy (XPS) using a Kratos AXIS Ultra X-ray photoelectron spectrometer. A monochromatic Al source, operating at 210 W with a pass energy of 20 eV and a step of 0.1 eV, was utilized. All XPS spectra were calibrated using the C 1s line at 284.6 eV. Curve fitting and background subtraction were accomplished using Casa XPS Version 2.3.13 software. The crystal structure of the Mn oxide rods was investigated using selected area electron diffraction (SAED) of samples prepared for transmission electron microscopy (TEM). A JEOL 2010 transmission electron microscope (TEM), operated at 200 kV, and equipped with a Noran ultra-thin window (UTW) X-ray detector was used. An

electron transparent sample was prepared by scraping some of a deposit from the substrate and then ultrasonically dispersing the residue in methanol for 10 min. One or two drops of the suspension were deposited onto a C-coated, Cu grid (300 mesh). After evaporation of the methanol, samples were ready for TEM analysis.

In order to determine the electrochemical behavior of the Mn oxide electrodes, a Gamry PC4/750 potentiostat/galvanostat was used for cyclic voltammetry (CV) in an electrolyte containing 0.5 M Na_2SO_4 at room temperature. A three-electrode cell configuration was applied: a working electrode (Mn oxide deposit on a Au coated Si), a platinum (Pt) mesh as a counter electrode and a saturated calomel electrode (SCE) as the reference electrode. Cyclic voltammograms were recorded between –0.1 and 0.8 V vs. SCE at a scanning rate of 20 mVs^{-1}. For consistency, all CV scans were done using fresh deposits. For each deposition current density, 5 samples were prepared and the capacitance values were calculated for all of them. The results were reproducible and showed less than 2% deviation.

2.3 Results and discussion

2.3.1 Morphology and crystal structure of as-prepared Mn oxide electrodes

The chemistry, morphology and crystal structure of Mn oxide coatings can be manipulated by adjusting the deposition parameters, such as complexing agents, deposition current density, voltage and pH. The morphology and crystal structure of the as-prepared Mn oxide coatings obtained from solutions composed of 0.01 M $MnSO_4$ or 0.01 M $Mn(CH_3COO)_2$ (acetate and sulphat act as complexing agent) were analyzed using SEM and TEM. Plan view secondary electron (SE) images, shown in Figure 2-1a and 2-1c, reveal two different types of morphology for the resultant oxides. The SE micrograph of the oxide deposited from a solution containing 0.01 M $MnSO_4$ (Figure 2-1a and 2-1b) is continuous but relatively porous, which is typical for electrochemically active MnO_2 [24]. In contrast, for deposits prepared from the 0.01 M $Mn(CH_3COO)_2$ solution, free standing rods (about 10 μm long and less than 1.5 μm in diameter) are clearly visible (Figure 2-

1c and 2-1d). In this case, Mn oxide may preferably grow on energetically favorable sites under galvanostatic control resulting in the highly porous structure. The rod-like structures exhibit large specific surface areas, which promote efficient contact between the active material and the electrolyte, providing more active sites for electrochemical reactions. It should be noted that structures with porosity and interconnectivity supply additional accessible space for ions while maintaining sufficient conductivity for solid-state electronic transfer. Significantly enhanced capacitance and high cycling rate capability can, therefore, be expected. Smaller diameter rods will provide larger specific surface areas for electrolyte access to improve the electrochemical capacity. Moreover, rod-like structures can provide short diffusion path lengths to both ions and electrons and also sufficient porosity for electrolyte penetration giving rise to high charge/discharge rates [38,40].

Since deposits produced from the $Mn(CH_3COO)_2$ solutions exhibited a more promising morphology, the rest of the chapter focuses on Mn oxide deposits obtained from the Mn acetate solutions.

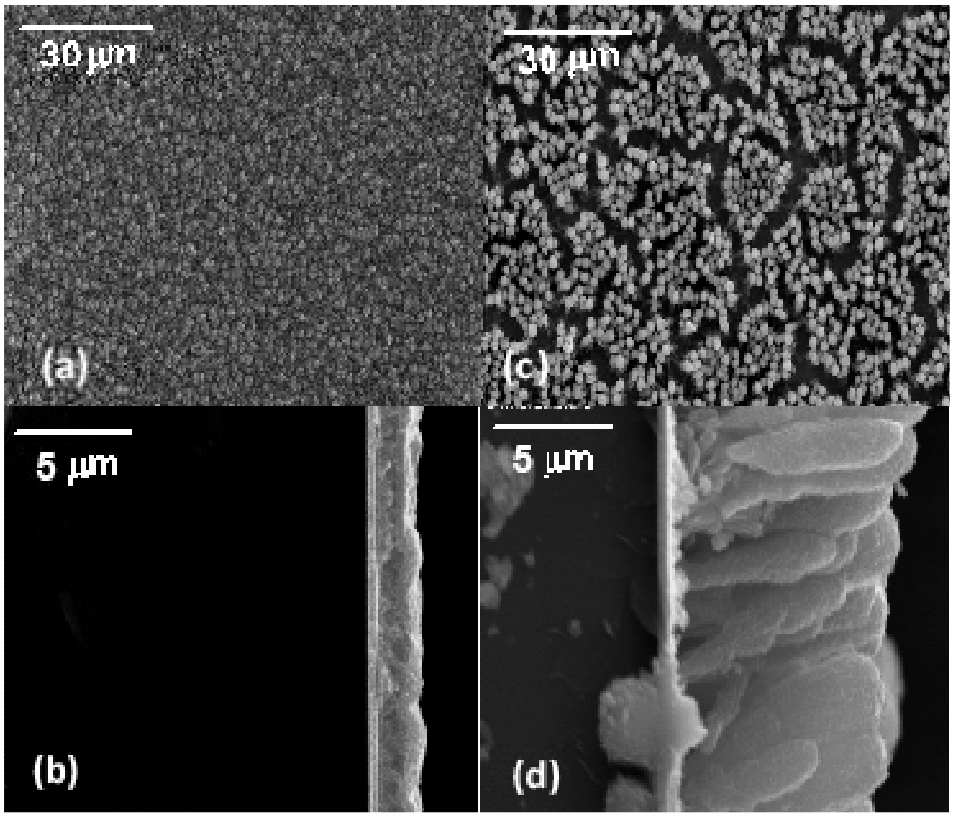

Figure 2-1 SE plan view and cross section images of Mn oxide prepared from a solution of (a), (b) 0.01 M $MnSO_4$ at i= 30 $mAcm^{-2}$; (c), (d) 0.01 M $Mn(CH_3COO)_2$ at i= 5 $mAcm^{-2}$ (pH= 7.5).

The morphology of the Mn oxide rods, prepared from the Mn acetate solutions, can be controlled by varying the deposition current density. This is shown in Figure 2-2, where the synthesized Mn oxide at lower deposition current densities (Figure 2-2a, b, d and e) has more uniform, vertical and free-standing rods. At higher deposition current densities (Figure 2-2c and f), the synthesized Mn oxide tends to form interconnected rods. As shown later in this chapter, the uniform microstructure provides better electrochemical behavior.

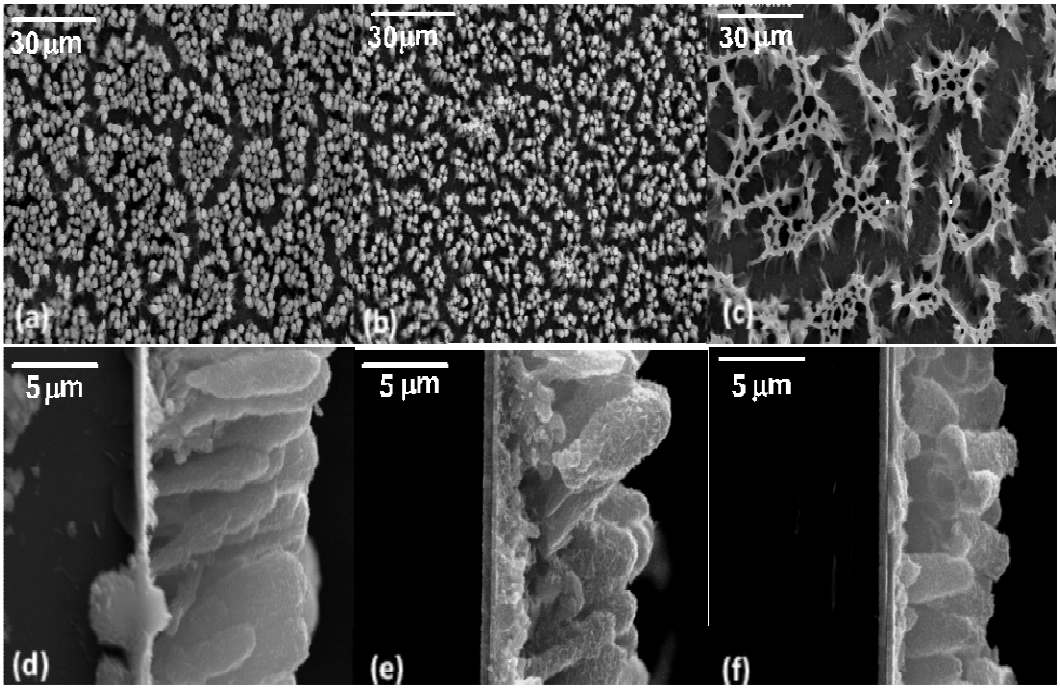

Figure 2-2 SE plan view and cross section images of Mn oxide deposits prepared from a 0.01 M $Mn(CH_3COO)_2$ solution at (a),(d) i= 5 $mAcm^{-2}$; (b),(e) i=15 $mAcm^{-2}$; (c),(f) i= 20 $mAcm^{-2}$ (pH= 7.5).

Individual Mn oxide rods were examined in more detail by TEM. A bright field (BF) image of 2 rods, from a sample deposited at 5 $mAcm^{-2}$, is shown in Figure 2-3a, where a fibrous surface is visible. An SAED pattern and a dark field (DF) image of the circled region shown in Figure 2-3a is shown in Figure 2-3b. The DF image was obtained using part of the first two diffraction rings. The diffraction pattern reveals that the rods are polycrystalline and the DF image shows that the oxide grains are less than 10 nm in diameter. The small crystallite size and fibrous nature of the surface should enhance diffusion transport of both electrons and ions, resulting in faster kinetics. XPS analysis in Section 2.3.2 shows that MnO_2 is the major component of deposited Mn oxide. As described in Chapter 1, Section 1.3.1.2, the most common polymorphs of MnO_2 are α, β, γ, δ, ε and η with various crystal structures which are not cubic. Therefore, a cubic structure is not among the most common polymorphs for MnO_2. However, the

SAED pattern was indexed to a defective antifluorite-type crystal structure (FCC with space group corresponding to Fm $\bar{3}$m) with a lattice parameter of 0.445 nm. The intensity profiles for the diffraction rings in Figure 2-3b show that the peak intensities decrease in the following order: (111) > (200) > (220) (Figure 2-3c). On the basis of simulated patterns for several FCC-type crystal structures, the intensity distribution is consistent with a defective antifluorite-type structure [44]. The defective antifluorite structure has O^{2-} ions occupying FCC positions, with Mn cations randomly occupying some of the tetrahedral interstices with all octahedral interstices unfilled. When all eight tetrahedral sites are occupied, an antifluorite-type structure is formed. However, the oxygen anion to Mn cation ratio would be 1:2 in an antifluorite-type structure, while as shown later in XPS results the deposited Mn oxide is mostly MnO_2. Therefore, only 25% of the tetrahedral interstices are occupied by Mn ions [44]. It has been shown that MnO_2 prepared from a sodium citrate-containing solution also has an antifluorite-type structure [45].

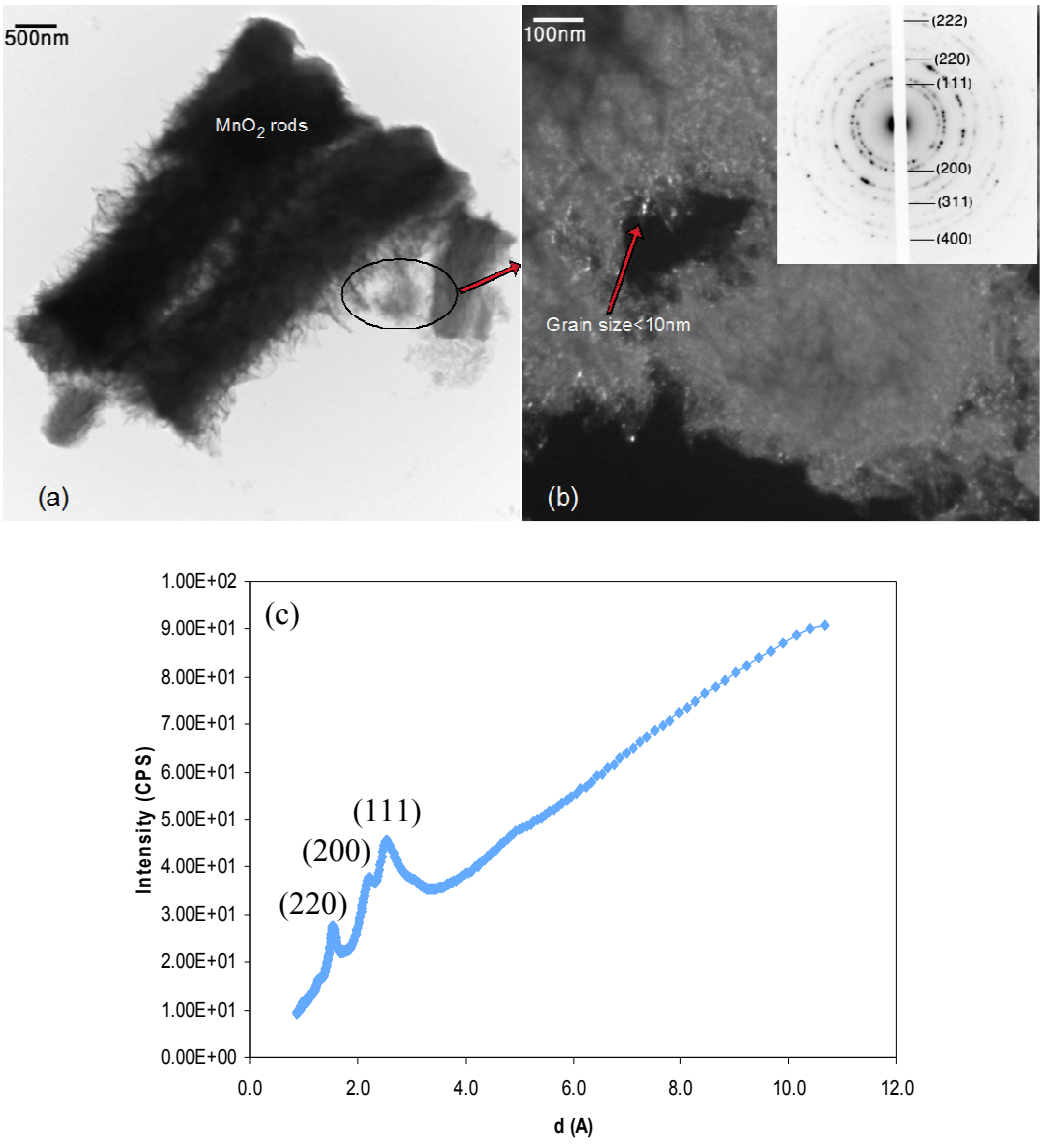

Figure 2-3 Morphology and crystal structure of Mn oxide prepared from a 0.01 M $Mn(CH_3COO)_2$ solution at i= 5mAcm^{-2}. (a) TEM BF image; (b) TEM DF image and SAED pattern; (c) Intensity profile for the SAED pattern in (b).

2.3.2 XPS analysis

XPS was applied to determine the oxygen anion content and the oxidation state of the Mn cations in Mn oxide deposits obtained from 0.01 M $Mn(CH_3COO)_2$

solutions. The Mn 3s spectrum can be used to approximate the valence of Mn cations using the 3s splitting widths. There is an approximately linear relationship between the Mn oxidation state and the 3s splitting width (ΔE) [24]. The splitting of the 3s peak increases when the valence of Mn in the oxide decreases due to fewer unpaired electrons in the 3d level [46]. A graphical representation of the separation of peak energies (ΔE) as a function of the Mn oxidation state is given in Figure 2-4 [46,47].

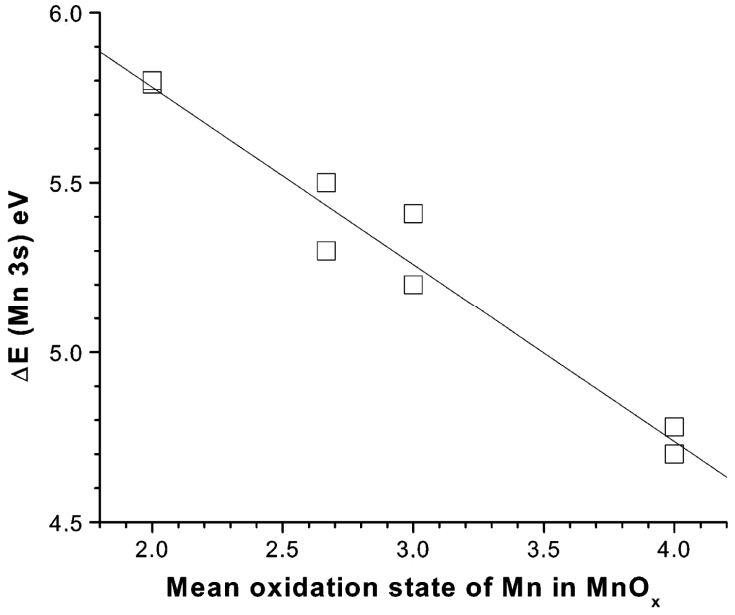

Figure 2-4 Separation of peak energies ΔE representative of Mn 3s multiplet splitting as a function of the mean Mn oxidation state according to sample data from references 46 and 47.

Unfortunately, the Au seed layer produced Au 4f peaks, which overlapped with the Mn 3s peaks making it impossible to determine the 3s splitting widths. The Mn 2p spectrum was examined instead. All XPS spectra for the deposits were essentially the same; representative Mn 2p and O 1s spectra are shown in Figure 2-5 a and b. The $2p_{3/2}$ binding energy peak is located at 642.25 eV and the $2p_{1/2}$ peak is located at 653.72 eV (Figure 2-5a). The peak positions and the separation

between Mn $2p_{3/2}$ and $2p_{1/2}$, which is about 11.47 eV, can be attributed to a Mn valence of 4+ and/or 3+.

In Chapter 4, XPS analysis is done on Mn oxides electrodeposited on Si substrates with Pt seed layers. The use of Pt eliminates the interference between the Mn 3s and Au 4f signals, so that the Mn 3s peaks can be used for Mn valence determination.

The O 1s spectrum was considered as well. The O 1s spectrum can be deconvoluted into three major bond components: oxide (O^{2-}), hydroxide (OH^-) and residual structural water (Figure 2-5b). This provides useful information about the state of oxygen bonding, hydration of the oxide nanocrystals and the valence of Mn cations. The formation of a hydrated film is considered to be critical to the capacitance mechanism as the fraction of reaction sites accessible to the Faradaic process is larger when the deposit is in a hydrous form [48]. Based on the O 1s XPS spectrum, the deposit consists of MnO_2 (Mn4+) and MnOOH (Mn3+) (which is thermodynamically favorable relative to $Mn(OH)_2$) [49]. For the deposit in Figure 2-5b, the amounts of MnO_2 and MnOOH were determined to be 58% and 37%, respectively. Other deposits had similar distributions. Since, no other crystalline phases were detected through TEM electron diffraction analysis; the MnOOH phase may be amorphous.

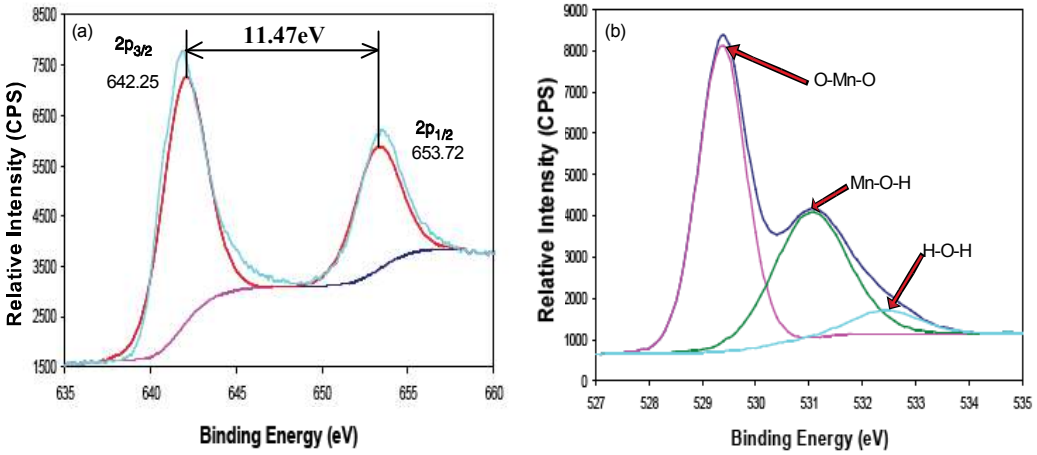

Figure 2-5 Typical (a) XPS Mn 2p spectrum and (b) XPS O 1s spectrum for Mn oxide deposited from a 0.01 M $Mn(CH_3COO)_2$ solution. This particular oxide was deposited at i= 5 $mAcm^{-2}$.

2.3.3 Electrochemical behaviour of Mn oxide electrodes

The electrochemical properties of the oxide coatings were evaluated using CV curves which were scanned at a rate of 20 mVs^{-1} for up to 250 cycles in a 0.5 M Na_2SO_4 solution. A representative plot for a deposit obtained at 5 $mAcm^{-2}$ from the $Mn(CH_3COO)_2$ solution is shown in Figure 2-6. A relatively low scan rate was used to ensure redox transformation for a relatively large fraction of the electrode material. The cyclic voltammogram initially exhibits a rectangular-shaped profile, which is characteristic of ideal capacitive behavior. As the cycling number increases, the area under the voltammetric curves decreases, which is typical for electrochemically active MnO_2. Also, the voltammetric curves exhibit broad anodic and cathodic peaks centered at about 0.55 and 0.42 V. These are attributed to cation de-intercalation upon oxidation and cation intercalation upon reduction. It has been noted that both diffusion and redox reactions contribute to charge transfer for electrochemical charge storage in MnO_2 materials. However, the partial cation intercalation/deintercalation reactions contribute more to the total capacitance with increased cycling, which intensifies the anodic and cathodic

peaks [44]. Also, morphology changes during cycling may facilitate electrolyte transport and reduce solid-state diffusion distances for ions into the oxides, which would increase the prominence of cation intercalation/deintercalation reactions [45].

The specific capacitance C (Fg^{-1}) of the active material was determined by integrating either the oxidative or the reductive parts of the cyclic voltammogram curve to obtain the voltammetric charge Q (C). This charge was subsequently divided by the mass of active material m (g) in the electrode and the width of the potential window of the cyclic voltammogram ΔE (V), i.e., $C = Q/(\Delta Em)$. The original specific capacitances are taken after the second cycle, because after the first charge/discharge cycle both electrodes demonstrate a small irreversible capacity in each sequential cycle. According to the charge/discharge behavior of transition metal oxides, the second CV curve differs considerably from the first because there are significant structural or textural modifications. The large irreversible capacity occurring only in the first cycle may be caused by decomposition reactions in the electrolyte and the formation of a solid electrolyte interphase film on the surface of the Mn oxide electrode [50].

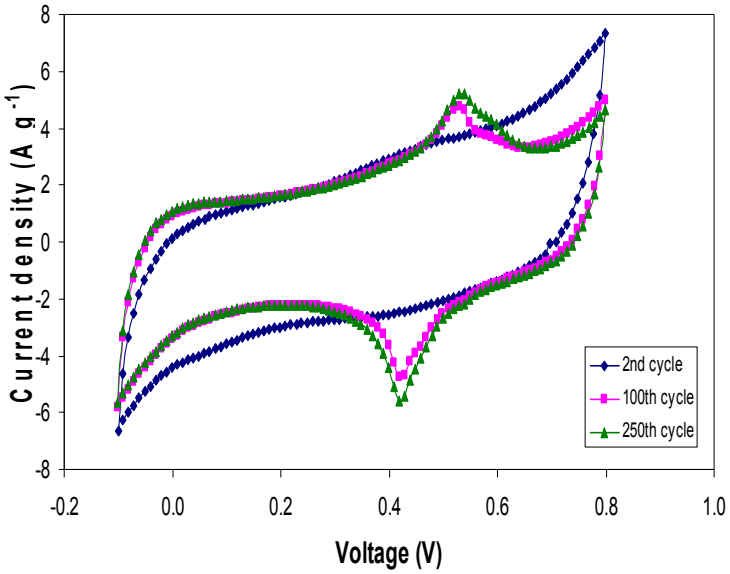

Figure 2-6 Representative cyclic voltammograms taken from Mn oxide electrodes prepared from a 0.01 M $Mn(CH_3COO)_2$ solution at i= 5 $mAcm^{-2}$ (cycled at 20 mVs^{-1} for up to 250 cycles).

Manganese oxide rods synthesized at lower deposition current densities had better specific capacitances. The specific capacitance values for MnO_2 with rod-like structures ($Mn(CH_3COO)_2$ solution), synthesized at different deposition current densities, are shown in Figure 2-7. The deposit prepared at a current density of 5 $mAcm^{-2}$ had the highest specific capacitance (185 Fg^{-1}). Capacitance decreased almost linearly with increasing deposition current density. The specific capacitance values for Mn oxide deposits obtained at different current densities after 2, 100 and 250 cycles in 0.5M Na_2SO_4 are listed in Table 2-1. After 250 cycles at 20 mVs^{-1}, the specific capacitance retention is about 75% of the original value for all deposits.

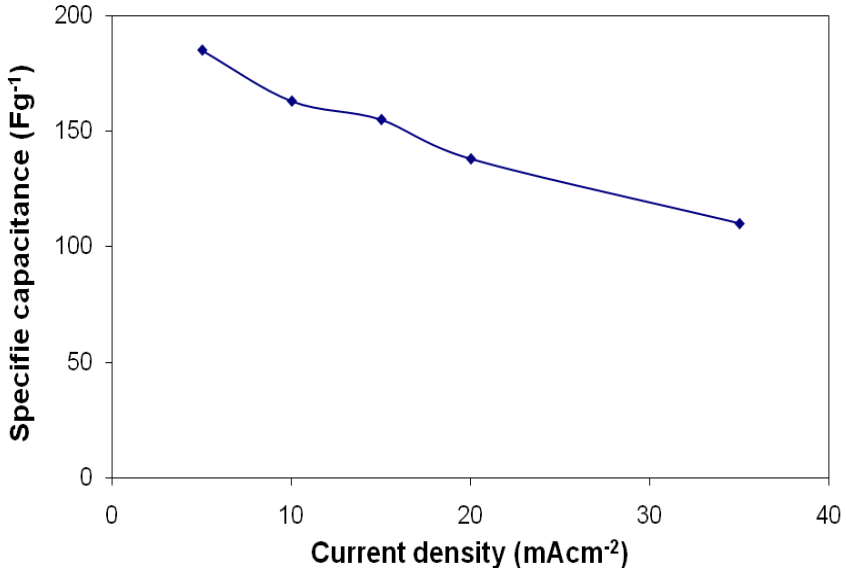

Figure 2-7 Specific capacitance of Mn oxide nanocrystals with a rod-like structure prepared from a 0.01 M $Mn(CH_3COO)_2$ solution at different current densities and cycled at 20 mVs^{-1} (2nd cycle).

Table 2-1 Specific capacitance values for Mn oxide deposits from $Mn(CH_3COO)_2$ solutions at different current densities

Deposition current density ($mAcm^{-2}$)	Specific capacitance after 2nd cycle (Fg^{-1})	Specific capacitance after 100 cycles (Fg^{-1})	Specific capacitance after 250 cycles (Fg^{-1})	Specific capacitance decrease after 250 cycles (%)
5	185	175	139	25
10	163	154	128	22
15	155	145	117	24
20	138	130	108	22
30	120	108	94	23
35	110	75	32	23

2.3.4 Morphology and crystal structure of cycled Mn oxide

Cycled samples were examined in the SEM to monitor any morphological changes. Figure 2-8a-c shows images of Mn oxide electrodes synthesized by anodic deposition from 0.01 M $Mn(CH_3COO)_2$ solutions at different deposition current densities after cycling at 20 mVs^{-1} for 250 cycles. There is not much change in the morphology of the deposits prepared at lower deposition current densities (relative to the as deposited morphology – Figure 2-2). However, the rod-like structure from samples prepared at high current densities has evolved into a petal-like morphology after cycling. This may be attributed to partial dissolution of Mn oxide during cycling, since the charge/discharge process in MnO_2 involves a redox reaction between the III and IV oxidation states of Mn. Some of the MnO_2 inevitably dissolves into the 0.5M Na_2SO_4 electrolyte and then redeposits.

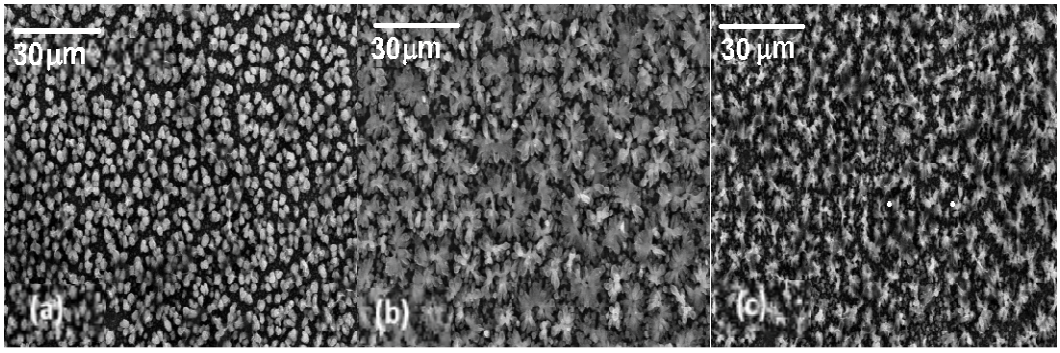

Figure 2-8 SE images of Mn oxide prepared from a solution of 0.01 M $Mn(CH_3COO)_2$ at (a) i= 5 $mAcm^{-2}$; (b) i= 15 $mAcm^{-2}$; (d) i= 20 $mAcm^{-2}$ after 250 cycles at 20 mVs^{-1} (pH= 7.5).

A TEM BF image and corresponding SAED pattern for a Mn oxide deposit, prepared from the 0.01 M $Mn(CH_3COO)_2$ solution at i= 5 $mAcm^{-2}$ after 250 cycles at 20 mVs^{-1}, are shown in Figure 2-9. One of the rods from the deposit is clearly visible in Figure 2-9a, with an internal fibrous structure. Careful examination of the SAED pattern (Figure 2-9b) reveals a total of five main diffraction rings with *d*-spacings of 0.436, 0.242, 0.211, 0.168 and 0.142 nm. The

d-spacings and intensities of these diffracted rings, with the exception of the 1st ring at 0.436 nm, are consistent with that of MnO_2 with an ε-NiAs-type crystal structure (HCP with space group corresponding to $P6_3/mmm$) with lattice parameters of a= 0.280 nm and c= 0.445 nm. In this structure, Mn4+ cations randomly occupy 50% of the octahedral positions of the hexagonal close packed (HCP) oxygen sub-lattice [51]. This structure is one of the common MnO_2 structures described in Chapter 1, Section 1.3.1.2. The four diffracted rings (2nd-5th) are indexed as the $(10\bar{1}0)$, $(10\bar{1}1)$, $(10\bar{1}2)$ and $(11\bar{2}1)$ reflections based on the ε-MnO_2 structure as shown in Figure 2-9. The 1st ring can be indexed to (0001), although the (0001) reflection is generally not allowed for the NiAs-type structure. However, given the highly defective nature of the deposit, the (0001) reflection may become allowable. The crystal structure of Mn oxide has changed to a more close packed structure after 250 cycles in the 0.5M Na_2SO_4 solution. Therefore, fewer electrochemically active sites are available for fast ionic transport and charge transfer, which may account for at least some of the capacitance fading with increasing cycle number.

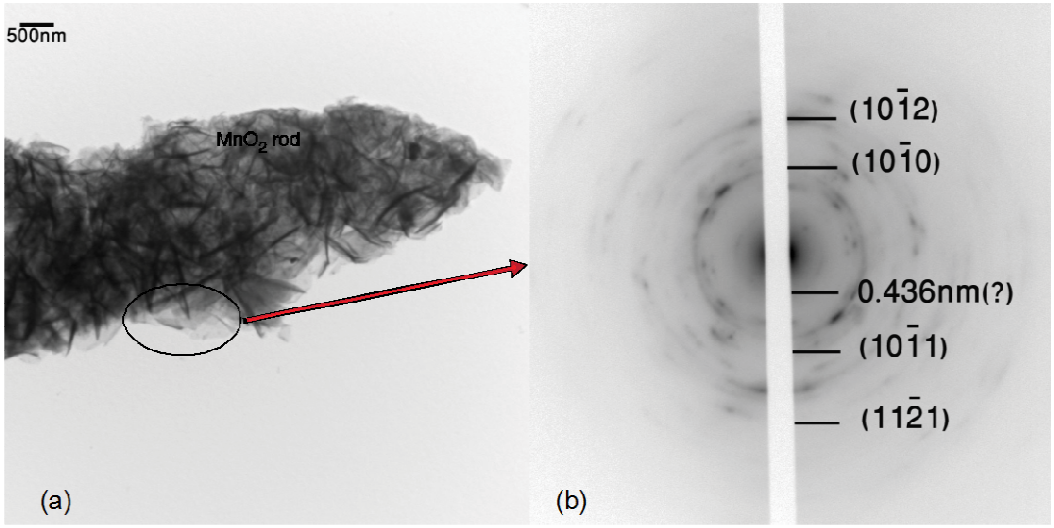

Figure 2-9 Morphology and crystal structure of Mn oxide prepared from a 0.01 M $Mn(CH_3COO)_2$ solution at i= 5mAcm^{-2} after 250 cycles at 20 mVs^{-1}. (a) TEM BF image; (b) SAED pattern.

Several factors can contribute to capacitance fading, including the change in crystal structure discussed in the previous paragraph. The decrease in capacity after cycling can also be attributed to increased electrode resistance with increasing cycle number. A possible reason is that during the charge/discharge processes, catalytic Mn metal may be isolated by a passive film, which forms as a side-reaction byproduct between water and sodium [52]. The evolution from equiaxed rods to a petal-shape, which reduces the effective surface area of the Mn oxide electrodes, may also contribute to capacitance fading with increasing cycle number [48]; however, this effect may be minor for the electrodes in this work. All electrodes showed similar amounts of fading (23-25%) whether or not a petal-shaped morphology formed on cycling.

It has been shown that the physicochemical feature evolution in Mn oxide electrodes has significant effects on the electrochemical behavior [48]. Manganese oxide rods synthesized at lower deposition current densities provide good capacitance behavior and reasonable capacitance retention after cycling. The Mn oxide coatings synthesized at a deposition current density of 5 $mAcm^{-2}$ show the highest specific capacitance (185 Fg^{-1}) and maintain 75% of their capacitance after cycling.

All Mn oxide electrodes prepared from $Mn(CH_3COO)_2$ solutions have a nanocrystalline structure. It should be noted that the nanocrystalline structure of the hydrated Mn oxide rods helps to decrease capacity fading. As previously mentioned, redox reactions (intercalation of Na^+ ions in the electrode during reduction and deintercalation on oxidation) contribute to charge transfer for electrochemical charge storage in MnO_2 materials. In well crystallized electrode materials, Na^+ ion intercalation may be accompanied by some lattice structure distortion, leading to some capacity fading with successive charge/discharge cycles which is reported to be related to stress effects [53]. In contrast, a nanocrystalline structure is less well packed and is therefore better able to

accommodate structural changes. In addition, there is more open free space for Na^+ ion intercalation and diffusion.

2.4 Conclusions

Nanocrystalline Mn oxide coatings were anodically electrodeposited from 0.01 M $MnSO_4$ and 0.01 M $Mn(CH_3COO)_2$ solutions onto the Au coated Si substrates under galvanostatic control. The morphology of Mn oxide deposited from a solution containing 0.01 M $MnSO_4$ was continuous but relatively porous, while rod-like structures were obtained for Mn oxide deposited from a solution containing 0.01 M $Mn(CH_3COO)_2$. Deposits synthesized at a current density of 5 $mAcm^{-2}$, from solutions with 0.01 M $Mn(CH_3COO)_2$, showed the highest specific capacitance (185 Fg^{-1}). As deposited Mn oxide, prepared at different current densities, was made up of MnO_2 with an antifluorite-type crystal structure and MnOOH which was likely amorphous.

The loss in capacitance with electrochemical cycling, which was 23-25% for all Mn oxide deposits, can be attributed to several factors. Increased Mn oxide electrode resistance with increasing cycle number can decrease capacitance. In addition, deposits synthesized at higher current densities underwent a microstructural change on cycling to a petal-shaped morphology; this structure reduced the specific surface area of the Mn oxide leading to the capacitance fading. Finally, MnO_2 transformed to a more ordered hexagonal NiAs-type crystal structure after cycling. As such, fewer electrochemically active sites were available for fast ionic transport and charge transfer.

References

[1] S. Sarangapani, B.V. Tilak and C.P. Chen, *J. Electrochem. Soc.*, **143**, 3791 (1996).

[2] B.E. Conway, Electrochemical Supercapacitors, Kluwer Academic/ Plenum Press, New York (1999).

[3] R.N. Reddy and R.G. Reddy, *J. Power Sources*, **132**, 315 (2004).

[4] A. Burke, *J. Power Sources*, **91**, 37 (2000).

[5] H.A. Andreas and B.E. Conway, *Electrochimica Acta*, **51**, 6510 (2006).

[6] C. Peng, S.W. Zhang and D. Jewell, *Prog. Nat. Sci.*, **18**, 777 (2008).

[7] S. Cho and S. B. Lee, *Acc. Chem. Res.*, **41**, 699 (2008).

[8] C. Peng, J. Jin and G. Chen, *Electrochimica Acta*, **53**, 525 (2007).

[9] A. Malinauskas, J. Malinauskiene and A. Ramanavicius, *Nanotechnology*, **16**, 51 (2005).

[10] D. Belanger, T. Brousse and J.W. Long, *Electrochem. Soc. Interface*, **17(1)**, 49 (2008).

[11] W. Sugimoto, K. Yokoshima and Y. Murakami, *Electrochim. Acta*, **52(4)**, 1742 (2006).

[12] V.D. Patake, C. D. Lokhande and O.S. Joo, *Appl. Surf. Sci.*, **255**, 4192 (2009).

[13] Y.R. Ahn, M.Y. Song, S.M. Jo and C.R. Park, *Nanotechnology*, **17**, 2865 (2006).

[14] C.C. Hu, Y.H. Huang and K.H. Chang, *J. Power Sources*, **108**, 117 (2002).

[15] J. Jiang and A. Kucernak. *Electrochimica Acta*, **27**, 2381 (2002).

[16] P.A. Nelson and J.R. Owen, J. *Electrochem. Soc.*, **150**, 1313 (2003).

[17] S.G. Kandalkar, J. L. Gunjakar and C.D. Lokhande, *Appl. Surf. Sci.*, **254**, 5540 (2008).

[18] L. Cheng, H. Li and Y. Xia, *J. Solid State Electrochem.*, **10**, 405 (2006).

[19] M. Hibino, K. Abe, M. Mochizuki and M. Miyayama, *J. Power Sources*, **126**, 139 (2004).

[20] N. Miura, S. Oonishi, K. Rajendra, *Electrochem. Solid State Lett.*, **7**, 247 (2004).

[21] D.L. Silva, R.G. Delattore and G. Pattanaik, *J. Electrochem. Soc.*, **155**, 14 (2008).

[22] C.C. Hu, C.M. Huang and K.H. Chang, *J. Power Sources*, **185**, 1594 (2008).

[23] X. Zhou, H. Chen, D. Shu and C. He, *J. Phys. Chem. Sol.*, **70**, 495 (2009).

[24] M. Nakayama, A. Tanaka and Y. Sato, *Langmuir*, **21**, 5907 (2005).

[25] S.E. Chun, S.I. Pyun and G. J. Lee, *Electrochimica Acta*, **51**, 6479 (2006).

[26] C.C. Hu and C.C. Wang, *J. Electrochem. Soc.*, **150**, A1079 (2003).

[27] M.S. Wu and P.J. Chiang, *Electrochem. Commu.*, **8**, 383 (2006).

[28] M. Nakayama, T. Kanaya, R. Inoue, *Electrochem. Commu.*, **9**, 1154 (2007).

[29] X. Wang and Y. Li, *J. Chem. Eur.*, **9**, 300 (2003).

[30] M. Toupin, T. Brousse and D. Belanger, *Chem. Mater.*, **16**, 3184 (2004).

[31] S.C. Pang and M.A. Anderson, *J. Mat. Res.*, **15**, 2096 (2000).

[32] S.F. Chin, S.C. Pang and M.A. Anderson, *J. Electrochem. Soc.*, **149**, A379 (2000).

[33] G.H.A. Therese and P.V. Kamath, *Chem. Mater.*, **12**, 1195 (2000).

[34] T. Brousse, M. Toupin, R. Dugas and L. Athouel, *J. Electrochem. Soc.*, **153**, 2171 (2006).

[35] K. Naoi and P. Simon, *Electrochem. Soc. Interface*, **17(1)**, 34 (2008).

[36] S. Comaba, A. Ogata and T. Tsuchikawa, *Electrochem. Commu.*, **10**, 1435 (2008).

[37] Y.C. Hsieh, K.T. Lee, Y.P. Lin, N.L. Wu and S.W. Donne, *J. Power Sources*, **177**, 660 (2008).

[38] R. Liu and S.B. Lee, *J. Am. Chem. Soc.*, **130**, 2942 (2008).

[39] R.K. Sharma, A.C. Rastogi and S.B. Desu, *Electrochimica Acta*, **53**, 7690 (2008).

[40] C.C. Hu, K.H. Chang, M.C. Lin and Y.T. Wu, *Nano Lett.*, **6**, 2690 (2006).

[41] F. Cheng, Z. Thao, J. Liang and J. Chen, *Chem. Mater.*, **2**, 667 (2008).

[42] G.Y. Zhao, C.L. Xu and H.L. Li, *J. Power Sources*, **163**, 1132 (2007).

[43] Y. Xia, P. Yang, Y. Sun and Y. Wu, *Adv. Mater.*, **15**, 353 (2000).

[44] W. Wei, W. Chen and D.G. Ivey, *J. Phys. Chem.*, **111**, 10398 (2007).

[45] W. Wei, X. Cui, W. Chen and D.G. Ivey, *Electrochimica Acta*, **54**, 2271 (2009).

[46] M. Toupin, T. Brousse and D. Blanger, *Chem. Mater.*, **14**, 3946 (2002).

[47] M. Chigane and M. Ishikawa, *J. Electrochem. Soc*., **147**, 2246 (2000).

[48] B. Djurfors, J.N. Broughton, M.J. Brett and D.G. Ivey, *Acta Mater.*, **53**, 957 (2005).

[49] W. Wei, X. Cui, W. Chen and D.G. Ivey, *J. Power Sources*, **186**, 543 (2009).

[50] R. Dedryvere, S. Laruelle, S. Grugeon, P. Poizot and J.M. Tarascon, *Chem. Mater.*, **16**, 1056 (2004).

[51] C.H. Kim, Z. Akase, L. Zhang and A.H. Heuer, *J. Solid State Chem.*, **179**, 753 (2006).

[52] M.S. Wu, P.C.J. Chiang, J.T. Lee and J.C. Lin, *J. Phys. Chem. B*, **109**, 23279 (2005).

[53] D. Liu, Q. Zhang, P. Xiao and B.B. Garcia, *Chem. Mater.*, **20**, 1376 (2008).

Chapter 3 Improved capacitive behavior of electrochemically synthesized Mn oxide/PEDOT electrodes utilized as electrochemical capacitors[2]

3.1 Introduction

Electrochemical capacitors are charge–storage devices of high power and energy density, which exhibit excellent reversibility and a long cycle life. The energy stored in these devices mainly comes from either the electrical double layer or the pseudocapacitance of electroactive materials [1,2].

Considerable effort has been devoted to the development and characterization of new electrode materials with improved performance for application as electrochemical capacitors. Among the various pseudocapacitor electrode materials, there is increasing interest in the development of electrode materials based on Mn oxides because of their low cost and environmentally friendly nature [3,4]. However, capacitance fading attributed to partial dissolution of MnO_2 films in the electrolyte during cycling is the main drawback of fabricated hydrous Mn oxide electrodes [5,6]. The electrochemical characteristics of electrode materials have been shown to be highly dependent on their texture, surface area and morphology, with ordered, high surface area structures enhancing the electrochemical properties [3,7,8]. Templated electrosynthesis has been widely used as an effective pathway to form one–dimensional and porous structures using anodic aluminum oxide (AAO) and polycarbonate membranes [9]. Transition metal oxides such as MnO_2 [10,11], SnO_2 [12,13], V_2O_5 [14,15], Co_2O_3[16] and Fe_3O_4 [17] nanowires, conducting polymers such as polyethylenedioxythiophene (PEDOT) [18] and polyaniline (PANI) [19] nanotubes and composites such as metal oxide/conducting polymer nanowires [20] and carbon nanotubes (CNT)/conducting polymers [21] with high energy and power density have been prepared by template methods. This method is not, however, easy to use in

[2] *A version of this chapter has been published. Banafsheh Babakhani, Douglas G. Ivey. Electrochimica Acta,* ***55*** *(2010) 4014–4024.*

practical applications due to the fragility of the oxide template and the need for dissolution of the aluminum oxide after fabrication [22].

In Chapter 2, Mn oxide films with rod–like structures were prepared through anodic deposition from a 0.01 M Mn acetate solution at various deposition current densities on Au coated Si substrates without the use of a template [8]. The best capacitance (185 Fg^{-1}) was achieved for deposits obtained at low current density (5 $mAcm^{-2}$). Also, after 250 cycles in 0.5M Na_2SO_4 at 20 mVs^{-1}, capacitance retention was ~75% of the original value (~139 Fg^{-1}) [8].

Several researchers have shown that the combination of rod–like Mn oxide with other materials, such as conducting polymers, can further increase the specific capacitance values and improve cycling retention [20,23–25]. Conducting polymers don't exhibit large pseudocapacitance, electrical conductivity, good stability and negligible solubility in aqueous solutions [26]. Therefore, the presence of a polymer in the appropriate configuration may suppress Mn dissolution and also improve resistance to mechanical failure [23]. Electrochemically conducting polymers exhibit pseudo-Faradaic behavior within the potential range where they are in their low oxidation state. At a higher oxidation state, charged centers become delocalized which gives a metal-like character to the electrochemically conducting polymers. In the latter case, the energy is stored in the conducting polymer by the accumulation of charges in the electrical double layer, by electrostatic forces [27]. However, the interchange rate is usually slow due to the rate–determining process of counter ion transport into the polymer layer for charge balance. By producing nanoscale porosity in the form of nanotubes or nanowire structures, the ion–transport resistance in the polymer can be reduced [28–31]. Therefore, the combination of a transition metal oxide and conducting polymer in one–dimensional structures may exhibit improved electrical, electrochemical and mechanical properties for electrochemical energy storage [20,23]. Conducting polymers can be obtained by either chemical or electrochemical polymerization. The type of polymerization

technique, with potentiostatic or galvanostatic control, and the type of monomer and its concentration affect the properties of the produced polymer [21,29, 32,33].

The aim of this chapter is to prepare Mn oxide/polyethylenedioxythiophene (PEDOT) coaxial core/shell electrodes by coating Mn oxide rods sequentially by electrochemical polymerization of PEDOT [8]. Detailed microstructural analysis of the Mn oxide/PEDOT electrodes is done and the microstructures are compared with the electrochemical behavior. The Mn oxide/PEDOT electrodes are prepared in both one–step (co–electrodeposition) and sequential methods.

3.2 Experimental procedure

For sequential electrodeposition, Mn oxide coatings were first deposited onto Au coated Si substrates, using the procedure described in Chapter 2. The Mn oxide rods were subsequently coated with a conducting polymer (PEDOT) obtained from the electro-polymerization of a solution of 0.08 M 3,4-ethylenedioxythiopene (EDOT), 0.2 M lithium tetrafluoroborate ($LiBF_4$) and 0.14M sodium dodecyl sulphate (SDS) [23]. Electro-polymerization was applied at 1V for a deposition time in the 10-60 s range. In one–step electrodeposition, Mn oxide and PEDOT were anodically deposited onto Au coated Si substrates under galvanostatic conditions, i.e., with current densities of 10 $mAcm^{-2}$ to 30 $mAcm^{-2}$ using a solution of four components: 0.01 M $Mn(CH_3COO)_2$, 0.08 M EDOT, 0.14 M SDS and 0.2 M $LiBF_4$. In all cases, a three electrode cell configuration was used and consisted of a platinum mesh counter electrode with the same dimensions as the working electrode placed vertically 20 mm away from the vertical working electrode and parallel to it. A saturated calomel electrode (SCE) was used as the reference electrode and all the potentials quoted are with respect to it. After electrodeposition the working electrodes were rinsed with deionized water, dried at 100°C for 60 min in air and then stored in a vacuum dessicator before further analysis. The mass of the Mn oxide/PEDOT deposits on the Au coated Si electrodes, prepared both sequentially and through co-

deposition, was determined from the weight difference between the Au coated Si electrode before and after anodic deposition, as described in Chapter 2.

The electrochemical behavior of the Mn oxide/PEDOT deposits was investigated with a Gamry PC4/750 potentiostat/galvanostat under cyclic voltammetry (CV) mode in an electrolyte containing 0.5 M Na_2SO_4 at room temperature [8]. Cyclic voltammograms were recorded between –0.1 and 0.9 V, at 20 mVs^{-1}, for uncoated Mn oxide and Mn oxide/PEDOT deposits prepared via the sequential method and between 0 and 1 V for co–electrodeposited Mn oxide/PEDOT. The Mn content in the 0.5 M Na_2SO_4 electrolyte after 2 and 250 cycles for both Mn oxide and sequential Mn oxide/PEDOT deposits was determined using a VARIAN 220 FS atomic absorption spectrometer (AAS).

Morphological and crystal structural analysis were conducted using SEM and TEM with the operating parameters described in Chapter 2. In most cases, to prepare an electron transparent sample for TEM, some of a deposit was scraped off the substrate and then ultrasonically dispersed in methanol for 10 minutes. One or two drops of the suspension were deposited onto a C–coated, Cu grid. Select TEM samples were prepared in cross section orientation using focused ion beam (FIB) milling with an FEI FIB200-SIMS ion microscope. Chemical state analysis of uncoated Mn oxide and Mn oxide/PEDOT rods was carried out by XPS, using the conditions given in Chapter 2, Section 2.2.

3.3 Results and discussion

3.3.1 Mn oxide/PEDOT deposit morphology

The morphology of the as–prepared Mn oxide/PEDOT deposits prepared in both sequential and one–step methods were analyzed using SEM. Plan view secondary electron (SE) images, shown in Figure 3-1, reveal free–standing Mn oxide/PEDOT coaxial core/shell rods prepared using the sequential template–free

method [23]. The structure of the coaxial rods, such as Mn oxide rod length and PEDOT shell thickness (less than 150 nm), can be controlled by varying the Mn oxide deposition current density and time [8] and the subsequent polymer applied potential and deposition time [23], respectively.

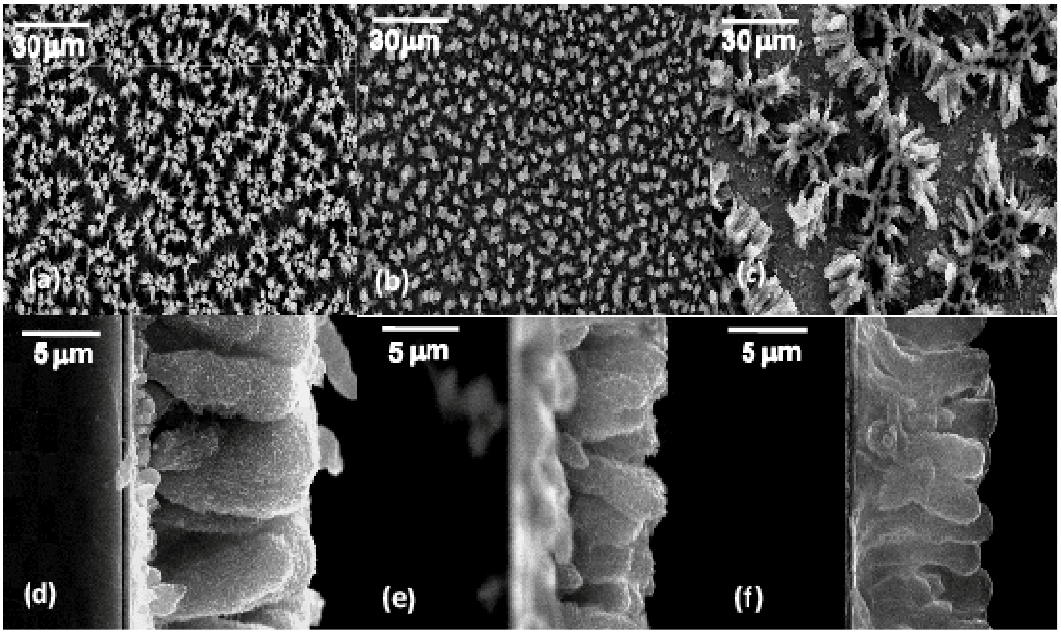

Figure 3-1 SEM SE plan view and cross–section images of Mn oxide/PEDOT coaxial core/shell rods prepared from a 0.01 M $Mn(CH_3COO)_2$ solution at (a) and (d) 5 $mAcm^{-2}$; (b) and (e) 15 $mAcm^{-2}$; (c) and (f) 20 $mAcm^{-2}$, followed by PEDOT deposition at 1V for 45s.

The Mn oxide electrodes with rod–like structures exhibit large specific surface areas, which promote efficient contact between the active material and the electrolyte, providing many active sites for electrochemical reactions. Structures with porosity and interconnectivity supply additional accessible space for ions, while maintaining sufficient conductivity for solid–state electronic transfer to improve the electrochemical capacity. This type of structure provides short diffusion path lengths to both ions and electrons and also sufficient porosity for electrolyte penetration to increase charge/discharge rates [3]. When applying the

PEDOT shell to the Mn oxide rods, the porous nature of the PEDOT also allows fast ion diffusion into the core Mn oxide of the coaxial electrodes. Moreover, the electrically conductive PEDOT shell, with conductivity values of up to 25 S cm^{-1} depending on the doping level [34], facilitates electron transport to the core Mn oxide, which has a relative low conductivity (~10^{-4} S cm^{-1}) that can limit its charge/discharge rate [20]. Therefore, enhanced capacitance and high cycling rate capability can be expected by applying a PEDOT shell on the Mn oxide rod like cores.

The morphology of the Mn oxide/PEDOT rods can be controlled by varying the deposition current density (Figure 3-1). Mn oxide/PEDOT rods prepared at lower deposition current densities (Figure 3-1a and d) are more uniform in size with smaller rod diameters, providing larger surface areas and, therefore, a higher number of active sites leading to better electrochemical capacity. To illustrate this, a simple order of magnitude calculation can be done. Mn oxide/PEDOT rods, prepared at a current density of 5 $mAcm^{-2}$ and electro–polymerized with PEDOT at 1 V for 45 s, have rods that are ~1-3 μm in diameter and ~10 μm in length, with a planar density of ~10 cm^2 of electrode surface per cm^2 of substrate surface (Figure 3-1a and 1d). Deposits prepared at a current density of 20 $mAcm^{-2}$ with the same PEDOT deposition condition as the former case, have rods that are ~2-4 μm in diameter and ~6 μm in length, with a planar density of ~3.3 cm^2 of electrode surface per cm^2 of substrate surface (Figure 3-1c and 1f). This represents an increase of more than 3 times in exposed surface for the deposits prepared at 5 $mAcm^{-2}$ compared with those prepared at 20 $mAcm^{-2}$. In addition, at higher deposition current densities (Figure 3-1c and f), synthesized Mn oxide/PEDOT tends to form interconnected rods.

The rod–like structure was not obtained via co–electrodeposition. Figure 3-2a–f show plan view and cross sectional SEM images of Mn oxide/PEDOT synthesized by co–electrodeposition for deposition current densities from 10 $mAcm^{-2}$ to 30 $mAcm^{-2}$ for 60 s. The agglomerated particles are about 5–10, 10–15

and ~20 μm in diameter for deposits prepared at 10, 20 and 30 $mAcm^{-2}$, respectively. The synthesized Mn oxide/PEDOT composites deposited at lower current density (Figure 3-2a) are less dense. At higher deposition current densities (Figure 3-2b and c), agglomeration is more prevalent. As shown later in this chapter, the deposits prepared at higher deposition current densities provide better electrochemical behavior.

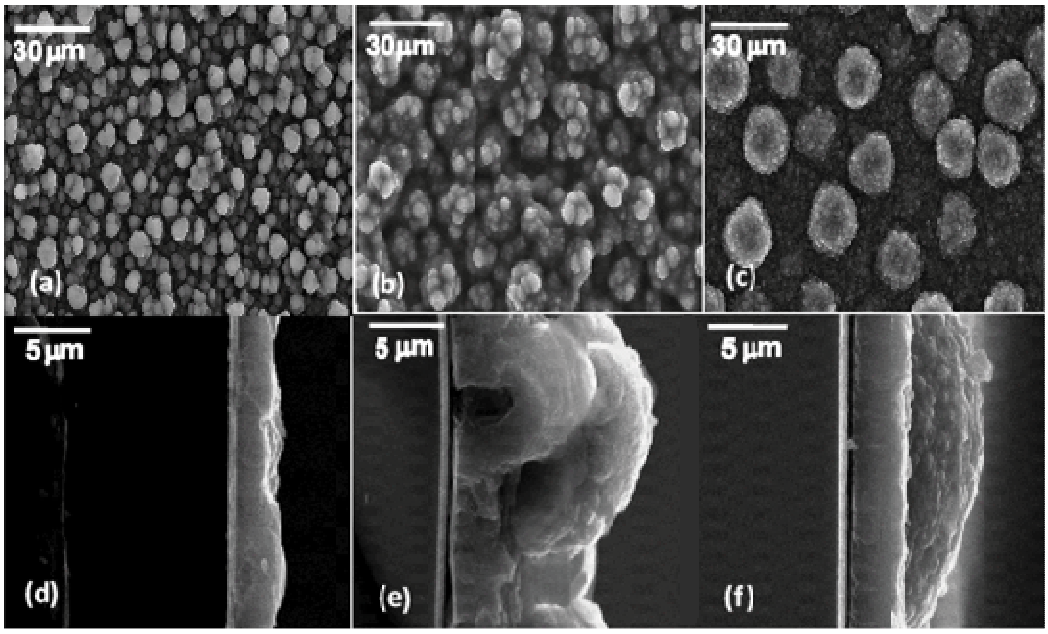

Figure 3-2 SEM SE plan view and cross section images of Mn oxide/PEDOT prepared by co–electrodeposition: (a) and (d) deposited at 10 $mAcm^{-2}$; (b) and (e) deposited at 20 $mAcm^{-2}$; (c) and (f) deposited at 30 $mAcm^{-2}$ for 60 s.

3.3.2 Electrochemical behavior of Mn oxide and Mn oxide/PEDOT

The electrochemical properties of the Mn oxide/PEDOT deposits synthesized by both sequential and one–step electrodeposition were evaluated by cyclic voltammetric analysis in a 0.5 M Na_2SO_4 solution. The specific capacitance C (Fg^{-1}) of the active material was determined from $C = Q/(\Delta Em)$, as described in Chapter 2.

Kinetic and thermodynamic control can be implemented by simply adjusting the current or potential at which the deposition is carried out. The observed voltammetric response is characteristic of a Faradaic electron transfer process that is proportional to the charge passed. This type of behavior is typical of 3D electro-insertion processes (electrochemical intercalation) where the electrode potential is a function of the progressive occupation of surface sites or is a function of the ratio of oxidant converted to reductant (or vice versa) in a redox system. As discussed by Conway *et al.* [35], these electrochemical systems are manifested by a redox pseudocapacitance, $C = \mathrm{d}(\Delta q)/\mathrm{d}V$, where the extent of charge, Δq, varies with potential, V. This redox pseudocapacitance can be described by a modified Nernst equation,

$$E = E_0 + \frac{RT}{nF}\left[\ln\left(\frac{k}{1-k}\right)\right] \qquad (3\text{-}1)$$

where the concentrations or activities of oxidants [Ox] and reductants [Red] are expressed as relative fractions, k, with k = [Ox]/([Ox] + [Red]). The voltammetric current ($i=C\,(dV/dt)$) is a direct measure of the capacitive charge ($\Delta q = C\,\Delta V$) and is directly related to the total concentration of [Ox] and [Red].

As shown in Chapter 2, Mn oxide rods prepared at a current density of 5 $mAcm^{-2}$ have the highest specific capacitance, due to their large surface area and high number of active sites for electrolyte access (see, e.g., Figure 3-1a and d for coated Mn oxide rods). These samples were then used for PEDOT electrodeposition. Specific capacitance values for the sequential Mn oxide/PEDOT deposits (Mn oxide synthesized at 5 $mAcm^{-2}$ and electro–polymerized with PEDOT at 1 V for various times) and co–electrodeposited Mn oxide/PEDOT (synthesized at different deposition current densities for 60 s) after 2, 100 and 250 cycles in 0.5 M Na_2SO_4 are listed in Table 3-1 and 3-2, respectively. The best specific capacitance (~285 Fg^{-1}) for Mn oxide/PEDOT

coaxial rods produced sequentially is significantly higher than the best capacitances for co–electrodeposited MnO_2/PEDOT (~195 Fg^{-1}) and uncoated Mn oxide rods (~185 Fg^{-1}). Also, after 250 cycles at 20 mVs^{-1}, the reduction in specific capacitance was 8% of the initial reversible capacity for the Mn oxide/PEDOT rods with a polymer deposition time of 45 s, while the capacitance fading for the co–electrodeposited Mn oxide/PEDOT and Mn oxide rods was ~13 and 25%, respectively. Reversible capacity decay indicates a decrease in the amount of active material with cycle number. For Mn oxide/PEDOT composites prepared by sequential electrodeposition, the presence of PEDOT as a shell on the Mn oxide can provide an interconnected network during the charge/discharge process to facilitate both charge–transfer reactions and electron conduction. Thus, the Mn oxide/PEDOT coaxial core/shell rods exhibit high capacitance and long redox cycling life. Mn oxide/PEDOT fabricated by co–electrodeposition consists of agglomerated particles of Mn oxide and PEDOT giving a less porous structure relative to the Mn oxide/PEDOT rods prepared by sequential electrodeposition, resulting in kinetic restrictions. This accounts for the lower capacitance in the former case. The co-electrodeposited composites show higher capacitance at higher deposition current densities (Table 3-2); however, there is an upper limit to the current density. At current densities exceeding 30 $mAcm^{-2}$, the deposits have poor adhesion to the substrate.

Table 3-1 Specific capacitance values for Mn oxide/PEDOT coaxial rods deposited from a 0.01 M $Mn(CH_3COO)_2$ solution at 5 $mAcm^{-2}$ and subsequently coated with electro–polymerized PEDOT at 1 V

Polymer deposition time (s)	Specific capacitance after second cycle (Fg^{-1})	Specific capacitance after 100 cycles (Fg^{-1})	Specific capacitance after 250 cycles (Fg^{-1})	Specific capacitance decrease after 250 cycles (%)
0	185	175	139	25
10	190	180	168	12
20	200	185	175	13
30	228	210	204	11
45	285	265	261	8
60	195	175	172	12

Table 3-2 Specific capacitance values for Mn oxide/PEDOT deposits prepared by co–electrodeposition for different deposition current densities for 60 s

Deposition current density ($mAcm^{-2}$)	Specific capacitance after second cycle (Fg^{-1})	Specific capacitance after 100 cycles (Fg^{-1})	Specific capacitance after 250 cycles (Fg^{-1})	Specific capacitance decrease after 250 cycles (%)
5	98	90	86	12
10	110	100	95	13
15	130	120	112	13
20	160	148	140	12
30	195	180	172	12

Figure 3-3a-c shows cyclic voltammograms obtained from the deposits which show the best electrochemical properties, i.e., Mn oxide rods (prepared from a 0.01 M $Mn(CH_3COO)_2$ solution at 5 $mAcm^{-2}$ for 10 min) [8], Mn oxide/PEDOT coaxial core/shell rods (prepared from a 0.01 M $Mn(CH_3COO)_2$ solution at 5 $mAcm^{-2}$ for 10 min followed by electro–polymerization of PEDOT at 1 V for 45 s) [23] and Mn oxide/PEDOT deposits (co-electrodeposited from a solution of 0.01 M $Mn(CH_3COO)_2$, 0.08 M EDOT, 0.14 M SDS, 0.2 M $LiBF_4$ at 30 $mAcm^{-2}$ for 60s), at a scan rate of 20 mVs^{-1} for up to 250 cycles, respectively. All three curves show rectangular–like and symmetric voltammograms, demonstrating the

good capacitive behavior of these electrode materials. For the rod–like Mn oxide deposits (Figure 3-3a), the voltammetric curves exhibit anodic and cathodic peaks, characteristic of redox transitions resulting from ion exchange, with increasing cycle number. The peaks become gradually larger and the anodic peak potentials shift to a more positive direction as the number of potential cycles is increased. It appears that all the redox peaks overlap with neighboring peaks and became slightly larger with increasing cycle number.

For the Mn oxide/PEDOT coaxial core/shell rods prepared by sequential electrodeposition (Figure 3-3b) only weak redox peaks appear between 0.1 and 0.8 V [23]. There are no visible peaks for the Mn oxide/PEDOT deposits prepared by co–electrodeposition (Figure 3-3c), which indicates that the Mn oxide/PEDOT electrode capacitors prepared by both sequential electrodeposition and co–electrodeposition are charged and discharged at a constant rate over the complete voltammetric cycle [36,37]. Large and relatively constant currents are observed over an extensive potential window (0-0.8V) in the voltammograms, characterizing the capacitive nature of these materials [24]. Deviation from the rectangular shape for the voltammograms of the Mn oxide/PEDOT composites is also related to polarization resistance [24,38].

It should be noted that the large values of current in the voltammograms are not associated with double layer charging, but are likely the result of the pseudocapacitance attributed to the Mn(III)/Mn(II) and Mn(IV)/Mn(III) redox transitions [11]. These redox transitions lead to exchange of protons and/or alkali cations with the electrolytes. The initial reduction of MnO_2 to MnOOH involves incorporation of protons and electrons into the MnO_2 lattice. The reduction of MnO_2 proceeds with the dilation of the lattice, which leads to the eventual formation of an amorphous MnOOH phase. MnO_2 exhibits high charge storage capacity due to enhanced proton diffusion in and out of MnO_2 lattice [39].

The reductions in the area under the voltammetric curves with increasing cycle number are lower for the Mn oxide/PEDOT composites compared with the uncoated Mn oxide electrodes. For Mn oxide/PEDOT deposits prepared by sequential electrodeposition, the PEDOT shell on the core Mn oxide is believed to protect the Mn oxide from dissolution during cycling (this is discussed further in subsequent sections), so a large amount of active material is still available after cycling which results in improved electrochemical cyclability (Table 3-1). The Mn oxide/PEDOT rods showed a much higher initial specific capacitance (285 Fg^{-1} – Figure 3-3b) compared with the uncoated Mn oxide rods (185 Fg^{-1} – Figure 3-3a) or co–electrodeposited Mn oxide/PEDOT electrodes (195 Fg^{-1} – Figure 3-3c).

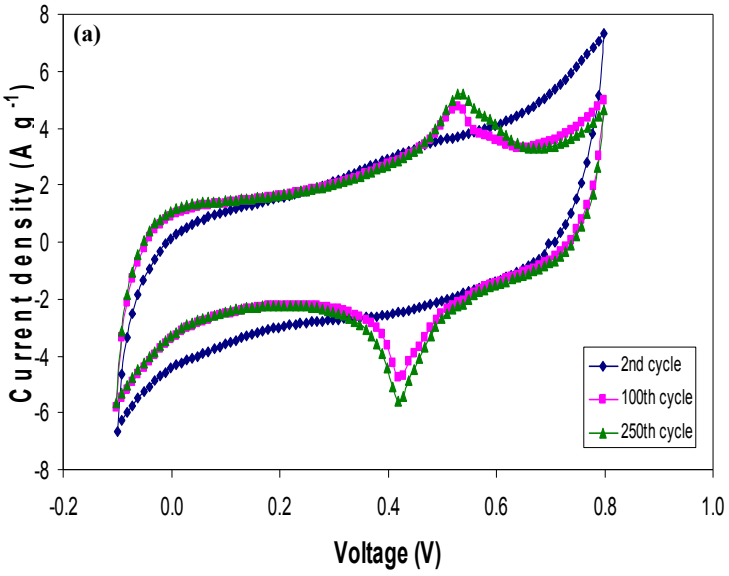

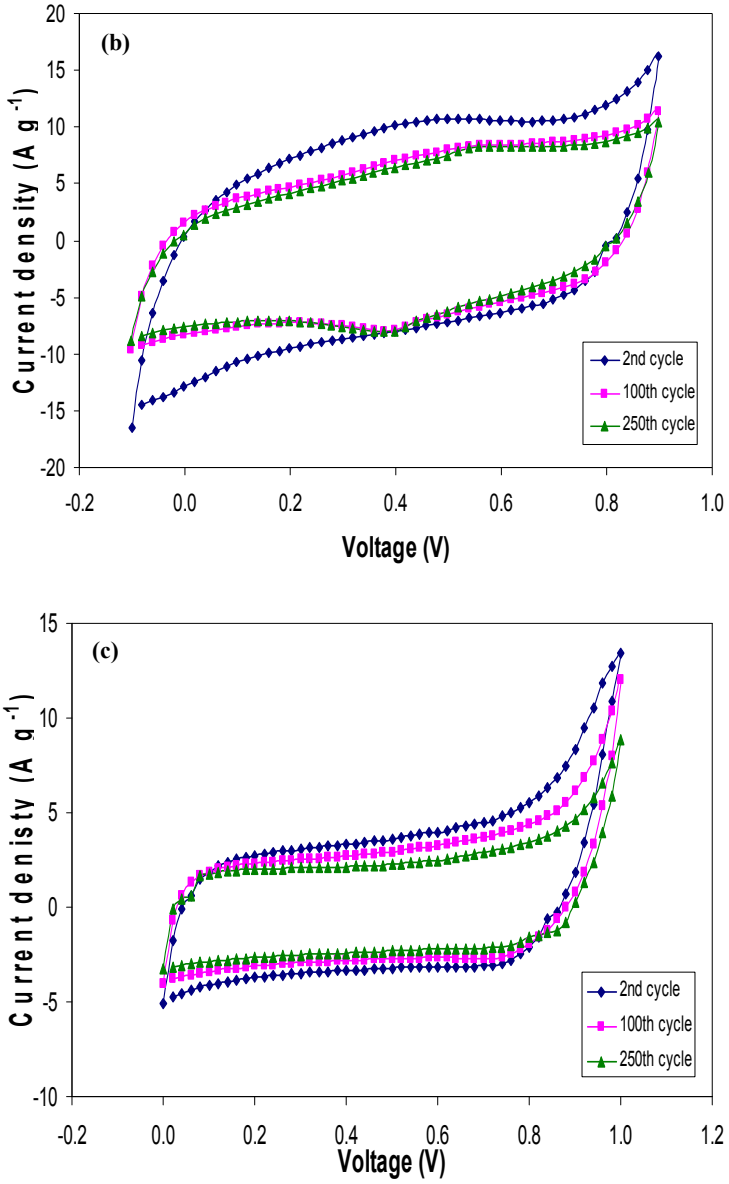

Figure 3-3 Representative cyclic voltammograms taken from (a) Mn oxide rods; (b) Mn oxide/PEDOT coaxial core/shell rods; (c) Mn oxide/PEDOT codeposits. The deposits in (a) and (b) were prepared from a 0.01 M $Mn(CH_3COO)_2$ solution at 5 $mAcm^{-2}$ for 10min; the deposit in (b) was subsequently coated with electro–polymerized PEDOT at 1 V for 45 s; the deposit in (c) was prepared by co–electrodeposition at 30 $mAcm^{-2}$ for 60 s. The samples were cycled at 20 mVs^{-1} for up to 250 cycles.

The enhancement in the charge storage capacity of Mn oxide/PEDOT composite electrodes prepared by co–electrodeposition, compared with deposits with no PEDOT is attributed to the structural modifications due to PEDOT deposition. Conducting polymers exhibit large pseudocapacitance, electrical conductivity and negligible solubility in aqueous solutions [26]. Therefore, the presence of PEDOT facilitates both ion diffusion and electron conduction compared with uncoated Mn oxide rods, leading to better capacitive behavior. During the growth of Mn oxide/conducting polymer composite electrodes prepared by co–electrodeposition, the conducting polymer provides a large surface to the growing Mn oxide due to its porous morphology, enabling a highly active surface for Mn oxide particles. Simultaneously, the nucleation of Mn oxide particles over growing polymer chains terminates their further growth by attachment, leading to fresh nucleation of a polymer chain on the same site or at another one. The polymer structure is an important parameter as shorter and more ordered polymer structures are reported to be better structures for charge storage [40].

The growth of the Mn oxide/PEDOT composites prepared by co-electrodeposition can be achieved by the anodic formation of Mn oxide and the simultaneous attachment of polycations to negative charges on the deposited Mn oxide. This can be represented by Equation 3-2, with reference to the electrodeposition of MnO_2 ($Mn^{2+} + 2H_2O \longrightarrow MnO_2 + 4H^+ + 2e^-$) [41,42].

$$Mn^{2+} + 2H_2O + xA^+ \longrightarrow A^+_x Mn^{3+}_x Mn^{4+}_{1-x} O_2 + 4H^+ + (2 - x)e^- \qquad (3\text{-}2)$$

where A^+ corresponds to one cationic unit.

As mentioned before, electrode capacitance depends on structure and morphology. The improved cyclability of co–electrodeposited Mn oxide/PEDOT composites compared with deposits with no PEDOT is attributed, in part, to the enhanced porosity of the composite material. As such, ions are still able to access the active regions of polymer chains and Mn oxide, so that the decrease in the

pseudo–capacitance during cycling occurs to a much lesser extent [24]. The 12–13% capacitance decline for co–electrodeposited Mn oxide/PEDOT composites may be attributed to the loss of unstable Mn ions by dissolution in the electrolyte solution [43]. Based on the Mn-H_2O Pourbaix diagram, some Mn dissolution in the 0.5 M Na_2SO_4 solution is expected during cycling from 0.9 to –0.1 V. The amount of dissolution, as determined through AAS measurements, was significantly lower for PEDOT coated Mn oxide compared with uncoated Mn oxide. For uncoated Mn oxide, solution Mn levels of 0.17 and 0.25 ppm were found after 2 and 250 cycles, respectively; for PEDOT coated Mn oxide deposits solution Mn levels were 0.08 and 0.12 ppm, respectively.

It has been established that the Faradaic reactions occurring on the surface and in the bulk of the materials are the major charge storage mechanisms for Mn oxide materials. The surface Faradaic reaction involves the surface adsorption of electrolyte cations ($A^+ = Na^+$) on the Mn oxides

$$(MnO_2)_{surface} + A^+ + e^- \longleftrightarrow (MnOOA)_{surface} \quad (3\text{-}3)$$

The bulk Faradaic reaction relies on the intercalation or deintercalation of H+ or alkaline metal cations in the bulk of the Mn oxides [39]:

$$MnO_2 + H^+ + e^- \longleftrightarrow MnOOH \quad (3\text{-}4)$$

$$MnO_2 + A^+ + e^- \longleftrightarrow MnOOA \quad (3\text{-}5)$$

The redox processes in conducting polymers involve mass and resistance changes as well as electron transitions, unlike other redox systems in electrochemistry where only electrons are involved. The oxidation (doping) of the polymer yields a charged polymer film with incorporated anions and during reduction (dedoping) these anions are expelled. It is interesting that in the Mn oxide/conducting polymer composites, prepared by both sequential deposition and co–

electrodeposition, the charge storage of Mn oxide utilizes the cations from the electrolyte; however, the anions are involved as charge compensating ions in the conducting polymer. It has been shown that PEDOT can be permselective, i.e., restricts cation transport through its layer, which depends on the concentration of the electrolyte [44]. At high electrolyte concentrations, i.e., when the concentration is comparable to the volume density of the active (charged) sites in the polymer, cations can enter the polymer. When the electrolyte concentration is sufficiently low, PEDOT is permselective and cation incorporation can be neglected [44]. In this work, the solution is concentrated enough so that PEDOT is not permselective.

The improved performance of sequentially deposited Mn oxide/PEDOT composite electrodes, compared with co-electrodeposited Mn oxide/PEDOT electrodes, is attributed to the enhanced surface area (porosity) of the material of the former [20]. For sequentially prepared Mn oxide/PEDOT composites, the PEDOT shell also inhibits Mn oxide dissolution into the electrolyte during cycling, minimizing the loss of active electrode material and capacitance reduction.

Since the Mn oxide/PEDOT deposits prepared sequentially exhibited the best capacitive behavior and the most desirable morphology (rod-like structures), more detailed microstructural analysis was carried out on these materials.

3.3.3 Crystal structure analysis of Mn oxide and Mn oxide/PEDOT electrodes

The crystal structure of the as–prepared Mn oxide and Mn oxide/PEDOT deposits prepared sequentially was analyzed using TEM (Figure 3-4). Figure 3-4a and b show TEM bright field (BF) images of Mn oxide and Mn oxide/PEDOT core/shell rods, respectively, in which the fibrous surfaces are clearly visible. A dark field (DF) image and a selected area electron diffraction (SAED) pattern of the circled region in Figure 3-4a (Figure 3-4c) reveal that the Mn oxide consists of

polycrystalline grains with a diameter less than 10 nm. As described in Chapter 2, Section 2.3.1, the SAED pattern was indexed to an antifluorite-type crystal structure (FCC with space group corresponding to Fm $\bar{3}$m) with a lattice parameter of 0.445 nm.

A similar, but less distinct, SAED pattern was obtained for the Mn oxide/PEDOT deposits (Figure 3-4d). The ring pattern is from the Mn oxide core, while the faint, diffuse pattern is from the amorphous PEDOT shell. The *d*–spacings measured from the SAED pattern for Mn oxide are also consistent with an antifluorite–type crystal structure and a lattice parameter of 0.450 nm was determined, which is similar to that for the uncoated Mn oxide rods (Figure 3-4c). The first four diffracted rings for both samples can be indexed as (111), (200), (220) and (311) in increasing distance away from the central spot.

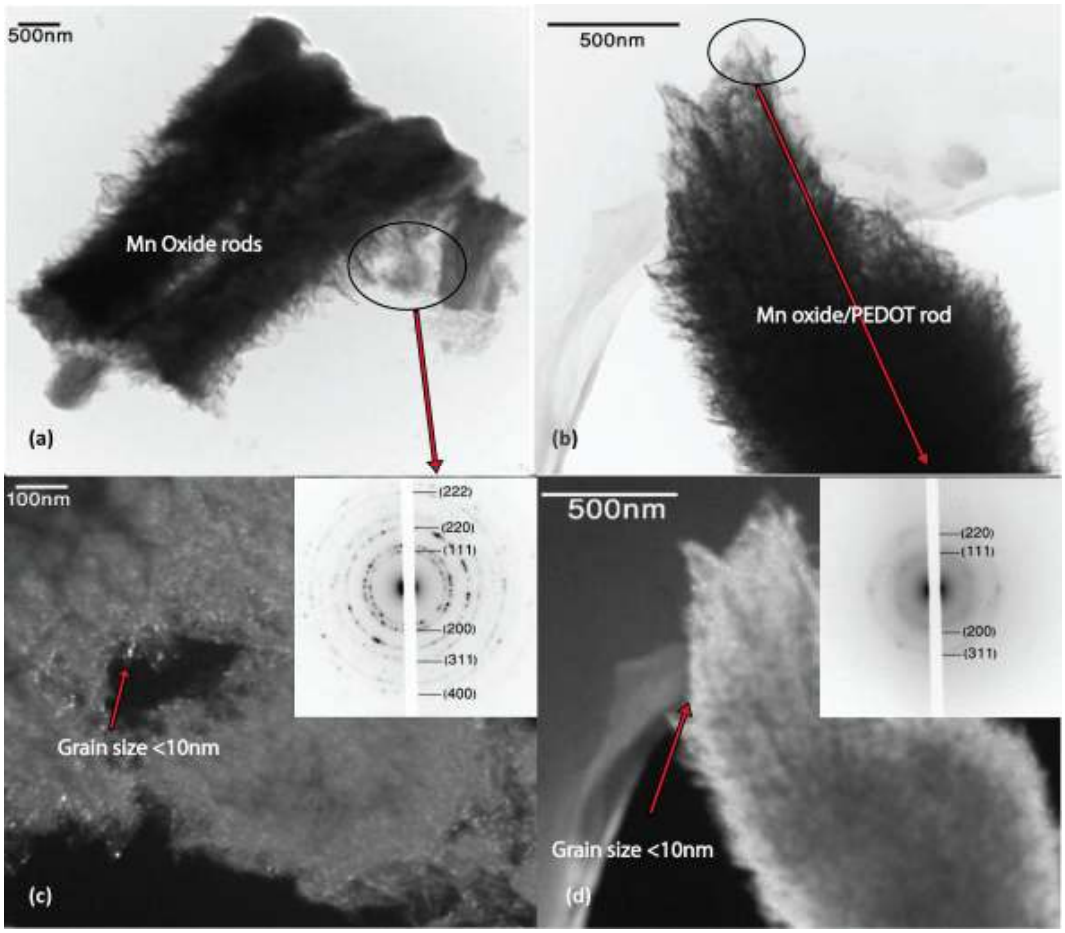

Figure 3-4 TEM BF images of (a) Mn oxide rods prepared from the 0.01 M $Mn(CH_3COO)_2$ solution at 5 $mAcm^{-2}$ and (b) Mn oxide/PEDOT coaxial core/shell rods, prepared from the 0.01 M $Mn(CH_3COO)_2$ solution at 5$mAcm^{-2}$ and subsequently coated with PEDOT at 1 V for 30 s. (c) and (d) TEM DF images and SAED patterns of regions indicated in (a) and (b), respectively.

Although the diffraction patterns indicate a antifluorite–type structure (Chapter 2, Section 2.3.1), the nanocrystals are in fact MnO_2 (Mn valence of 4+). This is confirmed in the XPS analysis presented in Section 3.3.4. A similar result was obtained for MnO_2 prepared from a $MnSO_4$ solution containing sodium citrate. The deposited MnO_2 had an antifluorite-type structure which was described as a FCC array of oxygen anions with Mn cations randomly occupying tetrahedral

interstices [45]. Only 25% of the octahedral sites are occupied by Mn, the other 75% being cation vacancies [46].

A FIB cross section sample was prepared in order to better image the PEDOT layer of the coaxial structure. A TEM BF image of two Mn oxide/PEDOT core/shell rods, from a sample deposited at 5 $mAcm^{-2}$ and subsequently coated with PEDOT at 1 V for 45 s, is shown in Figure 3-5a where a shell of PEDOT on the surface of the rods is clearly visible. In addition, PEDOT penetration into the porous Mn oxide is evident. An SAED pattern and a dark field (DF) image of the circled region shown in Figure 3-5a are shown in Figure 3-5b and reveal the polycrystalline grains with a diameter less that 10 nm for the Mn oxide core and the amorphous PEDOT shell (100–150 nm thick) on the surface. EDX analysis of the core did not show any S (Figure 3-5c) while EDX analysis from the surface of rods (Figure 3-5d) detected the presence of S, which confirms that the Mn oxide is coated with electro–polymerized PEDOT. The Cu peaks present in the EDX spectra are an artifact from the grid supporting the FIB sample.

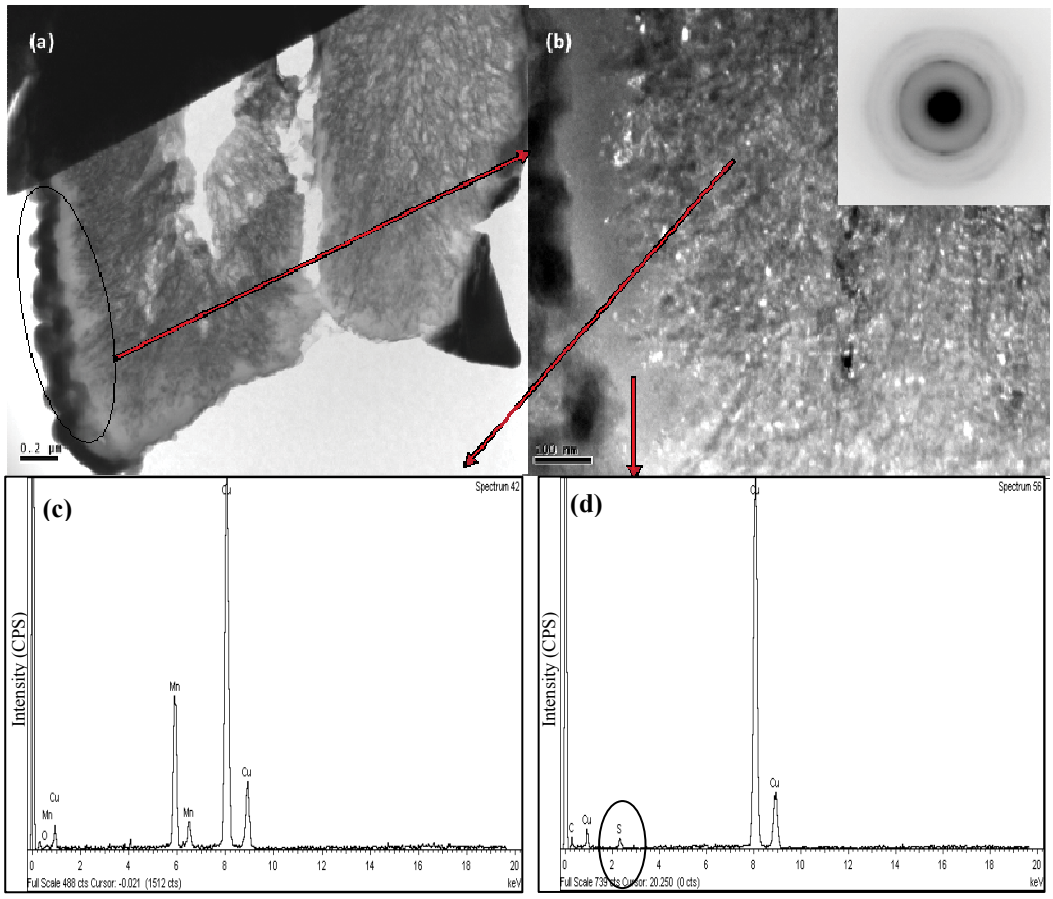

Figure 3-5 (a) TEM BF image of 2 PEDOT coated Mn oxide rods, prepared by FIB milling; (b) TEM–FIB DF image and SAED pattern of region indicated in (a); (c) and (d) EDX spectra from the regions indicated in (b). The sample was prepared sequentially from the 0.01 M $Mn(CH_3COO)_2$ solution at 5 $mAcm^{-2}$ and then coated with PEDOT at 1 V for 45 s. The dark contrast regions in (a) along the outside of the rods is Pt that has been deposited before the FIB process. The dark region at the top of (a) is where the FIB sample is attached to the Cu support grid.

The coaxial structure (core Mn oxide and PEDOT shell) can also be distinguished through Auger electron spectroscopy (AES). Figure 3-6 shows a Mn oxide rod with a PEDOT shell. This rod was scraped from a deposit and placed onto a carbon coated Cu grid (300 mesh). Three spectra are shown from the regions indicated. Regions 2 and 3 clearly show the presence of S and O (major

components of the polymer) but no Mn, indicating that the polymer has coated the Mn oxide rods and the coating is more than 10 nm thick, which corroborates the TEM results. Region 1 shows the presence of both S and Mn, although the S level is lower than in regions 2 and 3. Region 1 represents the base of the rod where the polymer coverage is not as good, likely due to polymer access issues during deposition. Note that all three Auger spectra have a significant C peak, which is likely surface contamination. The presence of the PEDOT shell on the Mn oxide rods should allow for fast ion/electron diffusion into the core Mn oxide of the coaxial electrodes due to its porous and conductive nature leading to fast charge/discharge rates. Also, the porous surface provides more sites that are susceptible to redox reactions, a greater active area and, consequently, higher capacitance and improved electrochemical behavior. Moreover, a shell of PEDOT protects the Mn oxide from dissolution during cycling and improves the mechanical stability, which also provides better electrochemical cyclability.

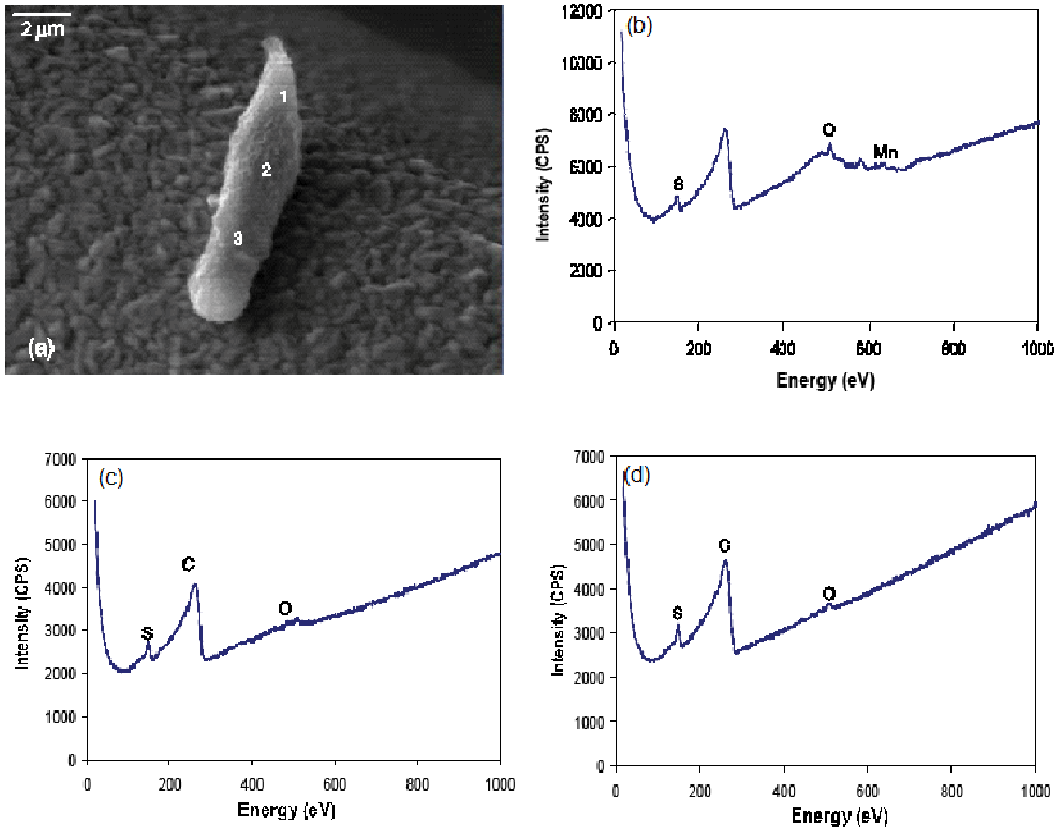

Figure 3-6 AES analysis for Mn oxide/PEDOT coaxial rods prepared from the 0.01 M $Mn(CH_3COO)_2$ solution at 5 $mAcm^{-2}$ and then coated with PEDOT at 1 V for 30 s. (a) SE image of a single rod; (b), (c), (d) Auger spectra for points 1, 2 and 3, respectively.

3.3.4. Chemical state analysis of Mn oxide and Mn oxide/PEDOT

XPS spectra for Mn oxide rods (Figure 3-7a and 3-7b) and Mn oxide/PEDOT coaxial core/shell rods (Figure 3-7c and 3-7d) deposited on Au coated Si substrates were studied. As discussed in Chapter 2, the Mn 3s spectrum is generally used to determine the valence of Mn cations using the 3s splitting widths, since there is an approximately linear relationship between the Mn oxidation state and the 3s splitting width (ΔE) [47], but Mn 3s overlaps with Au 4f peaks. The Mn 2p spectrum was examined instead (Figure 3-7a and 3-7c). The

Mn spectra for the two structures are similar. The Mn $2p_{3/2}$ and Mn $2p_{1/2}$ binding energy peaks have similar separations (11.47 – 11.7 eV) and can be attributed to Mn valences of 3+ and 4+. For comparison purposes, pure MnO_2 has the $2p_{3/2}$ and $2p_{1/2}$ peaks located at 641.9 eV and 653.5 eV (separation of 11.6 eV). The Mn 2p spectrum for the Mn oxide/PEDOT sample has a much lower intensity (Figure 3-7c) compared with that of the Mn oxide deposit (Figure 3-7a), which can be attributed to the PEDOT coating in the former case. The O 1s spectra for the two deposits are quite different. Deconvolution of the O 1s spectrum for the Mn oxide deposit (Figure 3-7b) indicates three bonding states for O, i.e., O–Mn–O (Mn4+), Mn–O–H (Mn3+) and water. Deconvolution of the O 1s XPS spectrum for the Mn oxide/PEDOT sample (Figure 3-7d) indicates just two different oxygen bonding configurations, i.e., O–Mn–O (Mn4+) at 529 eV and water or SO_4^{2-} bonded oxygen at 530.5 eV (both have the same shape [24]). The Mn–O–H bonding configuration is not visible in Figure 3-7d and the O–Mn–O configuration is much lower in intensity compared with the Mn oxide deposit. A large portion of the mean oxygen concentration in the Mn oxide/PEDOT O 1s spectrum is bonded as SO_4^{2-}. Coupled with the S concentration (~40.5%) determined from S 2p XPS peak (not shown), there is a high concentration of SO_4^{2-} ions at the surface which confirms that the Mn oxide is coated with electro–polymerized PEDOT and is in agreement with the AES results and the TEM–FIB results.

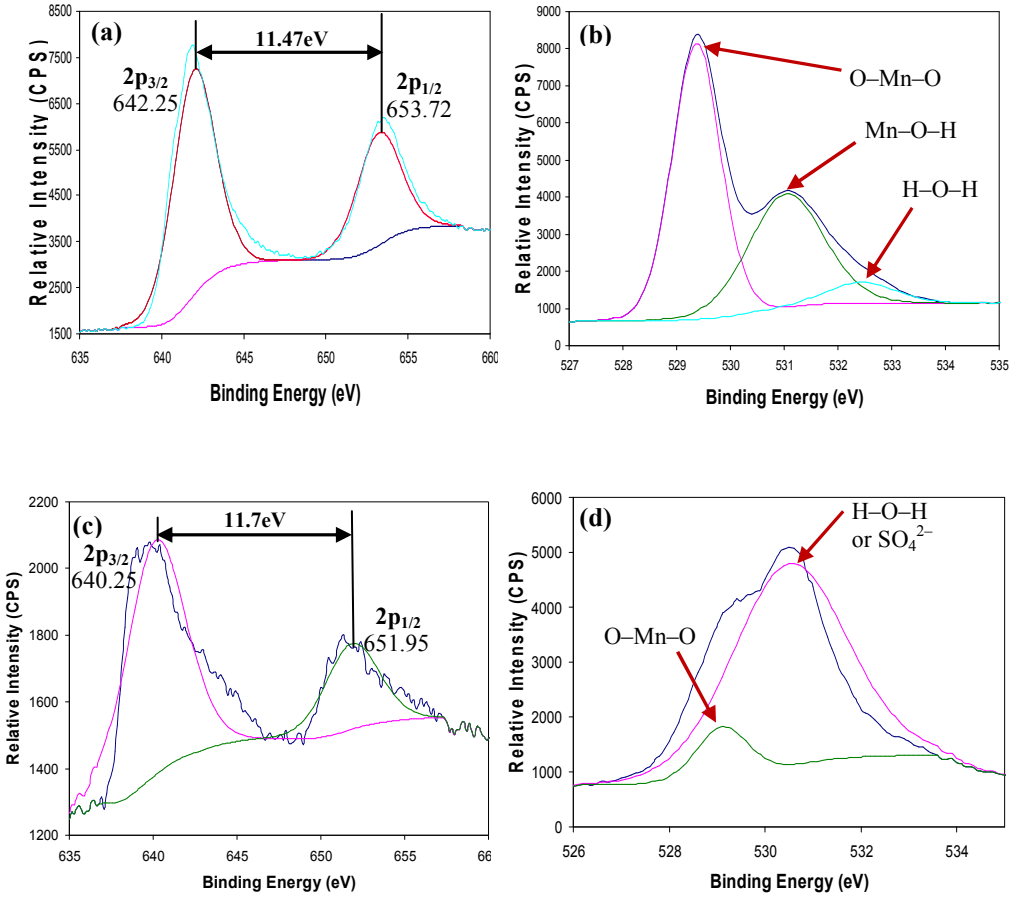

Figure 3-7 Typical (a) XPS Mn 2p spectrum and (b) XPS O 1s spectrum for Mn oxide rods deposited from a 0.01 M $Mn(CH_3COO)_2$ solution at 5 $mAcm^{-2}$. (c) and (d) Mn and O spectra for Mn oxide/PEDOT coaxial rods deposited from a 0.01 M $Mn(CH_3COO)_2$ solution at 5 $mAcm^{-2}$ and then coated with PEDOT at 1 V for 30 s.

3.3.5. Morphology and crystal structure of cycled electrodes

The morphological and structural evolution of Mn oxide and Mn oxide/PEDOT core/shell coaxial rods during cycling were examined using SEM and TEM. The plan view images shown in Figure 3-8a–f compare the morphology of Mn oxide and Mn oxide/PEDOT deposits cycled in 0.5 M Na_2SO_4 at 20 mVs^{-1} for 250

cycles. In Chapter 2, Section 2.3.3, it was shown that the Mn oxide with a rod–like structure evolved into a petal–like morphology (Figure 3-8a–c) caused by the partial dissolution of Mn oxide into the electrolyte as Mn^{2+} cations during cycling followed by re–oxidation to Mn oxide and re–deposition on the electrode surface. The petal–like morphology reduces the specific surface area of the Mn oxide electrodes leading to a decrease in capacitance for the cycled electrodes. However, a porous morphology is still observed for Mn oxide/PEDOT deposits after cycling (Figure 3-8d–f). The microstructure has not changed much relative to the as–deposited ones (Figure 3-1a–c) due to the presence of PEDOT. The PEDOT shell in the Mn oxide/PEDOT deposits inhibits the dissolution of Mn oxide in the 0.5 M Na_2SO_4 electrolyte during cycling. The morphology of Mn oxide/PEDOT after cycling provides almost the same surface area as the as–deposited one. Therefore, Mn oxide/PEDOT coaxial rods are able to maintain much of their capacitance after cycling with higher capacitance retention compared with the Mn oxide rods.

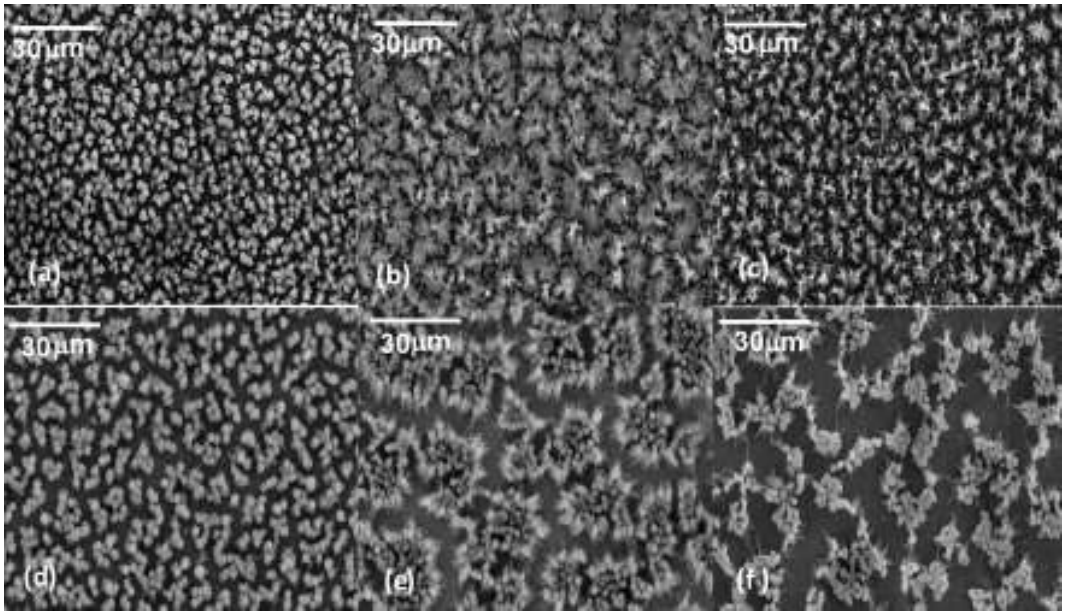

Figure 3-8 SEM SE plan view images of Mn oxide rods at (a) 5 $mAcm^{-2}$; (b) 15 $mAcm^{-2}$; (c) 20 $mAcm^{-2}$ (after 250 cycles at 20 mVs^{-1}) and Mn oxide/PEDOT coaxial core/shell rods deposited at (d) 5 $mAcm^{-2}$; (e) 15 $mAcm^{-2}$; (f) 20 $mAcm^{-2}$ coated with PEDOT at 1V for 45s (after 250 cycles at 20 mVs^{-1}).

Figure 3-9 shows representative cross–sectional SE images of Mn oxide and Mn oxide/PEDOT coaxial rods after 250 cycles in the 0.5 M Na_2SO_4 solution at 20 mVs^{-1}. It is clear that the Mn oxide/PEDOT deposit has maintained its morphology after cycling. Distinct rods are still visible, while the morphology of the Mn oxide deposits has changed due to partial dissolution.

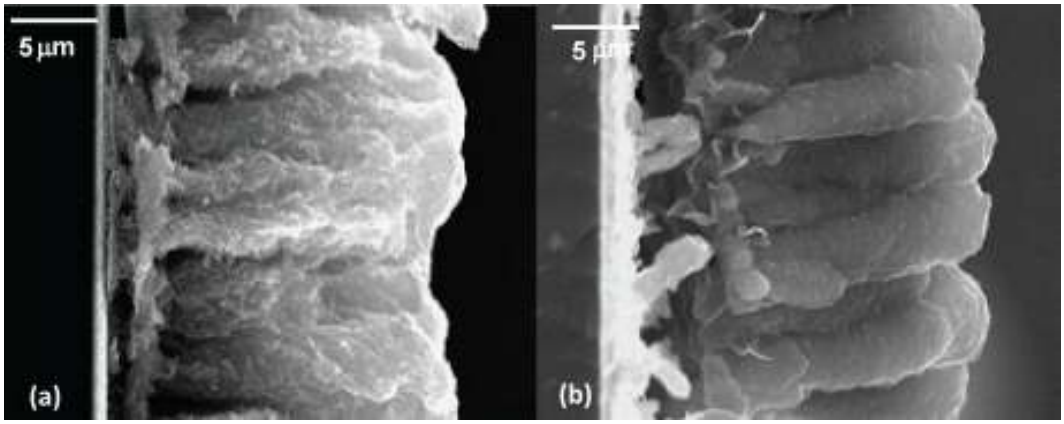

Figure 3-9 SEM SE cross section images of (a) Mn oxide rods at 5 $mAcm^{-2}$ after 250 cycles at 20 mVs^{-1}; (b) Mn oxide/PEDOT coaxial core/shell rods deposited at 5 $mAcm^{-2}$ and then coated with PEDOT at 1V for 45 s.

TEM micrographs and corresponding SAED patterns were taken from the Mn oxide and Mn oxide/PEDOT coaxial core/shell rods after 250 cycles in 0.5M Na_2SO_4 at 20 mVs^{-1}. As mentioned in Chapter 2, Section 2.3.1 and 2.3.4, the diffraction rings of cycled Mn oxide samples were indexed to MnO_2 with an ε-NiAs-type crystal structure (HCP with space group corresponding to $P6_3/mmm$), while the as–deposited Mn oxide sample showed an antifluorite–type structure [8]. The crystal structure of Mn oxide had changed to a more close packed structure after cycling with fewer electrochemically active sites leading to some capacitance fading with increasing cycle number.

Figure 3-10a shows parts of two Mn oxide/PEDOT rods with their fibrous structure. The SAED pattern for Mn oxide/PEDOT rods (Figure 3-10b) can be indexed to the antifluorite-type crystal structure, which is the same structure determined for the as–deposited Mn oxide/PEDOT samples (Figure 3-4d). The presence of the PEDOT shell on the Mn oxide core prevents major crystallographic changes. The d–spacing sequence for the first four diffraction rings of the cycled Mn oxide/PEDOT sample is ~0.256, 0.213, 0.152 and 0.134 nm, whereas the corresponding d–spacings from the as–prepared Mn

oxide/PEDOT sample were ~0.276, 0.228, 0.167 and 0.142 nm. The unit cell of the Mn oxide/PEDOT deposit has decreased during cycling indicating a more dense structure.

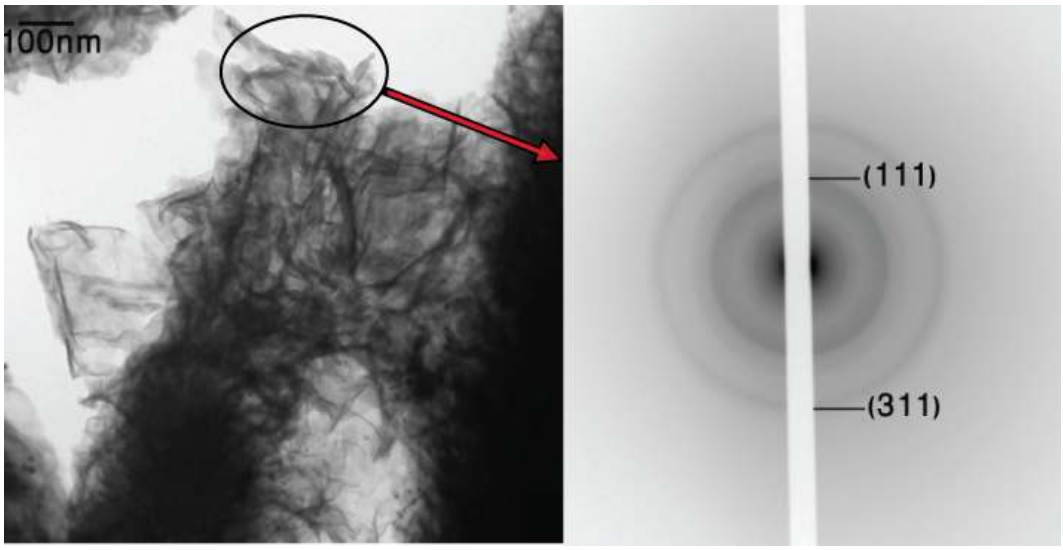

Figure 3-10 (a) TEM BF image and (b) SAED pattern for Mn oxide/PEDOT core/shell rods prepared from the 0.01 M $Mn(CH_3COO)_2$ solution at 5 $mAcm^{-2}$ and subsequently coated with electro–polymerized PEDOT at 1 V for 30 s after 250 cycles at 20 mVs^{-1}.

3.4 Conclusions

Electrochemical properties (specific capacitance and cyclability) of Mn oxide/PEDOT electrodes for application in electrochemical capacitors were investigated. Sequential and one–step methods were used to produce Mn oxide/PEDOT coaxial core/shell rods and agglomerated Mn oxide/PEDOT particles, respectively. The Mn oxide rods in the former case were coated by a shell of PEDOT, which improved the specific capacitance and electrochemical cyclability of the deposits. Manganese oxide rods synthesized at a current density of 5 $mAcm^{-2}$ and then coated with PEDOT at 1 V for 45 s showed the highest specific capacitance (~285 Fg^{-1}). The specific capacitance retention (after 250

cycles) for this coating was determined to be ~92% of the original value, while the best capacitance for co–electrodeposited (one-step) Mn oxide/PEDOT was ~195 Fg^{-1} with a retention ~87% of the original value. After cycling, the Mn oxide/PEDOT coaxial core/shell rods maintained the same crystal structure as the as–deposited structure, i.e., MnO_2 with an antifluorite–type structure coated with amorphous PEDOT.

References

[1] B.E. Conway, Electrochemical Supercapacitors, Kluwer Academic/ Plenum Press, New York (1999).

[2] S. Sarangapani, B.V. Tilak and C.P. Chen, *J. Electrochem. Soc.*, **143**, 3791, (1996).

[3] C.C. Hu, K.H. Chang, M.C. Lin and Y.T. Wu, *Nano Lett.*, **6**, 2690 (2006).

[4] S.E. Chun, S.I. Pyun and G. J. Lee, *Electrochimica Acta*, **51**, 6479 (2006).

[5] T. Brousse, M. Toupin, R. Dugas and L. Athouel, *J. Electrochem. Soc.*, **153**, 2171 (2006).

[6] Y.C. Hsieh, K.T. Lee, Y.P. Lin, N.L. Wu and S.W. Donne, *J. Power Sources*, **177**, 660 (2008).

[7] C.L. Xu, S.J. Bao and L.B. Kong, *J. Solid State Chem.*, **179**, 1351 (2006).

[8] B. Babakhani and D.G. Ivey, *J. Power Sources*, **195**, 2110 (2010).

[9] M. Lai and D.J. Riley, *J. Colloid Interface Sci.*, **323**, 203 (2008).

[10] W.C.West, N.V. Myung and J.F. Whitacre, *J. Power Sources*, **126**, 203 (2004).

[11] G.Y. Zhao, C.L. Xu and H.L. Li, *J. Power Sources*, **163**, 1132 (2007).

[12] N. Li, C.R. Martin and B. Scrosati, *Electrochem. Solid State Lett.*, **3**, 316 (2000).

[13] N. Li, C.R. Martin and B. Scrosati, *J. Power Sources*, **97-98**, 240 (2001).

[14] K. Takahashi, S.J. Limmer and Y. Wang, *J. Phys. Chem. B*, **108**, 9795 (2004).

[15] C.J. Patrissi and C.R. Martin, *J. Electrochem. Soc.*, **146**, 3176 (1999).

[16] J. Bao, Z. Xu, J. Hong and X. Ma, *Scripta Materialia*, **50**, 19 (2004).

[17] C. Terrier, M. Abid and C. Arm, *J. Appl. Phys.*, **98**, 086102 (2005).

[18] J.L. Duvail, P. Retho and S. Garreau, *Synth. Met.*, **131**, 123 (2002).

[19] M. Delvaux, J. Duchet and P.Y. Stavaux, *Synth. Met.*, **113**, 275, (2000).

[20] R. Liu and S.B. Lee, *J. Am. Chem. Soc.*, **130**, 2942 (2008).

[21] C. Peng, J. Jin and G. Chen, *Electrochimica Acta*, **53**, 525 (2007).

[22] F. Cheng, Z. Thao, J. Liang and J. Chen, *J. Chem. Mater.*, **2**, 667 (2008).

[23] B. Babakhani and D.G. Ivey, *ECS Transactions*, **25(35)**, 173 (2010).

[24] R.K. Sharma, A.C. Rastogi and S.B. Desu, *Electrochimica Acta*, **53**, 7690 (2008).

[25] S. Komaba, A.Ogata and T.Tsuchikawa, *Electrochem. Commu.*, **10**, 1435 (2008).

[26] H. Randriamahazaka, V. Noel and C. Chevrot, *J. Electroanal. Chem.*, **472**, 103 (1999).

[27] V. Barsukov and S. Chivikov, *Electrochimica Acta*, **41**, 1773 (1996).

[28] R.M. Penner, L. S. Van Dyke and C.R. Martin, *J. Phys. Chem.*, **92**, 5274 (1988).

[29] C. Peng, S. Zhang and D. Jewell, *Prog. Nat. Sci.*, **18**, 777 (2008).

[30] S. Cho and S. Lee, *Acc. Chem. Res.*, **41**, 699 (2008).

[31] A.S. Arico, P. Bruce and B. Scrosati, *Nat. Mater. J.*, **4**, 366 (2005).

[32] J.S. Moreno, S. Pareno and B. Scrosati, *Electrochimica Acta*, **53**, 2154 (2008).

[33] S. Demoustier, E. Ferain and C. Jerome, *Eur. poly. J.*, **34**, 1767 (1998).

[34] T. Johansson, L.A. Pettersson and O. Inganas, *Synth. Met.*, **129**, 269 (2002).

[35] B. E. Conway, V. Birss and J Wojtowicz, *J. Power Sources*, **66**, 1 (1997).

[36] S.J. Bao, B.L. He and Y.Y. Liang, *Mat. Sci. Eng. A*, **397**, 305 (2005).

[37] Y.K. Zhou, B.L. He and F.B. Zhang, *J. Solid State Electrochem.*, **8**, 482 (2004).

[38] R. Jiang, T. Huang, Y. Tang and J. Liu, *Electrochimica Acta*, **54**, 7173 (2009).

[39] S.C. Pang, M.A. Anderson and T.W. Chapman, *J. Electrochem. Soc.*, **147**, 444 (2000).

[40] R.K. Sharma, A.C. Rastogi and S.B. Desu, *Electrochem. Commun.*, **10**, 268 (2008).

[41] L.J. Sun, X.X. Liu, K.K.T. Lau and L. Chen, *Electrochimica Acta*, **53**, 3036 (2008).

[42] M. Nakamaya and H. Tagashira, *Langmuir*, **22**, 3864 (2006).

[43] P. Soudan, J. Gaudet, D. Guay, D. Belanger and D. Schulz, *Chem. Mater.*, **14**, 1210 (2002).

[44] A. Bund and R. Peipmann, *Electrochimica Acta*, **53**, 3772 (2008).

[45] W. Wei, X. Cui, W. Chen and D.G. Ivey, *J. Power Sources*, **186**, 543 (2009).

[46] W. Wei, W. Chen and D.G. Ivey, *J. Phys. Chem. C*, **111**, 10398 (2007).

[47] M. Nakayama, A. Tanaka and Y. Sato, *Langmuir*, **21**, 5907 (2005).

Chapter 4 Investigation of electrochemical behavior of Mn-Co doped oxide electrodes for electrochemical capacitors[3]

4.1 Introduction

Electrochemical capacitors are currently receiving considerable attention because of their high power density coupled with good energy density, excellent reversibility and long cycle life [1]. Amorphous hydrous ruthenium oxide (RuO_2) exhibits ideal pseudocapacitive behaviour and has a very large specific capacitance (over 700 Fg^{-1}) with excellent reversibility; however, the high cost of Ru has limited its commercial use. Therefore, there is an ongoing search for cheaper oxide alternatives with similar characteristics [2,3].

For several years Mn oxides and derivative compounds have attracted interest, because of their structural flexibility combined with novel chemical and physical properties, which are of interest for applications such as Li/MnO_2 batteries and electrochemical capacitors [4-7]. Transition metal oxide based materials, such as MnO_2 [4-11], Co_2O_3 [12,13], MoO [14] and V_2O_5 [15], and conducting polymers, such as polyethylenedioxythiophene (PEDOT) [16,17], polyaniline (PANI) [18,19] and polypyrrole (PPY) [20], have several oxidation states or structures that lead to redox transitions within the potential region of water decomposition. Therefore, charge can be stored within the reversible redox transitions of these electroactive materials making them appropriate materials for charge storage devices. It has been reported that up to 86% of the electrochemical activity of PEDOT can be maintained after polarization for 1200 cycles in aqueous solutions due to the good stability of the thin PEDOT film on the electrode surface [21].

As shown in Chapter 2 and 3, Mn oxide electrodes with ordered, high surface area structures can enhance the specific capacitance, but the electrochemical stability of Mn oxide is still not satisfactory [22,23]. Komaba *et al.* [24] have shown that

[3] *A version of this chapter has been published. Banafsheh Babakhani, Douglas G. Ivey. Electrochimica Acta,* ***56*** *(2011) 4753–4762.*

the cyclic stability of amorphous MnO_2 (α-MnO_2) can be improved using certain anions such as phosphate (HPO_4^{2-}) and carbonate (HCO_3^-) [25]. In addition, Hu *et al.* [26] have reported that the cyclic stability of α-MnO_2 is enhanced by adding Mn_3O_4, due to the simultaneous dissolution/transformation of Mn_3O_4 nanocrystals and α-MnO_2 nanorods into an amorphous Mn oxide with sheet-like morphology after high cycle testing [26]. Combining Mn oxide with conducting polymers, such as PEDOT (see Chapter 3), is another approach to reducing both MnO_2 dissolution and mechanical failure during charge-discharge cycling and to provide appropriate electrochemical and mechanical properties for electrochemical energy storage [2,27-30]. To further improve electrochemical capacitors, much effort has focused on the development of bimetal composite materials. For example, the pseudocapacitive performance of Mn oxide electrodes has been improved by addition of other transition metal oxides such as Mo [14], V [31], Fe [32] and Ni [33] oxides. Cobalt oxide additions, on the other hand, have displayed mixed results. Prasad and Miura [33] reported that the addition of Co oxide can improve the specific capacitance of Mn oxide electrodes prepared using potentiodynamic methods from 482 Fg^{-1} to 498 Fg^{-1} when scanned at a rate of 10 mVs^{-1} [33,34]. Zheng *et al.* [35] also reported a high capacitance value (507 Fg^{-1}) and long cycling durability (less than 2% capacity loss after 5000 charge/discharge cycles) for multilayered films of cobalt oxyhydroxide nanowires and exfoliated Mn oxide nanosheets fabricated by potentiostatic deposition [35]. However, Chuang and Hu [36] reported that the specific capacitance of Co-doped Mn oxide remained unchanged relative to the Mn oxide electrode. Cobalt and its oxides are considered to be rather noble; therefore, Co doping may be able to enhance the redox reversibility of Mn oxide electrodes.

As discussed in Chapter 3, Mn oxide and Mn oxide/PEDOT deposits with a rod-like structure, can be prepared without a template through anodic deposition from a 0.01 M Mn acetate solution at various deposition current densities. The best capacitance value for Mn oxide rods (deposited at 5 $mAcm^{-2}$) was ~185 Fg^{-1} with 89 and 75% retention of the original value after 100 and 250 cycles, respectively,

in 0.5 M Na_2SO_4 at 20 mVs^{-1} [22]. In order to increase the specific capacitance values and improve the electrochemical cyclability, Mn oxide/PEDOT coaxial rods were synthesized. Mn oxide/PEDOT coaxial rods, prepared with electrochemically polymerized PEDOT under potentiostatc control at 1V for 45 s, had a high specific capacitance (~285 Fg^{-1}) with a capacitance retention of ~93 and 92% after 100 and 250 cycles, respectively [29,30].

The aim of the present chapter is to investigate the effect of Co oxide additions on the morphology, chemistry, crystal structure and electrochemical properties of Co-doped Mn oxide electrodes. In addition, the structure and electrochemical behavior of PEDOT coated Co-doped Mn oxides are investigated.

4.2 Experimental procedure

Mn-Co oxide deposits were anodically deposited from a dilute solution containing 0.01 M Mn acetate ($Mn(CH_3COO)_2$), based on Chapters 2 and 3 [22], and Co sulphate ($CoSO_4$) at concentrations of 0.001 M, 0.005 M and 0.01 M. Mn-Co oxide was deposited on Au (500 nm thick) coated Si substrates under galvanostatic control, with current densities in the 5-30 $mAcm^{-2}$ range and deposition duration of 300 s. The deposition procedure for Mn-Co oxide was similar to that for Mn oxide described in Chapter 2. In order to produce coaxial Mn-Co oxide/PEDOT rods, the Mn-Co oxide deposits were subsequently coated with PEDOT, as described in Chapter 3. Electropolymerization was done under potentiostatic control at 1 V for 45 s at room temperature [29,30]. As explained in Chapter 2 and 3 [29,30], a three electrode cell configuration was used, consisting of a Pt mesh counter electrode placed vertically 20 mm away from and parallel to the vertical working electrode (Au coated Si). A saturated calomel electrode (SCE) was used as the reference electrode and all potentials quoted are with respect to it.

Morphological and structural analysis of the Mn-Co oxide and Mn-Co oxide/PEDOT deposits were investigated using SEM and TEM, based on the conditions described in Chapter 2. Chemical state analysis was carried out by XPS, with the conditions also given in Chapter 2.

A Gamry PC4/750 potentiostat/galvanostat was used for cyclic voltammetry (CV) in an electrolyte of 0.5 M Na_2SO_4. Cyclic voltammograms were recorded between −0.1 and 0.9 V vs. SCE for all deposits at different scan rates, i.e., 5-1000 mVs^{-1}, at room temperature. The specific capacitance C (Fg^{-1}) of the active material was determined using equation (4-1), which was also presented in Chapter 2.

$$C = Q/m\Delta E \quad (4\text{-}1)$$

Electrochemical impedance spectroscopy (EIS) measurements were conducted on Mn-Co oxide electrodes in constant voltage mode (0.2 V vs. SCE) by sweeping frequencies from 100 kHz to 10 mHz at an amplitude of 5 mV.

The Mn content in the 0.5 M Na_2SO_4 electrolyte after cycling for both Mn-Co oxide and Mn-Co oxide/PEDOT deposits was determined using a VARIAN 220 FS atomic absorption spectrophotometer (AAS).

4.3 Results and discussion

4.3.1 Morphology and crystal structure of Mn-Co oxide and Mn-Co oxide/PEDOT deposits

The morphology and crystal structure of as-prepared Mn-Co oxide and Mn-Co/PEDOT rods were analyzed using SEM and TEM.

The best Mn-Co deposits, both in terms of obtaining a rod-like structure and mechanical integrity, were fabricated at a current density of 15 $mAcm^{-2}$ and from solutions with 0.01 M $Mn(CH_3COO)_2$ and 0.001 M $CoSO_4$. As discussed in

Chapters 2 and 3 [22,29], the structure of the rods, e.g., Mn-Co oxide rod size (e.g., ~7 μm length and ~3.5 μm diameter for samples prepared at 15 $mAcm^{-2}$) and PEDOT shell thickness (less than 100 nm), can be controlled by varying the Mn oxide deposition current density and time and the subsequent polymer applied potential and deposition time. Rod-like morphologies were obtained at current densities ≤15 $mAcm^{-2}$; however, delamination of deposits occurred at ≤10 $mAcm^{-2}$ (Figure 4-1a and 4-1d). Rod-like structures were not obtained at current densities ≥20 $mAcm^{-2}$ (Figure 4-1c and 4-1f). Adherent and rod-like structures were obtained only for current densities between 10 and 20 $mAcm^{-2}$ (Figure 4-1b and 4-1e), which also corresponded to the best capacitance values as discussed later.

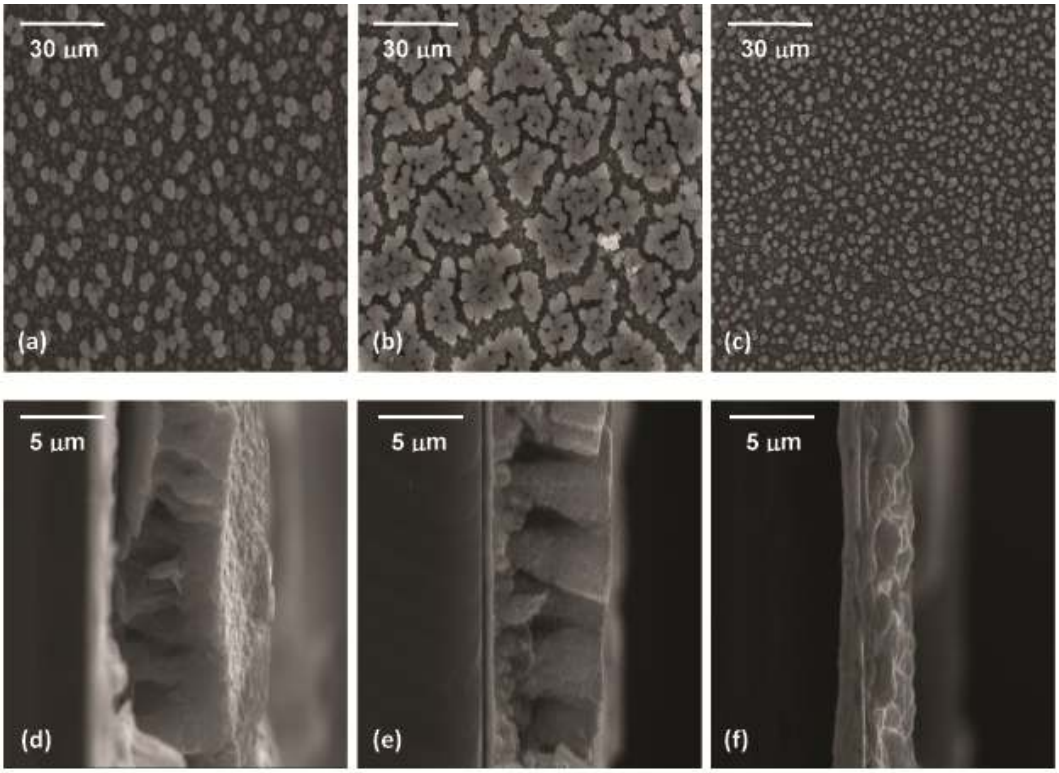

Figure 4-1 SEM SE plan view and cross–sectional images of Mn-Co oxide deposits prepared from a 0.01 M $Mn(CH_3COO)_2$ and 0.001 M $CoSO_4$ solution at (a) and (d) 10 $mAcm^{-2}$; (b) and (e) 15 $mAcm^{-2}$; (c) and (f) 20 $mAcm^{-2}$ for 300 s.

Mn-Co oxide deposited from solutions with higher concentrations of Co, i.e., 0.005 M and 0.01 M, were also prepared but adhesion to the substrate was poor, so that morphological analysis and electrochemical measurements could not be done. Chang *et al.* [37] have reported that a large amount of added Co (≥0.05 M) should be avoided, since Co can cause a reduction in the specific capacitance of the oxide, as Co oxide is less electroactive compared with the Mn oxide in terms of pseudocapacitance [37].

Plan view and cross sectional secondary electron (SE) images (Figure 4-2) reveal the free-standing Mn-Co/PEDOT coaxial core/shell rods prepared using the sequential template-free method. PEDOT was deposited onto the Mn-Co oxide sample shown in Figure 4-1a and 4-2b. The morphology is similar to that obtained for Mn oxide/PEDOT in Chapter 3 [29] without the presence of Co. In addition, there is essentially no change to the morphology when compared to the Mn-Co oxide deposit in Figure 4-1b and 4-1e. This is an indication that PEDOT is deposited around the Mn-Co oxide rods and not between the rods.

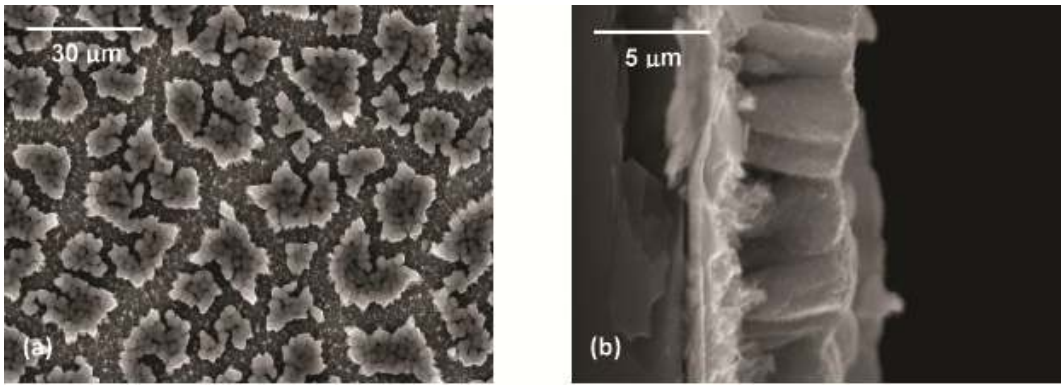

Figure 4-2 (a) SEM SE plan view and (b) cross–sectional images of Mn-Co oxide/PEDOT coaxial rods prepared sequentially from a 0.01 M $Mn(CH_3COO)_2$ and 0.001 M $CoSO_4$ solution (at 15 $mAcm^{-2}$ for 300 s) followed by PEDOT deposition at 1V for 45 s.

The crystal structure of the Mn-Co oxide rods and Mn-Co oxide/PEDOT coaxial rods was analyzed using electron diffraction in the TEM. TEM bright field (BF) images (Figure 4-3a and 4-3d) reveal the fibrous surfaces for both Mn-Co oxide and Mn-Co oxide/PEDOT coaxial rods. Figure 4-3b and 4-3e show dark field (DF) images of Mn-Co oxide and Mn-Co oxide/PEDOT rods, which consist of polycrystalline grains with a diameter less than 10 nm. Corresponding SAED patterns taken from these two deposits are shown in Figure 4-3c and 4-3f and the continuous ring patterns confirm their nanocrystalline nature. The DF images were taken from part of the first two diffracted rings for both deposits.

As described in Chapter 1, Section 1.3.1.3, the most common Mn-Co oxide is $Mn_xCo_{3-x}O_4$ ($0 < x < 3$), with different crystal structures including cubic spinel-type, tetragonal and a mixture of cubic and tetragonal spinel-type, depending on the compositional range of x. However, the *d*-spacings measured from the SAED pattern for the Mn-Co oxide (Figure 4-3c) are consistent with a face-centered cubic (FCC) crystal structure with a lattice parameter of 0.461 nm. The same crystal structure was obtained for all deposits regardless of the current densities. A less distinct SAED pattern was obtained for the Mn-Co oxide/PEDOT deposits (Figure 4-3f), due to the amorphous PEDOT coating. The *d*-spacings measured for the PEDOT coated deposit were similar to those for the uncoated Mn-Co oxide. The first four diffracted rings can be indexed as (111), (200), (220) and (311), respectively, in increasing distance away from the central spot. The intensity profiles for the diffraction rings in Figure 4-3c and 4-3f show that the peak intensities decrease in the following order: (111) > (200) > (220) > (311). This intensity distribution is similar to that obtained for Mn oxide in Chapter 2, Section 2.3.1, and it is most likely related to an antifluorite-type crystal structure. The antifluorite structure has O^{2-} ions occupying FCC positions, with Mn cations (and Co cations for Mn-Co oxide) randomly occupying some of the tetrahedral interstices [38]. EDX microanalysis (Figure 4-3g - taken from point 1 in Figure 4-3a) indicates that the deposits have the same Mn:Co composition ratio (10:1) as the Mn-Co electrolyte and no separate Co oxide phases have formed. Although,

both Mn oxide and Mn-Co oxide deposits have an antifluorite-type crystal structure, there are some differences in terms of lattice parameters and cell volumes. These differences can be attributed to ion size differences for Co and Mn. For instance, both Co^{2+} and Co^{3+} ions are larger (although Co^{3+} is only marginally larger) than the Mn^{4+} ion (R_{Co2+} = 0.065 nm, R_{Co3+} = 0.0545 nm and R_{Mn4+} = 0.053 nm). In addition, when Co ions substitute for Mn ions in the lattice structure, extra Co ions will be needed for charge compensation and will likely go into interstitial positions. Therefore, if Co^{2+} and/or Co^{3+} replace Mn^{4+} in the lattice, a slight increase in cell lattice parameter and cell volume can be expected. For the Mn-Co oxides in this work, there was an increase in the MnO_2 lattice parameter by about 3.4% compared with that for Mn oxide with the addition of Co, which correlates to ~11% reduction in density. XPS analysis, as discussed in Section 4.3.2, shows that the Co in Mn-Co oxide deposits is present in relative amounts corresponding to ~73% Co^{2+} and ~27% Co^{3+}. The theoretical densities for MnO_2 and Mn-Co oxide, assuming 9.1 at% Co (with 73% Co^{2+} and 27% Co^{3+} making up the Co content) are 3.32 and 2.94 gcm^{-3}, respectively. This corresponds to ~11% reduction in density for Mn-Co oxide relative to Mn oxide, which agrees quite well with the measured change in lattice parameter. The chemical formulation of Mn-Co oxide is $(Mn_{0.91}Co_{0.09})O_2$ for this work or more generally $(Mn_{1-x}Co_x)O_2$.

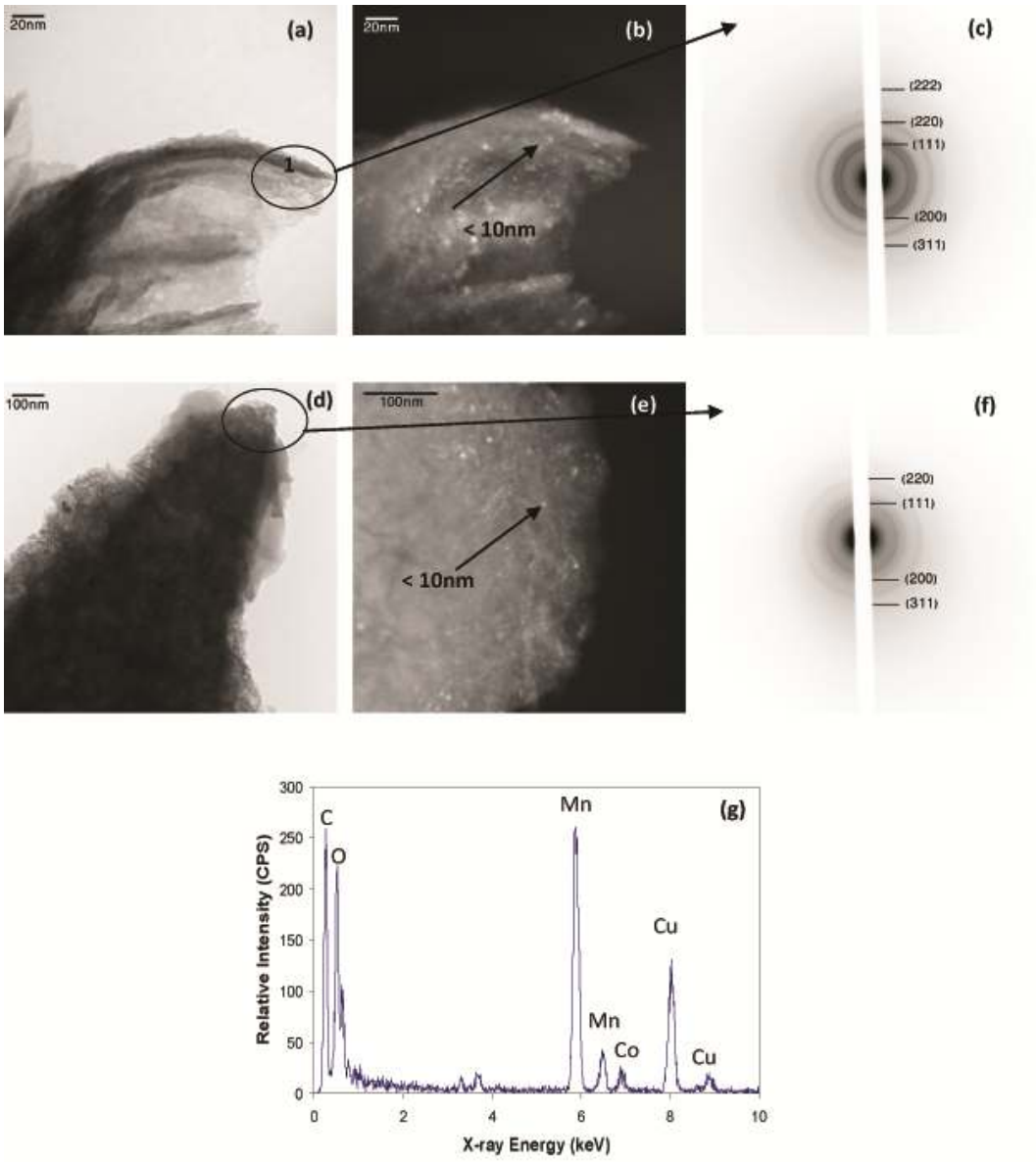

Figure 4-3 (a) TEM BF image; (b) TEM DF image; (c) SAED pattern of circled region for Mn-Co oxide deposit prepared from 0.01 M $Mn(CH_3COO)_2$ and 0.001 M $CoSO_4$ solution (at 15 $mAcm^{-2}$ for 300 s). (d) TEM BF image; (e) TEM DF image; (f) SAED pattern of circled region for Mn-Co oxide/PEDOT coaxial rod prepared sequentially from a 0.01 M $Mn(CH_3COO)_2$ and 0.001 M $CoSO_4$ solution (at 15 $mAcm^{-2}$ for 300 s) followed by PEDOT deposition at 1V for 45 s; (g) EDX spectrum for Mn-Co oxide taken from point 1 in (a).

4.3.2 Chemical states for Mn-Co oxide deposits

A detailed chemical state analysis for the Mn-Co oxide deposits prepared at 15 $mAcm^{-2}$ for 300 s was conducted, using XPS (Figure 4-4). The Mn 3s and Co 2p XPS spectra were used to determine the oxidation states of Mn and Co, respectively. As described in Chapter 2, Section 2.3.2, the Mn 3s spectrum is generally used to approximate the valence of Mn cations using the 3s splitting widths, since there is an approximately linear relationship between the Mn oxidation state and the 3s splitting width (ΔE) [14]. To prevent the overlap between the Au 4f peaks from the Au seed layer and the Mn 3s peaks (see Chapter 2, Section 2.3.2), Mn-Co oxide was deposited on Pt coated Si substrates for XPS analysis. The experimental splitting width (ΔE) in the Mn 3s spectrum for Mn-Co oxide is 4.4 eV, which corresponds to an oxidation valence of +4 (i.e., MnO_2) based on the approximately linear relationship between the splitting width (ΔE) and the Mn oxidation state.

The possible variations in oxidation states for Co can be determined from the Co 2p peaks in the XPS spectra. The Co 2p spectrum consists of two main spin–orbital lines, i.e., $2p_{3/2}$ and $2p_{1/2}$, at ~780 and 795 eV, respectively, separated by about 15.0 eV (Figure 4-4b). Also, two satellite peaks are detected with binding energy about 6.3 eV (S1) above the $2p_{3/2}$ main peak and 9.5 eV (S2) above the $2p_{1/2}$ main peak. The energy gap between the Co 2p main peak and the satellite peaks is generally considered to be highly related to the oxidation states. When the energy gap is ~6.0 eV, the Co cation valence is assigned a value of 2+. If the energy gap is 9-10 eV, the spectrum is associated with Co cations having a valence of 3+ [39-41]. Therefore, both Co^{2+} and Co^{3+} cations exist in the Mn-Co oxide deposits. The amount of Co^{2+} cations is higher than the amount of Co^{3+} cations in the codeposited Mn-Co oxide, as the electrooxidation of Co^{2+} to a higher oxidation state can be constrained by the presence of Mn ions [38]. For the

deposit in Figure 4-4b, the amounts of Co^{2+} and Co^{3+} were determined to be ~73% and ~27%, respectively.

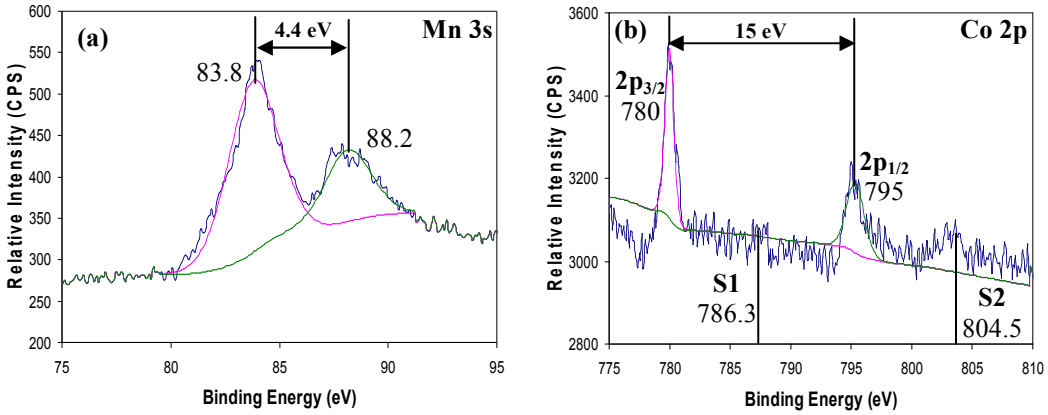

Figure 4-4 Typical (a) XPS Mn 3s spectrum and (b) Co 2p spectrum for Mn-Co oxide rods prepared from 0.01 M $Mn(CH_3COO)_2$ and 0.001 M $CoSO_4$ solution (15 $mAcm^{-2}$ for 300 s).

4.3.3. Electrochemical behavior of Mn-Co oxide and Mn-Co oxide /PEDOT deposits

The electrochemical properties of Mn-Co oxide deposits, prepared at 15 $mAcm^{-2}$ and 20 $mAcm^{-2}$ for 300 s and Mn-Co oxide/PEDOT prepared at 15 $mAcm^{-2}$ for 300 s (Mn-Co oxide) followed by PEDOT deposition at 1 V for 45 s, were evaluated by cyclic voltammetric analysis in a 0.5 M Na_2SO_4 solution. Data for uncoated and coated Mn oxide deposits, without Co additions, are also shown for comparison. Several scan rates were tested for the voltammetry work, i.e., 5, 20, 100, 500 and 1000 mVs^{-1}. The original specific capacitances were taken after the second cycle. The highest specific capacitance values were obtained at 100 mVs^{-1} for uncoated Mn-Co oxide (Figure 4-5a), Mn-Co oxide/PEDOT (Figure 4-5b), uncoated Mn oxide (Figure 4-5c) and Mn oxide/PEDOT deposits (Figure 4-5d).

The Mn-Co oxide/PEDOT electrode prepared at 15 $mAcm^{-2}$ had the highest initial specific capacitance (~310 Fg^{-1}), about 5% higher than the best value obtained for Mn oxide/PEDOT (~295 Fg^{-1}), and significantly better than the best Mn-Co oxide (~213 Fg^{-1}) and Mn oxide electrodes (~203 Fg^{-1}). The initial specific capacitance of the Mn-Co oxide deposit prepared at 20 $mAcm^{-2}$, which was a more uniform and continuous deposit, was 198 Fg^{-1}, which was 7% lower than the capacitance for Mn-Co oxide with a rod-like morphology. All five cyclic voltammogram curves show a rectangular-shaped profile, demonstrating the good capacitive behavior of these electrode materials. For the rod-like Mn oxide deposit and continuous Mn-Co oxide deposit (Figure 4-5c and 4-5e), the voltammetric curves exhibit anodic peaks centered at about 0.59 V and 0.56 V and cathodic peaks centered at about 0.34 V and 0.36 V, respectively, which are characteristic of redox transitions resulting from ion exchange. The peaks become gradually larger as the number of cycles is increased, suggesting higher insertion capacity and faster kinetics for Na^+ intercalation/deintercalation in the MnO_2 electrode occurring within this voltage range. For the Mn-Co oxide samples (Figure 4-5a), weaker anodic and cathodic peaks appear between -0.1 and 0.9 V (at 0.34 V and 0.58 V) and there are no visible peaks for the Mn-Co oxide/PEDOT (Figure 4-5b) and the Mn oxide/PEDOT (Figure 4-5d) deposits. This indicates that these electrode capacitors are charged and discharged at or near a constant rate over the complete voltammetric cycle [42].

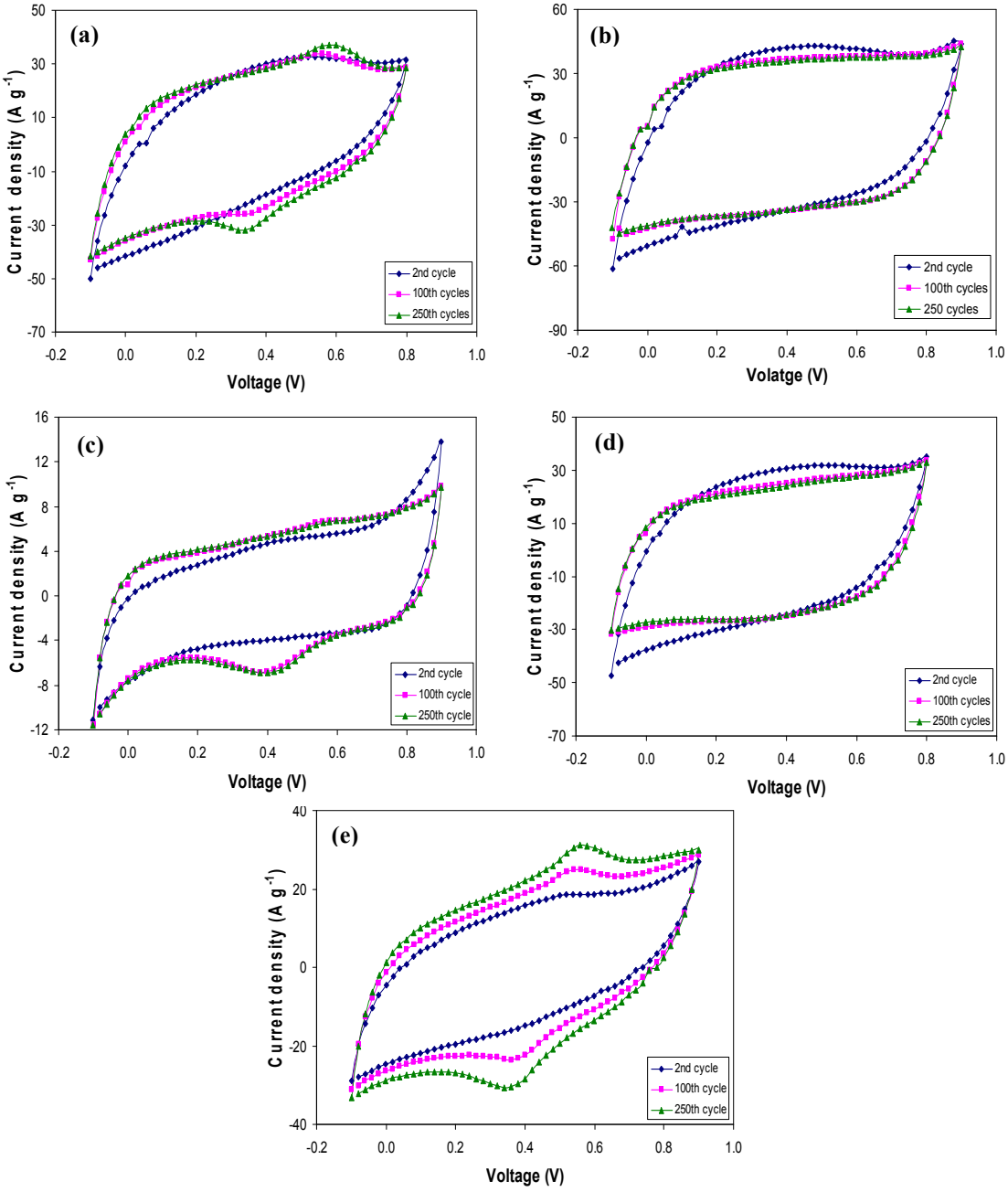

Figure 4-5 Representative cyclic voltammograms taken from (a) Mn-Co oxide prepared from a 0.01 M $Mn(CH_3COO)_2$ and 0.001 M $CoSO_4$ solution (at 15 $mAcm^{-2}$ for 300 s); (b) Mn-Co oxide/PEDOT prepared from a 0.01 M $Mn(CH_3COO)_2$ and 0.001 M $CoSO_4$ solution (at 15 $mAcm^{-2}$ for 300 s) followed by PEDOT deposition at 1V for 45 s; (c) Mn oxide prepared from a 0.01 M $Mn(CH_3COO)_2$ solution; (d) Mn oxide/PEDOT oxide prepared from a 0.01 M $Mn(CH_3COO)_2$ solution followed by PEDOT deposition at 1V for 45 s; (e) Mn-Co oxide deposit prepared from a 0.01 M $Mn(CH_3COO)_2$ and 0.001 M $CoSO_4$ solution (at 20 $mAcm^{-2}$ for 300 s). All samples were cycled for up to 500 cycles at 100 mVs^{-1}.

Figure 4-6a-d shows the capacitance values for uncoated Mn oxide and Mn-Co oxide rods and Mn oxide/PEDOT and Mn-Co oxide/PEDOT coaxial rods at different scan rates, i.e., 5-1000 mVs^{-1}, and with cycling. In all cases, there was an increase in capacitance values for increasing scan rate up to 100 mVs^{-1}, followed by a decrease in capacitance with increasing scan rate after 100 mVs^{-1}.

After 500 cycles at 100 mVs^{-1}, the specific capacitance value for the Mn-Co oxide/PEDOT electrodes was 281 Fg^{-1} (reduction in capacitance was 9% of the initial reversible capacity), while the capacitance value for the Mn-Co oxide electrodes was 176 Fg^{-1} (capacitance fading was about 18%). Capacitance fading for Mn oxide/PEDOT electrodes (267 Fg^{-1} after 500 cycles) and Mn oxide rods (153 Fg^{-1} after 500 cycles) was 9% and 25%, respectively. Since the capacitance reduction between 250 and 500 cycles was small (up to 1% for PEDOT coated deposits and up to 4% for uncoated deposits), all other samples were tested for only 250 cycles. Reversible capacity decay indicates a decrease in the amount of active material with cycling. The presence of PEDOT as a shell on the Mn oxide and Mn-Co oxide provides an interconnected network during the charge/discharge process to facilitate both the charge-transfer reaction and electron conduction. Also, the PEDOT shell on the core Mn oxide and Mn-Co oxide is believed to protect the oxide from dissolution during cycling, so a large amount of active material remains after cycling resulting in improved electrochemical cyclability. Thus, the Mn oxide/PEDOT and Mn-Co oxide/PEDOT coaxial core/shell rods exhibit high capacitance and long redox cycling life.

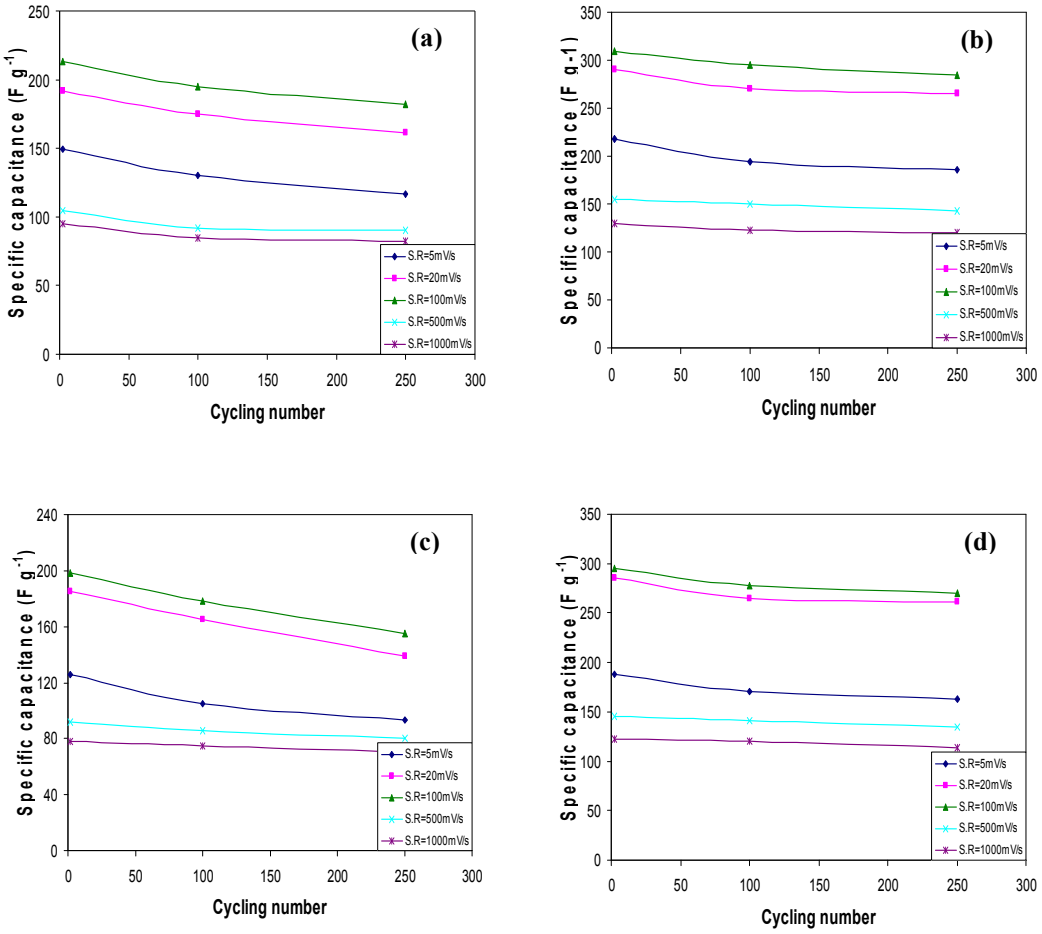

Figure 4-6 Specific capacitance values for (a) Mn-Co oxide rod samples; (b) Mn-Co oxide/PEDOT coaxial samples; (c) Mn oxide rod samples; (d) Mn oxide/PEDOT coaxial samples cycled at different scan rates.

Mn-Co oxide electrodes provide higher capacitance values (~5% higher for the best electrodes) and better electrochemical cyclability relative to the Mn oxide electrodes. As discussed previously, the addition of Co to Mn oxide results in ~11% reduction in density. A less dense structure should facilitate ion transport and charge transfer leading to higher capacitance values. Deviation from ideal capacitive behavior during electrochemical cycling for Mn oxide can be attributed to irreversible anodic dissolution of the oxide ($MnO_2 + 2H_2O \rightarrow MnO_4^- + 4H^+ + 3e^-$) according to the Pourbaix diagram [43]. Chang *et al.* [37] have shown that

incorporating Co into the deposited oxides can improve cyclic stability. The added Co can suppress anodic dissolution of the oxide and, therefore, improve the electrochemical reversibility. In order to confirm the effect of Co addition on Mn dissolution, the Mn content in electrolyte solutions after electrochemical cycling was analyzed using AAS. The amount of dissolution was lower for Mn-Co oxide compared with Mn oxide. After 250 cycles, solution Mn levels were 0.25 ppm for Mn oxide and 0.21 ppm for Mn-Co oxide, i.e., lower Mn loss for Mn-Co oxide deposits. The capacitance value for Mn-Co oxide was ~13% higher than that for Mn oxide after 250 cycles. The larger amount of Mn loss for Mn oxide deposits may be a major reason for the greater capacitance reduction for Mn oxide deposits relative to Mn-Co oxide.

Mn dissolution for PEDOT coated Mn and Mn-Co oxide was lower relative to uncoated Mn and Mn-Co oxide. For PEDOT coated Mn oxide and Mn-Co oxide deposits, solution Mn levels were 0.12 ppm and 0.10 ppm after 250 cycles, respectively. This shows that the Mn loss after 250 cycles for uncoated Mn oxide and Mn-Co oxide deposits is about 2 times greater than that for coated deposits. The capacitance values for uncoated Mn oxide and Mn-Co oxide deposits are 41 and 36% lower relative to those for coated deposits after 250 cycles.

All the capacitance values quoted above were calculated based on the original mass of the deposit. In order to determine whether the loss in capacitance on cycling was primarily due to loss of Mn (and Co for Mn-Co deposits), capacitance values were calculated using the actual deposit mass, i.e., the mass after each of the number of cycles in question. The mass did not measurably change for any of the samples after two cycles, but the change was significant after 250 cycles, particularly for the Mn oxide sample in Figure 4-5c (15% loss in deposit mass). Based on this approach, the capacitance values were recalculated for the samples in Figure 4-5 for a scan rate of 100 mVs^{-1} (Table 4-1). The capacitance reductions for the uncoated samples, after cycling, are decreased to ~8% and 6% for Mn oxide and Mn-Co oxide, respectively. As such, loss of material is a major

contributing factor to capacitance reduction, but is not the only factor. For the PEDOT samples, the adjusted capacitance values (after 250 cycles) are essentially the same (within measurement error) as the original capacitance values (after 2 cycles). One can then surmise that capacitance reduction on cycling is due almost exclusively to material loss.

Table 4-1 Capacitance values for samples shown in Figure 5 for a scan rate of 100 mVs^{-1} using original mass and mass after specified number of cycles.

Type of electrode	Capacitance (Fg^{-1})			
	Original mass		Mass after cycling	
	2 cycles	250 cycles	2 cycles	250 cycles
Mn oxide	203	159	203	186
Mn oxide/PEDOT	295	270	295	292
Mn-Co oxide	213	182	213	200
Mn-Co oxide/PEDOT	310	283	310	308

As mentioned above, specific capacitance shows an anomalous trend with scan rate for all four deposit types. Faradaic reactions occurring on the surface and in the bulk of these materials are the major charge storage mechanisms for MnO_2 and Mn-Co oxide materials. The surface Faradaic reaction involves the adsorption of electrolyte cations ($C^+ = Na^+$) on the electrode surface (M= Mn or Co) from the electrolyte.

$$(MO_2)_{surface} + C^+ + e^- \longleftrightarrow (MOOC)_{surface} \qquad (4\text{-}2)$$

The bulk Faradaic reactions are based on the intercalation of H^+ or Na^+ ions in the electrode during reduction and deintercalation on oxidation [9]:

$$MO_2 + H^+ + e^- \longleftrightarrow MOOH \quad (4\text{-}3)$$

$$MO_2 + C^+ + e^- \longleftrightarrow MOOC \quad (4\text{-}4)$$

In both charge storage mechanisms, diffusion and redox reactions involving charge transfer occur. It should be noted that the charge processes should be less favorable at higher scan rates leading to lower capacitances. However, as shown in Figure 4-7a and 4-7b, an increase in capacitance occurs at higher scan rates up to 100 mVs^{-1}, where maximum values of 203 and 295 Fg^{-1} are achieved for Mn oxide and Mn oxide/PEDOT, respectively, and maximum values of 213 and 310 Fg^{-1} for Mn-Co oxide and Mn-Co oxide/PEDOT are achieved, respectively. As shown in Figure 4-7b, the electrochemical reversibility of the Mn oxide electrode was clearly enhanced by the addition of Co.

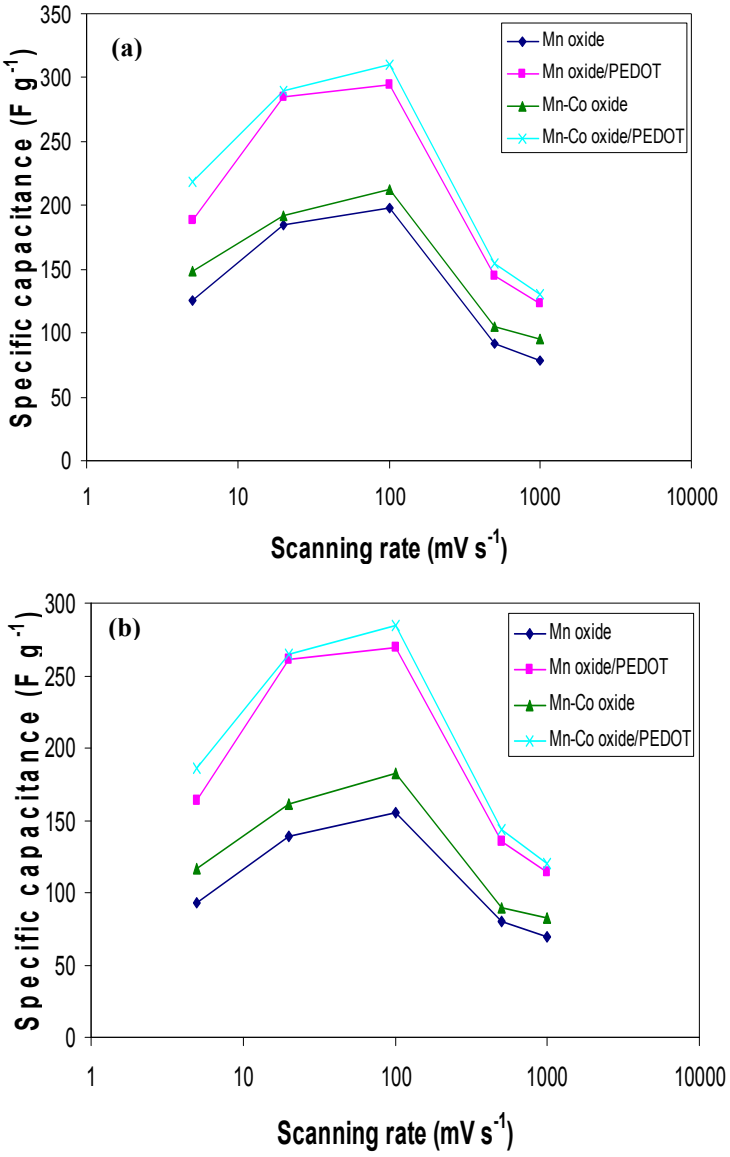

Figure 4-7 Specific capacitance values for Mn-Co oxide and Mn-Co oxide/PEDOT deposits prepared from a 0.01 M $Mn(CH_3COO)_2$ and 0.001 M $CoSO_4$ solution at 15 $mAcm^{-2}$ for 300 s followed by PEDOT deposition at 1V for 45 s and Mn oxide and Mn oxide/PEDOT deposit prepared from a 0.01 M $Mn(CH_3COO)_2$ solution at 5 $mAcm^{-2}$ for 10 min followed by PEDOT deposition at 1V for 45 s; after (a) 2 cycles and (b) 250 cycles in 0.5M Na_2SO_4 at different scan rates.

To further understand the capacitance behavior, EIS was applied to evaluate Mn oxide and Mn-Co oxide deposits after 250 cycles at 5, 20, 100, 500 and 1000 mVs^{-1}. In the impedance plots (Figure 4-8), straight lines with various slopes are observed and are related to the electrolyte diffusion and cation intercalation/deintercalation processes. An impedance line with a larger slope corresponds to a lower diffusive resistance for the electrolyte in the electrode. It is apparent that the slope of the impedance curves increases with scan rate up to 100 mVs^{-1} for both Mn oxide and Mn-Co oxide deposits and then decreases. These results indicate that the lowest electrolyte diffusion resistance occurs for electrodes cycled at 100 mVs^{-1}. At very high frequencies, a very small impedance arc is present, while at high frequencies a semi-circle is present, in each impedance spectrum (inset of Figure 4-8a and 4-8b) which accounts for the double layer (dl) and charge transfer processes, respectively. It appears that the charge transfer resistance of the electrode materials is reduced with scan rates up to 100 mVs^{-1} for both Mn-Co oxide and Mn oxide deposits. Therefore, electrodes cycled at 100 mVs^{-1} exhibit the lowest charge transfer resistances for both Mn-Co oxide and Mn oxide deposits. The next lowest resistances in increasing order of resistance occur for scanning rates of 20, 5, 500 and 1000 mVs^{-1}, respectively. These results correlate with the capacitance behavior, with the highest capacitance measured for a scan rate of 100 mVs^{-1}.

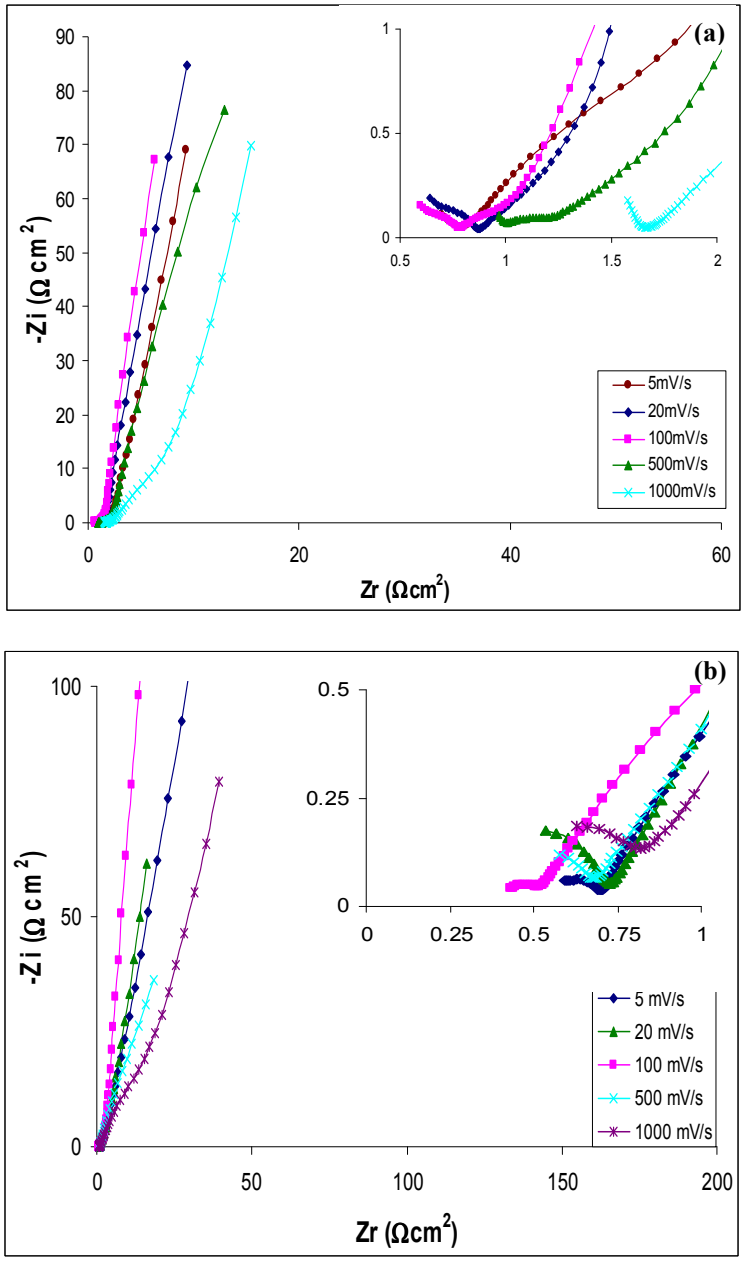

Figure 4-8 Nyquist plots for (a) Mn-Co oxide and (b) Mn oxide deposits cycled at different scan rates (0.5 M Na_2SO_4 solution at 0.2 V vs. SCE) after 250 cycles.

Simulations were carried out by fitting equivalent circuits to illustrate the effects of different scan rates. The scope of this study is limited to consideration of the different possible processes and only then to propose the equivalent circuit. All

the nomenclature used is based on Zview Version 2.7 software, which was utilized for the construction of the equivalent electrical circuits.

The impedance data can be fit assuming three major processes in the entire frequency range [44-47]. Figure 4-9 shows an equivalent circuit model to fit the experimental impedance data, where *R*s is the solution resistance. *R*1 is the electronic resistance between the oxide nanocrystals and *C*1 is the double layer capacitance [25,48]. *R*2 is the ionic resistance related to the charge transfer process on the surface of the electrode in contact with the electrolyte and *CPE*1 is the constant phase element related to the charge transfer process. An increasing value of *R*2 implies that the Faradaic charge transfer reaction is slower and, hence, the resulting impedance increases. (*R*3*CPE*2)*W*1 is a circuit to fit the diffusion process of the electrolyte in the electrode, where *R*3 is the diffusive resistance and *CPE*2 is the constant phase element, which accounts for the inhomogeneity of the nanocrystalline oxide electrode. The effects of mass transport on the Faradaic charge transfer reaction are determined through the Warburg prefactor (*W*1), which is inversely related to the square root of the diffusion coefficient of the electroactive material. When *W*1 increases, the mass transport of electroactive material to the electrode/electrolyte interface becomes slower and the electrode impedance is increased [44-46].

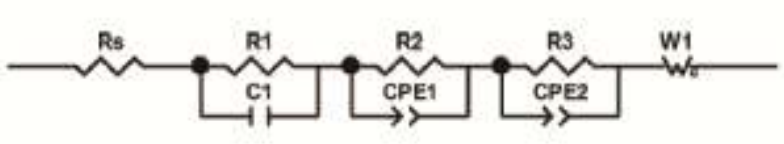

Figure 4-9 An equivalent circuit for modeling the experimental impedance spectra obtained from Mn-Co oxide and Mn oxide electrodes cycled at different scan rates.

Resistance values obtained from fitting the experimental impedance data to the equivalent circuit (Figure 4-9) are tabulated in Tables 4-2 and 4-3. For both Mn

oxide and Mn-Co oxide deposits, the resistance values decreased with increasing scan rate up to 100 mVs^{-1} and then increased. The exception was for R1 (electronic resistance) which showed the same trend, but had its lowest value for a scan rate of 20 mVs^{-1}. The R1 and R2 resistance values (electronic and charge transfer resistances) are lower for Mn oxide compared to those for Mn-Co oxide deposits, while R3 resistance values (diffusive resistance) are higher for scan rates less than and equal to 100 mVs^{-1}. As shown in Figure 4-8, Mn oxide and Mn-Co oxide electrodes have different semi-circles at high frequencies leading to different charge transfer resistances. The high frequency loop is dependent on film morphology and is attributed to the substrate/oxide interface. The lower charge transfer resistance for Mn oxide relative to Mn-Co oxide is attributed to faster electron transport through the Mn oxide electrode. The Mn oxide rods have smaller dimensions (1.0-1.5 μm in diameter) compared with Mn-Co oxide rods (2.5-3.5 μm in diameter), providing shorter paths for electron transfer. The linear parts of the impedance spectra are typical for the capacitive response of the electrodes, which is dominated by the electrolyte diffusion process. In terms of proton intercalation and diffusion, Mn oxide and Mn-Co oxide behave differently due to their different densities, as described previously. Mn-Co oxide is less dense, thereby promoting proton diffusion. Mn-Co oxide rods offer more electrochemically accessible active sites compared to Mn oxide electrodes, facilitating ion transport. The R3 values confirm that the diffusive resistance of the electrolyte ions for Mn oxide is larger relative to Mn-Co oxide electrodes. Faradaic reactions occurring on the surface (adsorption of electrolyte cations) and in the bulk of Mn oxide and Mn-Co oxide (intercalation/deintercalation of electrolyte ions) are highly dependent on cation diffusion within the electrolyte. Since better capacitance values were obtained for Mn-Co oxides relative to Mn oxides, electrolyte diffusion resistance appears to be the major resistance component affecting capacitance.

Table 4-2 Resistance values obtained from fitting experimental impedance data to the equivalent circuit in Figure 4-9 for Mn-Co oxide deposits

Scan rate (mVs^{-1})	R1 ($\Omega\ cm^2$)	R2 ($\Omega\ cm^2$)	R3 ($\Omega\ cm^2$)
5	0.31	0.95	1.4
20	0.28	0.69	0.47
100	0.28	0.57	0.23
500	0.32	0.87	1.72
1000	0.5	1.14	2.1

Table 4-3 Resistance values obtained from fitting experimental impedance data to the equivalent circuit in Figure 4-9 for Mn oxide deposits

Scan rate (mVs^{-1})	R1 ($\Omega\ cm^2$)	R2 ($\Omega\ cm^2$)	R3 ($\Omega\ cm^2$)
5	0.28	0.75	2.20
20	0.18	0.58	1.80
100	0.20	0.45	1.42
500	0.31	0.72	1.57
1000	0.42	0.9	1.85

The reduction in capacitance values after the peak value can be understood as follows. At slower scan rates (~100 mVs^{-1}), intercalation and deintercalation within the electrode are readily achieved and ion transport is not a problem, leading to high capacitance. At higher scan rates, however, adsorption becomes predominant (Reaction 4-2), leading to a decrease in capacitance [49]. The anomalous trend observed at scan rates less than 100 mVs^{-1} is in contradiction to the generally accepted charge storage mechanisms for electrochemical capacitors. As described previously, electronic, charge transfer and diffusive resistances are reduced as the scan rate is increased to 100 mVs^{-1}, followed by an increase at higher scan rates for both Mn-Co oxide and Mn oxide deposits. This correlates

with the highest capacitance value at 100 mVs^{-1}. However, there is still no explanation to clarify the reasons for the anomalous trend observed at scan rates less than 100 mVs^{-1}. Additional analysis is needed to uncover the underlying reasons for this trend.

4.3.4. Morphology and crystal structure of cycled electrodes

Morphological and structural changes for Mn-Co oxide and Mn-Co oxide/PEDOT samples were monitored after cycling. Cross-sectional SEM SE images are shown in Figure 10a-d for as-deposited Mn-Co oxide and Mn-Co oxide/PEDOT electrodes and those cycled in 0.5 M Na_2SO_4 at 100 mVs^{-1} for 250 cycles. A rod-like morphology is still observed for the Mn-Co oxide/PEDOT deposit after cycling (Figure 4-10d) and the microstructure has not changed much relative to the as-deposited structure (Figure 4-10c), i.e., the surface area is almost the same. This behavior can be attributed to the presence of protective PEDOT. The capacitance reduction in the deposits may be attributed mainly to the loss of unstable Mn ions by dissolution in the electrolyte solution [50] as discussed in Chapter 3, Section 3.3. Based on the Mn-H_2O Pourbaix diagram, some Mn dissolution in the 0.5 M Na_2SO_4 solution, as Mn^{2+} cations, is expected during cycling from 0.9 to −0.1 V. The amount of Mn dissolution through AAS measurements after 250 cycles was lower for PEDOT coated Mn-Co oxide (0.10 ppm) compared with uncoated Mn-Co oxide (0.21 ppm). In addition, during forward cycling, some of the dissolved Mn^{2+} cations will be re-oxidized to MnO_2 and redeposited on the electrode surface. Redeposition results in a morphology change for uncoated Mn-Co oxide deposits (Figure 4-10a - the rods are less distinct and appear to be interconnected) leading to a reduction in the specific surface area of the electrode and a corresponding larger decrease in capacitance compared with PEDOT coated electrodes. Therefore, morphology changes in uncoated samples may be another contributing factor to the loss in capacitance.

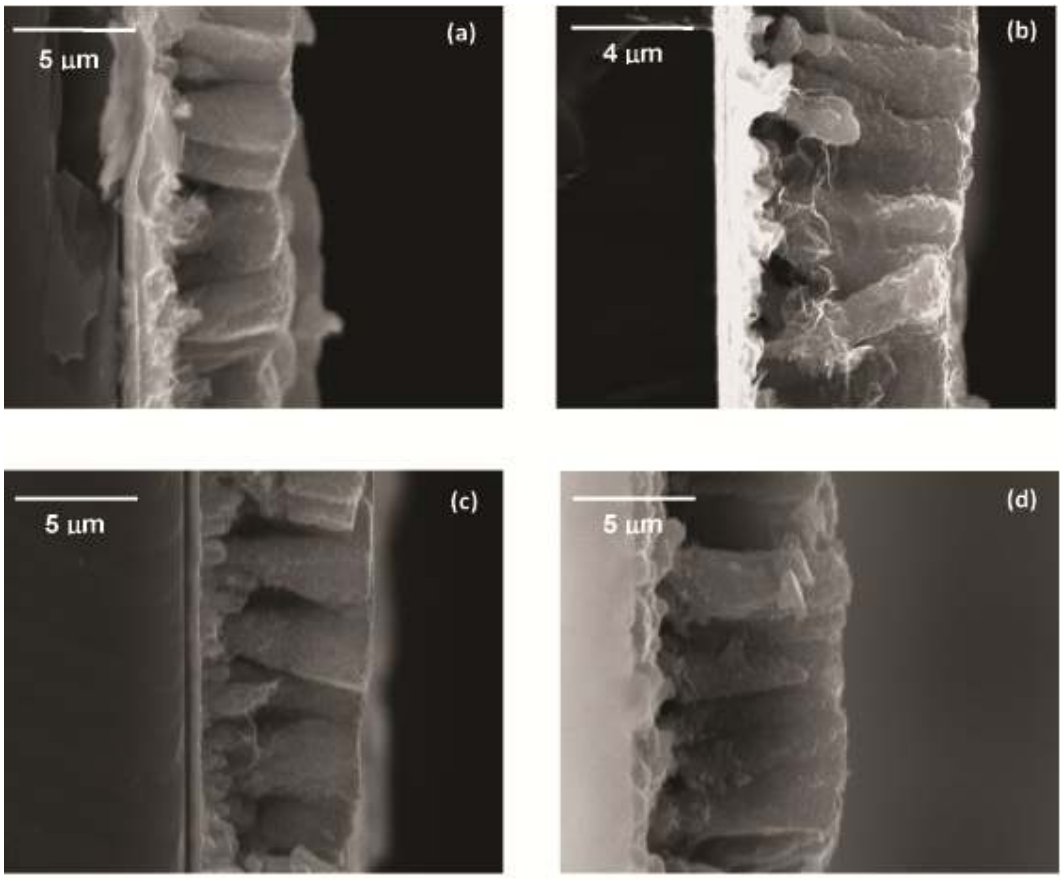

Figure 4-10 Cross-sectional SE images of Mn-Co oxide samples: (a) as-deposited and (b) cycled (250 cycles at 100 mVs^{-1}). Cross-sectional SE images of Mn-Co oxide samples: Mn-Co oxide/PEDOT samples; (c) as-deposited and (d) cycled (250 cycles at 100 mVs^{-1}).

TEM BF and DF images and corresponding SAED patterns were taken from the Mn-Co oxide deposits after 250 cycles in 0.5 M Na_2SO_4 at 100 mVs^{-1}. Figure 4-11a shows a Mn-Co oxide deposit with a fibrous structure. The SAED pattern for Mn-Co oxide deposits (inset of Figure 4-11b) can be indexed to the antifluorite-type crystal structure, which is the same structure determined for the as-deposited Mn-Co oxide (Figure 4-3c). The *d*-spacings were carefully measured (using Au particles as an internal standard) and compared to those for the as deposited samples. Any changes were negligible (≤1%), so that cycling did not appreciably affect the deposit crystal structure for either PEDOT coated or uncoated samples.

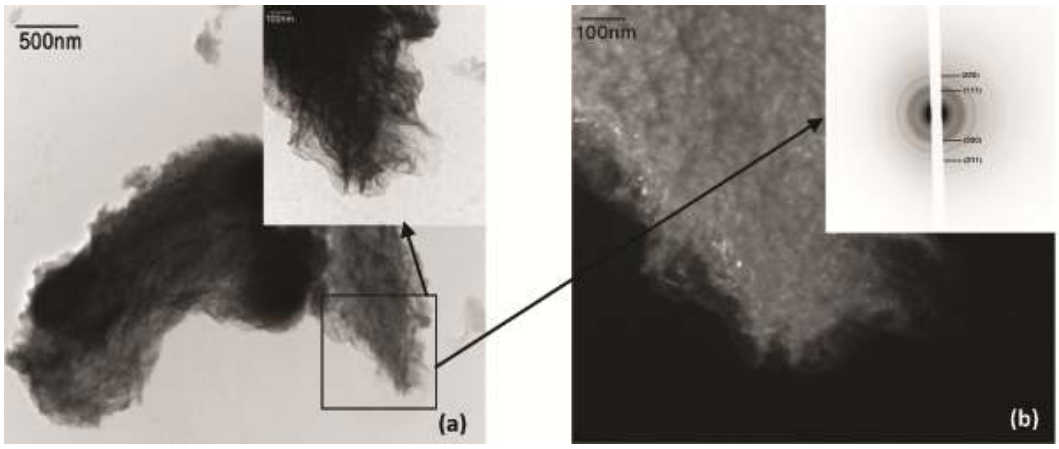

Figure 4-11 (a) TEM BF image; (b) TEM DF image and SAED pattern for Mn-Co oxide deposit prepared from 0.01 M $Mn(CH_3COO)_2$ and 0.001 M $CoSO_4$ solution (at 15 $mAcm^{-2}$ for 300 s) after 250 cycles at 100 mVs^{-1}.

4.4 Conclusions

Mn-Co oxide and Mn-Co oxide/PEDOT coaxial rod-like electrodes were electrochemically synthesized without any catalysts or templates. The presence of the PEDOT shell improved the specific capacitance and electrochemical cyclability of the deposits. Mn-Co oxide/PEDOT electrodes consisted of MnO_2, with partial Co^{2+} and Co^{3+} ion substitution for Mn^{4+}, and amorphous PEDOT. Mn-Co oxide/PEDOT electrodes with a rod-like morphology and antifluorite-type structure had high capacitances (up to 310 Fg^{-1}) at 100 mVs^{-1} and maintained their capacitance after 500 cycles in 0.5 M Na_2SO_4 (91% retention). For all deposits, capacitance values increased with increasing scan rate to 100 mVs^{-1}, and then steadily decreased after 100 mVs^{-1}. This represents an anomalous trend with potential scanning rate, as capacitance values are generally expected to decrease with increasing scan rate.

References

[1] B.E. Conway, Electrochemical Supercapacitors, Kluwer Academic/Plenum Press, New York (1999).

[2] C.C. Hu, K.H. Chang, M.C. Lin and Y.T. Wu, *Nano Lett.*, **6**, 2690 (2006).

[3] K.H. Chang, C.C. Hu and C.Y. Chou, *Chem. Mater.*, **19**, 2112 (2007).

[4] M. Toupin, T. Brousse and D. Belanger, *Chem. Mater.*, **16**, 3184 (2004).

[5] C.C. Hu and C.C. Wang, *J. Electrochem. Soc.*, **150**, A1079 (2003).

[6] M. Nakayama, T. Kanaya and R. Inoue, *Electrochem. Commun.*, **9**, 1154 (2007).

[7] J. Jiang and A. Kucernak, *Electrochimica Acta*, **27**, 2381 (2002).

[8] G.Y. Zhao, C.L. Xu and H.L. Li, *J. Power Sources*, **163**, 1132 (2007).

[9] S.C. Pang and M.A. Anderson, *J. Mater. Res.*, **15**, 2096 (2000).

[10] X. Wang and Y. Li, *J. Chem. Eur.*, **9**, 300 (2003).

[11] M.S. Wu and P.J. Chiang, *Electrochem. Commun.*, **8**, 383 (2006).

[12] S.G. Kandalkar, J.L. Gunjakar and C.D. Lokhande, *Appl. Surf. Sci.*, **254**, 5540 (2008).

[13] J. Bao, Z. Xu, J. Hong and X. Ma, *Sci. Mater.*, **50**, 19 (2004).

[14] M. Nakayama, A. Tanaka and Y. Sato, *Langmuir*, **21**, 5907 (2005).

[15] C.J. Patrissi and C.R. Martin, *J. Electrochem. Soc.*, **146**, 3176 (1999).

[16] C. Peng, S.W. Zhang and D. Jewell, *Prog. Nat. Sci,* **18**, 777 (2008).

[17] S. Cho and S.B. Lee, *Acc. Chem. Res.*, **41**, 699 (2008).

[18] E.M. Genies and S. Picart, *Synth. Met.*, **69**, 165 (1995).

[19] K. Naoi, K.I. Kawase, M. Mori and M. Komiyama, *J. Electrochem.Soc.*, **144**, L173 (1997).

[20] C. Arbizzani, M. Mastragostino and L. Meneghello, *Electrochimica Acta*, **41(1)**, 21 (1996).

[21] H. Randriamahazaka, V. Noel and C. Chevrot, *J. Electroanal. Chem.*, **472(2)**, 103 (1999).

[22] B. Babakhani and D.G. Ivey, *J. Power Sources,* **195**, 2110 (2010).

[23] K. Naoi and P. Simon, *Electrochem. Soc. Interf.*, **17(1)**, 34 (2008).

[24] S. Komaba, A. Ogata and T. Tsuchikawa, *Electrochem. Commun.*, **10**, 1435 (2008).

[25] D.A. Brevnov and T.S. Olson, *Electrochimica Acta.*, **51**, 1172 (2006).

[26] C.C. Hu, C.Y. Hung and Y.L. Yang, *J. Power Sources*, **196**, 847 (2011).

[27] R. Liu and S.B. Lee, *J. Am. Chem. Soc.*, **130**, 2942 (2008).

[28] R.K. Sharma, A.C. Rastogi and S.B. Desu, *Electrochimica Acta*, **53**, 7690 (2008).

[29] B. Babakhani and D.G. Ivey, *Electrochimica Acta*, **55**, 4014 (2010).

[30] B. Babakhani and D.G. Ivey, *ECS Transactions*, **25 (35)**, 173 (2010).

[31] M. Nakayama, A. Tanaka and S. Konishi, *J. Mater. Res.*, **19**, 1509 (2004).

[32] M.T. Lee, J.K. Chang and W.T. Tsai, *J. Power Sources,* **178**, 476 (2008).

[33] K.R. Prasad and N. Miura, *Electrochem. Commun.*, **6**, 1004 (2004).

[34] K.R. Prasad and N. Miura, *J. Power Sources*, **135**, 354 (2004).

[35] H. Zheng, F. Tang and M. Lim, *J. Power Sources*, **195**, 680 (2010).

[36] P.Y. Chuang and C.C. Hu, *Mater. Chem. Phys.*, **92**, 138 (2005).

[37] J.K. Chang, M.T. Lee, C.H. Huang, *Mater. Chem. Phys.*, **108**, 124 (2008).

[38] W. Wei, W. Chen and D.G. Ivey, *J. Phys. Chem. C*, **111**, 10398 (2007).

[39] D. Barreca, C. Massignan and S. Daolio, *J. Chem. Mater.*, **13**, 588 (2001).

[40] M. Burriel, G. Garcia and J. Santiso, *Chem. Vap. Deposition*, **11**, 106 (2005).

[41] S. Pasko, A. Abrutis and L.G. Hubert, *J. Cryst. Growth*, **262**, 653 (2004).

[42] S.J. Bao, B.L. He, Y.Y. Liang, *Mater. Sci. Eng.*, **A 397**, 305 (2005).

[43] M. Pourbaix, *Atlas of Electrochemical Equilibria in Aqueous Solutions*, National Association of Corrosion Engineers, Houston, TX (1966).

[44] W. Wei, W. Chen and D.G. Ivey, *Electrochimica Acta*, **54**, 2271 (2009).

[45] S.W. Donne and J.H. Kennedy, *J. Appl. Electrochem.*, **34**, 477 (2004).

[46] R. Roto and G. Villemure, *Electrochimica Acta*, **51**, 2539 (2006).

[47] C.C. Hu and C.H. Chu., *J. Electroanal. Chem.*, **503**, 105 (2001).

[48] Y.R. Nian and H. Teng, *J. Electrochem. Soc.*, **149**, 1008 (2002).

[49] K. Kuratani, K. Tatsumi and N. Kuriyama, *Cryst. Growth Des.*, **7(8)**, 1375 (2007).

[50] P. Soudan, J. Gaudet, D. Guay, D. Belanger and D. Schulz, *Chem. Mater.*, **14**, 1210 (2002).

Chapter 5 Effect of electrodeposition conditions on the electrochemical capacitive behaviour of synthesized Mn oxide electrodes[4]

5.1 Introduction

Electrochemical capacitors are currently receiving considerable attention, since they are extremely useful as energy storage devices in systems requiring quick bursts of energy such as portable electronic devices [1].

It is believed that surface morphology, which depends on the preparation method and processing parameters, significantly affects the capacitive behavior of electrode materials. Therefore, the fabrication of materials with appropriate morphology has become an important strategy to enhance the electrochemical performance of electrode materials. One–dimensional (1D) nanomaterials such as nanowires [2], nanorods [3], nanotubes [4] and two–dimensional (2D) nanosheets [5] are reported to exhibit outstanding charge storage properties, because they have large surface areas for charge storage and fast redox reactions. Diffusion resistance in the solid phase can be mitigated by shortening the diffusion paths [2, 6–11].

Transition metal oxides are suitable materials to host small ions like H^+ and alkaline cations (Li^+, Na^+, K^+) during intercalation/deintercalation processes, which make them suitable materials for energy storage devices [12]. Among different transition metal oxides, Mn oxide has attracted considerable attention due to its high energy density, low cost, natural abundance and environmentally friendly nature. In recent years, electrodeposition techniques [13–18] have been increasingly explored due to their relatively easy and accurate control of the surface microstructure of deposited films by changing deposition variables, such

[4] *A version of this chapter has been accepted for publication. Banafsheh Babakhani, Douglas G. Ivey. Journal of Power Sources, 2011.*

as the electrolyte, deposition potential and bath temperature, to produce novel electroactive materials [19,20]. Many investigations have attributed the capacity of Mn dioxides to their structural, morphological and compositional characteristics [21–25]. Generally, most important physicochemical properties of Mn dioxide deposits depend on electrokinetic phenomena during the synthesis process. In general, it is postulated that oxidation of Mn^{2+} to MnO_2 occurs [26–28].

$$Mn^{2+} + 4\ OH^- \rightarrow MnO_2 + 2\ H_2O + 2e^- \quad (5\text{-}1)$$

By adjusting the deposition parameters, it is possible to modify the electrocrystallization process of MnO_2. This process can be controlled via two fundamental electrokinetic phenomena, i.e., nucleation and growth of crystal grains. Generally, nucleation is either instantaneous or progressive and subsequent growth of nuclei is either two dimensional (2D) or three–dimensional (3D). It is believed that the nucleation mechanism during electrodeposition depends strongly on the bath composition, pH value of the electrolytes, overpotential (current density) and solution temperature [29,30].

Morphology–controlled growth can generally be achieved by controlling the deposition parameters. Mn oxide electrodes with different surface morphologies, such as equiaxed and agglomerated particles [23], fibrous features (micro and nano–scale fibers) [24], rod–like morphologies and aggregated rods [21,25], can be obtained under different electrodeposition conditions. As described in Chapter 2, Mn oxide with a rod–like morphology was prepared without a template, through anodic deposition from a 0.01 M Mn acetate solution at various deposition current densities. Deposits prepared at a current density of 5 mA cm^{-2} showed the best capacitance (185 Fg^{-1}) and retention (~75% of the original value – ~139 Fg^{-1}) after 250 cycles in 0.5 M Na_2SO_4 at a scan rate of 20 mVs^{-1} (Chapter 2, Section 2.3.3) [21]. However, there still has been little done to clarify the formation mechanism of Mn oxide electrodes and the relationship between the

synthesis parameters and morphological, structural and electrochemical properties of electrodes. It has been shown that the morphology of Mn oxides is qualitatively determined by the supersaturation ratio (S), which affects the reaction kinetics in aqueous solutions [31]. As the supersaturation ratio is increased, the deposition rate increases leading to the formation of several different morphologies from interconnected nanosheets (low S values) to columnar structures to discrete oxide clusters to petal- and flower-like morphologies to continuous coatings (high S values) with equiaxed and fibrous features [31]. However, the nucleation and growth mechanisms for Mn oxide electrodes with different morphologies are still not clarified.

This chapter reports on the synthesis and nucleation and growth mechanisms of Mn oxide electrodes prepared from Mn acetate–containing aqueous solutions under various deposition parameters, i.e., current density, electrolyte composition and pH, deposition temperature and time, and presents a detailed electrochemical, morphological and structural analysis of electrochemically synthesized Mn oxide electrodes. The relationship between the physicochemical features of Mn oxide electrodes and the corresponding electrochemical behavior of the electrodes is investigated.

Mn acetate–containing solutions are used, rather than other Mn components or additives, in this Chapter since high surface area morphologies such as rod–like structures are attainable from this electrolyte without any additives or the use of templates (Chapter 2, Section 2.3.3) [21]. In addition, Rangappa et al. [32] have used anodic processes to produce Mn(+4) acetate and Mn(+4) sulfate. They observed that Mn(+3) acetate was significantly more stable than Mn(+3) sulfate, which indicates a thermodynamic favorability in the kinetics of oxidizing the acetate versus the sulfate. A stable intermediate Mn(+3) species increases the reaction rate producing Mn(+4) as the final product. Therefore, Mn acetate allows for more rapid deposition at fixed potentials relative to Mn sulfate [32]. Moreover, it is suggested that in order to grow 1D nanostructures through

template–free electrodeposition, the targeted materials must have intrinsic crystal structures that will form along one of the crystal axis or alternatively some growth modifier must be employed [33]. However, template–free electrodeposition has only been used for a limited set of materials. It is highly desirable to widen the applicability of this approach to a broader set of materials. Fully understanding the growth mechanism during the electrodeposition process and finding out the crucial parameters to control anisotropic growth are required to extend the applicability range of template–free electrodeposition of 1D nanostructures.

5.2 Experimental procedure

Mn oxide coatings were deposited from acetate–containing aqueous solutions ($Mn(CH_3COO)_2$) with various concentrations, i.e., from 0.003 to 0.05 M onto Au coated Si substrates, using the procedure described in Chapter 2, Section 2.2. Current densities ranging from 0.25–35 $mAcm^{-2}$ were used to fabricate deposits, through anodic electrodeposition. The deposition temperatures were controlled with a hot water bath and deposits were synthesized at 25, 60 and 85ºC. Electrolyte pH values were adjusted using dilute H_2SO_4 and NaOH solutions and deposits were synthesized at pH values of 5–8.5. Deposition times varied from 3–10 minutes.

Morphological and crystal structural analysis of the oxide deposits was conducted using SEM and TEM with the operating parameters described in Chapter 2, Section 2.2.

In order to determine the electrochemical behavior of the Mn oxide electrodes, a Gamry PC4/750 potentiostat/galvanostat was used for cyclic voltammetry (CV) in an electrolyte containing 0.5 M Na_2SO_4 at room temperature, as described in Chapter 2, Section 2.2. Cyclic voltammograms were recorded between –0.1 and 0.9 V vs. SCE at a scanning rate of 20 mVs^{-1}. For consistency, all CV scans were done using fresh deposits.

The Mn content in 0.5 M Na_2SO_4 electrolytes after 2 and 250 cycles for various Mn oxide deposits was determined using a VARIAN 220 FS atomic absorption spectrometer (AAS).

Electrochemical impedance spectroscopy (EIS) measurements were conducted on cycled Mn oxide electrodes after 250 cycles in constant voltage mode (0.2 V vs. SCE) by sweeping frequencies from 100 kHz to 10 mHz at an amplitude of 5 mV.

5.3 Results and discussion

5.3.1. Surface morphology and crystal structure of Mn oxide deposits

5.3.1.1. Effect of deposition current density

Nucleation strongly depends on the overpotential (current density) during electrochemical deposition. According to Faraday's law, the quantity of an electrochemical reaction at an electrode is proportional to the amount of electric charge. Therefore, for all deposition current densities, deposition rate can be estimated from [34]

$$V = \frac{i_k \eta_k E}{\rho} \tag{5-2}$$

where V is deposition rate, i_k is current density, η_k is current efficiency, E is electrochemical equivalent for Mn (0.29282 g $(Ah)^{-1}$) and ρ is the density of Mn (7.21 gcm^{-3}). According to Equation (5-2), the deposition rate is correlated with the current density and current efficiency. At a constant current efficiency the relationship between the deposition rate and current density should be linear.

Mn oxide electrodes were prepared from a 0.01 M Mn acetate solution (60ºC with natural pH (7.5)); depositions were done for 10 min. At low deposition current densities (0.25–1 $mAcm^{-2}$), nucleation rates are low, leading to the formation of

only a few oxide nuclei on the electrode surfaces during the initial stages of electrodeposition. As such, a continuous layer is not formed initially on the surface under these conditions. Oxide particles serve as seeds for the growth of thin, single crystal sheets. Thin sheets have very smooth surfaces and grow preferentially on the seed layer. Therefore, a thin sheet morphology (Figure 5-1a and b) is obtained. A transition from thin sheet to rod–like structure is observed at 2 $mAcm^{-2}$ (Figure 5-1c). At higher magnifications (inset of Figure 5-1c) thin sheets are apparent within the growing rods. As the deposition current density is increased, both nucleation and growth rate increase and rod–like structures are formed at intermediate current densities (5–15 $mAcm^{-2}$) (Figure 5-1d and e). The rods (~1–3 μm in diameter) [25] are oriented perpendicular to the surface of the substrate for deposits prepared at 5 $mAcm^{-2}$. Mn oxides with both rod–like and thin sheet structures provide large surface areas.

A further increase in overpotential results in a greater increase in the nucleation and growth rate. Therefore, the diameter of the oxide rods increases slightly, while the spaces between oxide rods decrease dramatically. As a result, rods with slightly larger radii (~1.5–3.5 μm in diameter) are formed at higher current densities of 15 $mAcm^{-2}$ (Figure 5-1e). At even higher current densities (e.g., 20 $mAcm^{-2}$), aggregated rods are formed and these have larger diameters (~2–4 μm) [25] (Figure 5-1f). It was reported previously that Mn oxide synthesized at lower deposition current densities (5 $mAcm^{-2}$) had more uniform, vertical and free–standing rods relative to deposits prepared at higher deposition current densities (>15 $mAcm^{-2}$) (Chapter 2, Section 2.3.3) [21].

An additional increase in deposition current density (~35 $mAcm^{-2}$) leads to the formation of a more continuous, but still porous, coating (Figure 5-1g). In summary, as the deposition current density is increased, the morphology of Mn oxide deposits changes from thin sheets to rod–like to aggregated rods to continuous coatings.

Mn oxide thin sheets possess a higher crystallization degree relative to rods, aggregated rods and continuous coatings. Figure 5-1h and 5-1i depict a TEM BF image and a corresponding SAED pattern for several thin sheets. The SAED pattern is a single crystal pattern, which can be indexed to an antifluorite crystal structure with a zone axis close to a <111>-type orientation, i.e., the sheet planes are parallel to {111}-type planes. This result indicates that the thin sheets are single crystalline Mn oxides.

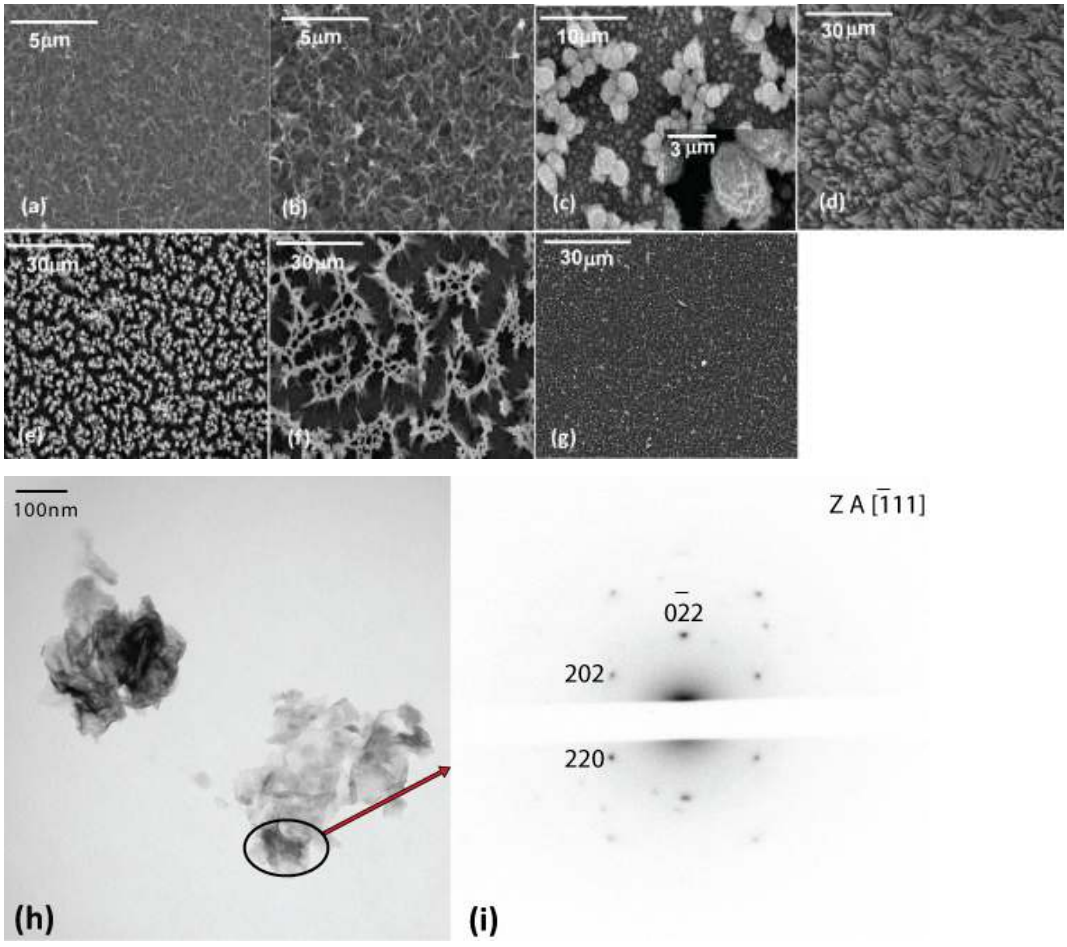

Figure 5-1 SEM secondary electron (SE) plan view images of Mn oxide deposits prepared from 0.01 M $Mn(CH_3COO)_2$ solution at various current densities. (a) 0.25 mA cm^{-2}; (b) 1 mA cm^{-2}; (c) 2 mA cm^{-2}; (d) 5 mA cm^{-2}; (e) 15 mA cm^{-2}; (f) 20 mA cm^{-2}; (g) 35 mA cm^{-2}; (h) and (i) TEM BF image and SAED pattern of Mn oxide prepared at 1 mA cm^{-2} (natural pH= 7.5, T= 60ºC for 10 min).

5.3.1.2. Effect of concentration of Mn acetate in solution

The influence of solution concentration was also evaluated for electrochemical deposition of Mn oxide. Mn oxide deposits were prepared from Mn acetate–containing solutions, with different concentrations, at 5 $mAcm^{-2}$, natural pH and 60ºC for 10 min. As the concentration of the Mn^{2+} species is varied from 0.003 to 0.05 M, various morphologies are observed. At higher Mn acetate concentrations (≥0.05 M), adhesion to the substrate was poor so morphological analysis could not be done. At a low solution concentration, the electrodeposition rate of MnO_2 ($Mn^{2+} + 2H_2O \rightarrow MnO_2 + 4H^+ + 2e^-$) is low. As shown in Figure 5-2a and 5-2b, discrete oxide clusters are dominant for the lowest Mn acetate concentrations studied (0.003 and 0.005 M). The higher magnification SEM images (inset of image 5-2a and 5-2b) show that the discrete oxide clusters are essentially numerous oxide thin sheets grown vertically on the substrate. At low Mn oxide concentrations, not enough Mn oxide nuclei are generated to form a continuous coating; therefore, discrete oxide clusters are formed. As the concentration is increased from 0.005 to 0.007 M, oriented morphologies (free–standing micron–scale Mn oxide rods with fibrous surfaces) are realized (Figure 5-2c). When a solution with higher concentration (0.01 M Mn acetate) is used, free–standing Mn oxide rods similar to those obtained at the 0.007 M solution concentration are observed; however, the density of rods is higher (Figure 5-2d). As the concentration is increased from 0.01 to 0.02 M, aggregated rods are formed (Figure 5-2e) while continuous morphologies are produced for Mn oxide deposits prepared from a 0.03 M Mn acetate solution (Figure 5-2f). Increasing the solution concentration then has a similar effect on the morphology as an increase in current density, i.e., as the solution concentration increases the morphology changes from thin sheets to rod-like to continuous coatings.

TEM micrographs and an SAED pattern for Mn oxide nanocrystals prepared from a 0.005 M Mn acetate solution at 5 $mAcm^{-2}$ (Figure 5-2b) are shown in Figure 5-

2g and 5-2h. The BF image (Figure 5-2g) reveals fibrous features for the Mn oxide. Also, thin sheets are grown interlaced with one another. It is apparent that, based on the dark field (DF) image (Figure 5-2h) and SAED ring pattern (inset of Figure 5-2h), the Mn oxide deposits consist of discrete oxide clusters with thin sheets within them, and possess a higher crystallization degree when compared with aggregated rods (Figure 5-3e) and continuous coatings (Figure 5-4h), as shown later. Mn oxide, in this case, consists of crystalline grains less than 10 nm in size with an antifluorite–type structure, which is consistent with previous studies [21,25].

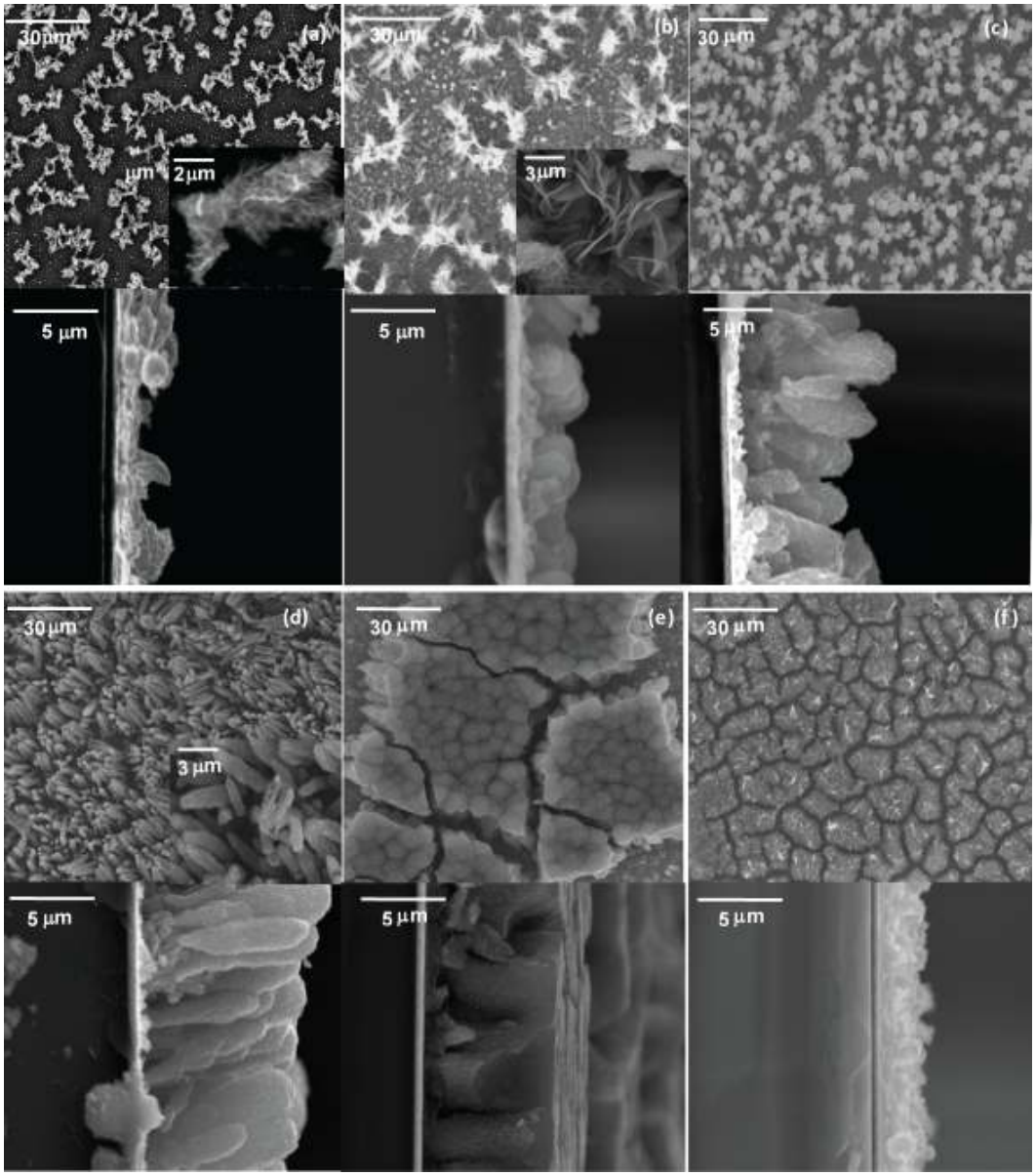
30 μm
(a)
μm
2 μm
30 μm
(b)
3μm
30 μm
(c)
5 μm
5 μm
5 μm
30 μm
(d)
3 μm
30 μm
(e)
30 μm
(f)
5 μm
5 μm
5 μm

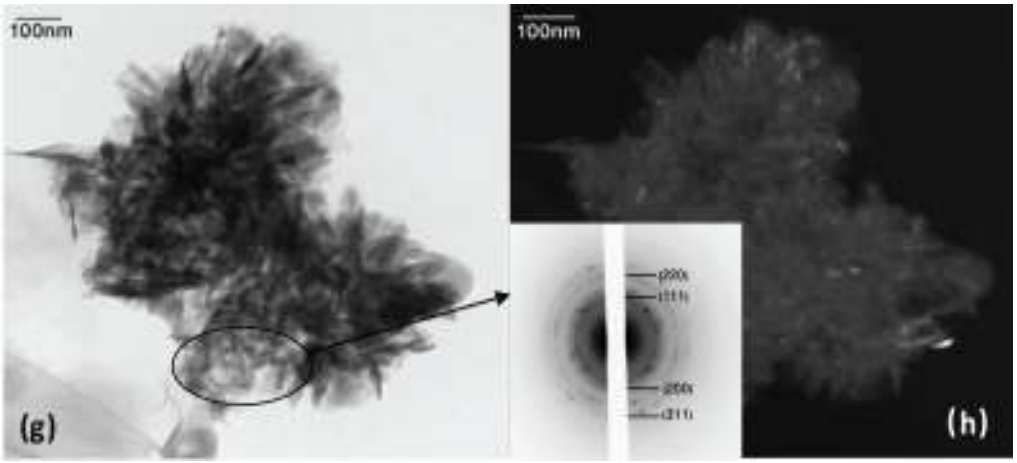

Figure 5-2 SEM SE plan view and cross–sectional images of Mn oxide deposits prepared from (a) 0.003 M $Mn(CH_3COO)_2$ solution at 0.25 mA cm^{-2}; (b) 0.005 M; (c) 0.007 M; (d) 0.01 M; (e) 0.02 M; (f) 0.03 M $Mn(CH_3COO)_2$ solution at 5 mA cm^{-2} for 10 min (T= 60 ºC and pH= 7.5); (g) 0.005 M $Mn(CH_3COO)_2$ – TEM BF image; (h) TEM DF image and SAED pattern from the circled region in (g).

5.3.1.3. Effect of Mn acetate solution temperature

Figure 5-3a–c depicts the morphologies of Mn oxide electrodes prepared from a 0.01 M Mn acetate solution at 5 $mAcm^{-2}$ and natural pH, at room temperature and elevated temperatures. As shown in Figure 5-3a, lower nucleation rates occur at room temperature, so that very few oxide nuclei form on the electrode surface during the initial stages of electrodeposition. As such, a continuous coating is not formed; instead discrete oxide particles are formed. There are numerous microcracks within the oxide coatings prepared at room temperature. As shown previously [21,25], Mn oxide deposits obtained at 60ºC have a well–ordered rod–like structure consisting of rods ~1–3 μm in diameter (Chpater 2, Section 2.3.1) [21,25] (Figure 5-3b), whereas the deposits obtained at the higher temperature of 85ºC (Figure 5-3c) exhibit aggregated rods similar to that obtained at high current densities (20 $mAcm^{-2}$ – Figure 5-1f) and a high acetate concentration (0.02 M – Figure 5-2b) during deposition at 60ºC. High temperatures result in a more fibrous

morphology (inset of Figure 5-3c) while at low temperatures (room temperature) discrete oxide particles become predominant (inset of Figure 5-3a).

Wang et al. [18] have shown that a higher temperature is preferable for the anisotropic growth of crystals and results in a product with higher aspect ratios [18]. Liang et al. [35] have shown that the surface morphology (surface area) is highly affected by electrolyte temperature [35]. As the temperature is increased, the morphology is changed from discrete oxide particles to rod–like to aggregated rods.

TEM micrographs and an SAED pattern for Mn oxide nanocrystals prepared at 85ºC (Figure 5-3c) are shown in Figure 5-3d and 5-3e. The TEM BF image (Figure 5-3d) reveals some fibers with a thickness of several nanometers attached to the surface of the rods. The DF image shown in Figure 5-3e reveals nanocrystalline grains with diameters less than 6 nm. Some larger grains from the Au seed layer are also visible in the DF image. The SAED pattern (inset of Figure 5-3e) reveals that a nanocrystalline antifluorite–type structure is formed.

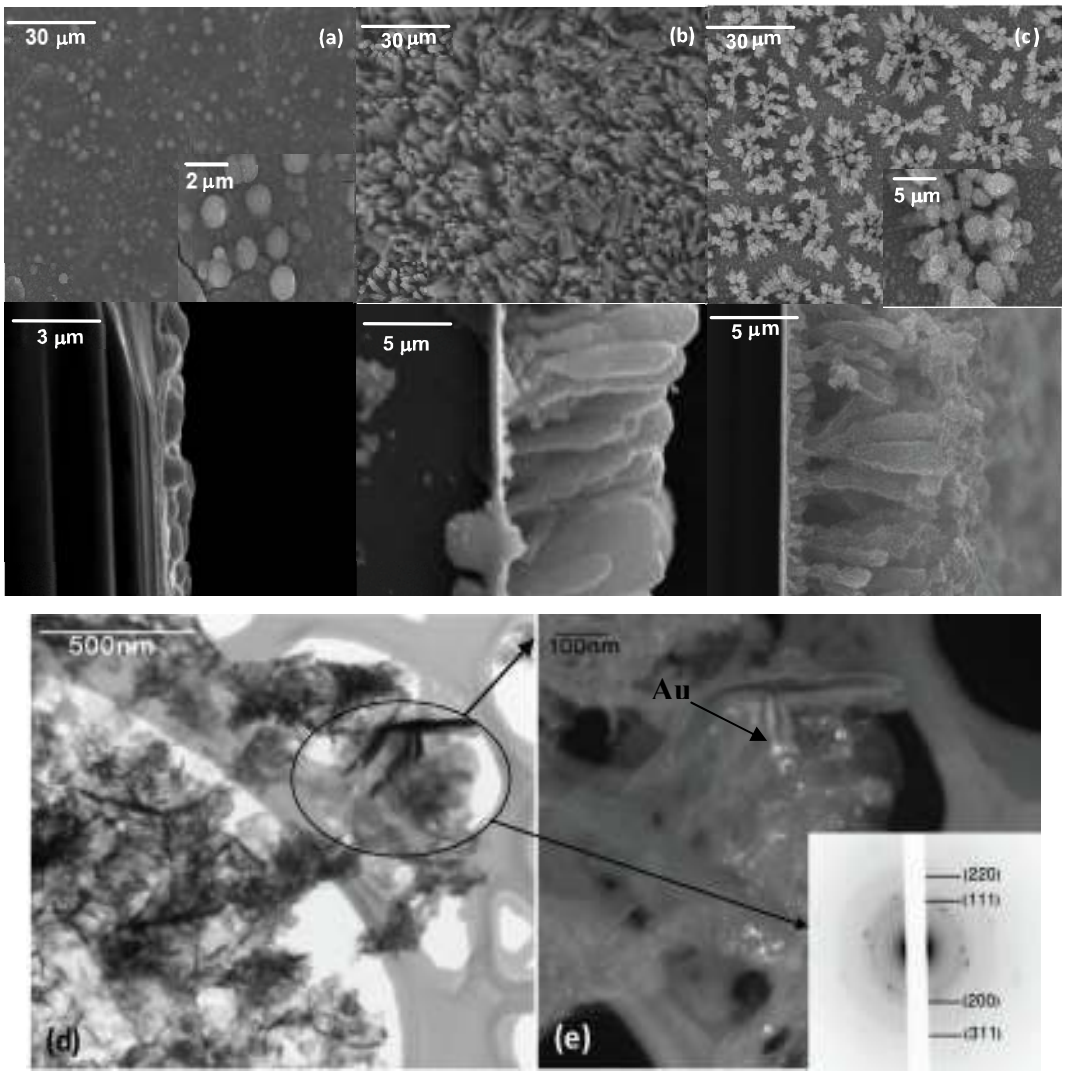

Figure 5-3 SEM SE plan view and cross–sectional images of Mn oxide deposits prepared from a 0.01 M $Mn(CH_3COO)_2$ solution at 5 mA cm^{-2} for 10 min, pH= 7.5, (a) T= 25ºC; (b) T= 60ºC; (c) T= 85ºC; (d) T= 85ºC – TEM BF image; (e) TEM DF image and SAED pattern from the circled region in (d).

5.3.1.4. Effect of Mn acetate solution pH

According to the reaction for the electrodeposition of MnO_2 ($Mn^{2+} + 4OH^- = MnO_2 + 2H_2O + 2e^-$), Mn^{2+} consumes OH^- anions to produce MnO_2. Therefore,

higher pH values are more favorable for the formation of MnO_2, and the effect should be pronounced because of the prefactor of 4 in the above equation. Higher pH values lead to the formation of a large number of nuclei, and the surface coverage improves as pH is increased, so that a continuous coating is expected at high pH values. Figure 5-4 shows SEM images of Mn oxide deposits prepared from a 0.01 M Mn acetate solution at 5 $mAcm^{-2}$ and 60ºC for different electrolyte pH values.

The morphology changes with varying pH can be explained by considering the formation of intermediates of the Mn^{3+} species, such as MnOOH, during the electro–oxidation of Mn^{2+} to MnO_2. The physicochemical stability of MnOOH plays an important role in the morphology of MnO_2 deposits by inhibiting grain growth on the anode/electrolyte interface [36,37]. MnOOH is thermodynamically more stable at higher pH and dissolves in lower pH solutions. The nucleation rate is lower at low pH values (~5–6). As the solution pH increases from 5 to 8.5, various morphologies are observed. At a pH value of 5, oxide protrusions with fibrous features are formed on the surface (Figure 5-4a). Thin sheets are apparent within the oxide protrusions at higher magnification (inset of Figure 5-4a). The density of the oxide protrusions increases as the pH value is increased to 6. Rod–like structures are obtained as the pH value is increased to 7–7.5 (Figure 5-4c and 5-4d), while continuous coatings are obtained when the Mn oxides are deposited in alkaline solutions, e.g., for solutions with pH= 8 and 8.5 as shown in Figure 5-4e and 5-4f, respectively. The higher magnification SEM image (inset of Figure 5-4f) shows that some of the oxide particles are connected together. To summarize, as pH is increased, the morphology is changed from oxide protrusions with fibrous features (thin sheets within the oxides), to rod–like to continuous coatings.

Typical TEM BF and DF micrographs and a corresponding SAED pattern of an as–deposited, continuous Mn oxide coating (Figure 5-4f) are shown in Figure 5-4g and h. The BF image (Figure 5-4g) also reveals fibrous surfaces for the Mn

oxide particles. The DF image (Figure 5-4h) shows that the Mn oxide consists of nanocrystalline grains with diameters less than 6 nm. The diffuse ring pattern (inset of Figure 5-4h) confirms that the Mn oxide coating is nanocrystalline and the *d*–spacings canbe indexed to the antifluorite–type structure. Comparing TEM analysis for Mn oxide deposits with different morphologies, it can be concluded that the deposition parameters do not affect the crystal structure of Mn oxide deposits but the crystallization degree is affected.

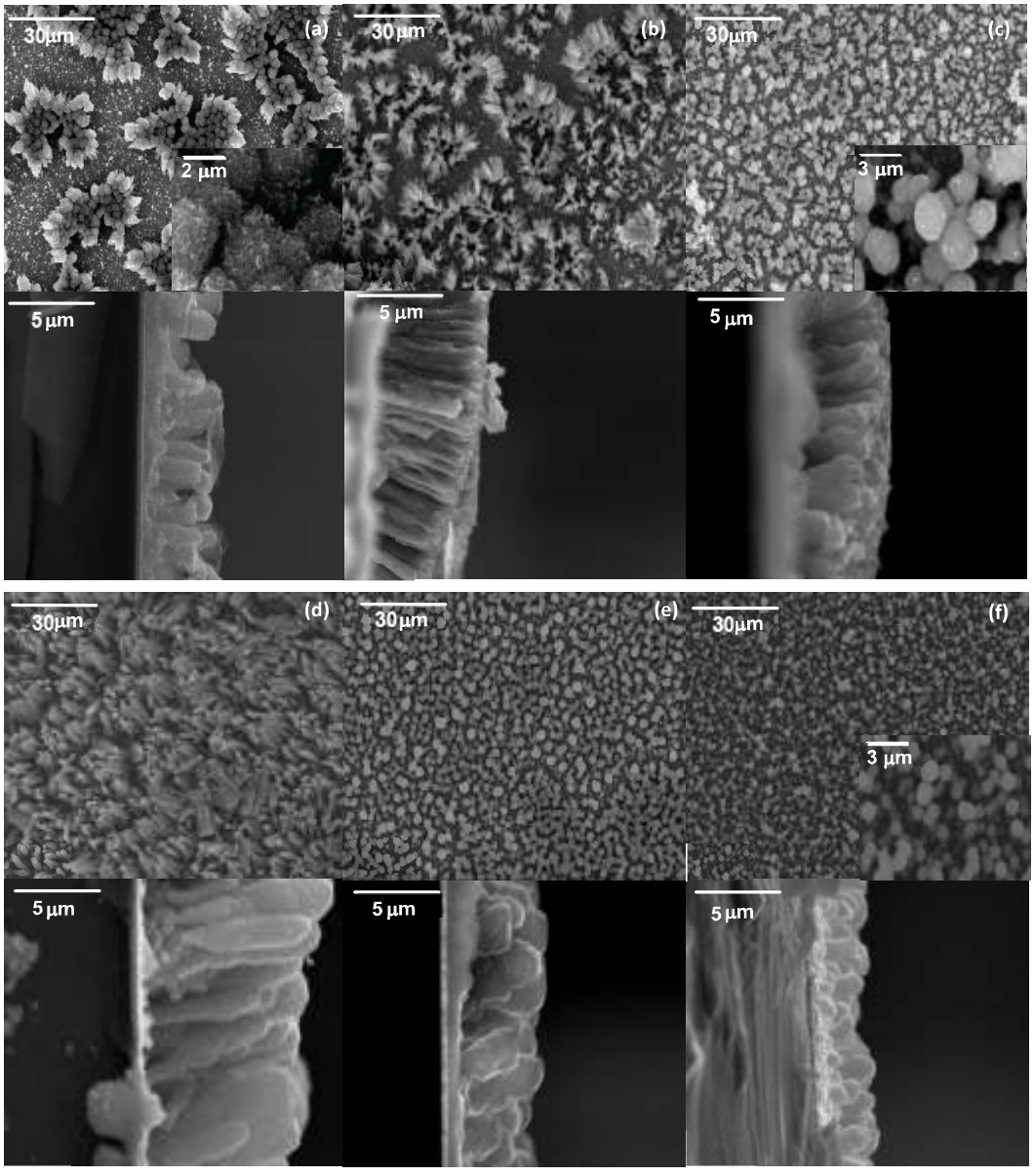

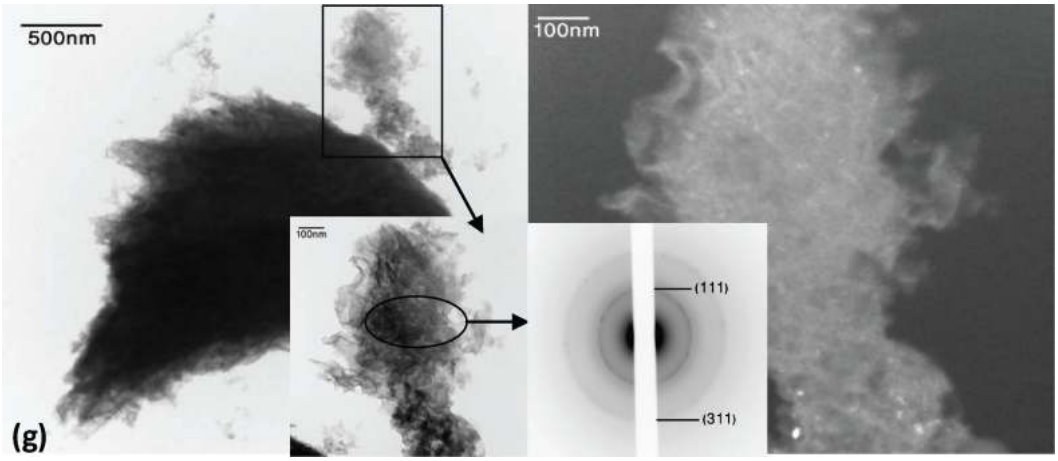

Figure 5-4 SEM SE plan view and cross–sectional images of Mn oxide deposits prepared from a 0.01 M $Mn(CH_3COO)_2$ solution at 5 mA cm^{-2} for 10 min, T= 60ºC, (a) pH= 5; (b) pH= 6; (c) pH= 7; (d) pH= 7.5; (e) pH= 8 ; (f) pH= 8.5; (g) pH= 8.5 - TEM BF image; (h) TEM DF image and SAED pattern from the circled region in (g).

5.3.2. Effect of supersaturation ratio on formation of Mn oxide deposits

The schematic diagram in Figure 5-5 correlates the changes in supersaturation ratio with morphological evolution for Mn oxide deposits during anodic electrodeposition.

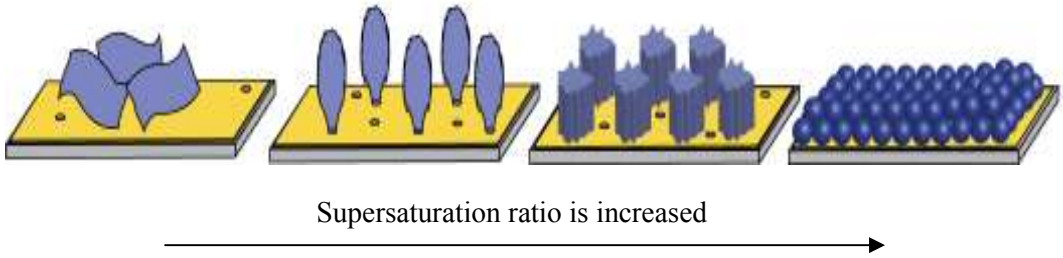

Figure 5-5 Schematic diagram correlating Mn oxide morphology evolution with supersaturation ratio changes. Thin sheets, rods, aggregated rods and non–uniform continuous coatings are formed as the current density, solution concentration, pH and temperature are increased.

Supersaturation ratio for a Mn acetate solution containing Mn^{2+} and OH^- ions for the formation of Mn oxide ($Mn^{2+} + 4\ OH^- = MnO_2 + 2\ H_2O + 2e^-$) can be defined as:

$$S = \frac{\alpha_{Mn^{2+}}\ \alpha^4_{OH^-}}{\alpha_{Mn^{2+},e}\ \alpha^4_{OH^-,e}} \tag{5-3}$$

where α_i and $\alpha_{i,e}$ are the actual and equilibrium activities, respectively, for component i. Under equilibrium conditions, S=1. When S>1, there is a driving force for nucleation and growth. Rastogi et al. [38] have shown that the frequency of nucleation increases with an increase in the supersaturation ratio and rapidly decreases as the supersaturation ratio is lowered below 10^3 [38]. Li et al. [39] have studied the influence of supersaturation ratio on the morphology of $BaSO_4$ crystals. Various morphologies from rod–like to snow–like (similar to aggregated rods in this work) to almost sphere–like (similar to the continuous coatings in this work) were produced by controlling supersaturation ratio. The supersaturation ratios were ~$2.3x10^3$, $5.8x10^4$ and $2.3x10^7$ for rod–like, snow–like and sphere–like morphologies, respectively [39].

As the various deposition parameters, including current density, solution concentration, pH and temperature, are increased, the supersaturation ratio increases. The relationship between the activities of ions in solution and overpotential (current density) is given by the Nernst equation:

$$E = E_0 - \frac{RT}{ZF} \ln \frac{\alpha_{MnO_2} \alpha_{H_2O}^2}{\alpha_{Mn^{2+}} \alpha_{OH^-}^4} \tag{5-4}$$

$$\eta = E - E_0 \tag{5-5}$$

where η, Z, F, R, T, E_0 and E are the overpotential, the number of moles of electrons transferred in the cell reaction, Faraday's constant, the gas constant, temperature, the standard cell potential (0.519 V vs. SCE at 298 K) and cell potential, respectively.

As the current density is increased, the cell potential increases which causes an increase in the overpotential value. Therefore, ($\alpha_{Mn2+}.\alpha_{OH-}$) is increased, while the equilibrium activities remain constant, leading to an increase in the supersaturation ratio. Activities are directly proportional to the ion concentrations, so any increase in Mn^{2+} or OH^- concentration will cause an increase in S. For OH^- concentrations (or pH), the effect should be more pronounced because of the exponent of 4. OH^- activity increases with increasing pH according to:

$$pH = 14 + \log \alpha_{OH^-} \tag{5-6}$$

In determining the effect of temperature on supersaturation ratio, it should be noted that the equilibrium activities are affected by changing the temperature. The

reaction for formation of MnO_2 is endothermic ($\Delta H° = 49.2$ kJ/mol at 298 K). According to the Van't Hoff equation

$$\frac{d \ln K}{d(\frac{1}{T})} = -\frac{\Delta H^0}{R} \tag{5-7}$$

when the reaction is endothermic (ΔH^0 is positive), the equilibrium constant (K) increases with increasing temperature. This causes a reduction in ($\alpha_{Mn2+,e}.\alpha_{OH-,e}$). Therefore, as the temperature is increased, the supersaturation ratio increases.

The relationship between the deposition rate and supersaturation ratio is shown in Equation (5-8) [40].

$$V = kNS^n \tag{5-8}$$

where V is the deposition rate, k is the kinetic constant for a given temperature (Arrhenius-type dependence), N is proportional to the number of active sites on the surface, S is the supersaturation ratio and n is the effective order of the reaction [40]. Based on the above equation, as supersaturation ratio increases, the deposition rate is increased. The supersaturation ratio values, for deposits obtained at different current densities at 60ºC in this work, are calculated from Equations (2) and (3) as ~153 (1 $mAcm^{-2}$), $2.1x10^3$ (5 $mAcm^{-2}$), $8.1x10^5$ (15 $mAcm^{-2}$) and $1.3x10^7$ (30 $mAcm^{-2}$) for thin sheets, rods, aggregated rods and continuous coatings, respectively. The approximate deposition rates ($V = \Delta m/\Delta t$) are $2.5x10^{-4}$, $3.3x10^{-4}$, $3.6x10^{-4}$ and $4.2x10^{-4}$ $mgcm^{-2}s^{-1}$ for thin sheets, rods, aggregated rods and continuous coatings, respectively.

The natural logarithm of the deposition rate versus natural logarithm of the supersaturation ratio for deposits prepared at 60ºC is plotted in Figure 5-6. There

is an approximately linear relationship and the value for *n*, determined from the slope of the line, is quite small (~0.04). According to Combes et al. [40], the value of *n* should be ≥1. Values of n equal to 1 and 2 are attributed to bulk diffusion controlled processes and spiral growth mechanisms, respectively. A value of *n* in excess of 2 corresponds to surface polynucleation. The small value for n is related to the assumption above that k and N are constant. The latter is a reasonable assumption, but k likely changes significantly as S is varied, since the current efficiency (η_k) varies markedly as the current density changes from 1 to 30 $mAcm^{-2}$. In fact, η_k is ~90% at 1 $mAcm^{-2}$ and only 50% at 30 $mAcm^{-2}$.

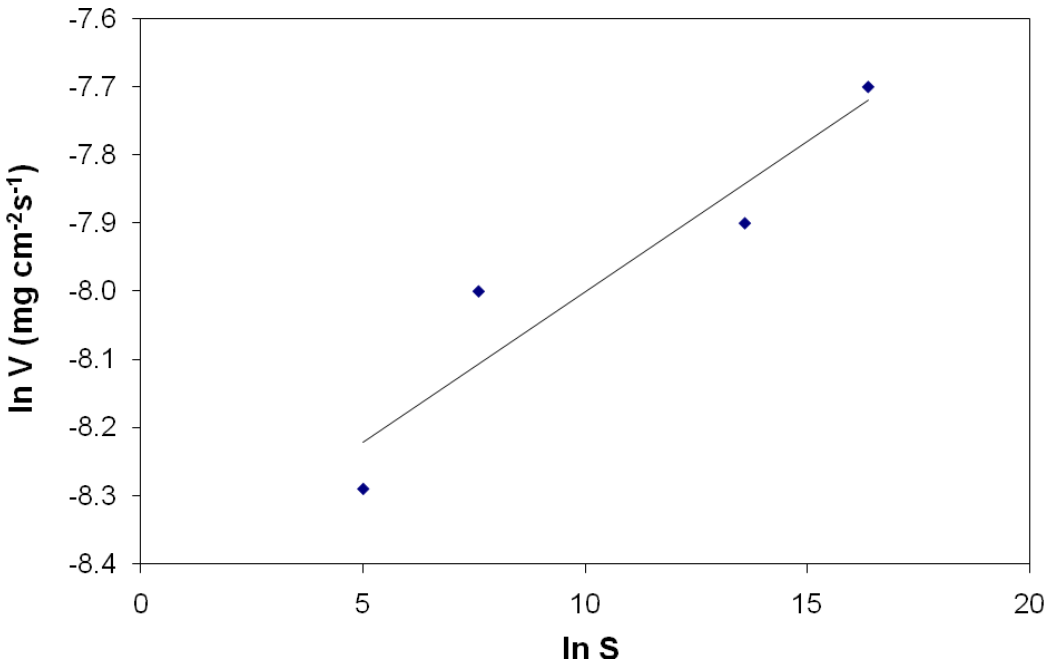

Figure 5-6 Deposition rate versus supersaturation ratio for deposits prepared at different current densities at 60ºC.

5.3.3. Nucleation and growth mechanisms for Mn oxide deposits

There are two main nucleation mechanisms, instantaneous and progressive. Instantaneous nucleation favors the growth of existing nuclei instead of the formation of new ones, achieving better crystalline quality relative to that for progressive nucleation [41]. Therefore, the single crystalline growth of thin sheets (Figure 5-1h and 5-1i) at low supersaturation ratios and low deposition rates would be expected to follow an instantaneous nucleation mechanism with a constant number of nuclei. Figure 5-7a shows the morphology of Mn oxide thin sheets prepared from a 0.01 M Mn acetate solution at 1 $mAcm^{-2}$ (natural pH and T= 60ºC) for deposition times of 1 to 10 min. The plan view SEM images show that the number of nuclei are constant for different deposition times and confirm that Mn oxide thin sheets form by instantaneous nucleation.

Hwang *et al.* [42] have shown that progressive nucleation occurs on a larger number of active sites relative to instantaneous nucleation, resulting in the growth of compact grains. The nuclei not only form on substrate surface positions but also on previously formed nuclei [42].

The formation process for Mn oxide rods prepared from a 0.01 M Mn acetate solution at 5 $mAcm^{-2}$ (natural pH and T= 60ºC) for different deposition times is shown in Figure 5-7b. The number of nuclei on the surface for different deposition times is constant. Therefore, Mn oxide rods show instantaneous nucleation initially. However, TEM analysis for aggregated rods (Figure 5-3e), and rods reported in Chapters 2, Section 2.3.1 and Chapter 3, Section 3.3.3 [21,25] show that the rods are polycrystalline so that further formation is through progressive nucleation. Therefore, initial instantaneous nucleation is followed by progressive nucleation to form polycrystalline rods. For continuous Mn oxide deposits, the number of nuclei increases with deposition time from 1 to 10 min, which confirms the progressive nucleation mechanism for continuous coatings (Figure 5-7c).

The formation mechanisms for Mn oxide deposits can also be rationalized by considering the effect of supersaturation ratio. Schematic diagrams for the different morphologies are shown in Figure 5-8a−c. Thin sheets show instantaneous nucleation and single crystalline growth (Figure 5-8a) and are formed at very low supersaturation ratios. At low deposition current densities or solution concentrations, the very small supersaturation ratio provides only a few nucleation sites and the formation of only a few critical nuclei. Surface diffusion of ad–ions on the substrate allows for the growth of single crystal Mn oxide films. In fact, at very low supersaturation ratio, growth by surface diffusion is dominant [43]. This kind of growth mode leads to the formation of anisotropic crystals [44]. Thin sheets have high 2D anisotropy with thicknesses on the nanoscale and lateral dimensions on the microscale, as growth of the sheets is more favorable in the lateral direction compared with the thickness direction [45]. One reason for 2D growth is that low current densities and low reactant concentrations cause the reactions to proceed slowly. Thus, the initial nuclei have sufficient time to accommodate diffusion ad-ions and grow in the lateral directions, resulting in the formation of thin sheets [46]. Each thin sheet is a single crystal of Mn oxide with an antifluorite–type structure as shown in Figure 5-1i. The lateral growth of Mn oxide does not occur on all faces but only on faces where the energy of incorporation of an ad–atom at the surface of the face is the lowest. Wang et al. [47] have shown that for FCC structures, the relative surface energies for crystallographic planes is: $\gamma(111) < \gamma(100) < \gamma(110)$ [47]. This is confirmed in Figure 5-1i, where the thin sheets are shown to have a {111}-type orientation.

Nucleation for the rod-like structures is unlikely to be instantaneous alone, otherwise the rods would be expected to be single crystalline. Instead, a mix of instantaneous and progressive nucleation is proposed. Initial nuclei form instantaneously, but during rod formation additional nuclei, shown as small circles in Figure 5-8b, form on the surface of growing rods. The number of nuclei on the surface is constant for different deposition times (Figure 5-7b), which is characteristic of instantaneous nucleation. The growing rods are then preferential

sites for the new nuclei as the electric field is higher locally, leading to progressive nucleation. This results in a preferential formation in the electric field direction, perpendicular to the substrate surface for polycrystalline Mn oxide rods. The atomic arrangement rate along the electric field direction is high, resulting in preferential growth perpendicular to the substrate and the formation of a rod–like structure since the growth rate of one direction is faster than that of the others [44].

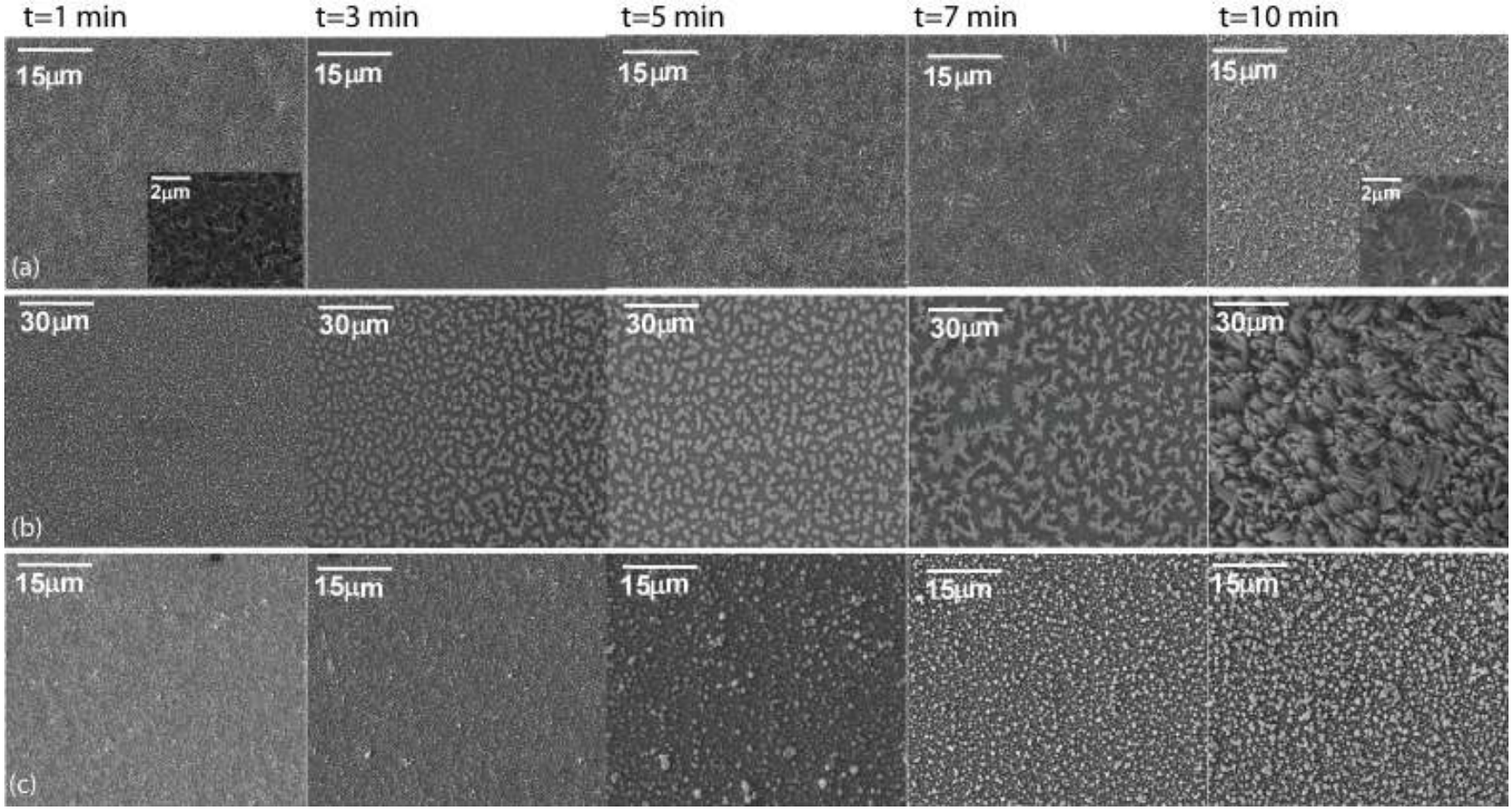

Figure 5-7 SEM plan view images of Mn oxide deposits prepared from a 0.01 M $Mn(CH_3COO)_2$ solution at (a) 1 $mAcm^{-2}$; (b) 5 $mAcm^{-2}$; (c) 35 $mAcm^{-2}$ - T= 60ºC, pH= 7.5 and depositions were done for 1, 3, 5, 7 and 10 min.

As the supersaturation ratio is increased further, the nucleation rate is increased accordingly. The deposition rate increases, so that atoms do not have enough time to arrange on the lowest energy sites. As a result, the growth rate in all directions is almost the same, leading to a more continuous coating. Figure 5-8c shows schematic diagrams for nucleation and growth of continuous coatings. Mn oxide continuous coatings are polycrystalline in nature (Figure 5-4h) and form through progressive nucleation.

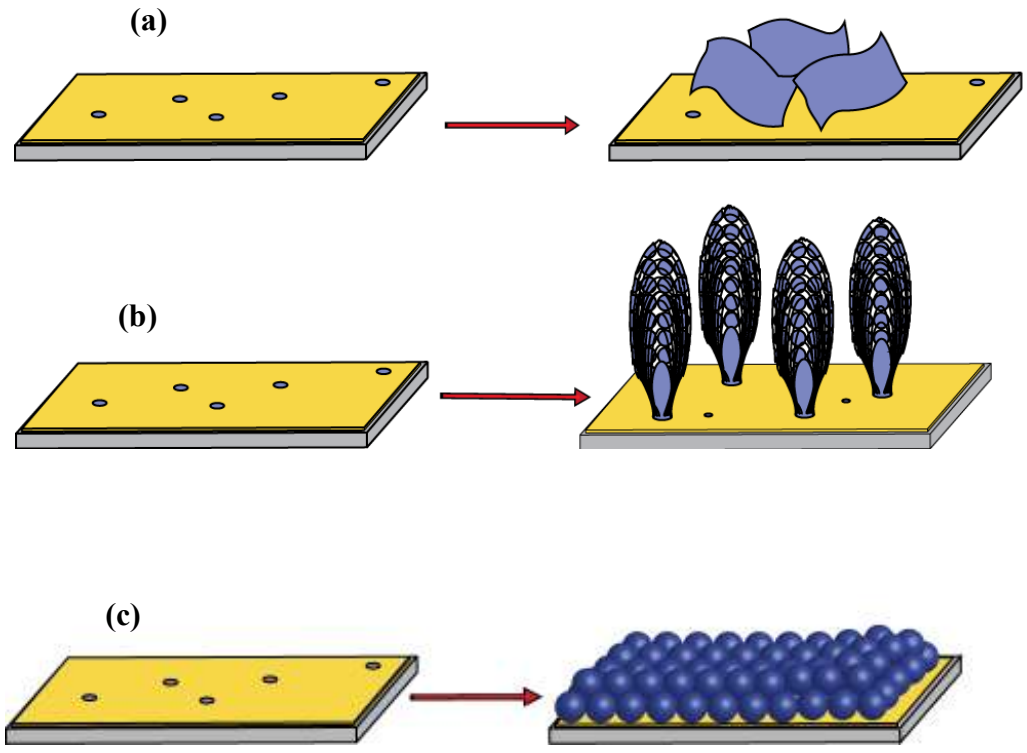

Figure 5-8 Schematic diagrams showing nucleation and growth mechanisms for Mn oxide. a) Thin sheet formation (instantaneous nucleation and single crystalline growth); b) rod formation (a mix of instantaneous/progressive nucleation and polycrystalline growth); c) continuous coating formation (progressive nucleation and polycrystalline growth).

5.3.4. Electrochemical properties of Mn oxide deposits

The capacitive behavior of electrode materials is generally characterized by means of cyclic voltammetry. Figure 5-9 shows CV curves, after 2 cycles in 0.5 M Na_2SO_4, for Mn oxide deposits obtained for one of the deposition parameters discussed above (electrolyte concentration). The CV profiles of as–prepared Mn oxide deposits taken at a scan rate of 20 mVs^{-1} show a nearly rectangular shape, indicating good pseudocapacitive behavior attributed to a continuous and reversible Faradaic redox transition of Mn oxide over the potential range. Comparison of the CV curves shown in Figure 5-9 reveals that the enclosed areas for deposits with different morphologies are different, indicating a different charge–storage capability for the oxide films deposited.

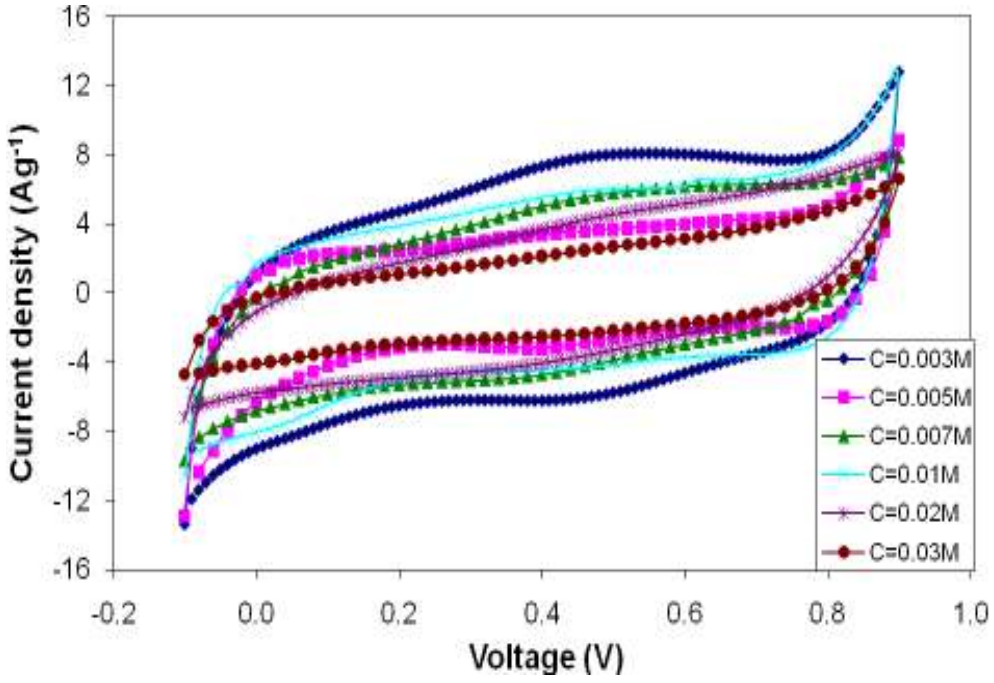

Figure 5-9 Representative cyclic voltammogram taken from Mn oxide deposits prepared from a Mn acetate–containing solution at i= 5 mA cm^{-2}, pH= 7.5, T= 60ºC and t= 10 min (cycled in 0.5 M Na_2SO_4 for 2 cycles at 20 mVs^{-1}).

Specific capacitance values, as a function of cycling, of Mn oxide deposits prepared under different deposition conditions are tabulated in Tables I–IV. The capacitance retention rates for Mn oxide with thin sheet and rod–like morphologies are higher than those observed for continuous Mn oxide deposits. It is apparent that Mn oxides, with a thin sheet morphology, exhibit the highest capacity and rate capability, followed by rod–like structures and then continuous coatings.

As described in Chapter 2, electrode materials with ordered and high surface area structures have enhanced electrochemical characteristics. Large specific surface areas promote efficient contact between the active material and the electrolyte, providing more electrochemically accessible sites for electrochemical reactions relative to continuous coatings. In addition to supplying more accessible space for ions, electrodes with high porosity and large surface area maintain sufficient electronic conductivity for solid–state electron transfer. Therefore, Mn oxide with thin sheet and rod–like structures can provide short diffusion path lengths to both ions and electrons and also sufficient porosity for electrolyte penetration giving rise to high charge–discharge rates. Mn oxide thin sheets provide higher capacitance values and better capacitance retention rates relative to Mn oxide rods. Higher capacitance values may be attributed to lower thicknesses for the thin sheets compared to rods. Electrolyte ion transport is improved and solid–state diffusion distances for ions into the oxides are reduced, which enhance cation intercalation/deintercalation reactions compared to Mn oxide rods leading to higher specific capacitance values. The loss in capacitance with electrochemical cycling can be attributed to several factors, such as increased manganese ion dissolution and morphological/structural changes [21]. TEM analysis of cycled manganese oxide thin sheets (not shown here) revealed that the crystal structure did not change, i.e., the antifluorite-type structure was maintained. The *d*-spacings were essentially the same (≤2% difference on cycling), so that cycling did not appreciably affect the deposit crystal structure. However, as shown in (Chapter 2, Section 2.3.1) [21], MnO_2 rods transformed to a more ordered hexagonal NiAs-

type crystal structure after cycling. As such, fewer electrochemically active sites were available for fast ionic transport and charge transfer resulting. Therefore, structural changes can be considered as one of the factors for capacitance fading.

As described in [48], some Mn dissolution as Mn^{2+} cations in the electrolyte is expected during cycling, based on the Mn–H_2O Pourbaix diagram. In addition, during forward cycling, some of the dissolved Mn^{2+} cations will be re-oxidized to MnO_2 and re-deposited on the electrode surface resulting in a morphology change for Mn oxide rods. This is another factor for capacitance reduction during cycling for Mn oxide rods. However, the morphology of manganese oxide thin sheets (not shown here) did not change much relative to the as-deposited sample.

It has been shown that the capacity fading is characteristic of progressive dissolution of electroactive material in the electrolyte during long term cycling [48,49]. Therefore, capacitance fading is mainly attributed to the loss of unstable Mn ions by dissolution in the electrolyte solution. The amount of dissolution, as determined through AAS measurements, was lower for Mn oxide thin sheets compared with rod-like structures. For Mn oxide rods, solution Mn levels of 0.17 and 0.25 ppm [25] were found after 2 and 250 cycles, respectively (Chpater 3, Section 3.3.2); for thin sheets, solution Mn levels were 0.15 and 0.17 ppm, respectively. Therefore, the Mn dissolution rate for rod-like structures is higher relative to thin sheets, which results in more capacitance reduction on cycling for rods relative to thin sheets.

Continuous coatings provide the lowest specific surface area relative to rods and thin sheets. Electron transfer through the denser continuous Mn oxide coatings is slower relative to rods and thin sheets. Also, ion diffusion transport of electrolytic species into the electrode material is more difficult for continuous coatings relative to rods and thin sheets due to lower specific surface areas. As such, continuous coatings have the lowest capacitance values. Also, the poor capacitance retention of continuous coatings is due to significantly higher Mn

oxide dissolution rates relative to thin sheets and rods. For Mn oxide continuous coatings, solution Mn levels of 0.61 and 0.85 ppm were found after 2 and 250 cycles, respectively. The type of morphology can affect Mn dissolution during cycling. This is likely due to the trapping of soluble Mn ions within the electrode structure for rods and thin sheets, which enhances redeposition of Mn oxide on the electrode during forward cycling. Therefore, a large amount of active material is still available after cycling which results in improved electrochemical cyclability [50].

Table 5-1 Specific capacitance values for Mn oxide deposits prepared at different current densities (cycled in 0.5 M Na_2SO_4 at 20 mVs^{-1}).

Deposition current density ($mA\ cm^{-2}$)	Specific capacitance after 2nd cycle (Fg^{-1})	Specific capacitance after 250 cycles (Fg^{-1})	Specific capacitance decrease after 250 cycles (%)	Deposit morphology
0.25	192	157	18	Thin sheets
1	230	202	12	Thin sheets
2	205	160	22	Thin sheets & rods
5	185	139	25	Rods
15	155	117	24	Rods
30	120	94	22	Aggregated rods
35	110	75	32	Continuous coatings

Table 5-2 Specific capacitance values for Mn oxide deposits prepared at different solution concentrations (cycled in 0.5 M Na_2SO_4 at 20 mVs^{-1}).

Solution concentration (M)	Specific capacitance after 2nd cycle (Fg^{-1})	Specific capacitance after 250 cycles (Fg^{-1})	Specific capacitance decrease after 250 cycles (%)	Deposit morphology
0.003	200	170	15	Thin sheets
0.005	164	135	18	Thin sheets & rods
0.007	180	140	22	Rods
0.01	185	139	25	Rods
0.02	155	112	28	Aggregated rods
0.03	145	85	41	Continuous coatings

Table 5-3 Specific capacitance values for Mn oxide deposits prepared at different solution pH values (cycled in 0.5 M Na_2SO_4 at 20 mVs^{-1}).

Solution pH	Specific capacitance after 2nd cycle (Fg^{-1})	Specific capacitance after 250 cycles (Fg^{-1})	Specific capacitance decrease after 250 cycles (%)	Deposit morphology
5	170	138	19	Oxide protrusions & thin sheets within them
6	175	143	18	Oxide protrusions & thin sheets within them
7	178	132	25	Rods
7.5	185	139	25	Rods
8	165	120	27	Continuous coatings
8.5	160	115	28	Continuous coatings

Table 5-4 Specific capacitance values for Mn oxide deposits prepared at different solution temperatures (cycled in 0.5 M Na_2SO_4 at 20 mVs^{-1}).

Solution temperature (ºC)	Specific capacitance after 2nd cycle (Fg^{-1})	Specific capacitance after 250 cycles (Fg^{-1})	Specific capacitance decrease after 250 cycles (%)	Deposit morphology
25	123	75	39	Small oxide particles
60	185	139	25	Rods
85	147	115	22	Aggregated rods

To further understand the capacitance behavior of Mn oxide electrodes prepared under different deposition conditions, EIS was applied to evaluate Mn oxide deposits after 250 cycles at 20 mVs^{-1}, by sweeping the frequency from 100 kHz to 10 mHz with a DC bias of 0.2 V. Mn oxide deposits with thin sheet and rod–like structures were prepared from 0.01 M Mn acetate solution at 1and 5 $mAcm^{-2}$, respectively and continuous coatings were prepared from 0.03 M Mn acetate solution at 5 $mAcm^{-2}$ (natural pH, T= 60ºC for 10 min). The corresponding impedance spectra of Mn oxide electrodes with different morphologies are compared in Figure 5-10. Each impedance spectrum can be divided into three regions corresponding to three processes. At very high frequencies (>10 kHz) small arcs are present, which account for the double layer (dl) processes. The small semi-circles present at high frequencies (>50 Hz) are related to charge transfer processes [16]. Approximately straight lines with various slopes are present in the impedance plots within the low frequency range. These linear parts are typical of the capacitive response of porous electrode materials, which is related to the electrolyte diffusion process and cation intercalation–deintercalation processes [1]. Normally, a higher slope for the impedance line means a lower diffusive resistance for the electrolyte in the electrode. For better comparison, AC

frequencies are shown on the Nyquist plots. At frequencies higher than ~10 kHz, the three plots show comparable electronic resistances (inset of Figure 5-10). For frequencies ranging from ~200 Hz down to ~7.8 Hz, continuous coatings show a higher charge transfer resistance relative to thin sheets and rod–like deposits, as its plot shifts more along the real axis to higher resistances. The experimental impedance data was fit to an equivalent circuit using Zview, based on previous work [48]. The corresponding charge transfer resistances for the thin sheets and rods were ~0.5 and 0.58 Ωcm^2, respectively. However, the resistance value for continuous coatings was ~1.5 Ωcm^2. The higher charge transfer resistance for the continuous coating is attributed to slow electron transport through the electrode. Rod–like morphologies and thin sheets have lower charge transfer resistances due to short path lengths for electron transport. For frequencies from 7.8 Hz down to 0.1 Hz, thin sheets show the lowest diffusive resistance (1.65 Ωcm^2) followed by rod–like structures (1.80 Ωcm^2) and then continuous coatings (2.70 Ωcm^2). Porous electrodes may facilitate electrolyte transport and cation intercalation/deintercalation in thin sheets and rods relative to continuous coatings, which is supported by the reduced resistance values and improved capacitor responses. Also, the lower thickness dimension provides shorter diffusion paths for cation intercalation/deintercalation for thin sheets relative to rods.

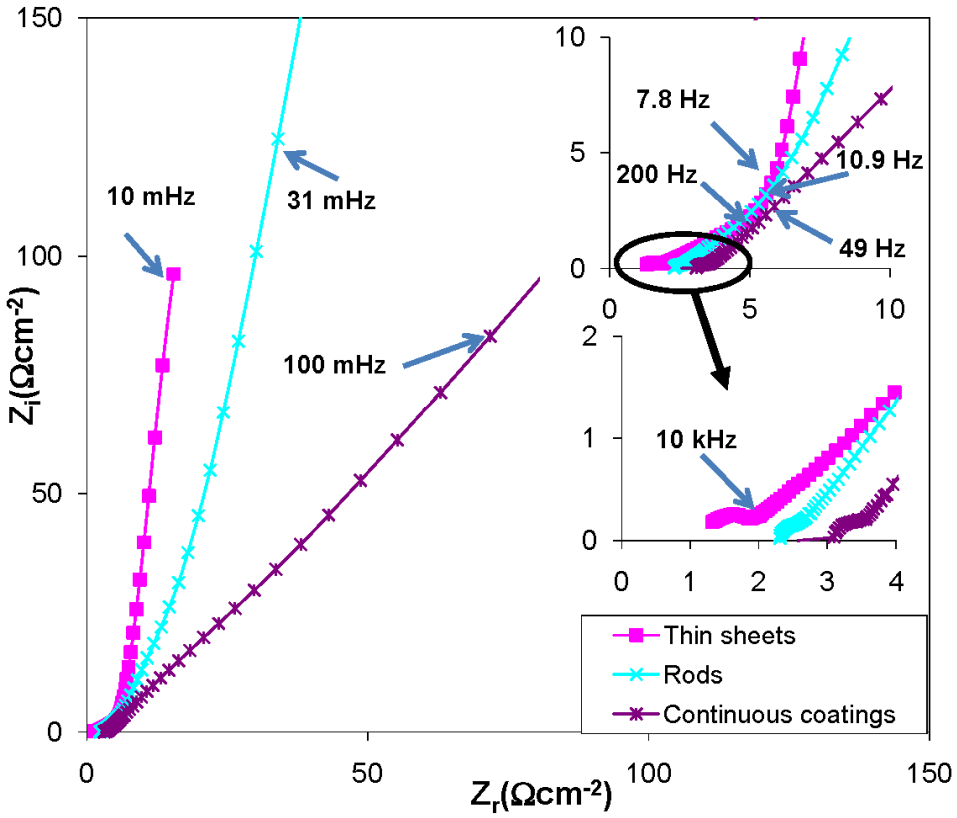

Figure 5-10 Nyquist plots for Mn oxide deposits with different morphologies cycled at 20 mVs^{-1} (0.5 M Na_2SO_4 solution at 0.2 V vs. SCE) after 250 cycles.

5.4 Conclusions

Morphology–controlled growth of Mn oxide nanostructures prepared from acetate–containing aqueous solutions was investigated. A variety of nanostructured Mn oxide electrodes, all with an antifluorite–type crystal structure and including continuous coatings, rod–like structures, aggregated rods and thin sheets, were obtained by changing the supersaturation ratio which affects the nucleation and growth processes. The crystal structure of Mn oxide is not affected by the supersaturation ratio, but crystallization degree is affected. The investigation of nucleation and growth mechanisms for Mn oxide deposits with

different morphologies reveals that thin sheets form by instantaneous nucleation and single crystal growth, continuous coatings show progressive nucleation and polycrystalline growth and rods have a mix of instantaneous/progressive nucleation and polycrystalline growth.

Electrochemical analysis of Mn oxide electrodes revealed that oriented structures such as Mn oxide rods and thin sheets exhibit superior capacitive behaviour relative to continuous coatings. Also, thin sheets with lower thicknesses relative to rods had the highest specific capacitance (~230 Fg^{-1}) and capacitance retention (~88% after 250 cycles) in 0.5 M Na_2SO_4 at 20 mVs^{-1}. Electrochemical impedance spectroscopy showed a lower double layer process resistance and charge transfer resistance for thin sheets and rod–like structures compared with continuous coatings. Also, Nyquist diagrams confirmed that Mn oxide thin sheets had the lowest diffusive resistance followed by rods and then continuous coatings.

References

[1] B.E. Conway, Electrochemical Supercapacitors, Kluwer Academic/Plenum Press, New York (1999).

[2] R. Liu and S. Lee, *J. Am. Chem. Soc.*, **130**, 2942 (2008).

[3] M.S. Wu, Y.H. Ou and Y.P. Lin, *Electrochim. Acta*, **55**, 3240 (2010).

[4] R. Xiao, S.I. Cho and R. Liu, *J. Am. Chem. Soc.*, **129**, 4483 (2007).

[5] H. Zheng, F. Tang, M. Lim and A. Mukherji, *J. Power Sources*, **195**, 680 (2010).

[6] D. Belanger, T. Brousse and J.W. Long, *Electrochem. Soc. Interf.*, **17 (1)**, 49 (2008).

[7] K. Naoi and P. Simon, *Electrochem. Soc. Interf.*, **17 (1)**, 34 (2008).

[8] C.C. Hu, K.H. Chang, M.C. Lin and Y.T. Wu, *Nano Lett.*, **6**, 2690 (2006).

[9] R.K. Sharma, A.C. Rastogi and S.B. Desu, *Electrochim. Acta*, **53**, 7690 (2008).

[10] W. Sugimoto, H. Iwata and Y. Yasunaga, *Angew. Chem. Int. Ed.*, **42**, 4092 (2003).

[11] Y.H. Lee, K.H. An, W.S. Kim and Y.S. Park, *Adv. Mater.*, **13**, 497 (2001).

[12] S.C. Pang and M.A. Anderson, *J. Mater. Res.*, **15**, 2096 (2000).

[13] M. Nakayama, T. Kanaya and R. Inoue, *Electrochem. Commun.*, **9**, 1154 (2007).

[14] S.E. Chun, S.I. Pyun and G.J. Lee, *Electrochim. Acta*, **51**, 6479 (2006).

[15] M. Toupin, T. Brousse and D. Belanger, *Chem. Mater.*, **16**, 3184 (2004).

[16] C.C. Hu and C.C. Wang, *J. Electrochem. Soc.*, **150**, A1079 (2003).

[17] M.S. Wu and P.J. Chiang, *Electrochem. Commun.*, **8**, 383 (2006).

[18] X. Wang and Y. Li, *J. Chem. Eur.*, **9**, 300 (2003).

[19] P.A. Nelson, J.M. Elliott, G.S. Attard and J.R. Owen, *Chem. Mater.*, **14**, 524 (2002).

[20] W.J. Zhou, D.D. Zhao and M.W. Xu, *Electrochimica Acta*, **53**, 7210 (2008).

[21] B. Babakhani and D.G. Ivey, *J. Power Sources*, **195**, 2110 (2010).

[22] H. Xia, J.K. Feng, H.L. Wang, M.O. Lai and L. Lu, *J. Power Sources*, **195**, 4410 (2010).

[23] W. Wei, X.W. Cui, W.X. Chen and D.G. Ivey, *Electrochim. Acta*, **54**, 2271 (2009).

[24] W. Wei, X. Cui, W. Chen and D.G. Ivey, *J. Power Sources*, **186**, 543 (2009).

[25] B. Babakhani and D.G. Ivey, *Electrochim. Acta*, **55**, 4014 (2010).

[26] A.S. Pilla, M.M. Duarte and C.E. Mayer, *J. Electroanal. Chem.*, **569**, 7 (2004).

[27] W.H. Kao and V.J. Weibel, *J. Appl. Electrochem.*, **22**, 21 (1992).

[28] S. Nijjer, J. Thonstad and G.M. Haarberg, *Electrochim. Acta*, **46**, 395 (2000).

[29] M. Gu, *Electrochim. Acta*, **52**, 4443 (2007).

[30] M.S. Wu and R.H. Lee, *J. Electrochem. Soc.*, **156(9)**, A737 (2009).

[31] W. Wei, X.W. Cui, W.X. Chen and D.G. Ivey, *Electrochim. Acta*, **56**, 1619 (2011).

[32] K.S. Rangappa, S. Chandraju and N.M. Madegowda, *Int. J. Chem. Kinet.*, **30**, 7 (1998).

[33] G. She, L. Mu and W. Shi, *Recent Patent on Nanotech.*, **3**, 182 (2009).

[34] J.X. Kang, W.Z. Zhao and G.F. Zhang, Surf. Coat. Tech. 203 (2009) 1815.

[35] C.H. Liang and C.S. Hwang, J. Appl. Phys. 47 (6) (2008) 4682.

[36] Z. Rogulski, H. Siwek and I. Paleska, J. Electroanal. Chem. 543 (2003) 175.

[37] S. Nijjer, J. Thonstad, and D. M. Haarberg, Electrochim. Acta 46 (2000) 395.

[38] A.C. Rastogi and K.S. Balakrishnan, J. Electrochem. Soc. 136 (1989) 1502.

[39] S. Li, J. Xu and G. Luo, J. Cryst. Growth 304 (2007) 219.

[40] C. Combes, M. Freche and C. Rey, J. Mat. Sci. 10 (1999) 231.

[41] H. Gomez, G. Riveros and D. Ramirez, J. Solid State Electrochem. (2011).

[42] B.J. Hwang, R. Santhanam and Y.L. Lin, J. Electrochem. Soc. 147 (2000) 2252.

[43] A.C. Rastogi and K.S. Balakrishnan, Sol. Energy Mater. Sol. Cells 36 (1995) 121.

[44] D. Chu, Y. Masuda and T. Ohji, Langmuir 26(18) (2010) 14814.

[45] T. Shibata, K. Fukuda, Y. Ebina and T. Kogure, Adv. Mater. 20 (2008) 231.

[46] S. Yue, J. Lu and J. Zhang, Mater. Lett. 63 (2009) 2149.

[47] S.G. Wang, E.K. Tian and C.W. Lung, J. Phys. Chem. Solids 61 (2000) 1295.

[48] B. Babakhani and D.G. Ivey, Electrochimica Acta 56 (2011) 4753.

[49] Y.K. Zhou, M. Toupin, D. Belanger and F. Favier, J. Phys. Chem. Solids 67 (2006) 1351.

[50] K. Kinoshita and J.T. Lundquist, Electroanal. Chem. Interf. Electrochem., 48 (1973) 157.

Chapter 6 Mn-Fe and Mn-V doped oxide electrodes

6.1 Introduction

Over the past decades, Mn based oxides have received considerable attention because of their promising properties, such as satisfactory electrochemical performance, environmental compatibility, natural abundance and low cost, for application as electrodes for lithium-ion batteries and electrochemical capacitors [1,2].

Iron (Fe) oxide is another cost-effective material, which exhibits good pseudo-capacitive performance [3]. Fe is a versatile element and can form several phases with different oxidation states and structures, as shown below [4].

$$FeO \longleftrightarrow Fe_3O_4 \longleftrightarrow \gamma\text{-}Fe_2O_3 \longleftrightarrow \alpha\text{-}Fe_2O_3 \longleftrightarrow FeOOH \qquad (6\text{-}1)$$

Magnetite (Fe_3O_4), maghemite (γ-Fe_2O_3) and hematite (α-Fe_2O_3) are the most common of the many Fe oxides which exist in nature. Wang *et al.* [3] have reported that the magnetite (Fe_3O_4) electrode demonstrates ideal capacitive behavior and possesses a specific capacitance as high as 170 Fg^{-1} in Na_2SO_4 electrolytes [3]. Xie *et al.* [5] have prepared highly ordered α-Fe_2O_3 nanotube arrays by a simple anodization method on Fe foil. The α-Fe_2O_3 nanotube arrays exhibit relatively high specific capacitance (138 Fg^{-1}) and good cycling stability (89% capacitance retention after 500 cycles), due to the nanostructured feature of the α-Fe_2O_3 nanotube arrays, providing high surface area and fast ion transport pathways [5]. Also, Wu *et al.* [6] prepared porous Fe oxide (Fe_2O_3) films with different morphologies including nanorods and nanosheets by anodic deposition on nickel substrates using a plating bath containing $Fe(NH_4)_2(SO_4)_2 \cdot 6H_2O$ at room temperature. The morphology of the films deposited at a current density lower than 0.125 $mAcm^{-2}$ was in the form of nanosheets, while films deposited at

a current density higher than 0.125 $mAcm^{-2}$ were in the form of nanorods. The specific capacitance value for Fe oxide nanosheets was higher than that for Fe oxide nanorods. The highest specific capacitance of 146 Fg^{-1} at 5 mVs^{-1} was obtained for Fe oxide films annealed at 300ºC [6].

Vanadium pentoxide (V_2O_5) is also a candidate material for application in energy storage because of its layered structure, high capacity and ease of preparation [7]. It has been shown that amorphous V_2O_5 possesses high capacitance in neutral electrolytes. V_2O_5 acts as an advanced intercalation host material for Li^+, K^+, Na^+, Mg^{2+} and Ca^{2+} and so has attracted great interest in the field of electrochemistry [8,9]. Lithium ion insertion into V_2O_5 serves as the fundamental reaction:

$$x\mathrm{Li}^+ + \mathrm{V_2O_5} + x\mathrm{e}^- \longrightarrow \mathrm{Li_xV_2O_5} \qquad (6\text{-}2)$$

Lithium ions can be intercalated and deintercalated between the adjacent layers of V_2O_5. Therefore, electrical energy is stored and released in the V_2O_5 electrode during intercalation and deintercalation, respectively. However, the moderate electrical conductivity (10^{-2} -10^{-3} Scm^{-1}) of V_2O_5 [10] and the low diffusion coefficient of Li^+ ions (10^{-12} -10^{-13} cm^2s^{-1}) [11] in the V_2O_5 matrix results in a limitation in the intercalation capacity and charge/discharge rate of V_2O_5. To solve these problems, nanostructured V_2O_5 can be used, which provides short diffusion path lengths for ion diffusion and electron transfer. Reddy *et al.* [7] have reported that a nano-porous layered V_2O_5 structure prepared using sol-gel methods has a high capacitance value of 214 Fg^{-1} in a 2 M KCl electrolyte [7]. Also, Loa *et al.* [12] have indicated that chemically pure V_2O_5 powders prepared by co-precipitation show high specific capacitance of 262 Fg^{-1} [12].

The electrochemistry of transition metal oxides is closely related to the electronic conductivity in the solid phase and ionic mobility in the pores. Incorporation of other transition metals into the host oxide is a common approach for improving electrochemical performance. The electrochemical properties of Mn oxide can be

optimized by the partial replacement of Mn ions with other transition metal ions. Therefore, several attempts have been reported to substitute some of the Mn ions with other transition metal ions such as Co [13], Fe [14], V [14], Ni [15] and Cr [16,17]. Yoo *et al.* [14] have synthesized V and Fe doped Mn oxide nanowires via a hydrothermal reaction of a mixed solution of metal components and oxalate ligands. They reported an improvement in the electrochemical properties of 1D nanostructured Mn oxide electrodes doped with Fe and V. The improvement was more prominent for Fe additions relative to V additions [14]. Lee *et al.* [18] have investigated the effect of Fe concentration on the electrochemical capacitance behavior of Mn-Fe oxide electrodes prepared by electrodeposition [18]. For this purpose, up to 0.15 M $FeCl_3$ was added to a 0.25 M Mn acetate solution. The optimum specific capacitance of 212 Fg^{-1} (21% higher than that for Mn oxide) was obtained for the oxide deposited in a solution containing 0.05 M $FeCl_3$. Also, the capacitance retention of the Mn-Fe oxide after 1000 cycles was improved to 85% of original value, while the capacitance retention was 70% of original value for Mn oxide electrodes [18].

The aim of this chapter is to investigate the effect of the dopant Fe ions on the morphology, chemistry and crystal structure of Mn oxide electrodes, prepared using the methods described in Chapters 3-5. The specific capacitance and electrochemical cyclability of Fe doped Mn oxide electrodes are determined. Also, the effect of V additions on the morphology of Mn-V oxides is investigated.

6.2 Experimental procedure

Mn-Fe and Mn-V doped oxide coatings were anodically electrodeposited from three different types of dilute solutions onto Au coated Si substrates with current densities in the 1-20 $mAcm^{-2}$ range and deposition duration of 10 min, using the procedure described in Chapter 2, Section 2.2. Mn-V coatings were deposited from a solution of 0.01 M Mn acetate ($Mn(CH_3COO)_2$), 0.001 M sodium metavanadate ($NaVO_3$) and 0.05 M sodium nitrate ($NaNO_3$). Two different types of dilute solutions were used to deposit Mn-Fe oxide coatings, including 0.01 M

$Mn(CH_3COO)_2$, 0.0005 M iron ammonium sulfate ($Fe(NH_4)_2SO_4$) and 0.05 M sodium sulfate (Na_2SO_4) or 0.01 M $Mn(CH_3COO)_2$ and 0.001 M iron chloride ($FeCl_3$). A Pt counter electrode was placed vertically 20 mm away from a vertical Au coated Si working electrode. The solution temperature was adjusted to 60°C. After electrodeposition the working electrodes were rinsed with deionized water and dried in air. The mass of the Mn-Fe oxide deposits was determined using a microbalance, as explained in Chapter 2, Section 2.2.

Morphological and crystal structural analysis of the oxide deposits was conducted using SEM and TEM with the operating parameters described in Chapter 2, Section 2.2. Also, chemical state analysis was performed by XPS, under the conditions given in Chapter 2, Section 2.2.

The Mn content in 0.5 M Na_2SO_4 electrolytes after 2 and 250 cycles for Mn-Fe oxide deposits was determined using a VARIAN 220 FS atomic absorption spectrometer (AAS).

In order to determine the electrochemical behavior of the Mn-Fe oxide electrodes, a Gamry PC4/750 potentiostat/galvanostat was used for cyclic voltammetry (CV) in an electrolyte containing 0.5 M Na_2SO_4 at room temperature, as described in Chapter 2, Section 2.2. Cyclic voltammograms were recorded between –0.1 and 0.9 V vs. SCE at different scanning rates from 5 to 1000 mVs^{-1}. For consistency, all CV scans were done using fresh deposits.

6.3 Results and discussion

6.3.1 Mn-Fe oxide deposit morphologies

The morphology of as-prepared Mn-Fe oxide deposits was analyzed using SEM. Plan view and cross sectional SE images (Figure 6-1) reveal free-standing Mn-Fe rods prepared from two of the different dilute solutions, i.e., 0.01 M $Mn(CH_3COO)_2$ plus 0.001 M $FeCl_3$ (Figure 6-1a and b) and 0.01 M

$Mn(CH_3COO)_2$, 0.0005 M $Fe(NH_4)_2SO_4$ and 0.05 M Na_2SO_4 (Figure 6-1c and d) using a template-free method. The best Mn-Fe deposits, both in terms of obtaining a rod-like structure and mechanical integrity, were fabricated at a current density of 15 $mAcm^{-2}$. Adherent and rod-like structures were obtained only for current densities between 10 and 20 $mAcm^{-2}$ and delamination of deposits occurred at ≤10 $mAcm^{-2}$. This is similar to the results obtained for Mn-Co deposits, described in Chapter 4, Section 4.3.1. The SEM images reveal that Mn-Fe deposits obtained from a $FeCl_3$-containing solution have a more uniform rod-like structure and the surface coverage is higher relative to deposits prepared from a $Fe(NH_4)_2SO_4$-containing solution.

Mn-Fe oxide deposited from solutions with higher concentrations of Fe, i.e., 0.001 M for $Fe(NH_4)_2SO_4$ and 0.005 M for $FeCl_3$, were also prepared but adhesion to the substrate was poor, so that morphological analysis and electrochemical measurements could not be made.

During the oxide deposition process, the anodic reaction is as follows:

$$M^{2+} + xH_2O \longrightarrow MO_x + 2xH^+ + (2x\text{-}2)e^- \qquad (6\text{-}3)$$

The pH value of the solution decreases with the addition of Fe (from 7.5 to 6), which leads to retardation in the oxide deposition rate [18]. As explained in Chapter 5, Section 5.3.1.1, there is a linear relationship between current density and deposition rate. When the current density is increased, the deposition rate is increased. As the deposition rate increases, the amount of deposit formed on the surface is increased ($V = \Delta m/\Delta t$). For example, the mass of Mn oxides prepared at 5 and 15 $mAcm^{-2}$ was ~0.2 and 0.23 $mgcm^{-2}$, respectively. However, the mass of Mn-Fe oxide prepared at 15 $mAcm^{-2}$ (0.2 $mgcm^{-2}$) was lower than that obtained for Mn oxide prepared at 15 $mAcm^{-2}$ (0.23 $mgcm^{-2}$). Therefore, there was a decrease in the deposition rate due to a reduction in the solution pH value for Mn-Fe oxide deposits. As shown in Chapter 5, Section 5.3.1.1, the rod diameter

increases at higher deposition rate. However, the size of Mn-Fe oxide rods prepared at 15 $mAcm^{-2}$ is ~1.5μm, which is lower than that obtained for Mn oxide prepared at 15 $mAcm^{-2}$ (~1.7 μm). Therefore, the deposition rate for Mn-Fe oxide is reduced relative to Mn oxide at the same current density, due to lower pH value.

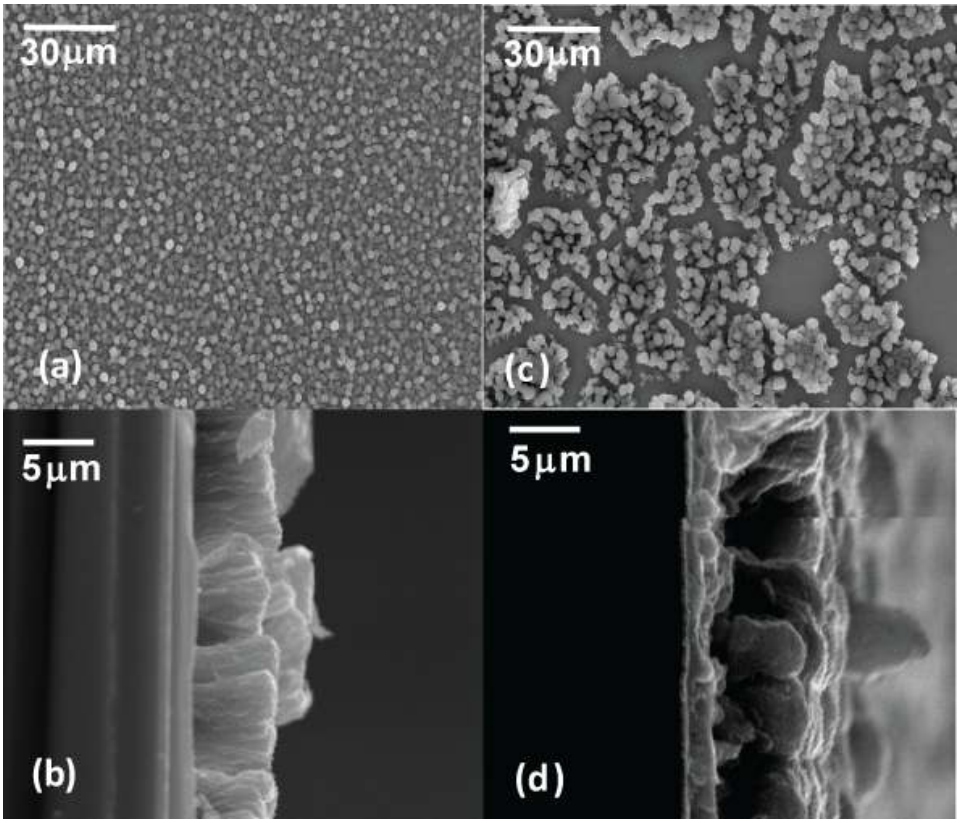

Figure 6-1 SEM SE plan view and cross–sectional images of Mn-Fe oxide deposits prepared from a solution of (a) and (b) 0.01 M $Mn(CH_3COO)_2$ and 0.001 M $FeCl_3$; (c) and (d) 0.01 M $Mn(CH_3COO)_2$, 0.0005 M $Fe(NH_4)_2SO_4$ and 0.05 M Na_2SO_4. Depositions were done at 15 $mAcm^{-2}$ for 10 min.

6.3.2 Crystal structure analysis of Mn-Fe oxide deposits

The crystal structure of the Mn-Fe oxide rods obtained from the two dilute solutions was analyzed using electron diffraction in the TEM. TEM BF images

(Figure 6-2a and 6-2c) reveal the fibrous surfaces for Mn-Fe oxide deposits prepared from a solution of 0.01 M $Mn(CH_3COO)_2$ and 0.001 M $FeCl_3$ as well as for deposits from a solution of 0.01 M $Mn(CH_3COO)_2$, 0.0005 M $Fe(NH_4)_2SO_4$ and 0.05 M Na_2SO_4. The deposit prepared from the $FeCl_3$-containing solution, shows a more fibrous surface relative to that prepared from the $Fe(NH_4)_2SO_4$-containing solution. Figure 6-2b and 6-2d show DF images taken from part of the first two diffracted rings, for Mn-Fe deposits prepared from the $FeCl_3$- and $Fe(NH_4)_2SO_4$-containing solutions, which consist of polycrystalline grains with diameters less than 10 and 8 nm, respectively. SAED patterns for Mn-Fe deposits are shown in the insets of Figure 6-2b and 6-2d. The continuous ring patterns confirm their nanocrystalline nature. Mn-Fe oxide prepared from a $Fe(NH_4)_2SO_4$-containing solution shows a more diffuse ring pattern relative to Mn-Fe oxide prepared from a $FeCl_3$-containing solution. This is further confirmation of the finer grain size for the deposits prepared from the $Fe(NH_4)_2SO_4$-containing solution. The *d*-spacings measured from the SAED patterns for the Mn-Fe oxides are consistent with a FCC crystal structure (antifluorite-type) with a lattice parameter of 0.455 nm. The antifluorite structure has O^{2-} ions occupying FCC positions, with Mn and Fe cations randomly occupying some of the tetrahedral interstices. Similar crystal structures were obtained for MnO_2 deposits (Chapter 2, Section 2.3.1 and Chapter 3, Section 3.3.3) and Mn-Co oxide deposits (Chapter 4, Section 4.3.1). This shows that the incorporated Fe oxide did not change the crystal structure of deposited Mn oxide, since no separate Fe oxide phases were formed. Although, both Mn oxide and Mn-Fe oxide deposits have an antifluorite-type crystal structure, there are some differences in terms of lattice parameters and cell volumes. As described for Mn-Co oxide in Chapter 4, Section 4.3.1, these differences can be attributed to ion size differences. Mn^{4+} ions (R_{Mn4+} = 0.053 nm) are smaller than both Fe^{2+} (R_{Fe2+} = 0.074 nm) and Fe^{3+} (R_{Fe3+} = 0.064 nm) ions. Also, when Fe ions substitute for Mn ions in the lattice structure, extra Fe ions will be needed for charge compensation and will likely go into interstitial positions. The theoretical densities for MnO_2 and Mn-Fe oxide prepared from the $FeCl_3$-containing solution, assuming 9.1 at% Fe (with 68% Fe^{2+} and 32% Fe^{3+}

making up the Fe content, described in Section 6.3.3), are 3.32 and 3.04 gcm^{-3}, respectively. For Mn-Fe oxides prepared from the $FeCl_3$-containing solution, there was an increase in the MnO_2 lattice parameter by about ~2.2% compared with that for Mn oxide, which correlates to ~8.5% reduction in density. Therefore, if $Fe^{2+}$and/or Fe^{3+} replace Mn^{4+} in the lattice, a slight increase in lattice parameter and cell volume can be expected.

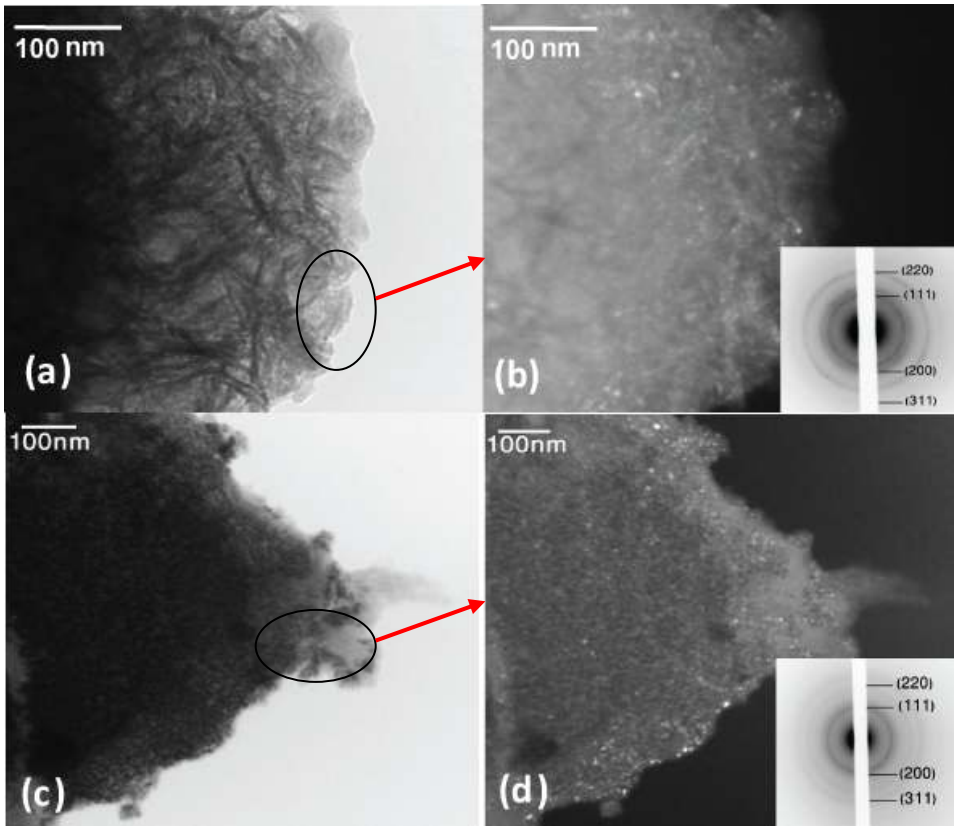

Figure 6-2 (a) TEM BF image for Mn-Fe oxide prepared from a solution of 0.01 M $Mn(CH_3COO)_2$ and 0.001 M $FeCl_3$; (b) TEM DF image and SAED pattern of region indicated in (a). (c) TEM BF image for Mn-Fe oxide prepared from a solution of 0.01 M $Mn(CH_3COO)_2$, 0.0005 M $Fe(NH_4)_2SO_4$ and 0.05 M Na_2SO_4 at 15 $mAcm^{-2}$; (d) TEM DF image and SAED pattern of region indicated in (c).

6.3.3 Chemical state analysis of Mn-Fe oxide deposits

Chemical state analysis for the Mn-Fe oxide deposits was conducted using XPS (Figure 6-3a-f). As explained in Chapter 4, Section 4.3.2, the Mn3s spectrum can be used to approximate the valence of Mn cations using the 3s splitting width for Mn oxide deposited on Pt coated Si substrates. Pt coated Si substrate are used to prevent overlap of the Au4f and Mn3s peaks. Unfortunately, the adhesion for Mn-Fe oxide deposits to Pt coated Si substrates was poor, so XPS analysis could not be performed on these samples. Therefore, Au coated substrates had to be used and the Mn2p spectrum was examined (Figure 6-3a and b). The $2p_{3/2}$ binding energy peaks are located at 642.4 eV and 642.32 eV and the $2p_{1/2}$ peaks are located at 653.9 eV and 653.87 eV for deposits prepared from the $FeCl_3$- and $Fe(NH_4)_2SO_4$-containing solutions, respectively. The peak positions and the separation between $Mn2p_{3/2}$ and $2p_{1/2}$, which is ~11.5 eV, can be attributed to a Mn valence of 3+ and/or 4+.

The possible variations in oxidation states for Fe are determined from the Fe 2p peaks in the XPS spectra. Figure 6-3c and d shows the Fe 2p spectra for Mn-Fe oxide prepared from the $FeCl_3$- and $Fe(NH_4)_2SO_4$-containing solutions, respectively. The Fe 2p spectrum consists of two main lines, i.e., $2p_{3/2}$ at 710.95 eV and 710.25 eV and $2p_{1/2}$ at 724.45 eV and 725.25 eV, separated by 13.5 eV and 15.0 eV, for Mn-Fe oxides prepared from the $FeCl_3$- and $Fe(NH_4)_2SO_4$-containing solutions, respectively. Also, a satellite peak is present at 716.35 eV for Mn-Fe oxide prepared from the $FeCl_3$- containing solution (Figure 6-3c). It has been shown that the binding energies of the peaks, which are related to the presence of Fe^{2+} or Fe^{3+}, systematically change with oxide composition [19]. There is a range of reported energy differences between the Fe^{2+} and Fe^{3+} main peaks and the satellite peaks in the Fe2p spectrum [20]. Fe $2p_{3/2}$ peaks located at 709.7 eV and 711.1 eV reveal the presence of Fe^{2+} and Fe^{3+}, respectively. When Fe $2p_{1/2}$ peaks are located at 723.3 eV and 724.7 eV, Fe^{2+} and Fe^{3+} are present in the deposits, respectively [19] .Therefore, both Fe^{2+} and Fe^{3+}cations exist in both Mn-Fe oxide deposits. The amount of Fe^{2+} cations is higher than the amount of

Fe^{3+}cations in the Mn-Fe oxides. For the deposit prepared from the $FeCl_3$-containing solutions in Figure 6-3e, the amounts of Fe^{2+} and Fe^{3+} were determined to be 68% and 32%, respectively, while for the deposit prepared from the $Fe(NH_4)_2SO_4$-containing solutions in Figure 6-3f, these values are 58% and 42%, respectively.

The O1s spectrum can be deconvoluted into three major bond components, i.e., metal oxide (M-O-M, M includes Mn and Fe), metal hydroxide (M-O-H) and residual structural water (H-O-H) (Figure 6-3e and f). It was difficult to distinguish between the Mn bond and the Fe bond because the difference in the binding energy between these two bonds is less than the resolution limit [21]. The formation of a hydrated film is considered to be critical to the capacitance mechanism as the fraction of reaction sites accessible to the Faradaic process is larger when the deposit is in a hydrous form [22]. For the deposit prepared from the $FeCl_3$-containing solutions in Figure 6-3e, the amounts of MnO_2, MnOOH and water were determined to be 57%, 39% and 4%, respectively, while for the deposit prepared from the $Fe(NH_4)_2SO_4$-containing in Figure 6-3f, these values are 60%, 34% and 6%, respectively.

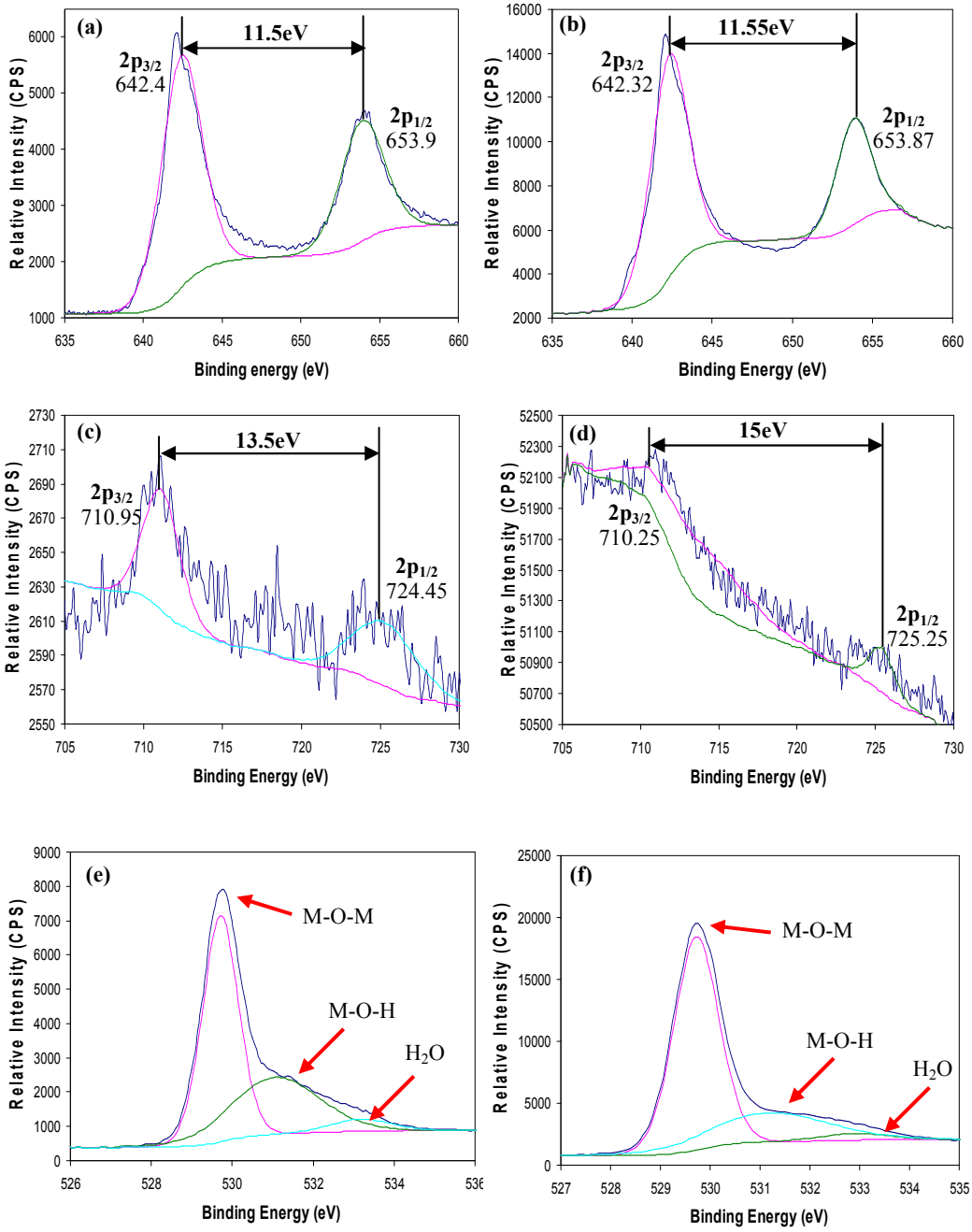

Figure 6-3(a) and (b) XPS Mn2p spectrum; (c) and (d) XPS Fe2p spectrum; (e) and (f) XPS O1s spectrum for Mn-Fe oxide deposits. Deposits in (a), (c) and (e) were prepared from a solution containing 0.01 M $Mn(CH_3COO)_2$ and 0.001 M $FeCl_3$, while deposits in (b), (d) and (f) were prepared from a solution containing 0.01 M $Mn(CH_3COO)_2$, 0.0005 M $Fe(NH_4)_2SO_4$ and 0.05 M Na_2SO_4. All oxides were deposited at 15 $mAcm^{-2}$.

6.3.4 Electrochemical behaviour of Mn-Fe oxide deposits

The electrochemical properties of the Mn-Fe oxide coatings were evaluated using CV curves. Several scan rates were tested for the voltammetry work, i.e., 5, 20, 100, 500 and 1000 mVs^{-1} for up to 250 cycles in a 0.5 M Na_2SO_4 solution. The original specific capacitances were taken after the second cycle. The highest specific capacitance values were obtained at 100 mVs^{-1}, similar to those obtained for Mn and Mn-Co oxides (Chapter4, Section 4.3.3). Two representative sets of plots for deposits prepared at 15 $mAcm^{-2}$ from the $FeCl_3$- and $Fe(NH_4)_2SO_4$-containing solutions, cycled at 100 mVs^{-1}, are shown in Figure 6-4. Even at the high potential scan rate, rectangular shapes and mirror-image characteristics for electrodes are achieved for Mn-Fe oxide prepared from the $FeCl_3$-containing solution. The satisfactory kinetic reactivity makes the binary oxides promising electrode materials for high-power electrochemical capacitor applications. The CV curves for Mn-Fe oxide prepared from the $Fe(NH_4)_2SO_4$-containing solutions are not that rectangular in shape. The voltammetric curves, for Mn-Fe oxide prepared from both solutions, exhibit weak anodic peaks centered at about 0.56 V and 0.59 V and cathodic peaks centered at about 0.38 V and 0.35 V for deposits prepared from the $FeCl_3$- and $Fe(NH_4)_2SO_4$-containing solutions, respectively. The anodic and cathodic peaks are characteristic of redox transitions resulting from ion exchange. The anodic and cathodic peaks for deposits prepared from the $FeCl_3$-containing solution are weaker relative to those prepared from the $Fe(NH_4)_2SO_4$-containing solution. This indicates that the former electrodes are charged and discharged at or near a constant rate over the complete voltammetric cycle [23].

Fe additions to the oxides appeared to affect the enclosed area of the CV curves. A larger enclosed area is obtained for Mn-Fe oxide deposits (Figure 6-4a and b) relative to Mn oxide deposits (Figure 4-5c). The area under the voltammetry curves is larger for deposits prepared from the $FeCl_3$-containing solution relative to those prepared from the $Fe(NH_4)_2SO_4$-containing solution, indicating the higher

energy density and superior charge storage capability of the oxide prepared from the $FeCl_3$-containing solution.

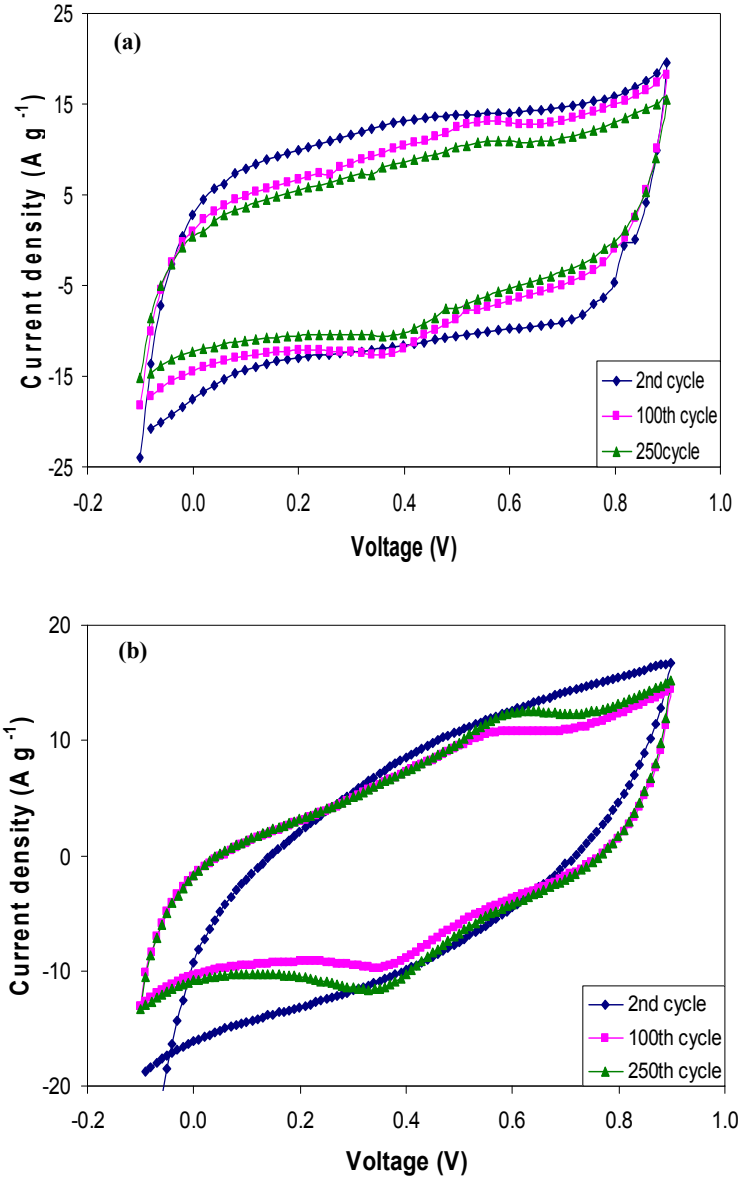

Figure 6-4 Representative cyclic voltammograms taken from Mn-Fe oxide prepared from (a) a 0.01 M $Mn(CH_3COO)_2$ and 0.001 M $FeCl_3$ solution; (b) a 0.01 M $Mn(CH_3COO)_2$, 0.0005 M $Fe(NH_4)_2SO_4$ and 0.05 M Na_2SO_4 solution. Deposits were prepared at15 $mAcm^{-2}$ and samples were cycled at 100 mVs^{-1} for up to 250 cycles.

The capacitance values for Mn-Fe oxide deposits prepared from the $FeCl_3$- and $Fe(NH_4)_2SO_4$-containing solutions, at different scan rates (5-1000 mVs^{-1}), are tabulated in Table 6-1 and 6-2, respectively. For both Mn-Fe oxides, there was an increase in capacitance values for increasing scan rate up to 100 mVs^{-1}, followed by a decrease in capacitance with increasing scan rate after 100 mVs^{-1}. This behavior is similar to that obtained for Mn and Mn-Co oxide (Chapter 4, Section 4.3.3). The best initial capacity for Mn-Fe oxide prepared from the $FeCl_3$-containing solution, cycled at 100 mVs^{-1}, was 208 Fg^{-1}, which was slightly higher than the best capacitance for the Mn oxide deposits (203 Fg^{-1} - Chapter 4, Section 4.3.3). The best capacitance for Mn-Fe oxide prepared form the $Fe(NH_4)_2SO_4$-containing solution was 195 Fg^{-1}, which was lower than both of the above values. After 250 cycles at 100 mVs^{-1}, the specific capacitance value for the Mn-Fe oxide deposit prepared from the $FeCl_3$-containing solution was 172 Fg^{-1} (reduction in capacitance was 17% of the initial reversible capacity). The same capacitance reduction (17% of the initial reversible capacity) was obtained for the Mn-Fe oxide deposit prepared from the $Fe(NH_4)_2SO_4$-containing solution. There was a monotonous decline in capacitance with increasing scan rate after 100 mVs^{-1}, due to kinetic limitations. The potential drop of the electrode and diffusion limitation of reactants near the electrode/electrolyte interface also cause a capacitance decay at high scan rates [21]. Also as discussed in Chapter 4, Section 4.3.3, at higher scan rates, charge storage by adsorption becomes predominant (Chapter4, Reaction 4-2), leading to a decrease in capacitance.

Table 6-1 Specific capacitance values for Mn-Fe oxide deposited at 15 $mAcm^{-2}$ from a solution of 0.01 M $Mn(CH_3COO)_2$ and 0.001 M $FeCl_3$

Scan rate (mVs^{-1})	Specific capacitance after second cycle (Fg^{-1})	Specific capacitance after 250 cycles (Fg^{-1})	Specific capacitance decrease after 250 cycles (%)
5	135	105	22
20	188	150	20
100	208	172	17
500	97	85	12
1000	85	75	12

Table 6-2 Specific capacitance values for Mn-Fe oxide deposited at 15 $mAcm^{-2}$ from a solution of 0.01 M $Mn(CH_3COO)_2$, 0.0005 M $Fe(NH_4)_2SO_4$ and 0.05 M Na_2SO_4

Scan rate (mVs^{-1})	Specific capacitance after second cycle (Fg^{-1})	Specific capacitance after 250 cycles (Fg^{-1})	Specific capacitance decrease after 250 cycles (%)
5	125	97	22
20	181	142	21
100	195	162	17
500	93	81	13
1000	80	70	12

Mn-Fe oxide electrodes prepared from a $FeCl_3$-containing solution provide higher capacitance values (~2.5% higher for the best electrodes) and better electrochemical cyclability relative to the Mn oxide electrodes. The capacitance values for the best Mn-Fe oxide electrodes prepared from a $FeCl_3$-containing solution are 7% higher relative to those for Mn oxide deposits after 250 cycles. One reason for higher capacitance value may be the lower water content for Mn-Fe oxides prepared from the $FeCl_3$-containing solution relative to Mn oxide (XPS analysis - Figure 6-3e for Mn-Fe oxide and Figure 2-5b for Mn oxide). The lower amount of electro-inactive species, which do not contribute to pseudocapacitance, leads to an overall improvement in the specific charge storage performance [21].

In addition, as described in Section 6.3.2, Mn–Fe oxide is less dense relative to Mn oxide, thereby promoting proton diffusion. Mn–Fe oxide rods offer more electrochemically accessible active sites compared to Mn oxide rods, facilitating ion transport.

The capacitance value for the best Mn-Fe oxides was ~7% higher than that for the best Mn oxides after 250 cycles, which according to ref. [18] maybe due to lower dissolution of Mn ions because of the presence of Fe. AAS analysis after 250 cycles, gave solution Mn levels of 0.25 ppm for Mn oxide and 0.23 ppm for Mn-Fe oxide prepared from the $FeCl_3$-containing solution. These values are not appreciably different, so it is not clear if Fe reduces the dissolution of Mn oxide.

Mn-Fe oxide prepared from the $Fe(NH_4)_2SO_4$-containing solution shows ~4% lower capacitance compared with Mn oxide, while the capacitance value is improved by 2% for the best electrodes after 250 cycles, relative to Mn oxide. Therefore, the $Fe(NH_4)_2SO_4$-containing solution does not significantly affect the capacitive behavior of Mn oxide electrodes. The higher water content and lower hydrous state for Mn-Fe oxides prepared from the $Fe(NH_4)_2SO_4$-containing solution, relative to Mn-Fe oxide prepared from the $FeCl_3$-containing solution and Mn oxide (Figure 6-3f for Mn-Fe oxide and Figure 2-5b for Mn oxide) are possible reasons for lower capacitance values for Mn-Fe oxide deposits [21]. However, Fe additions still help reduce Mn ion dissolution during cycling leading to an improvement in electrochemical cyclability of the electrodes.

Mn-Fe oxides prepared from the $FeCl_3$- and $Fe(NH_4)_2SO_4$-containing solutions show lower capacitance values (2% and 8% lower, respectively, for the best electrodes) compared with the best Mn-Co oxide electrodes (Chapter 4, Section 4.3.3). Also, Mn-Co oxides show better electrochemical cyclability relative to Mn-Fe oxides. The capacitance values for Mn-Fe oxide electrodes prepared from the $FeCl_3$- and $Fe(NH_4)_2SO_4$-containing solutions after 250 cycles are 5% and

12% lower, respectively, for the best electrodes compared with Mn-Co oxide electrodes (Chapter 4, Section 4.3.3).

As shown in Figure 6-1, deposits prepared from the $FeCl_3$-containing solution have a more uniform rod-like morphology and larger specific surface area, due to the higher number of the rods per cm^2 of substrate surface. To illustrate this, a simple order of magnitude calculation is done. Deposits prepared from the $FeCl_3$-containing solution have rods that are ~1.5 μm in diameter and ~8 μm in length. There are approximately 2 rods per 9 μm^2 of substrate surface. This provides a planar density of ~8.5 cm^2 of electrode surface per cm^2 of substrate surface, while a planar density of ~5 cm^2 of electrode surface per cm^2 of substrate surface is obtained for the deposits prepared from the $Fe(NH_4)_2SO_4$-containing solution. Deposits prepared from the $Fe(NH_4)_2SO_4$-containing solution had the same rod diameter and length as the deposits prepared form the $FeCl_3$-containing solution, however, the number of rods per cm^2 of substrate surface was significantly lower (2 rods per 15 μm^2 of substrate surface). It should be noted that the actual surface areas for both electrodes are higher than the surface areas calculated here, since the calculated surface areas do not account for the fibrous surface features on the rods. The increase in relative surface area can account for the higher specific capacitance values for $FeCl_3$-containing solutions. Also, Mn-Fe oxide prepared from the $FeCl_3$-containing solution has a higher crystallization degree (inset of Figure 6-2b) relative to Mn-Fe oxide prepared form the $Fe(NH_4)_2SO_4$-containing solution (inset of Figure 6-2d). As shown in Chapter 5, Section 5.3.4, deposits with a higher crystallization degree show better electrochemical capacitance behavior. It has been shown that in addition to morphology and crystal structure, the chemical composition and chemical state affect the electrochemical capacitance behavior of electrode materials [18]. The water content was higher and the hydrous state was lower for Mn-Fe oxides prepared from the $Fe(NH_4)_2SO_4$-containing solution relative to those prepared from the $FeCl_3$-containing solution.

6.3.5 Mn-V oxide deposits

The morphology of as-prepared Mn-V oxide deposits was analyzed using SEM. Figure 6-5 shows plan view and cross sectional SE images for Mn-V oxides deposited at 15 $mAcm^{-2}$ for 10 min, from a solution of 0.01 M $Mn(CH_3COO)_2$, 0.001 M $NaVO_3$ and 0.05 M $NaNO_3$. The Mn-V oxide deposits (Figure 6-5) are more continuous relative to the Mn-Fe oxide deposits (Figure 6-1). Therefore, the Mn-V oxide deposits have lower specific surface areas relative to Mn-Fe oxides. Note that there are numerous microcracks within the Mn-V oxide coatings. For current densities higher and lower than 15 $mAcm^{-2}$, the deposits had poor adhesion to the Au coated Si substrates. However, the adhesion at 15 $mAcm^{-2}$ was not still satisfactory. Therefore, electrochemical measurements and chemical and structural analysis, could not be done.

Potentiostatic control was also used to prepare Mn-V oxide deposits; however, the deposit adhesion to the substrate was still poor. Further investigation is required to obtain the best electrodeposition conditions to prepare oxide deposits with appropriate morphology, chemistry and crystal structure.

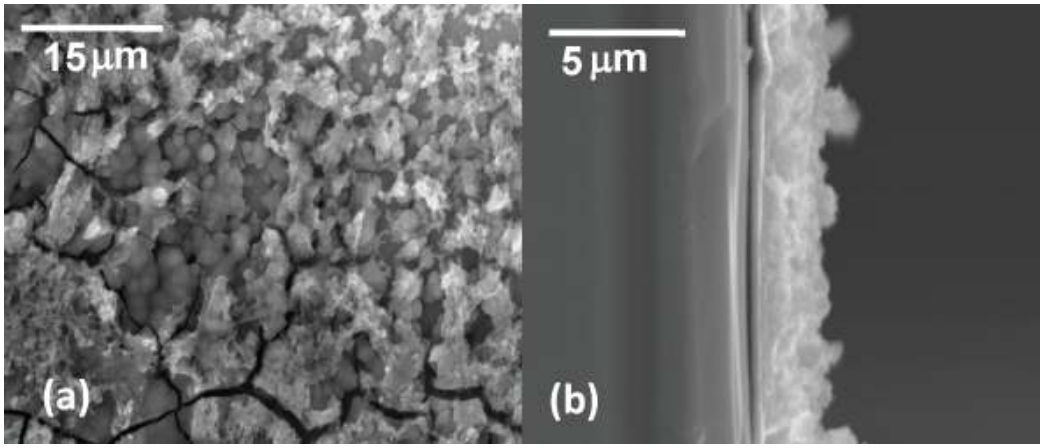

Figure 6-5(a) SEM SE plan view and (b) cross–sectional images of Mn-Fe oxide deposits prepared from a solution of 0.01 M $Mn(CH_3COO)_2$, 0.001 M $NaVO_3$ and 0.05 M $NaNO_3$ at 15 $mAcm^{-2}$.

6.4 Conclusions

Mn-Fe oxides with a rod-like morphology and antifluorite-type structure were electrochemically deposited from $FeCl_3$-containing and $Fe(NH_4)_2SO_4$-containing solutions. Mn-Fe oxide electrodes consisted of MnO_2, with partial Fe^{2+} and Fe^{3+} ion substitution for Mn^{4+}. Mn-Fe oxide prepared from $FeCl_3$-containing solutions had good capacitances (up to 208 Fg^{-1}) at a scanning rate of 100 mVs^{-1} and maintained a high capacitance after 250 cycles in 0.5 M Na_2SO_4 (83% retention). However, Mn-Fe oxide deposited from $Fe(NH_4)_2SO_4$-containing solutions had lower electrochemical capacitances relative to Mn-Fe oxide prepared from $FeCl_3$-containing solutions and did not significantly affect the capacitive behavior of Mn oxide. For both types of Mn-Fe oxide deposits, capacitance values increased with increasing scan rate to 100 mVs^{-1}, and then steadily decreased after 100 mVs^{-1}.

For Mn-V oxides, the adhesion to the substrate was poor. As such chemical, electrochemical and structural analysis was not done.

References

[1] A.L. Cabrera, M.B. Maple and G. Arrhenius, *Appl. Catal.*, **64**, 309(1990).

[2] M.M. Thackeray, *Prog. Solid State Chem.*, **25**, 1 (1997).

[3] S.Y. Wang, K.C. Ho, S.L. Kuo and N.L. Wu, *J. Electrochem. Soc.*, **153**, A75 (2006).

[4] R.W. Cornell and U. Schwertmann, The Iron Oxides, VCH, Weinheim (1996).

[5] K. Xie,J. Li, Y. Lai and H. Huang, *Electrochem. Commun.* (2011) In press.

[6] M.S. Wu and R.H. Lee, *J. Electrochem. Soc.*, **156(9)**, A737 (2009).

[7] R.N. Reddy and R.G. Reddy, *J. Power Sources*, **156**, 700 (2006).

[8] W. Li and S. H. Garofaliniz, *J. Electrochem. Soc.*, **152**, A364 (2005).

[9] C. Bolm, Coord. *Chem. Rev.*, **237**, 245 (2003).

[10] F. Coustier, J. Hill, B.B. Owens, S. Passerini and W.H. Smyrl, *J. Electrochem. Soc*., **146**, 1355(1999).

[11] F. Lantelme, A. Mantoux, H. Groult and D. Lincot, *J. Electrochem. Soc.*, **150**, A1202(2003).

[12] Z.J. Lao, K. Konstantinov, Y. Tournaire, S.H. Ng, G.X. Wang, H.K. Liu, *J. Power Sources*, **162**, 1451 (2006).

[13] S.H. Lee, T.W. Kim, D.H. Park, J.H. Choy, S.J. Hwang, N. Jiang, S.E. Park and Y.H. Lee, *Chem. Mater.*, **19**, 5010 (2007).

[14] H.N. Yoo, D.H. Park and S.J. Hwang, *J. Power Sources*, **185**, 1374 (2008).

[15] D.H. Park, S.T. Lim, S.J. Hwang, C.S. Yoon, Y.K. Sun and J.H. Choy, *Adv. Mater.*, **17**, 2834 (2005).

[16] D.H. Park, S.H. Lee, T.W. Kim, S.T. Lim, S.J. Hwang, Y.S. Yoon, Y.H. Lee and J.H. Choy, *Adv. Funct. Mater.*, **17**, 2949 (2007).

[17] D.H. Park, H.W. Ha, S.H. Lee, J.H. Choy and S.J. Hwang, *J. Phys. Chem. C*, **112**, 5160 (2008).

[18] M.T. Lee, J.K. Chang and W.T. Tsai, *J. Electrochem. Soc.*, **154(9)**, A875 (2007).

[19] T.C. Lin, G. Seshadri and J.A. Kelber, *Appl. Surf. Sci.*, **119**, 83 (1997).

[20] C.R. Brundel, T.J. Chuang, K. Wandelt, *Surf. Sci.*, **68**, 459 (1977).

[21] M.T. Lee, J.K. Chang, Y.T. Hsieh and W.T. Tsai, *J. Power Sources*, **185**, 1550 (2008).

[22] B. Djurfors, J.N. Broughton, M.J. Brett and D.G. Ivey, *Acta Mater.*, **53**, 957 (2005).

[23] S.J. Bao, B.L. He, Y.Y. Liang, *Mater. Sci. Eng.*, **A 397**, 305 (2005).

Chapter 7 General conclusions and recommendations

There are some novel conclusions obtained from this research work for electrochemical synthesis, physicochemical evolution and electrochemical capacitive behaviour of Mn oxide, Mn-Co oxide, Mn-Fe oxide, Mn oxide/PEDOT and Mn-Co oxide/PEDOT electrodes.

7.1 Electrochemical synthesis of nanocrystalline electrodes

1. As described in Chapter 1, templated electrosynthesis is widely used to form high surface area rod-like structures. This method is not, however, easy to use in practical applications due to the fragility of the AAO template. Moreover, dissolution of the template is complicated and the morphology of the materials is often poor, because the AAO membrane pores can become impregnated with the reagents producing smooth-faced materials. Therefore, it is more desirable to form rod-like structures without using any templates.

   In this work, nanocrystalline Mn oxide electrodes of high porosity and composed of ~1.5 μm diameter rods were anodically electrodeposited from a 0.01 M $Mn(CH_3COO)_2$ solution onto the Au coated Si substrates under galvanostatic control, i.e., 5 mA cm^{-2}, without any templates.

2. Mn oxide deposits synthesized at a lower current density (5 $mAcm^{-2}$), showed more uniform, vertical and free-standing rod-like structures. Structural analysis revealed that Mn oxide electrodes, prepared at different current densities, were made up of MnO_2 with a FCC crystal structure (defective antifluorite-type) and MnOOH which was likely amorphous. The defective antifluorite structure has O^{2-} ions occupying FCC positions,

with Mn cations randomly occupying 25% of the tetrahedral interstices and all octahedral interstices unfilled.

3. Sequential and one–step methods were used to produce Mn oxide/PEDOT coaxial core/shell rods and agglomerated Mn oxide/PEDOT particles, respectively. In the former case, the Mn oxide rods were anodically electrodeposited from a 0.01 M $Mn(CH_3COO)_2$ solution onto Au coated Si substrates at a current density of 5 $mAcm^{-2}$ and then coated with PEDOT at 1 V for 45 s. Structural analysis for the Mn oxide/PEDOT coaxial core/shell rods revealed MnO_2 with an antifluorite–type structure coated with amorphous PEDOT.

4. Mn-Co oxide and Mn-Co oxide/PEDOT coaxial rod-like electrodes were electrochemically synthesized without any templates or catalysts. Mn-Co oxide showed an antifluorite–type crystal structure. Mn-Co oxide/PEDOT electrodes consisted of MnO_2, with partial Co^{2+} and Co^{3+} ion substitution for Mn^{4+}, and amorphous PEDOT. The chemical formulation of Mn-Co oxide was $(Mn_{0.91}Co_{0.09})O_2$ or more generally $(Mn_{1-x}Co_x)O_2$.

5. Mn-Fe oxides with a rod-like morphology and antifluorite-type structure were electrochemically deposited from $FeCl_3$-containing and $Fe(NH_4)_2SO_4$-containing solutions, without any templates. Mn-Fe oxide electrodes consisted of MnO_2, with partial Fe^{2+} and Fe^{3+} ion substitution for Mn^{4+}.

7.2 Physicochemical properties of nanocrystalline electrodes

1. As described in Chapter 2, the rod-like structures exhibit large specific surface areas, which promote efficient contact between the active material and the electrolyte, providing more active sites for electrochemical reactions. It should be noted that structures with porosity and

interconnectivity supply additional accessible space for ions while maintaining sufficient conductivity for solid-state electron transfer. Therefore, significantly enhanced capacitance and high cycling rate capability is expected. Smaller diameter rods provide larger specific surface areas for electrolyte access to improve the electrochemical capacity. Therefore, deposits synthesized at a current density of 5 $mAcm^{-2}$ showed the highest specific capacitance (203 Fg^{-1}) at 100 mVs^{-1}.

2. As described in Chapter 2, there is a drawback to the application of Mn oxides, which is the loss of capacitance with electrochemical cycling. The loss of capacitance, which was 23-25% for Mn oxide deposits prepared at different current densities after 250 cycles in 0.5 M Na_2SO_4 at 20 mVs^{-1}, can be attributed to several factors. There was loss of Mn oxide through partial dissolution during cycling. Also, deposits synthesized at higher current densities underwent a microstructural change on cycling to a petal-shaped morphology; this structure reduced the specific surface area of the Mn oxide leading to the capacitance fading. Finally, MnO_2 transformed from the antifluorite-type crystal structure to a more ordered hexagonal NiAs-type crystal structure after cycling, which limited ionic transport and charge transfer.

3. When applying the PEDOT shell to the Mn oxide rods, the porous nature of the PEDOT also allows fast ion diffusion into the core Mn oxide of the coaxial electrodes. Moreover, the electrically conductive PEDOT shell, facilitates electron transport to the core Mn oxide. Therefore, enhanced capacitance and high cycling rate capability is expected by applying a PEDOT shell on the Mn oxide rod-like cores. Manganese oxide rods synthesized at a current density of 5 $mAcm^{-2}$ and then coated with PEDOT at 1 V for 45s showed the highest specific capacitance (~295 Fg^{-1}) at 100 mVs^{-1}. The specific capacitance retention (after 250 cycles) for this coating was determined to be ~92% of the original value. The best

capacitance for co–electrodeposited (one-step) Mn oxide/PEDOT was ~195 Fg^{-1} with a retention of ~87% of the original value. After cycling, the Mn oxide/PEDOT coaxial core/shell rods maintained the same crystal structure as the as–deposited structure, i.e., MnO_2 with an antifluorite–type structure coated with amorphous PEDOT.

4. Mn-Co oxide electrodes provide ~5% higher capacitance values for the best electrodes (cycled at 100 mVs^{-1}), and better electrochemical cyclability relative to the Mn oxide electrodes. The addition of Co to Mn oxide results in ~11% reduction in density. A less dense structure should facilitate ion transport and charge transfer leading to higher capacitance values. Also, the added Co suppresses anodic dissolution of the oxide and, therefore, improves the electrochemical reversibility which was confirmed with AAS.

5. Mn-Fe oxide prepared from $FeCl_3$-containing solutions had good capacitances (up to 208 Fg^{-1}) at a scanning rate of 100 mVs^{-1} and maintained a high capacitance after 250 cycles in 0.5 M Na_2SO_4 (83% retention). However, Mn-Fe oxide deposited from $Fe(NH_4)_2SO_4$-containing solutions had lower electrochemical capacitances relative to Mn-Fe oxide prepared from $FeCl_3$-containing solutions, but similar capacitive behavior to Mn oxide.

6. For Mn oxide, Mn-Co oxide and Mn-Fe oxide rods, and Mn oxide/PEDOT and Mn-Co oxide/PEDOT coaxial core/shell rods, capacitance values increased with increasing scan rate up to 100 mVs^{-1}, and then steadily decreased after 100 mVs^{-1}. This represents an anomalous trend with potential scanning rate, as capacitance values are generally expected to decrease with increasing scan rate.

7. EIS measurements revealed that the electronic resistances, charge transfer resistances and electrolyte diffusive resistances of the electrode materials are reduced with scan rates up to 100 mVs^{-1} for both Mn oxide and Mn-Co oxide deposits. Therefore, Mn oxide and Mn-Co oxide electrodes cycled at 100 mVs^{-1} exhibit the lowest resistances. This correlates with the highest capacitance value at 100 mVs^{-1}. The next lowest resistances in increasing order of resistance occur for scanning rates of 20, 5, 500 and 1000 mVs^{-1}, respectively.

8. Among different electrodes with rod-like structures, Mn-Co oxide/PEDOT electrodes had the highest capacitance (up to 310 Fg^{-1}) at 100 mVs^{-1} and maintained their capacitance after 500 cycles in 0.5 M Na_2SO_4 (91% retention).

9. Although synthesis of the high surface area rod-like structures was the purpose of this work, in order to improve the electrochemical behaviour of electrodes it was found that thin sheets with lower thicknesses relative to rods had higher specific capacitance (~230 Fg^{-1}) and capacitance retention (~88% after 250 cycles in 0.5 M Na_2SO_4 at 20 mVs^{-1}) relative to rods. This was confirmed with EIS measurements. Also, continuous coatings provided the lowest specific surface area relative to rods and thin sheets leading to the lowest capacitance values.

7.3 Nucleation and growth mechanisms for Mn oxide electrodes

1. Mn oxide electrodes were synthesized by anodic deposition from acetate–containing aqueous solutions on Au coated Si substrates through the control of nucleation and growth processes. A variety of nanostructured Mn oxide electrodes, including continuous coatings, rod–like structures, aggregated rods and thin sheets, were obtained by changing the supersaturation ratio (deposition current density, electrolyte composition, pH and temperature) which affected the nucleation and growth processes.

2. All Mn oxide deposits with different types of morphology had an antifluorite–type crystal structure. The crystal structure of Mn oxide was not affected by the supersaturation ratio, but crystallization degree was affected. The crystallization degree was decreased on going from thin sheets to rods to aggregated rods to continuous coatings.

3. The investigation of nucleation and growth mechanisms for Mn oxide deposits with different morphologies revealed that thin sheets form by instantaneous nucleation and single crystal growth, continuous coatings show progressive nucleation and polycrystalline growth and rods have a mix of instantaneous/progressive nucleation and polycrystalline growth.

7.4 Recommendations

1. Systematic research needs to be conducted to optimize the electrodeposition parameters to synthesize Mn oxide rods with dimensions on the nanoscale instead of the micron scale, to better improve the electrochemical behaviour of the electrodes.

2. To uncover the reasons for the anomalous capacitive behaviour observed for Mn oxide, Mn-Co oxide and Mn-Fe oxide rods, and Mn oxide/PEDOT and Mn-Co oxide/PEDOT coaxial core/shell rods, cycled at various scanning rates, more quantitative information on the physicochemical changes of electrodes during cycling is required.

3. The nucleation and growth mechanisms of Mn oxide electrodes are complicated because they involve many parameters, including solution concentration, temperature, pH values, amount of charge passed and nature of the substrate. Hence, in addition to morphological analyses, it is recommended to study the nucleation mechanism by some other

techniques such as chronoamperometry techniques using mathematical models to describe the nucleation process.

4. To improve the electrochemical capacitive behavior of Mn oxide, bimetal composite materials such as Mn-Co oxides and Mn-Fe oxides were synthesized. Since V oxide has a good pseudocapacitive performance, more efforts are needed to prepare Mn-V oxides with high surface area structures. Anodic deposition of Mn-V oxide on graphite substrate is recommended to improve the adhesion to substrate.

5. Since Mn oxide thin sheets showed better electrochemical capacitance behaviour relative to Mn oxide rods with dimensions on the microscale, it is recommended to synthesize bimetal composite materials such as Mn-Co, Mn-Fe and Mn-V oxides with thin sheet morphologies. Also, to further improve the electrochemical capacitive behavior of electrodes, a shell of PEDOT can be applied on the Mn oxide and Mn doped oxide thin sheets.